



## City Research Online

### City, University of London Institutional Repository

---

**Citation:** Singh, C. (2006). Application of airjet vortex generators to control helicopter retreating blade stall. (Unpublished Doctoral thesis, City, University of London)

This is the accepted version of the paper.

This version of the publication may differ from the final published version.

---

**Permanent repository link:** <https://openaccess.city.ac.uk/id/eprint/30908/>

**Link to published version:**

**Copyright:** City Research Online aims to make research outputs of City, University of London available to a wider audience. Copyright and Moral Rights remain with the author(s) and/or copyright holders. URLs from City Research Online may be freely distributed and linked to.

**Reuse:** Copies of full items can be used for personal research or study, educational, or not-for-profit purposes without prior permission or charge. Provided that the authors, title and full bibliographic details are credited, a hyperlink and/or URL is given for the original metadata page and the content is not changed in any way.

**Application of Airjet Vortex Generators to Control Helicopter  
Retreating Blade Stall**

Chrisminder Singh

Thesis submitted as part of the requirement for the degree of  
Doctor of Philosophy

Centre for Aeronautics  
School of Engineering and Mathematical Science  
City University  
Northampton Square  
London EC1V 0HB

## Abstract

A unique characteristic of helicopter stall is the occurrence of stall on the retreating side of the rotor disk. Operating in an unsteady environment, the most severe type of stall encountered by the retreating rotor blade is dynamic stall, which limits the helicopter maximum speed, adversely affect handling qualities and causes excessive cabin vibration. Dynamic stall is characterised by the formation, migration and shedding of a leading-edge vortex. The leading-edge vortex produces a large pressure wave moving aft on the aerofoil upper surface and creating abrupt changes in the flowfield. The pressure wave also contributes to large lift and moment overshoots in excess of static values and significant nonlinear hysteresis in the aerofoil behaviour.

The proposal of the experimental research programme is to study the capability of employing an active flowfield altering device utilising low energy systems known as Air-Jet Vortex Generators (AJVGs) to suppress helicopter dynamic stall as a means to expand the helicopter flight envelope, thereby enhancing the utility of these aircraft. AJVGs consist of small jets of air emerging from an aerodynamic surface via slots/holes that are pitched and skewed relative to the oncoming freestream. The interaction between the air-jets and the freestream flow forms longitudinal streamwise vortices that re-energise the “tired” boundary layer enabling it to negotiate severe adverse pressure gradients as these vortices penetrate downstream.

The aims of the research programme are to experimentally establish:

(a), the potential of operating a spanwise array of AJVGs continuously on an oscillating aerofoil to suppress the formation of the leading-edge vortex. Wind tunnel tests will be conducted on an unswept oscillating RAE 9645 aerofoil section of chord length 500mm in the University of Glasgow Handley Page low-speed wind tunnel ( $Re_c = 1.5 \times 10^6$ ). The sinusoidal-pitching motion tests will be conducted at  $\alpha = (15 + 10 \sin \omega t)$ deg, for the reduced oscillation frequency range of  $0.01 \leq k \leq 0.181$ . The aerofoil section is equipped with an array of 28 equi-spaced, co-rotating AJVGs across the span located at 12% and 62% chord with the AJVGs operating at jet momentum blowing coefficients between  $0.0 \leq C_{\mu} \leq 0.01$ ;

(b), the effect of aerodynamic sweep on the geometry requirements of the AJVGs, keeping in mind that the retreating rotor blade can experience  $\pm 30^\circ$  variation in sweep angle. Wind tunnel tests will be conducted on a swept wing ( $\Lambda = 35^\circ$ ) half model section with parallel leading and trailing edges, constant chord ( $c = 232\text{mm}$ ), semi-span ( $b = 958\text{mm}$ ) and aspect ratio of 4.5, in an incidence range  $0^\circ < \alpha < 20^\circ$  in the City University T2 low speed wind tunnel ( $Re_c = 0.5 \times 10^6$ ). Installed in the top surface of the swept wing is a spanwise array of AJVGs located at 10% chord with jet momentum values in the range of  $0.0 \leq C_\mu < 0.01$ ; and

(c), the capability of unsteady AJVGs to reduce the blowing mass flux of steady AJVGs required to effectively delay boundary-layer separation and hence improve lift/drag performance. Wind tunnel tests will be conducted on an unswept NACA 23012C aerofoil section of chord length 482.6mm at angles of attack  $6^\circ < \alpha < 21^\circ$  in the City University T2 low-speed wind tunnel ( $Re_c = 1.1 \times 10^6$ ). The blowing momentum coefficients and non-dimensional pulsing frequencies employed are in the range of  $0.0 \leq C_\mu < 0.01$  and  $0.3 \leq F^+ \leq 2.0$  respectively. The aerofoil section is equipped with an array of 15 equi-spaced, co-rotating AJVGs across the span located at 12% and 62% chord; but only the forward array of AJVGs will be utilised in the experimental study.

The results of the tests demonstrate that it is possible to:

- i) Utilise a spanwise array of AJVGs located at 12% chord at relatively low-blowing momentum coefficients ( $C_\mu \leq 0.01$ ) to delay the formation of, and suppress the effects of, a leading-edge vortex on a dynamically stalling aerofoil.
- ii) Reattach the stalled flow on a swept wing by directing the jet efflux towards the wing root.
- iii) Reduce the steady-state blowing mass flow required for effective boundary-layer separation control by up to 25% by operating the AJVGs intermittently.

# Contents

Abstract	i
Contents	iii
List of Tables	vi
List of Figures	vi
Nomenclature	xvi
Declaration	xix
Acknowledgements	xx
1. Introduction	1
1.1 Problem definition	1
1.2 Goal and key specific objectives	20
2. Literature Review and State of the Art	22
2.1 Introduction	22
2.2 Viscous flow control with Airjet Vortex Generators (AJVGs)	32
2.3 Control of dynamic stall	40
2.3.1 Dynamic stall control by geometric alteration	43
2.3.2 Dynamic stall control by boundary layer blowing or suction	46
2.4 Control of separation over swept wings by passive means	49
2.5 Periodic addition of momentum (Periodic blowing)	52
2.6 Summary of the current state of the art for control of helicopter retreating blade stall	59
3. Experimental Arrangement – Dynamic Stall Control	61
3.1 Introduction	61
3.2 Wind tunnel set-up	61
3.3 Wind tunnel model	64
3.4 Experimental arrangement, instrumentation and analysis	66

4. Results and Discussion – Dynamic Stall Control	71
4.1 Introduction	71
4.2 Quasi-steady tests	72
4.3 Dynamic stall tests, oscillating aerofoil at $\alpha = (15 + 10 \sin \omega t)$ deg	75
4.3.1 Reduced frequency, $k = 0.05$ with front AJVG operating, $0 \leq C_{\mu} \leq 0.01$	76
4.3.2 Effects of increasing reduced frequency	81
4.3.3 Effects of varying AJVG blowing location	86
5. Swept-Wing Experiments	112
5.1 Introduction	112
5.2 Swept wing flows	113
5.3 Experimental arrangement	115
5.4 Effect of varying AJVG configuration on the aerodynamic performance of the swept wing	116
5.5 Possible full-scale rotor blade AJVG configuration for dynamic stall control	119
6. Experimental Arrangement – Pulsed Blowing Experiment	136
6.1 Introduction	136
6.2 Wind-tunnel set-up	136
6.3 Wind tunnel model	138
6.4 Experimental arrangement, instrumentation and analysis	140
6.4.1 Surface static pressure measurements	141
6.4.2 Wake momentum deficit measurements	144
6.4.3 Dynamic pressure measurements	146
6.5 Air-jet vortex generator design	150
6.6 Pulsing device	152
6.7 Measurement of nominal mass flow rate supply via BS orifice plate rig	153

7. Results and Discussion – Pulse Blowing Experiment	156
7.1 Introduction	156
7.2 Preliminary unblown NACA 23012C aerofoil surface pressure investigation	157
7.3 Spanwise surface pressure variation	157
7.4 Steady and Unsteady AJVG tests	158
8. Concluding remarks	183
9. Recommendations for future work	186
10. References	188
Appendix A: Aerofoil/wing pressure orifice locations	202

## List of Tables

Table 1.1: General description of boundary-layer behaviour of a dynamically stalling aerofoil [Carr et al (1977)]

Table 2.1: Comparison of rectangular and circular AJVG utilised by Freestone (1985)

Table 2.2: Summary of recommended AJVG parameters

Table 3.1: Quasi-static and oscillatory tests for unblown and blown RAE 9645

Table 3.2: RAE 9645 surface pressure sensors. Their position and quantity

Table 6.1: NACA 23012C surface and plenum static pressure orifices. Their position and quantity

Table 6.2: NACA 23012C surface, plenum and wake rake dynamic pressure sensors. Their position and quantity

## List of Figures

Figure 1.1: Geometric and aerodynamic parameters of the rotor blade

Figure 1.2: Rotor disk velocity and orientation

Figure 1.3: Rotor disk velocity component in forward flight

Figure 1.4: Blade angle-of-attack distribution (in degrees) for a helicopter in forward flight at  $\mu = 0.25$  [reproduced from [Johnson \(1980\)](#)]

Figure 1.5: Representative rotor dynamic pressure conditions for high speed forward flight at  $\mu = 0.45$  [reproduced from [McCroskey \(1972\)](#)]

Figure 1.6: Helicopter forward flight lift pattern (courtesy of [www.dynamicflight.com](http://www.dynamicflight.com))

Figure 1.7: Dynamic stall events on a NACA 0012 aerofoil [Carr et al (1977)]

Figure 1.8: Instantaneous pressure distribution for various times through a RAE 9645 aerofoil oscillating cycle [Singh et al (2003)]

Figure 1.9: Schematic of the retreating blade stall region [Carr (1988)]

Figure 2.1: Co-rotating vortex arrays from equi-spaced vortex generators indicated by contours of velocity [reproduced from Pearcey (1961)]

Figure 2.2: Counter-rotating vortex arrays from equi-spaced vortex generators indicated by contours of velocity [reproduced from Pearcey (1961)]

Figure 2.3: Sketch of typical vortex formation as observed in water tunnel tests ( $\phi = 30^\circ$  and  $\psi = 45^\circ$ ) [courtesy of Rao (1988)]

Figure 2.4: Air-jet slot configuration

Figure 2.5: Location of leading edge and mid-chord blowing along the rotor radius

Figure 2.6: Instantaneous image of the flow without AJVGs operating;  $20^\circ$  divergence [courtesy of McManus et al (1994)]

Figure 2.7: Instantaneous images taken at different phase angles ( $\theta$ ) during a pulse cycle;  $\theta = 0^\circ, 90^\circ, 180^\circ$  and  $270^\circ$  (top to bottom) [courtesy of McManus et al (1994)]

Figure 2.8: Phase conditioned images of the formation and convection of large eddies over the upper surface with pulsed AJVG on;  $\alpha = 12^\circ, \alpha_f = 15^\circ$  [courtesy of McManus et al (1996)]

Figure 3.1: Plan view of the University of Glasgow's "HANDLEY PAGE" 7ft X 5ft 3in wind tunnel

Figure 3.2: University of Glasgow's Dynamic Stall Rig

Figure 3.3: Profile of the RAE 9645 aerofoil section showing AJVG locations at 12% and 62% chord

Figure 3.4: RAE 9645 aerofoil illustrating the two plenum chambers

Figure 3.5: Plan view of the RAE 9645 aerofoil installation

Figure 3.6: Surface dynamic pressure transducer locations at  $z/b = 0.50$  compared with AJVG position

Figure 3.7: Locations of dynamic pressure transducers along aerofoil chord at  $z/b = 0.50$  (20 pressure sensors on upper and 10 pressure sensors on lower surfaces)

Figure 3.8: Schematic of the experimental instantaneous pressure measurement

Figure 4.1: Sensitivity of chordwise surface pressure distribution for unblown RAE 9645 at  $\alpha = 10^0, 15^0$  and  $20^0$ ,  $Re_c = 1.5 \times 10^6$  and  $M_\infty = 0.13$

Figure 4.2: Sensitivity of chordwise surface pressure distribution to front AJVG operating for RAE 9645 at  $\alpha = 18^0$ ,  $Re_c = 1.5 \times 10^6$  and  $M_\infty = 0.13$

Figure 4.3: Sensitivity of leading edge suction to front AJVG operating for RAE 9645 at  $\alpha = 18^0$ ,  $Re_c = 1.5 \times 10^6$  and  $M_\infty = 0.13$

Figure 4.4: Sensitivity of chordwise surface pressure distribution to rear AJVG operating for RAE 9645 at  $\alpha = 18^0$ ,  $Re_c = 1.5 \times 10^6$  and  $M_\infty = 0.13$

Figure 4.5: Sensitivity of leading edge suction to rear AJVG operating for RAE 9645 at  $\alpha = 18^0$ ,  $Re_c = 1.5 \times 10^6$  and  $M_\infty = 0.13$

Figure 4.6: Sensitivity of chordwise surface pressure distribution to combined front and rear AJVG operating for RAE 9645 at  $\alpha = 18^0$ ,  $Re_c = 1.5 \times 10^6$  and  $M_\infty = 0.13$

Figure 4.7: Sensitivity of leading edge suction to combined front and rear AJVG operating for RAE 9645 at  $\alpha = 18^0$ ,  $Re_c = 1.5 \times 10^6$  and  $M_\infty = 0.13$

Figure 4.8: Variation of normal force coefficient with angle of attack for RAE 9645 with front AJVG operating,  $Re_c = 1.5 \times 10^6$  and  $M_\infty = 0.13$

Figure 4.9: Variation of  $1/4$ -chord pitching moment coefficient with angle of attack for RAE 9645 with front AJVG operating,  $Re_c = 1.5 \times 10^6$  and  $M_\infty = 0.13$

Figure 4.10: Variation of incremental normal force coefficient with angle of attack for RAE 9645 with front AJVG operating,  $Re_c = 1.5 \times 10^6$  and  $M_\infty = 0.13$

Figure 4.11: Variation of normal force coefficient with angle of attack for RAE 9645 with  $C_\mu = 0.005$ ,  $Re_c = 1.5 \times 10^6$  and  $M_\infty = 0.13$

Figure 4.12: Variation of  $1/4$ -chord pitching moment coefficient with angle of attack for RAE 9645 with  $C_\mu = 0.005$ ,  $Re_c = 1.5 \times 10^6$  and  $M_\infty = 0.13$

Figure 4.13: Normal force coefficient variation with angle of attack for unblown RAE 9645 at  $Re_c = 1.5 \times 10^6$  and  $M_\infty = 0.13$

Figure 4.14:  $1/4$ -chord pitching moment coefficient variation with angle of attack for unblown RAE 9645 at  $Re_c = 1.5 \times 10^6$  and  $M_\infty = 0.13$

Figure 4.15: Normal force coefficient variation with angle of attack for RAE 9645 at  $\alpha = (15 + 10 \sin \omega t)$ deg,  $k = 0.05$ ,  $Re_c = 1.5 \times 10^6$  and  $M_\infty = 0.13$  with front AJVG operating

Figure 4.16:  $\frac{1}{4}$ -chord pitching moment coefficient variation with angle of attack for RAE 9645 at  $\alpha = (15 + 10 \sin \omega t)$ deg,  $k = 0.05$ ,  $Re_c = 1.5 \times 10^6$  and  $M_\infty = 0.13$  with front AJVG operating

Figure 4.17: Normal force coefficient variation with angle of attack for RAE 9645 at  $\alpha = (15 + 10 \sin \omega t)$ deg,  $k = 0.05$ ,  $Re_c = 1.5 \times 10^6$  and  $M_\infty = 0.13$  with front AJVG operating

Figure 4.18:  $\frac{1}{4}$ -chord pitching moment coefficient variation with angle of attack for RAE 9645 at  $\alpha = (15 + 10 \sin \omega t)$ deg,  $k = 0.05$ ,  $Re_c = 1.5 \times 10^6$  and  $M_\infty = 0.13$  with front AJVG operating

Figure 4.19: Illustration of the formation of the trailing-edge vortex

Figure 4.20: Instantaneous chordwise pressure distribution for the unblown RAE 9645 oscillating at  $\alpha = (15^0 + 10^0 \sin \omega t)$ ,  $k = 0.05$ ,  $Re_c = 1.5 \times 10^6$  and  $M_\infty = 0.13$

Figure 4.21: Instantaneous chordwise pressure distribution for RAE 9645 oscillating at  $\alpha = (15 + 10 \sin \omega t)$ deg,  $k = 0.05$ ,  $Re_c = 1.5 \times 10^6$  and  $M_\infty = 0.13$  with front AJVG array operating at  $C_\mu = 0.005$

Figure 4.22: Instantaneous chordwise pressure distribution for RAE 9645 oscillating at  $\alpha = (15 + 10 \sin \omega t)$ deg,  $k = 0.05$ ,  $Re_c = 1.5 \times 10^6$  and  $M_\infty = 0.13$  with front AJVG array operating at  $C_\mu = 0.008$

Figure 4.23: Instantaneous chordwise pressure distribution for RAE 9645 oscillating at  $\alpha = (15 + 10 \sin \omega t)$ deg,  $k = 0.05$ ,  $Re_c = 1.5 \times 10^6$  and  $M_\infty = 0.13$  with front AJVG array operating at  $C_\mu = 0.01$

Figure 4.24: Normal force coefficient variation with angle of attack for unblown RAE 9645 oscillating at  $\alpha = (15 + 10 \sin \omega t)$ deg,  $Re_c = 1.5 \times 10^6$  and  $M_\infty = 0.13$

Figure 4.25:  $\frac{1}{4}$ -chord pitching moment coefficient variation with angle of attack for unblown aerofoil oscillating at  $\alpha = (15 + 10 \sin \omega t)$ deg,  $Re_c = 1.5 \times 10^6$  and  $M_\infty = 0.13$

Figure 4.26: Normal force coefficient variation with angle of attack for RAE 9645

at  $\alpha = (15 + 10 \sin \omega t)$ deg,  $k = 0.1$ ,  $Re_c = 1.5 \times 10^6$  and  $M_\infty = 0.13$  with front AJVG operating

Figure 4.27:  $\frac{1}{4}$ -chord pitching moment coefficient variation with angle of attack for RAE 9645 at  $\alpha = (15 + 10 \sin \omega t)$ deg,  $k = 0.1$ ,  $Re_c = 1.5 \times 10^6$  and  $M_\infty = 0.13$  with front AJVG operating

Figure 4.28: Instantaneous chordwise pressure distribution for unblown RAE 9645 oscillating at  $\alpha = (15 + 10 \sin \omega t)$ deg,  $k = 0.1$ ,  $Re_c = 1.5 \times 10^6$  and  $M_\infty = 0.13$

Figure 4.29: Instantaneous chordwise pressure distribution for RAE 9645 oscillating at  $\alpha = (15 + 10 \sin \omega t)$ deg,  $k = 0.1$ ,  $Re_c = 1.5 \times 10^6$  and  $M_\infty = 0.13$  with front AJVG array blowing at  $C_\mu = 0.01$

Figure 4.30: Trailing-edge vortex formation with rear array of AJVGs operating

Figure 4.31: Normal force coefficient variation with angle of attack for RAE 9645 at  $\alpha = (15 + 10 \sin \omega t)$ deg,  $k = 0.1$ ,  $Re_c = 1.5 \times 10^6$  and  $M_\infty = 0.13$  with  $C_\mu = 0.01$

Figure 4.32:  $\frac{1}{4}$ -chord pitching moment coefficient variation with angle of attack for RAE 9645 at  $\alpha = (15 + 10 \sin \omega t)$ deg,  $k = 0.1$ ,  $Re_c = 1.5 \times 10^6$  and  $M_\infty = 0.13$  with  $C_\mu = 0.01$

Figure 5.1: Schematic of the retreating blade stall region [Carr (1988)]

Figure 5.2: Contours of local sweep angle on rotor disc in forward flight at  $\mu = 0.33$  [Leishman (1989)]

Figure 5.3: Path of a particle outside the boundary layer (full line) and inside (broken line) on a swept-wing [Küchemann (1953)]

Figure 5.4: Surface flow pattern for a type of rear separation on a swept-wing [Maskel (1955)]

Figure 5.5: Sketched interpretation of the surface flow once separation has occurred [Broadley and Garry (1997)]

Figure 5.6: Surface flow streamlines in the separation region [Broadley and Garry (1997)]

Figure 5.7: Schematic diagram of the swept wing illustrating (a), test model set-up, (b), surface static pressure orifices and (c), AJVG geometries

Figure 5.8: Orientation of AJVG skew angle

Figure 5.9: Chordwise profiles of the RAE 5225 aerofoil section showing (a), AJVG location at  $x/c = 0.10$  and (b), surface static pressure orifices along the chord at spanwise locations of  $z/b = 0.25, 0.50$  and  $0.75$

Figure 5.10: Sensitivity of chordwise surface pressure distribution for the unblown swept-wing at  $z/b = 0.25$ ,  $Re_c = 0.5 \times 10^6$  and  $M_\infty = 0.1$

Figure 5.11: Sensitivity of chordwise surface pressure distribution for the unblown swept-wing at  $z/b = 0.50$ ,  $Re_c = 0.5 \times 10^6$  and  $M_\infty = 0.1$

Figure 5.12: Sensitivity of chordwise surface pressure distribution for the unblown swept-wing at  $z/b = 0.75$ ,  $Re_c = 0.5 \times 10^6$  and  $M_\infty = 0.1$

Figure 5.13: Flow visualisation using fluorescent tufts for the unblown swept wing increasing angle of attack at  $Re_c = 0.5 \times 10^6$  and  $M_\infty = 0.1$

Figure 5.14: Sensitivity of chordwise surface pressure distribution with AJVG operating at  $\alpha = 12^\circ$ ,  $z/b = 0.25$ ,  $Re_c = 0.5 \times 10^6$  and  $M_\infty = 0.1$

Figure 5.15: Sensitivity of chordwise surface pressure distribution with AJVG operating at  $\alpha = 12^\circ$ ,  $z/b = 0.50$ ,  $Re_c = 0.5 \times 10^6$  and  $M_\infty = 0.1$

Figure 5.16: Sensitivity of chordwise surface pressure distribution with AJVG operating at  $\alpha = 12^\circ$ ,  $z/b = 0.75$ ,  $Re_c = 0.5 \times 10^6$  and  $M_\infty = 0.1$

Figure 5.17: The orientation of various VVG systems for a swept-back wing with respect to wing sweep and local flow direction [Pearcey (1961)]

Figure 5.18: Orientation of the AJVG yaw angle based on recommendations of Pearcey (1961); **Config B** with  $\phi = 30^\circ$  and  $\psi_2 = 55^\circ$

Figure 5.19: Flow visualisation using fluorescent tufts for **Config B** AJVG at  $\alpha = 12^\circ$ ,  $Re_c = 0.5 \times 10^6$  and  $M_\infty = 0.1$

Figure 5.20: Variation of incremental normal force coefficient with angle of attack for the  $35^\circ$  swept-back wing with AJVG operating at  $z/b = 0.25$ ,  $Re_c = 1.5 \times 10^6$  and  $M_\infty = 0.13$

Figure 5.21: Variation of incremental normal force coefficient with angle of attack for the  $35^\circ$  swept-back wing with AJVG operating at  $z/b = 0.50$ ,  $Re_c = 1.5 \times 10^6$  and  $M_\infty = 0.13$

Figure 5.22: Variation of incremental normal force coefficient with angle of attack for the  $35^{\circ}$  swept-back wing with AJVG operating at  $z/b = 0.75$ ,  $Re_c = 1.5 \times 10^6$  and  $M_{\infty} = 0.13$

Figure 5.23: The AJVG set-up as *Config A* and *Config B* and its influence on swept wing boundary-layer separation

Figure 5.24: Schematic of the AJVG skew angle when incorporated into a full-scale rotor blade

Figure 6.1: Schematic of T2 low speed wind tunnel

Figure 6.2: Plan view of the NACA 23012C aerofoil mounted vertically in T2 wind tunnel

Figure 6.3: Profile of the NACA 23012C aerofoil section showing AJVG locations at 12% and 62% chord

Figure 6.4: Schematic diagram of experimental data acquisition

Figure 6.5: Surface static pressure orifice and dynamic pressure sensor locations compared with AJVG position

Figure 6.6: (a) Locations of static pressure orifices along the aerofoil chord at  $z/b = 0.26, 0.52$  and  $0.62$  (17 pressure orifices on upper and 11 pressure orifices on lower surfaces); (b) Locations of dynamic pressure sensors along aerofoil chord at  $z/b = 0.46$  (6 pressure sensors on upper and 1 pressure sensors on lower surfaces)

Figure 6.7: Top view showing the NACA 23012C aerofoil and wake rake arrangement

Figure 6.8: Schematic of the wake rake

Figure 6.9: Schematic of the experimental dynamic pressure data acquisition

Figure 6.10: Example of pulse signal in the aerofoil plenum chamber at mean and unsteady levels of 0.1psig and 0.16psig (RMS amp = 0.18) at  $F^+ = 0.7$  and  $DC = 0.65$

Figure 6.11: AJVG geometry configuration (a), pitch angle,  $\phi = 30^{\circ}$  ( $l = 0.025c$ ;  $l/w = 8$ ) and (b), yaw angle  $\psi = 60^{\circ}$

Figure 6.12: Side view schematic of the pulsing device

Figure 6.13: "Exploded" cross section (A – A) of the pulsing device

Figure 7.1: Sensitivity of chordwise surface pressure distributions to angle of attack for unblown NACA 23012C at  $Re_c = 1.1 \times 10^6$  and  $M_\infty = 0.10$

Figure 7.2: Spanwise variation of normal force coefficient with angle of attack for the unblown NACA 23012C at  $Re_c = 1.1 \times 10^6$  and  $M_\infty = 0.10$

Figure 7.3: Schematic of the vortex dynamics in the diffuser subject to unsteady forcing [Narayanan and Banaszuk (2003)]

Figure 7.4: Sensitivity of chordwise surface pressure distributions to angle of attack for unblown NACA 23012C at  $Re_c = 1.1 \times 10^6$  and  $M_\infty = 0.10$

Figure 7.5: Illustration of rear boundary-layer separation, shear layer and wake profile growth with increasing angle of attack

Figure 7.6: Wake profiles, measured one chord length downstream of the model trailing edge, for unblown NACA 23012C at  $Re_c = 1.1 \times 10^6$  and  $M_\infty = 0.10$

Figure 7.7: Sensitivity of chordwise surface pressure distributions to steady and pulsed AJVGs operating from  $x/c = 0.12$  for NACA 23012C at  $\alpha = 18^\circ$ ,  $Re_c = 1.1 \times 10^6$  and  $M_\infty = 0.10$

Figure 7.8: Sensitivity of leading edge suction to steady and pulsed AJVGs operating from  $x/c = 0.12$  for NACA 23012C at  $\alpha = 18^\circ$ ,  $Re_c = 1.1 \times 10^6$  and  $M_\infty = 0.10$

Figure 7.9: Wake profiles, measured one chord length downstream of the model trailing edge, with steady and pulsed AJVGs operating from  $x/c = 0.12$  for NACA 23012C at  $\alpha = 18^\circ$ ,  $Re_c = 1.1 \times 10^6$  and  $M_\infty = 0.10$

Figure 7.10: Sensitivity of chordwise surface pressure distributions to steady and pulsed AJVGs operating from  $x/c = 0.12$  for NACA 23012C at  $\alpha = 20^\circ$ ,  $Re_c = 1.1 \times 10^6$  and  $M_\infty = 0.10$

Figure 7.11: Sensitivity of leading edge suction to steady and pulsed AJVGs operating from  $x/c = 0.12$  for NACA 23012C at  $\alpha = 20^\circ$ ,  $Re_c = 1.1 \times 10^6$  and  $M_\infty = 0.10$

Figure 7.12: Wake profiles, measured one chord length downstream of the model trailing edge, with steady and pulsed AJVGs operating from  $x/c = 0.12$  for NACA 23012C at  $\alpha = 20^\circ$ ,  $Re_c = 1.1 \times 10^6$  and  $M_\infty = 0.10$

Figure 7.13: Sensitivity of chordwise surface pressure distributions to steady and pulsed AJVGs operating from  $x/c = 0.12$  for NACA 23012C at  $\alpha = 20^\circ$ ,  $Re_c = 1.1 \times 10^6$  and  $M_\infty = 0.10$

Figure 7.14: Sensitivity of leading edge suction to steady and pulsed AJVGs operating from  $x/c = 0.12$  for NACA 23012C at  $\alpha = 20^\circ$ ,  $Re_c = 1.1 \times 10^6$  and  $M_\infty = 0.10$

Figure 7.15: Wake profiles, measured one chord length downstream of the model trailing edge, with steady and pulsed AJVGs operating from  $x/c = 0.12$  for NACA 23012C at  $\alpha = 20^\circ$ ,  $Re_c = 1.1 \times 10^6$  and  $M_\infty = 0.10$

Figure 7.16: Variation of normal force coefficient with angle of attack to steady and pulsed AJVGs operating from  $x/c = 0.12$  for NACA 23012C,  $Re_c = 1.1 \times 10^6$  and  $M_\infty = 0.10$

Figure 7.17: Variation of wake profile drag coefficient with angle of attack to steady and pulsed AJVGs operating from  $x/c = 0.12$  for NACA 23012C,  $Re_c = 1.1 \times 10^6$  and  $M_\infty = 0.10$

Figure 7.18: Variation of  $1/4$ -chord pitching moment coefficient with angle of attack to steady and pulsed AJVGs operating from  $x/c = 0.12$  for NACA 23012C,  $Re_c = 1.1 \times 10^6$  and  $M_\infty = 0.10$

Figure 7.19: Variation of normal force coefficient increment with angle of attack to steady and pulsed AJVGs operating from  $x/c = 0.12$  for NACA 23012C,  $Re_c = 1.1 \times 10^6$  and  $M_\infty = 0.10$

Figure 7.20: Centreline variation of normal force coefficient increments with  $C_{\mu total}$  for NACA 23012C at  $\alpha = 20^\circ$ ,  $Re_c = 1.1 \times 10^6$  and  $M_\infty = 0.10$

Figure 7.21: Illustration demonstrating the effect of varying the length scale  $L$  to define the dimensionless pulsing frequency  $F^+$

Figure 7.22: Variation of root-mean-square pressure fluctuations along the aerofoil top surface to steady and pulsed AJVGs operating from  $x/c = 0.12$  for NACA 23012C at  $\alpha = 18^\circ$ ,  $Re_c = 1.1 \times 10^6$  and  $M_\infty = 0.10$

Figure 7.23: Variation of root-mean-square pressure fluctuations across the wake traverse to steady and pulsed AJVGs operating from  $x/c = 0.12$  for NACA 23012C at  $\alpha = 18^\circ$ ,  $Re_c = 1.1 \times 10^6$  and  $M_\infty = 0.10$

Figure 7.24: Variation of root-mean-square pressure fluctuations along the aerofoil top surface to steady and pulsed AJVGs operating from  $x/c = 0.12$  for NACA 23012C at  $\alpha = 20^\circ$ ,  $Re_c = 1.1 \times 10^6$  and  $M_\infty = 0.10$

Figure 7.25: Variation of root-mean-square pressure fluctuations across the wake traverse to steady and pulsed AJVGs operating from  $x/c = 0.12$  for NACA 23012C at  $\alpha = 20^\circ$ ,  $Re_c = 1.1 \times 10^6$  and  $M_\infty = 0.10$

Figure 7.26: Variation of root-mean-square pressure fluctuations along the aerofoil top surface at different chordwise positions for the unblown NACA 23012C at  $Re_c = 1.1 \times 10^6$  and  $M_\infty = 0.10$

Figure 9.1: Schematic of the DARP smart flow control research programme

## Nomenclature

AJVG	Air-jet vortex generator
b	Span of the aerofoil/wing system in wind tunnel
c	Chord of the aerofoil/wing system in wind tunnel
$C_{Dw}$	Wake profile drag coefficient
$C_{\mu}$	Steady jet or mean steady level blowing momentum coefficient $\equiv \dot{m}U_j / \frac{1}{2}\rho U_{\infty}^2 bc$
$\langle C_{\mu} \rangle$	RMS unsteady level blowing momentum coefficient $\equiv \dot{m} \langle U_j \rangle / \frac{1}{2}\rho U_{\infty}^2 bc$
$C_{\mu S/US}$	Combined blowing momentum coefficient $\equiv [C_{\mu}, \langle C_{\mu} \rangle]$
$C_{M0.25c} = \oint C_p x d(\frac{x}{c})$	Pitching moment coefficient about the quarter-chord of the aerofoil
$C_N = \oint C_p d(\frac{x}{c})$	Normal force coefficient integrated from chordwise static pressure distribution on aerofoil model
$C_p = \frac{p - p_{\infty}}{\frac{1}{2}\rho U_{\infty}^2}$	Static pressure coefficient on aerofoil/wing surface; or
$C_p = \sqrt{\frac{H_1 - p_1}{H_{\infty} - p_{\infty}}} \left( 1 - \sqrt{\frac{H_1 - p_{\infty}}{H_{\infty} - p_{\infty}}} \right)$	Total pressure coefficient in the aerofoil wake downstream of the aerofoil trailing edge
$\langle C_p \rangle = \frac{\langle p \rangle}{\frac{1}{2}\rho U_{\infty}^2}$	RMS static or total pressure coefficient
DSV	Dynamic stall vortex
f	Dominant pulsing frequency
$F^+$	Non-dimensional pulsing frequency $\equiv \frac{fL}{U_{\infty}}$
fb	Front blowing or front AJVG in operation
frb	Front and rear blowing or front and rear AJVG both operating simultaneously
$H_1$	local total head one chord length downstream of the aerofoil
$H_{\infty}$	total head in the freestream

K	Wind tunnel calibration constant in static pressure coefficient calculation
$k, \alpha^+$	Aerofoil reduced oscillation frequency $\equiv \frac{\omega c}{2U_\infty}$
L	Distance between actuator and aerofoil trailing edge
LEV	Leading edge vortex
$\dot{m}$	AJVG mass flow rate obtained from orifice plate in blowing supply line to the wind tunnel model
M	Freestream Mach number
p	Local mean static and pitot pressure measured at the aerofoil surface and wake downstream of the aerofoil
$\langle p \rangle$	Local fluctuating static and pitot pressure measured at the aerofoil surface and wake downstream of the aerofoil
r	the rotor radius measured from hub to tip
rb	Rear blowing or rear AJVG in operation
$Re_c$	Reynolds number based on aerofoil chord length and tunnel freestream conditions
s	Spanwise spacing between AJVGs
TEV	Trailing edge vortex
$U_\infty$	Freestream velocity
$U_j$	Velocity at jet exit
$u_T$	Tangential component of the air velocity seen by the rotor blade section
$u_R$	Radial component of the air velocity seen by the rotor blade section
$\alpha$	Angle of attack measured in degrees with respect to the freestream direction
$\phi$	AJVG pitch angle measured relative to the aerofoil local surface tangent
$\mu$	Rotor advance ratio
$\Lambda$	Wing sweep angle
$\rho$	Fluid density
$\omega$	Aerofoil oscillation frequency
$\Omega$	Rotor rotational speed

$\Psi$

Azimuth angle of the blade or rotor disk

$\psi$

AJVG skew angle with respect to the freestream direction

### Subscripts

$\infty$

Freestream

te

Trailing edge

## **Declaration**

I grant powers of discretion to the University Librarian to allow my thesis to be copied in whole or in part without further reference to the author. This permission covers only single copies made for study purposes, subject to normal conditions of acknowledgement.

## Acknowledgements

This thesis is evidence of the support I have received from my family, friends and colleagues for the duration of this project.

I would especially like to thank my supervisors, Prof. D.J. Peake and Prof. A. Kokkalis at City University as well as Prof R.A.McD. Galbraith and Prof. F. Coton at University of Glasgow for their guidance and support throughout my research and the thesis write-up.

Thanks are due to Westland Helicopters Ltd., Qinetiq and EPSRC for giving me the opportunity to realise this project and to Mr. Chris Barber and Mr. Mike Smith (at City University) and Mr. Robert Gilmour (at University of Glasgow) for their assistance in the wind tunnel laboratory.

I am also grateful to Dr. Christoph Küpper and Dr. Gaby Fischer for their constant reminder that this thesis needs finishing. Also to Mr. Vahik Khadogolian with whom many “interesting” discussions were held about this work, both in and out of office hours.

I would like to also thank Miss Louise Leclerc who encouraged and provided me with the release from this endeavour from the very beginning, but due to personal circumstances was not able to see me complete it. I would like to also thank Mr. Ronald E. Andre who provided the “holiday pad” in Belgium when I needed to get away from the stress of work.

Finally, I would also like to take this opportunity to express my gratitude my wife Miss Noraida Saibon whose presence during the final hours of this thesis helped me complete the arduous task of pushing right through the finish whilst maintaining my sanity.

# 1. Introduction

## 1.1 Problem Definition

One of the primary limitations with many current helicopter designs is the tendency of the retreating blade to stall, which in high-speed forward flight produces an increase in rotor and control system loads and helicopter vibration, severe enough to limit the flight speed. Improving helicopter rotor aerodynamic performance in terms of delaying stall, increasing lift and reducing drag and pitching moment is, therefore, seen as a major area where helicopter performance improvements can be generated. Currently, alleviation of helicopter retreating blade stall relies on conventional shape design techniques such as optimising the blade twist distribution along the blade radius, careful blade planform design and the use of multi-aerofoil sections along the rotor radius – thick, high lift sections inboard and thin, transonic sections for the tip region. In order to continue to improve rotor capability in the future, more novel flow control techniques will need to be developed as well as an improved understanding of the causes of flow breakdown will be required, particularly under dynamic conditions.

Before proceeding to examine the helicopter rotor blade aerodynamic environment, a brief description is provided of the important aerodynamic and geometric parameters involved in the analysis of the helicopter rotor blade. The illustration in Figure 1.1 summarises the principal nomenclature to be used in this thesis and also to familiarise the reader with the basic physical description of the rotor blade. The reference length scale for the rotor is the blade radius,  $R$ , measured from the rotor hub to the blade tip. The radial location on the blade,  $r$ , is measured from the blade hub ( $r = 0$ ) to the blade tip ( $r = R$ ). The direction of rotation is conventionally assumed to be counter clockwise (viewed from above) with the blade azimuth angle,  $\Psi$ , defined as zero degrees at the axis of forward speed and opposite of the direction of motion. The azimuth angle is measured from the position of  $\Psi = 0^\circ$  to the blade span axis, in the direction of rotation of the blade. The right side of the rotor disk is called the advancing side and the left side is called the retreating side. The rotational speed of the helicopter rotor blade is given as,  $\Omega$ .

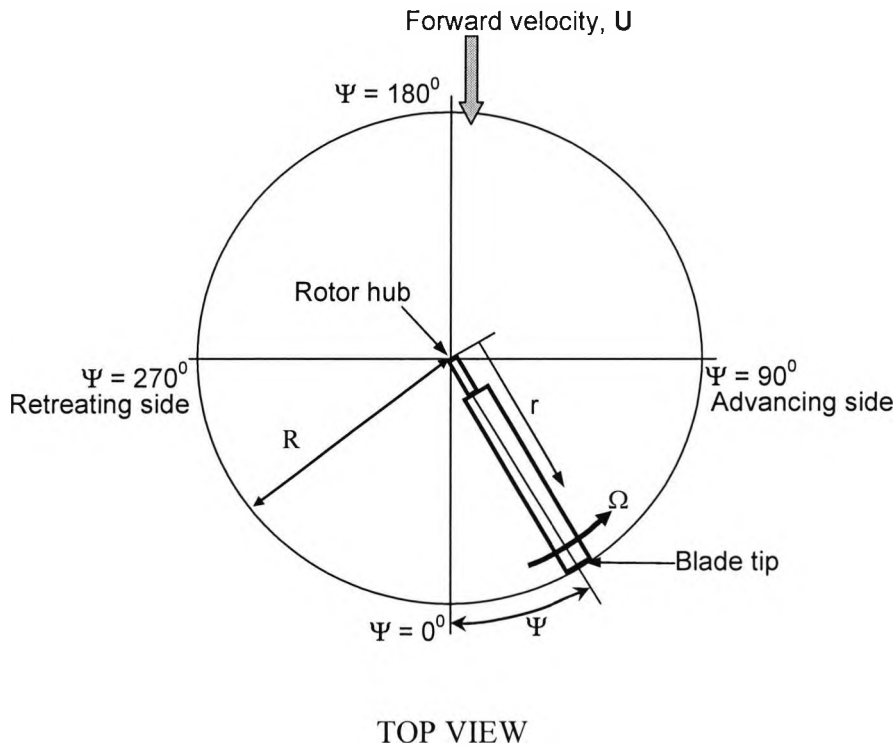
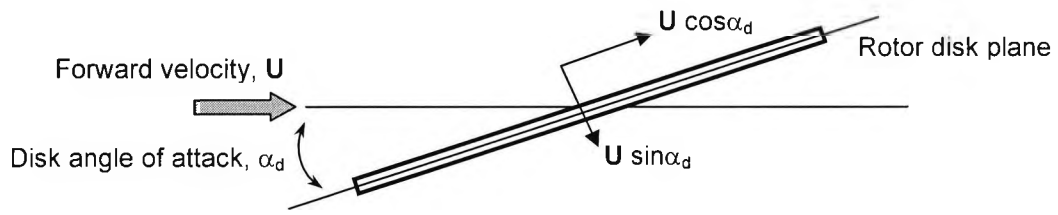


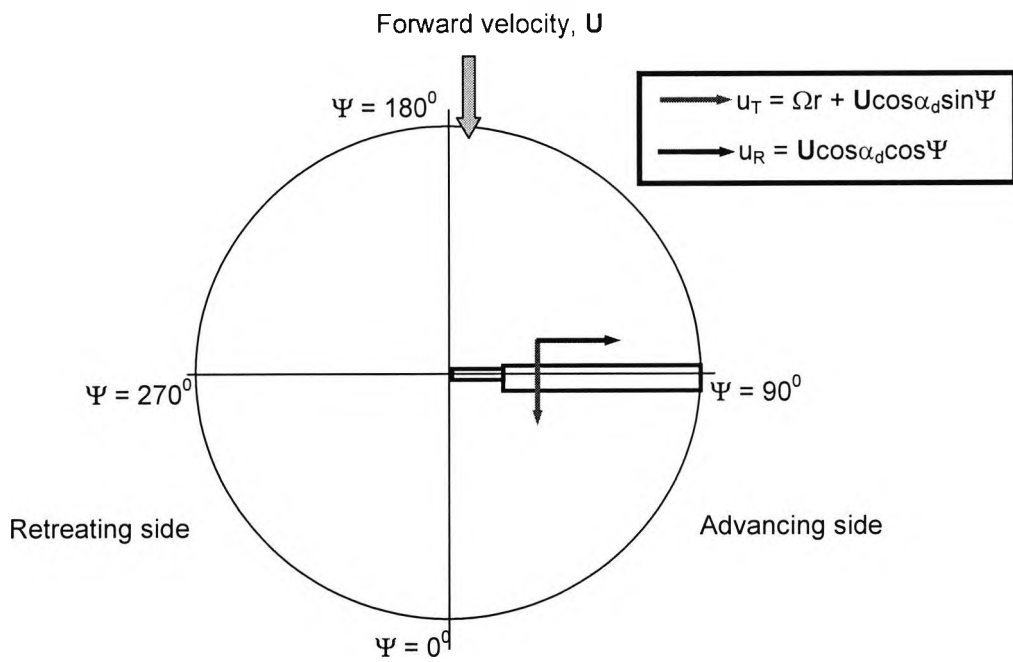
Figure 1.1: Geometric and aerodynamic parameters of the rotor blade

Let us now examine the velocity components seen by the rotating blade in forward flight. The resultant velocity seen by the rotor of a helicopter with a forward velocity,  $U$ , and disk angle of attack,  $\alpha_d$  (positive for forward tilt of the rotor) can be resolved into components parallel and normal to the rotor disk plane as illustrated in Figure 1.2. The component of the helicopter velocity in the plane of the rotor disk is usually normalised by the rotor tip speed and is known as the rotor advance ratio,  $\mu = \frac{U \cos \alpha_d}{\Omega R}$ . For a helicopter with a forward velocity,  $U$ , disk angle of attack,  $\alpha_d$  and the rotor rotating with speed,  $\Omega$ , the velocity components seen by individual rotating blades in forward flight can be further resolved into two components. There are the tangential component of the velocity seen by the blade,  $u_T = \Omega r + U \cos \alpha_d \sin \Psi$  and the radial component of the velocity seen by the blade,  $u_R = U \cos \alpha_d \cos \Psi$ , as illustrated in Figure 1.3.



SIDE VIEW

Figure 1.2: Rotor disk velocity and orientation



TOP VIEW

Figure 1.3: Rotor disk velocity component in forward flight

A helicopter in forward flight has a great influence on the angle-of-attack distribution over the rotor disk, and therefore on the rotor stall behaviour. A typical example of the rotor blade angle-of-attack for a helicopter in forward flight ( $\mu = 0.25$ ) is shown in Figure 1.4. It can be seen that as the rotor blade rotates around the azimuth of the rotor disk, the blade operates at low angle of attack on the advancing side and high angle of attack on the retreating side of the rotor disk.

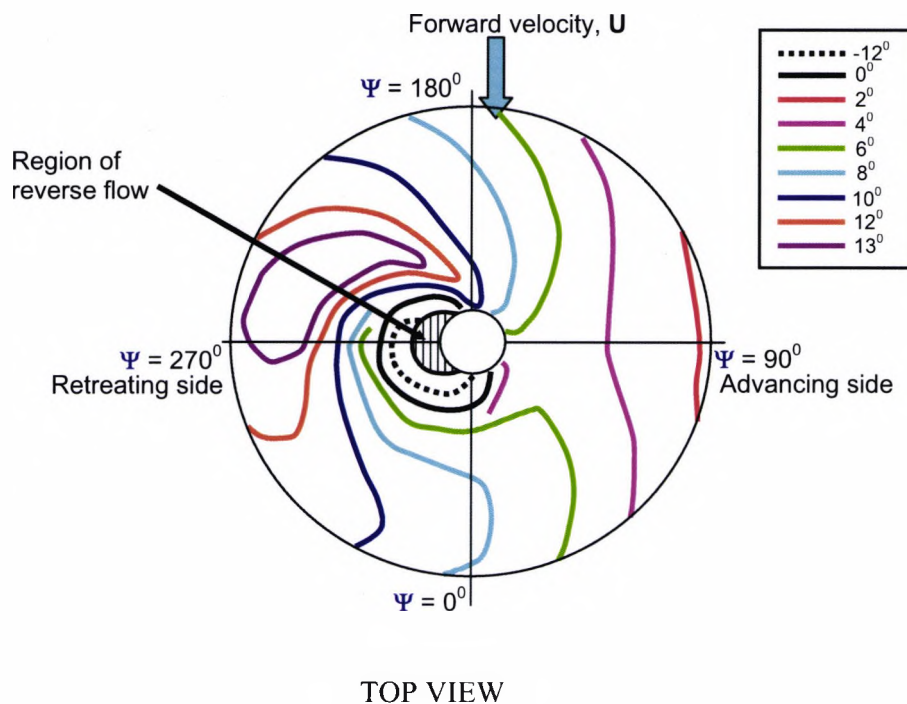


Figure 1.4: Blade angle-of-attack distribution (in degrees) for a helicopter in forward flight at  $\mu = 0.25$  [reproduced from Johnson (1980)]

The asymmetric angle-of-attack distribution observed over the rotor disk for a helicopter in forward flight is due to the combination of the forward velocity and rotor rotational velocity. For a given advance ratio, say,  $\mu = 0.05$  the tangential velocity seen by the blade at the advancing side of the rotor disk is higher than that of the tangential velocity seen by the blade on the retreating side of the rotor disk. This is because the forward velocity component ( $U \cos \alpha_a \sin \Psi$ ) is positive on the advancing side and

negative on the retreating side of the rotor disk, while the rotor rotational velocity ( $\Omega r$ ) is positive around the azimuth of the rotor disk. The local blade element velocity on the advancing side is given as  $u_T = (\Omega r + U \cos \alpha_d \sin \Psi)$  whilst on the retreating side it is  $u_T = (\Omega r - U \cos \alpha_d \sin \Psi)$ . Therefore, by defining the local blade dynamic pressure as  $\frac{1}{2} \rho u_T^2$ , the dynamic pressure on the advancing side will be higher than that of the retreating side of the rotor disk of a helicopter in forward flight. An example of the dynamic pressure variation around the azimuth of the rotor disk for a helicopter in high-speed forward flight is illustrated in Figure 1.5.

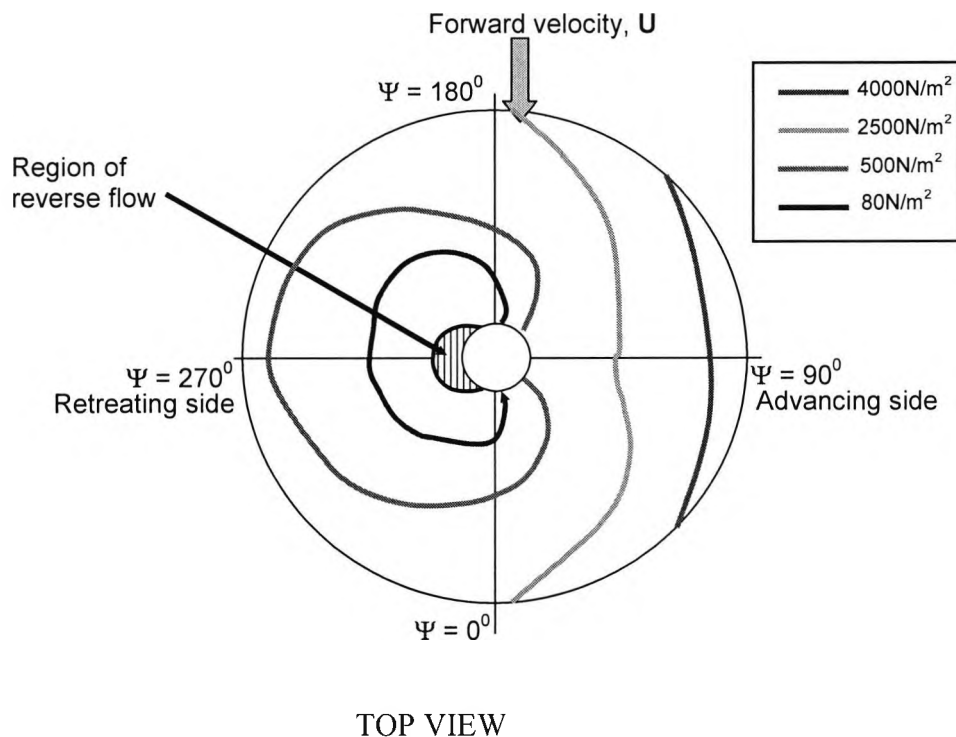


Figure 1.5: Representative rotor dynamic pressure conditions for high speed forward flight at  $\mu = 0.45$  [reproduced from McCroskey (1972)]

As the advance ratio of a helicopter in forward flight increases, the dynamic pressure increases on the advancing side and decreases on the retreating side of the rotor disk. The asymmetric aerodynamic environment requires the retreating blade to produce an amount of lift equal to that of the advancing blade. The sketch of a helicopter forward flight pattern, as depicted in Figure 1.6, shows that to maintain the same lift on both

sides of the rotor disk, the rotor blade has to work at low angle of attack on the advancing side and at high angle of attack on the retreating side. The lateral asymmetry in the aerodynamic environment increases with helicopter advance ratio so that at a given advance ratio stall eventually occurs on the retreating side of the rotor disk.

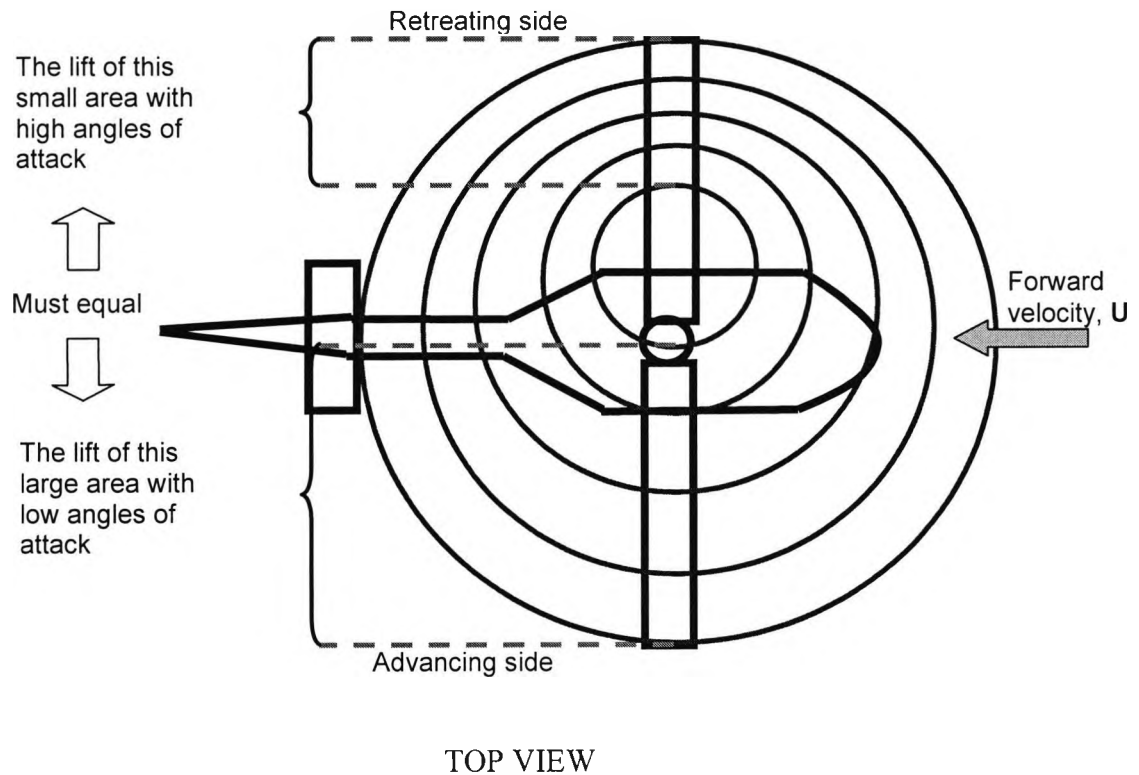


Figure 1.6: Helicopter forward flight lift pattern (courtesy of [www.dynamicflight.com](http://www.dynamicflight.com))

The periodic variation of the aerodynamic environment (time varying dynamic pressure and angle of attack) in which the blade in the retreating side of the rotor disk operate, causes the blade to experience *dynamic stall*. Before control and modification of the stall process can be implemented, it is necessary to understand the flow behaviour, on and away from the, surface of an aerofoil experiencing dynamic stall.

Carr et al (1977) successfully detailed events associated with dynamic stall by a combination of flow visualisation, hot-wire anemometry and normal-force and pitching moment data obtained over a NACA 0012 oscillating aerofoil with a sinusoidal-pitching motion defined by:

$$\alpha = (\alpha_m + \alpha_a \sin \omega t) \text{deg and } k = 0.15$$

where:

$$\alpha_a = \text{amplitude} = 10^\circ$$

$$\alpha_m = \text{mean angle} = 15^\circ$$

$$k = \text{reduced frequency} = \left( \frac{\omega c}{2U_\infty} \right)$$

The development of normal force,  $C_N$ , and pitching moment,  $C_M$ , versus angle of attack,  $\alpha$ , for the dynamically stalling NACA 0012 aerofoil is shown in Figure 1.7 whilst a description of the corresponding boundary-layer behaviour for the dynamically stalling aerofoil is given in Table 1.1.

Moreover, a correlation of the instantaneous chordwise pressure distributions for various times through an aerofoil oscillating cycle with the chronology of dynamic stall events described in Figure 1.7 and Table 1.1 is carried out with the aim of understanding the events observed in the instantaneous pressure distributions for a dynamically stalling aerofoil. The chordwise pressure distributions utilised for the correlation of dynamic stall events is that of a RAE 9645 aerofoil oscillating with a sinusoidal-pitching motion defined by  $\alpha = (15 + 10 \sin \omega t) \text{deg}$  with the reduced frequency,  $k$ , of 0.15 and are shown in Figure 1.8. Although the dynamic-stall events of Figure 1.6 and Figure 1.7 is representative of two different aerofoil sections oscillated in pitch, the stall development described in Table 1.1 is typical of virtually all aerofoils experiencing fully developed dynamic stall.

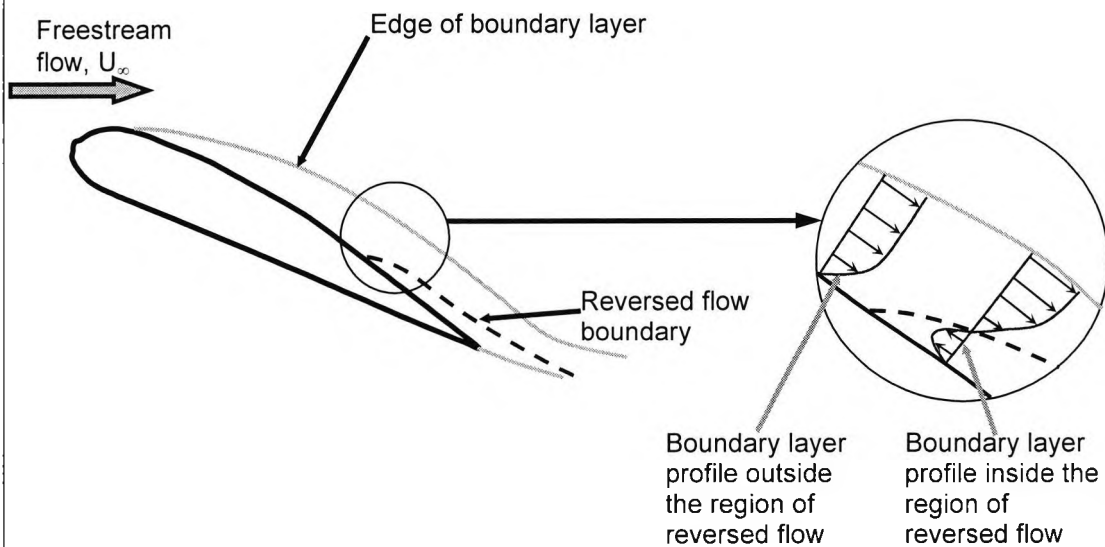
**Table 1.1: General description of boundary-layer behaviour of a dynamically stalling aerofoil [Carr et al (1977)]**

**Static stall angle exceeded – Figure 1.7 (a)**

The aerofoil passes the static stall angle without any detectable change in the normal force-curve slope. The boundary layer has the ability to tolerate large regions of reverse flow before experiencing large-scale boundary-layer separation; allowing the aerofoil to rotate well beyond the quasi-steady stall angle producing lift forces in excess of quasi-steady lift. This phenomenon is known as “*lift overshoot*”. Explanations for this phenomenon include (i), the aerofoil pitching motion compresses the upper surface boundary layer towards the aerofoil surface [Yu et al (1995)] and (ii), the boundary layer requires a finite time period to react to the pitching motion [Weaver et al (1996)].

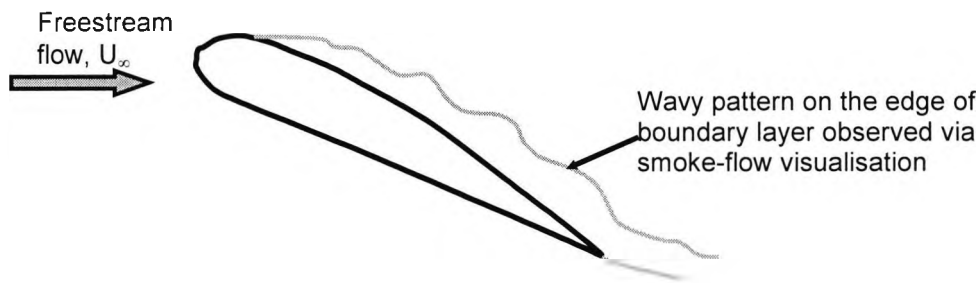
**First appearance of flow reversal – Figure 1.7 (b)**

As the aerofoil rotates beyond the static stall angle, the first appearance of flow reversal is detected, by hot-wire probes, at the bottom of the boundary layer adjacent to the aerofoil upper surface. This tongue of reversed flow initiates at the aerofoil trailing edge.



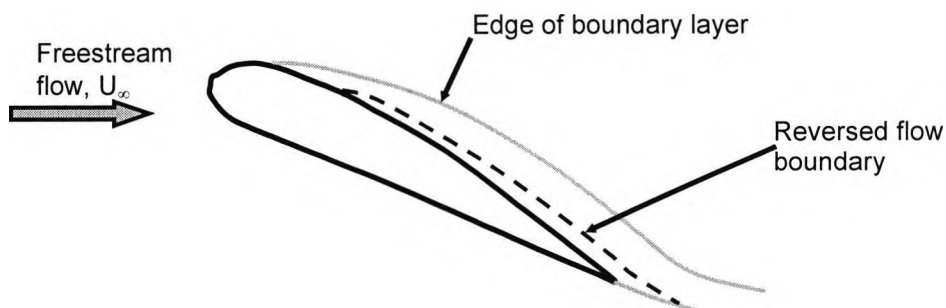
### **Presence of large eddies in the boundary layer – Figure 1.7 (c)**

Using smoke-flow visualisation the boundary layer on the aerofoil upper surface shows a wavy pattern on the edge of the boundary layer. The wavy patterns observed is characteristic of the type of flow that would appear if large eddies were moving down the aerofoil.



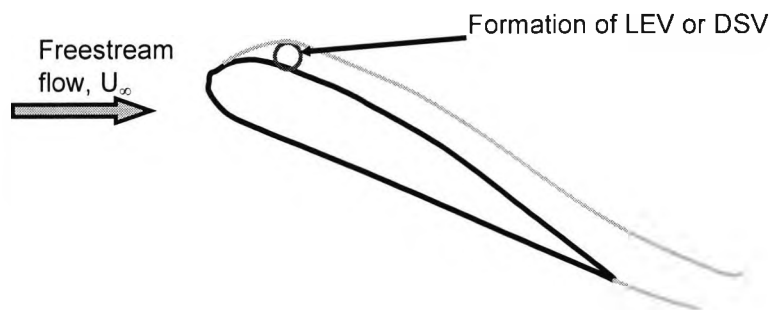
### **Spreading of flow reversal upstream – Figure 1.7 (d)**

As the aerofoil continues on its upward rotation, the flow reversal first observed at the aerofoil trailing edge [see Figure 1.7 (b)] moves upstream of the aerofoil, eventually encompassing the entire aerofoil upper surface. Upstream spreading rate of flow reversal is dependent on parameters such as aerofoil shape, pitch rate, reduced frequency, Reynolds number and Mach number. The region of reversed flow observed in the boundary layer manifests itself within a thin layer at the bottom of the boundary layer. Therefore, although a region of reversed flow encompasses the entire aerofoil upper surface, the boundary layer development on the upper surface of the aerofoil is not significantly distorted to contribute to a detectable change in the normal force and pitching moment curves.



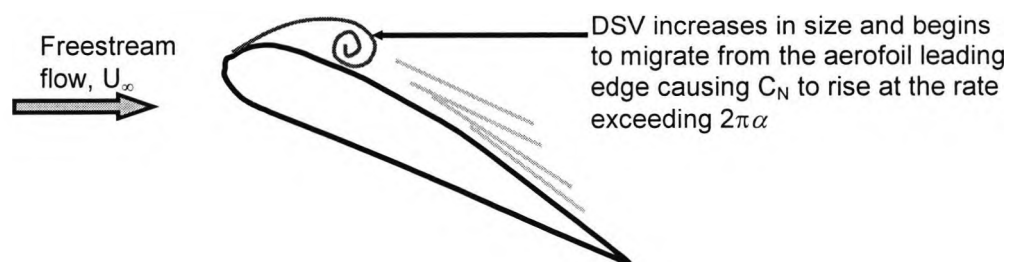
**LEV (or DSV) is formed near the aerofoil leading edge – Figure 1.7 (e)**

The upper surface pressure distributions ( $C_p$ ) as a function of space ( $x/c$ ) and time ( $\alpha$ ) shows that with increasing angle of attack, the aerofoil peak suction increases up to P1 (see Figure 1.8). This value is well in excess of the static peak suction as a result of the dynamic suppression of trailing edge separation as suggested by Singh et al (2004). Also, just prior to the achievement of this peak, a localised increase in suction pressure appears in the vicinity of the aerofoil quarter chord, which is due to the formation of a *leading edge vortex (LEV)* or *dynamic stall vortex (DSV)*. Initiation of a DSV in the vicinity of the aerofoil leading edge upper surface indicates the commencement of the dynamic stall process. A further increase in angle of attack leads to the collapse of the leading edge suction peak and the migration of the DSV downstream towards the trailing edge (Figure 1.8).



**The slope of the lift-curve increases – Figure 1.7 (f)**

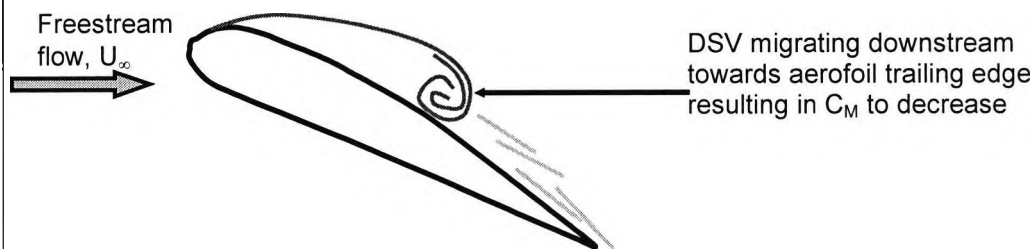
The first effect of dynamic stall on the force and moment characteristics appears as a change in the slope of  $C_N$  vs.  $\alpha$  curve. As the aerofoil continues on its upward rotation, the dynamic-stall vortex increases in size causing the normal force to rise at the rate exceeding  $2\pi\alpha$ , which is the upper limit to the lift-curve slope in quasi-static flows. The observed increase in the normal force-curve slope is due to the vortex lift of the DSV; and the normal force-curve slope continues to increase until the vortex approaches the aerofoil mid-chord.



### **Moment stall – Figure 1.7 (g)**

The change in the pitching moment characteristics first appears when the  $C_M$  vs.  $\alpha$  curve exhibits a strong downward break, which is initiated by the rearward movement of the DSV. This occurrence is known as *moment stall*. Moment stall is defined as the point where the pressure distribution is altered sufficiently to produce a noticeable negative divergence in the aerodynamic pitching moment. As the dynamic-stall vortex migrates downstream over the aerofoil chord towards the trailing edge, the  $C_M$  continues to decrease until it reaches a maximum negative moment.

The rearward movement of the dynamic-stall vortex over the aerofoil chord is illustrated by the suction pressure ridges observed in the instantaneous chordwise pressure distributions (see Figure 1.8).



### **Lift stall – Figure 1.7 (h)**

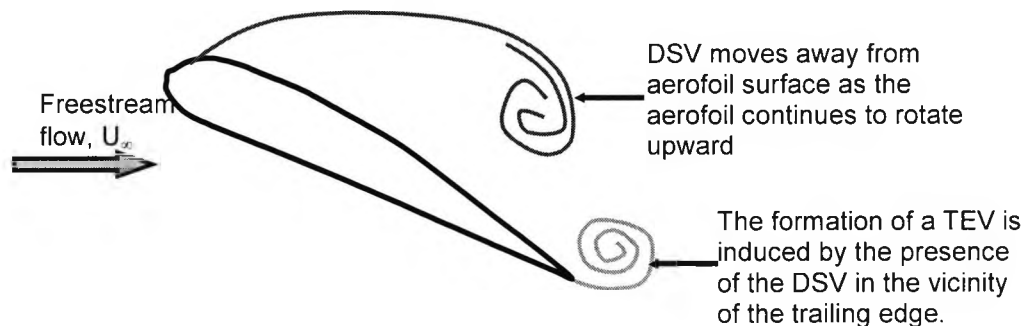
Lift stall occurs when a significant portion of the aerofoil upper surface is enveloped by boundary-layer separation altering the pressure distribution such that lift ceases to increase with further increase in angle of attack. The vortex is now approximately at the aerofoil mid-chord.

### **Maximum negative moment – Figure 1.7 (i)**

The peak nose-down moment (or maximum negative moment) observed in the pitching moment curve is achieved when the DSV has reached the aerofoil trailing edge. However, there is a suggestion that the peak nose-down moment is not a direct but indirect consequence of the DSV shedding from the aerofoil trailing edge. The following discussion provides an explanation to the suggestion above:

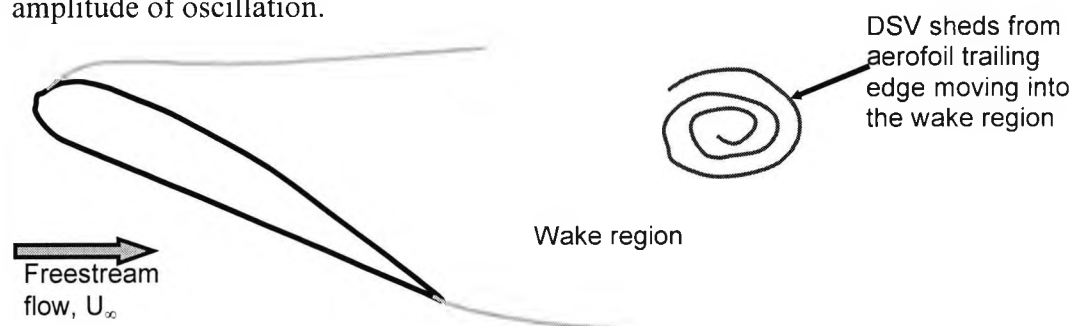
A characteristic not shown by the normal force and pitching moment curves is the suction pressure increase at the aerofoil trailing edge, P3 or P4, as shown in Figure 1.8. Robinson et al (1986) and Feszty et al (2003) has suggested that the increase in

suction P3 (and P4) at the aerofoil trailing edge (Figure 1.8) is not induced by the DSV but by a trailing-edge vortex (TEV). Suction of the DSV migrating downstream causes the mass influx from the high-pressure aerofoil lower surface to the upper surface generating a TEV. As the DSV approaches the trailing edge, the TEV grows in size forming a pair of counter rotating vortices, with the DSV, at the trailing edge. Prior to shedding from the aerofoil trailing edge, the DSV “rolls over” the TEV making the TEV largely responsible for the suction over the trailing edge region. It can, therefore, be hypothesised that the shedding of the TEV causes the peak nose-down moment observed in Figure 1.7 (i).



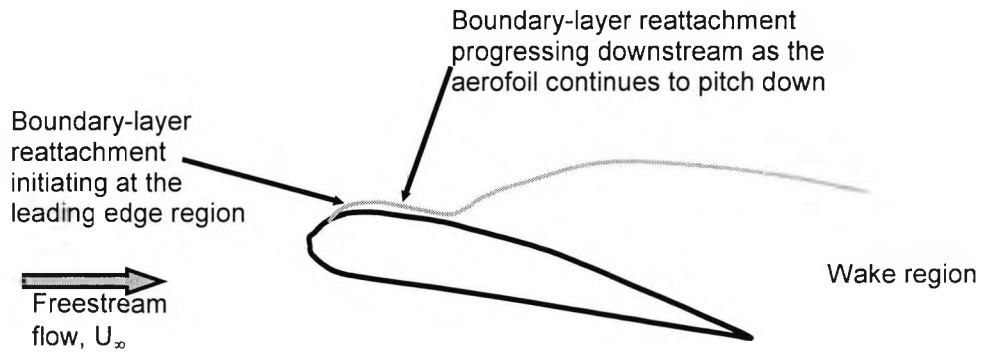
**Full stall – Figure 1.7 (i)**

The sinusoidally pitching aerofoil encounters full stall when the vortex sheds from the aerofoil trailing edge. Sometimes secondary (and tertiary) vortices will form and convect rearwards over the aerofoil as observed by the presence of the second suction ridge in Figure 1.8. The formation of the secondary and/or tertiary stall vortex depends on the aerofoil oscillation frequency, mean angle of attack and amplitude of oscillation.



### **Boundary-layer reattachment – Figure 1.7 (k)**

The aerofoil downstroke motion promotes boundary layer reattachment which begins at leading edge and, as the aerofoil continues on its downward rotation, the reattachment process progresses downstream towards the aerofoil trailing edge. This process is usually slow and only completes at the end of the downstroke motion.



### **Return to unstalled values – Figure 1.7 (l)**

Although the boundary layer has fully reattached during the downstroke motion of the aerofoil, only on the upstroke motion does the rest of the inviscid outer flow appear to return to unstalled conditions. The delay of the inviscid flow returning to unstalled conditions is probably associated with the time it takes for the separated region to close and for this disturbed region to move downstream.

Table 1.1: General description of boundary-layer behaviour of a dynamically stalling aerofoil [Carr et al (1977)]

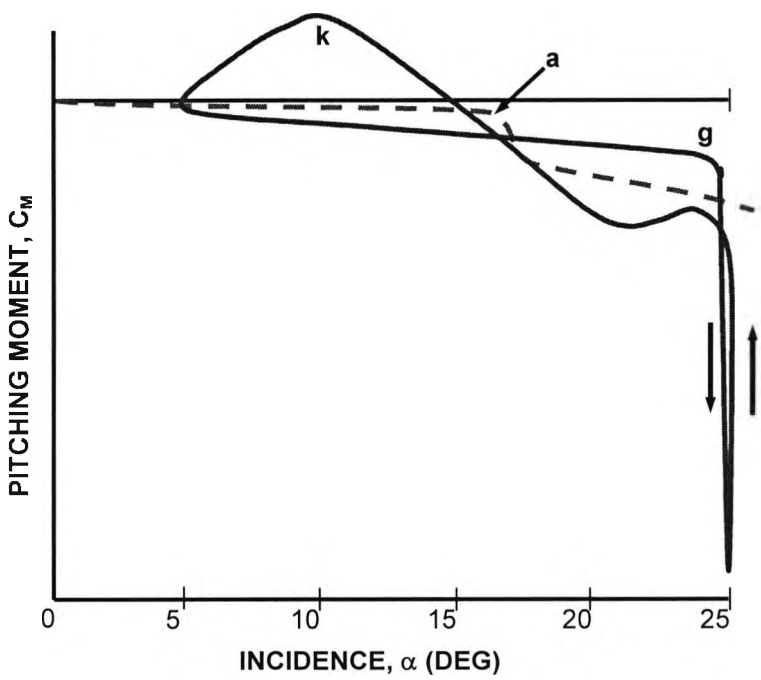
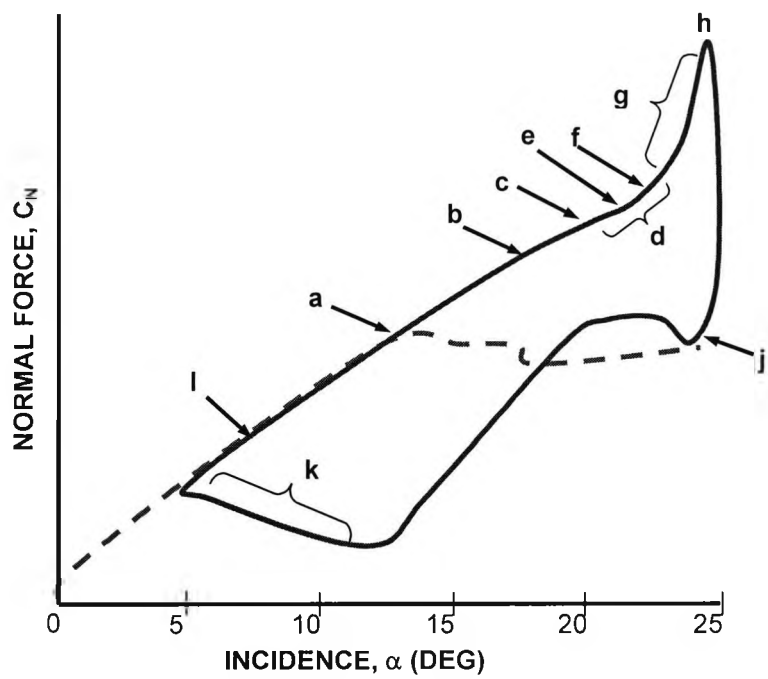


Figure 1.7: Dynamic stall events on a NACA 0012 aerofoil [Carr et al (1977)]

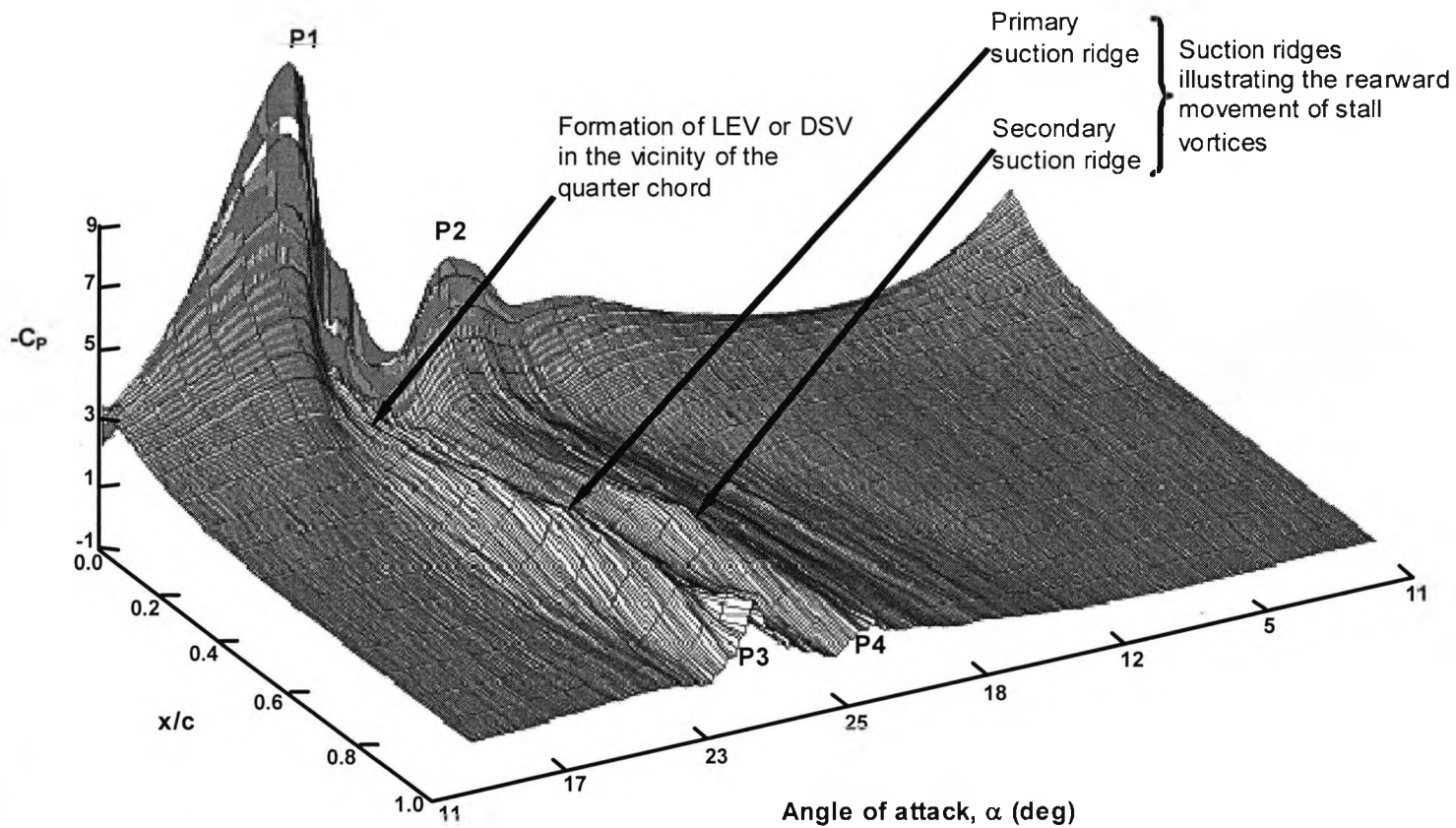


Figure 1.8: Instantaneous pressure distribution for various times through a RAE 9645 aerofoil oscillating cycle [Singh et al (2003)]

Dynamic stall is the most severe type of stall that can be encountered by the retreating blade of a helicopter in high-speed forward flight or manoeuvring flight. The occurrence of dynamic stall on a rotor blade has adverse effects on the performance of the helicopter which include:

- High control system loads
- Vibration affecting the helicopter dynamic performance in terms of speed, lift, manoeuvre capability and handling qualities
- Aerodynamic performance limitation such as a loss of lift, thrust and control
- Stall flutter, causing blade structural damage and excessive cabin vibration.

The desire to alleviate rotor blade dynamic stall to potentially restore the full aerodynamic capabilities and performance of the helicopter is still a major thrust of research activity. Hitherto, research activities to alleviate dynamic stall and subsequently expand the helicopter flight envelope and utility have focussed on:

- a) Active flowfield altering devices such as tangential wall blowing and suction
- b) Geometric altering devices such as leading-and trailing-edge flap, deformable aerofoil techniques and dynamic drooping of the leading edge
- c) Blade root actuation systems such as Individual-Blade-Control (IBC) and Higher Harmonic Control (HHC).

The design philosophy here is that incorporating novel active flow control techniques into the design of rotor blades at source is a preferred strategy. This should allow the fabrication of a simpler rotor blade geometry with built-in low energy systems to control rotor blade dynamic stall. The active flow control method investigated herein is the addition of small quantities of momentum to control the boundary-layer behaviour on the aerofoil upper surface, termed Air-Jet Vortex Generators (AJVGs). The AJVG consists of a small air jet emerging from the aerodynamic surface, via slots/holes, with the jet pitched and skewed relative to the local freestream flow direction. The longitudinal streamwise vortices generated by an array of AJVGs re-energise the “tired” boundary layer enabling it to negotiate severe adverse pressure gradients as the air jet vortices penetrate downstream.

Utilising AJVGs to control flow separation and enhance skin friction has been the main thrust of active flow control research at City University’s Centre for Aeronautics over the last 15 years. Application of steady AJVGs as a flow control mechanism covering a variety of external and internal flows have indicated potentially useful skin friction enhancement with noticeable suppression of flow separation in both subsonic and transonic flows.

Interactive experimental and computational AJVG research at City University has shown that the AJVG system is capable of enhancing the aerodynamic performance of single-element and multi-element wings under quasi-steady flow conditions. In particular Lewington et al (2000) demonstrated that steady AJVGs considerably

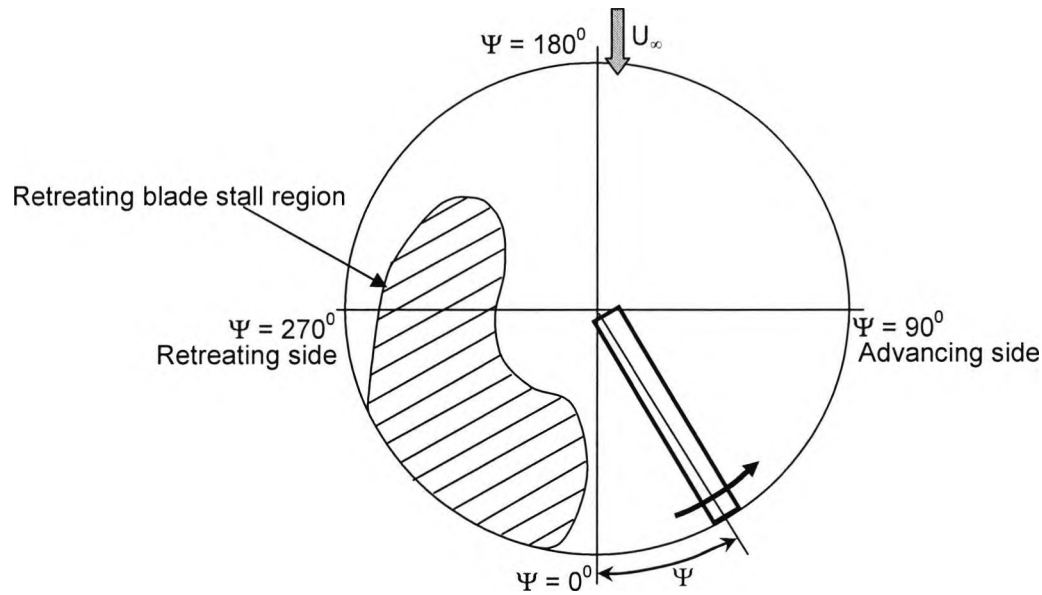


Figure 1.9: Schematic of the retreating blade stall region [Carr (1988)]

Surface pressure measurements obtained from the rotor blade of a helicopter in high-speed forward flight shows that the rapid variation seen in the pitching moment of the rotor blade is the best indicator of the shedding of a dynamic stall vortex [Kufeld et al (1994)]. Detailed investigation of the dynamic stall vortex shedding around the azimuth of the rotor disk reveals that dynamic stall occurs primarily between the azimuth angles  $230^\circ < \Psi < 310^\circ$  [Bousman (1997)]. Because the retreating rotor blade is only instantaneously unswept at the azimuth angle  $\Psi = 270^\circ$ , the effect of sweep becomes an important criterion when deciding the AJVG geometric configuration required to control or eliminate the dynamic stall vortex. A series of exploratory experiments were carried out at City University aimed at deducing the optimum AJVG geometrical configuration to control three-dimensional quasi-steady separation on a swept leading- and trailing-edge wing. The results from this study have crossover application to rotor blade designers to decide the most effective AJVG set-up to be incorporated into a full-scale rotor blade.

Hitherto, flow control research using either AJVGs or tangential wall jets (TWJs) as a flow control mechanism relies on the active and **steady** addition of momentum to delay

separation on lifting surfaces. McManus et al (1994) and Seifert et al (1996) have recently shown that the steady-state blowing mass flow required for effective separation control can be reduced by up to 50% by means of active and **periodic** addition of momentum, i.e. pulsed AJVGs or TWJs. The success of the research above led to the initiation of the third and final part of the current experimental programme focusing on the feasibility of operating the AJVGs intermittently to reduce the mass flux (and ensuing momentum) requirement, whilst maintaining aerodynamic performance enhancements attributable to steady AJVGs. The pulsed AJVG experiments were conducted at City University on the modified NACA 23012 unswept aerofoil where steady AJVGs have been successfully employed to mitigate the onset of stall, whilst generating a  $C_{N_{max}}$  25% above that of the unblown aerofoil [see Lewington et al (2000)]. Using the modified NACA 23012 aerofoil as a baseline model would allow a back-to-back comparison on the potential of pulsed AJVGs to reduce the steady-state blowing mass flow required and to improve the aerofoil aerodynamic characteristics.

The prospect of eventually utilising an active flow control device, i.e. pulsed AJVGs, to control dynamic stall on the retreating blade of a helicopter is dependent on the outcome of the experimental research programmes.

## 1.2 Goals and key specific objectives

The goals of these experimental research programmes are to elucidate in detail the way in which AJVGs enhance mixing in the shear layers about the rotor blade section; and to study how the concept may be best incorporated into the rotor blade for specific applications of controlling stall, extending the useful design angle-of-attack range with sweep effects included. The key specific objectives are to determine the optimum configuration for the AJVG installation in the rotor blade section by deducing:

- a) The optimum configuration, i.e. location, spacing, size, slot geometry, blowing momentum and velocity ratio, for the AJVG installation in the rotor blade section.
- b) Whether a rearward location of AJVGs (say, at 60% chord) can successfully suppress trailing-edge stall and whether a forward location (say, at 20% chord) can suppress leading-edge stall, or whether a combination of forward and aft AJVG locations is preferred to meet the angle of attack excursions of the rotor blade.
- c) The effect of aerodynamic sweep on the geometry requirements of the AJVGs, remembering that dynamic stall on a helicopter rotor blade in high-speed forward flight occurs primarily between the azimuth angles  $230^{\circ} < \Psi < 310^{\circ}$ .
- d) The effectiveness of pulsed AJVGs compared to steady AJVGs, in terms of the induced lift obtained per unit mass flux available.

These experimental research programmes forms the core of the work for the first Rotorcraft Aeromechanics Defence Aerospace Research Partnership (DARP) initiative aimed at providing an essential opportunity to strengthen the existing helicopter aeromechanics research framework and hence position the Westland/Augusta team to meet the research and technology base for the next-generation rotary-wing vehicle. City University's Centre for Aeronautics and Glasgow University's Department of Aerospace Engineering are key university partners in this DARP initiative that is supported by the Engineering and Physical Science Research Council (EPSRC), Westland Helicopters Ltd. (WHL) and Defence Science and Technology Laboratory (DSTL).

The research, reported in this thesis, is divided into the following sections:

- An assessment of the effectiveness of two spanwise AJVG arrays located at 12% and 62% chord to delay the forward movement of trailing edge separation and controlling or eliminating the dynamic stall vortex on an unswept oscillating aerofoil. These experiments were carried out at Glasgow University's low-speed dynamic stall test facility.
- An experimental investigation into the effect of varying AJVG configuration, such as pitch angle, skew angle, blowing momentum and velocity ratio, to suppress separation on a swept wing with parallel leading and trailing edges and sweepback angle of  $\Lambda = 35^\circ$ . These experiments were carried out at City University's T2 low-speed wind tunnel.
- An assessment of the potential of utilising pulsed AJVGs to reduce the steady-state blowing mass flux requirement whilst maintaining the aerodynamic performance enhancements of the modified NACA 23012 aerofoil attained via steady state blowing. These experiments were carried out at City University's T2 low-speed wind tunnel.

## 2. Literature review and state of the art

### 2.1 Introduction

As mentioned in Chapter 1, the overall performance of a helicopter in moderate to high-speed forward flight is substantially limited by the occurrence of dynamic stall on the retreating blade. Therefore, most of the work on dynamic stall was motivated by the need to understand the unsteady flow environment around helicopter rotor blades. Wind tunnel experiments such as the one carried out by McCroskey et al (1974) and Carr et al (1977) have successfully provided a chronology of the complex series of events that occur on an aerofoil experiencing dynamic stall. Understanding the phenomena affecting dynamic stall will enable the utilisation of countering techniques to optimise the rotor blade aerodynamic performance and hence extend the helicopter flight envelope and vehicle utility.

Designs of new rotor systems tend to evolve by small improvements, from one service-proven design to the next, resulting from studies of modifications of a basic rotor configuration. These modifications usually rely on optimising aerofoil geometric characteristics such as thickness and camber-line distributions [Thibert and Gallot (1980) and Horstmann et. al (1982)]. Unlike the fixed wing industry, installing mechanical devices such as slats or flaps to further increase rotor blade aerodynamic performance, as suggested by Carr and McAllister (1983) and Chan and Brocklehurst (2001), is not as feasible due to much greater structural limitations involved.

The proposal in the current experimental programme is to incorporate an array of active flowfield altering devices known as Air-Jet Vortex Generators (AJVGs) (*see also pg 150*) to provide similar aerodynamic performance enhancements to those achieved by the deployment of mechanical devices; but with less detrimental impact in terms of complexity and weight. Confidence in this viscous flow control mechanism comes from the results of a systematic programme of interactive experimental and computational AJVG research that has proceeded at City University over the last 15 years. Innes (1995), Oliver (1997), Vronsky (1999) and Lewington (2000) have achieved notable success in considerably enhancing maximum lift by up to 50% and increasing stall angle by typically up to  $6^{\circ}$  on single- and multi-component aerofoils, all at the expense

of relatively low momentum feed air supplying the AJVGs. The potential inclusion of pulsed AJVGs and/or smart materials to allow the airjets to breathe into the flow at managed times permits the notion of Smart AJVGs (SAJVGs). An experimental research programme was carefully constructed, aimed at demonstrating the fundamental aspects of how SAJVGs installed in a next-generation rotor blade section under quasi-steady, swept and unsteady flow conditions could potentially provide a step-function impetus to the aerodynamic performance of the entire rotor blade.

The following table summaries some of the useful experimental and computational research on the development of viscous flow control with passive solid and active (steady and pulsed) pneumatic vortex generators as well as the current methodology used to control dynamic stall on an oscillating aerofoil and to suppress flow separation on swept wings.

<u>Date, Author</u>	<u>Application + Test conditions</u>	<u>Key results</u>
<b>Passive and active flow control with vortex generators</b>		
1950, Taylor	Solid vane vortex generators (VVGs) as fluid mixing devices.	Employing VVGs on aerofoils resulted in useful suppression of boundary layer growth and hence increase maximum lift and decrease drag.
1952, Wallis	Tests on a NACA 2214 aerofoil with chord of 0.45m chord; attempt to develop a new method of delaying the onset of turbulent boundary layer separation. Circular AJVGs; jet diameter, $D_j$ , of 7.5%. Reynolds number based on chord, $Re_c = 4 \times 10^6$ .	Blowing jets of air through a spanwise row of small holes successfully demonstrated the application of a pneumatic device to increase the rate of momentum transfer between high speed freestream flow and low speed flow adjacent to the surface.
1956, Wallis	Tests on a 0.3m chord aerofoil; compare the ability of VVGs and AJVGs to delay separation. Co-rotating VVGs & AJVGs located at 25% chord. VVG; height of 0.011c. AJVG; circular, $D_j = 0.01c$ , normal to surface ( $\phi = 90^\circ$ ) & pitched at $45^\circ$ and skewed at $90^\circ$ to the oncoming freestream. Reynolds number based on chord, $Re_c = 5 \times 10^6$ .	Results showed that: <ul style="list-style-type: none"> <li>▪ Normal jets created two counter-rotating weak vortices that moved away from the surface and decayed rapidly downstream.</li> <li>▪ Inclined jets produced one main, strong and persistent vortex per jet similar to that, which trails from a single VVG. These longitudinal vortices trail far downstream close to the surface.</li> </ul>
1990, Johnston & Nishi	Tests on a flat plate; investigate effectiveness of AJVGs to suppress turbulent boundary layer separation. Circular jets inclined $45^\circ$ and yawed $\pm 90^\circ$ relative to local freestream flow and ratio of jet-to-freestream velocity ratio, $0 < VR \leq 1$ . Inlet velocity, $U_\infty = 15\text{m/s}$ .	AJVGs shown to produce longitudinal streamwise vortices in downstream direction in a turbulent boundary layer; vortices are strong to reduce/eliminate stalled region of turbulent separated flow. Co- and counter-rotating AJVGs, skew angle, $\psi$ , of $90^\circ$ relative to freestream, substantially reduced stalled region for $VR > 0.8$

1992, Compton & Johnston	Test model of Johnston and Nishi <sup>60</sup> (1990); study effectiveness of varying AJVG skew angle $0^{\circ} < \psi < 180^{\circ}$ to control separation.	Verified that pitched and skewed AJVG in crossflow generates longitudinal streamwise vortex. Optimal AJVG skew angle $45^{\circ} < \psi < 90^{\circ}$ .
1993, Pearcey et al	Tests on half-aerofoil/bump with chord of 305mm; investigate and compare effectiveness of AJVGs to suppress shock-induced separation. Co-rotating rectangular AJVG positioned at 35% chord; pitch angle $\phi = 30^{\circ}$ & $45^{\circ}$ , and skew angle $45^{\circ} \leq \psi \leq 90^{\circ}$ . Mach number based on freestream, $1.0 < M_{\infty} < 1.7$ .	Pitched and skewed AJVGs are effective to suppress shock-induced boundary layer separation. Results demonstrated that: <ul style="list-style-type: none"> <li>▪ Optimum skew angles <math>45^{\circ} \leq \psi \leq 60^{\circ}</math>.</li> <li>▪ Optimum pitch angle, <math>30^{\circ} \leq \phi \leq 45^{\circ}</math>.</li> </ul>
1994, Henry & Pearcey	Numerical tests on a flat plate; study ability of AJVGs to control boundary layer separation in zero- and adverse-pressure gradient. Co-rotating rectangular AJVGs; pitch angle $15^{\circ} \leq \phi \leq 90^{\circ}$ , skew angle $0^{\circ} \leq \psi \leq 60^{\circ}$ and velocity ratio $0 \leq VR \leq 2$ . Reynolds number based on flat plate length of $5 \times 10^6$ .	Analysis showed that: <ul style="list-style-type: none"> <li>▪ The most effective jet configuration to delay the onset of separation is a jet pitched at <math>\phi = 30^{\circ}</math> and skewed at <math>\psi = 60^{\circ}</math>.</li> <li>▪ Increasing jet VR increases strength of longitudinal streamwise vortices.</li> <li>▪ For a given jet mass flow rate, jet slot aspect ratio had little/no effect on the resulting vortices.</li> </ul>
1995, Akanni & Henry	Utilised test model of Henry and Pearcey <sup>53</sup> (1994); investigate effectiveness of co- and contra-rotating AJVGs to control separation. Rectangular AJVGs; pitch angle, $\phi = 30^{\circ}$ , skew angle, $\psi = 90^{\circ}$ and velocity ratio, $0 < VR < 1.2$ . Reynolds number based on distance between flat plate leading edge to jet slots, $Re_x = 2.37 \times 10^6$ .	Comparing wall shear stress distribution downstream of arrays of co- and counter-rotating vortices demonstrated that: <ul style="list-style-type: none"> <li>▪ Counter-rotating vortices increased skin friction over a larger area immediately downstream (<math>x = 3\delta</math> &amp; <math>7\delta</math>) of the jet exit before moving away from the surface further downstream (<math>x = 22\delta</math> &amp; <math>28\delta</math>).</li> <li>▪ Co-rotating vortices remained closer to the surface and increased skin friction over a longer downstream distance (up to <math>x = 28\delta</math>).</li> </ul>

<b>Outline of concepts utilised to control dynamic stall</b>		
1995, Yu et al	Experimental and computational programmes to study the concepts of slatted, deformable and surface-blown aerofoils to control dynamic stall. Reynolds number based on (basic aerofoil) chord, $Re_c = 0.2 \times 10^6$ .	Dynamic stall was successfully controlled by utilising: <ul style="list-style-type: none"> <li>▪ Slatted aerofoil (with an optimum slat location).</li> <li>▪ Deformable aerofoils, by drooping the aerofoil leading edge.</li> <li>▪ Surface-blown aerofoils, via tangential slots at aerofoil <math>\frac{1}{4}</math> chord, at <math>C_{\mu} = 0.45</math>.</li> </ul>
<b>Geometric altering devices to control dynamic stall</b>		
1983, Carr & McAllister	Tests on VR-7 aerofoil with chord of 0.6m; investigate effectiveness of leading edge slat to control dynamic stall. Mach number based on freestream, $M_{\infty} = 0.2$ and Reynolds number based on chord, $Re_c = 2.5 \times 10^6$ .	Use of a leading-edge slat delays forward movement of flow reversal (see also Figure 1.7b and Figure 1.7d) and hence: <ul style="list-style-type: none"> <li>▪ Eliminated dynamic stall for the aerofoil oscillating at <math>\alpha = (15 + 10 \sin \alpha) \text{deg}</math> with reduced frequency <math>0.05 \leq k \leq 0.25</math>.</li> <li>▪ Delayed dynamic stall up to <math>30^{\circ}</math> for <math>k = 0.10</math> and <math>\alpha = (20 + 10 \sin \alpha) \text{deg}</math>.</li> <li>▪ Alleviated severity of stall for angles as high as <math>34^{\circ}</math> for <math>k = 0.10</math> and <math>\alpha = (24 + 10 \sin \alpha) \text{deg}</math>.</li> </ul>
1993, Geissler & Raffel	Numerical and experimental investigations to study the influence of dynamic aerofoil deformation on dynamic stall process. Numerical tests at freestream Mach number, $M_{\infty} = 0.28$ and chord Reynolds number, $Re_c = 3 \times 10^6$ . Experimental tests at freestream Mach number, $M_{\infty} = 0.1$ and chord Reynolds number, $Re_c = 0.4 \times 10^6$ .	Numerical investigations showed that the small bubble formed at the aerofoil leading edge during the upstroke motion of a basic aerofoil is delayed to a higher angle when aerofoil is allowed to dynamically deform during oscillation cycle. The formation and shedding of the dynamic stall vortex is delayed which in turn delays lift- and moment-stall as well as reduces the lift-curve hysteresis loop. Experimental investigations exhibited similar observations although it was conducted at incompressible Mach numbers.

2001, Reuster & Baeder	Numerical simulation on NACA 0012; investigate effectiveness of continuous aerofoil leading edge deformation to control dynamic stall, due to pitching and plunging motions. Mach number based on freestream, $M_\infty = 0.3$ and Reynolds numbers based on chord, $Re_c = 6 \times 10^6$ .	Pitching dynamic stall manifests from large pressure gradients increase near the leading edge causing the flow to lose energy and eventually separate. Leading edge reduces the leading edge adverse pressure gradients and thus prevents onset of pitching dynamic stall. Plunging dynamic stall manifests from a large increase in apparent thickness of the aerofoil, aft of the leading edge. Leading edge deformation has little effect on preventing plunging dynamic stall because of the increased apparent thickness.
2001, Chan & Brocklehurst	Analytical evaluation of the potential benefits of an actuated trailing edge flap using the coupled rotor-fuselage model (CRFM).	Actuated trailing edge flap is most effective in suppressing retreating blade stall, and hence offers an expansion of the flight envelope. Performance enhancements were theoretically demonstrated on a Lynx aircraft with both metal and BERP blades, where the flight envelope was expanded by some 20kt.
2003, Festzy et al	Numerical tests of NACA 0012 aerofoil with a trailing edge flap to control/eliminate dynamic stall vortex. Mach number based on freestream, $M_\infty = 0.12$ and Reynolds numbers based on chord, $Re_c = 1.46 \times 10^6$ .	Periodically actuated trailing edge flap successfully improved rotor performance by removing large pitching moments associated with blade dynamic stall. Dynamic stall is essentially a leading edge phenomenon, therefore, the most the trailing edge actuator could provide is to mitigate the effects of the process rather than to delay or suppress dynamic stall.
<b>Active flowfield altering devices to control dynamic stall</b>		
1960, McCloud et al	Full-scale wind tunnel testing of retreating blade stall delay via steady blowing from rotor blade leading edge and/or mid-chord. Slots positioned between 64% and 95% of rotor radius.	For rotor blade advance ratios between ratios $0.3 < \mu < 0.46$ : <ul style="list-style-type: none"> <li>▪ Retreating blade stall boundary significantly delayed by leading edge blowing between <math>0.0003 \leq C_\mu \leq 0.0033</math>.</li> <li>▪ No change in the stall boundary with blowing from rotor blade mid-chord for the blowing range investigated, <math>0.0002 \leq C_\mu \leq 0.0022</math>.</li> </ul>

1995, Alferai & Acharya	NACA 0012 aerofoil section with a chord of 30cm; investigate effectiveness of boundary layer suction to control dynamic stall. Slot width 0.002c located at 2% chord. Reynolds number based on chord, $Re_c = 1.1 \times 10^5$ .	At pitch rate, say $\alpha^+ = 0.15$ , and angle of attack, say $\alpha = 35^\circ$ , complete suppression of dynamic-stall vortex could be achieved by increasing the suction rate until an optimum volumetric suction flow rate, $Q_{opt} = 0.0074$ . Suction rates higher than optimum value had no effect on the flow field or pressure distribution. Suction rates less than the optimum value resulted in the presence of a dynamic-stall vortex.
1996, Weaver et al	Tests on VR-7 aerofoil section with chord of 0.1m; investigate effectiveness of steady tangential slot blowing to control dynamic stall. Slot width 0.0008c located at 25% chord. Reynolds number based on chord, $Re_c = 0.1 \times 10^6$ .	Steady blowing: <ul style="list-style-type: none"> <li>▪ Prevents any significant trailing-edge separation from occurring, during upstroke portion of oscillation cycle, eliminating moment stall and lift stall and significantly enhance lift.</li> <li>▪ Reduces severity of lift and pitching moment hysteresis caused by flow reversal and the formation &amp; initial movement of the dynamic stall vortex.</li> </ul> Best steady-blowing results were at lowest reduced frequency, $k = 0.005$ , lowest mean angle of attack, $\alpha_m = 10^\circ$ , and highest blowing value, $C_{\mu} = 0.54$ .
<b>Separation control on swept wings</b>		
1989, Mabey et al	Test on a large half model RAE High Incidence Research Model; investigate leading-edge notch/fence configuration required to delay separation and improve steady force characteristics. Reynolds number based on mean chord, $Re_c = 3.7 \times 10^6$ .	Test results, applicable to wings with sweep $15^\circ < \Lambda < 55^\circ$ , showed that: <ul style="list-style-type: none"> <li>▪ Carefully designed leading-edge notches placed at selected positions can inhibit growth of leading-edge separation bubbles.</li> <li>▪ Leading-edge notches reduced wing buffeting and improve overall force characteristics.</li> <li>▪ Leading-edge fence is as effective as leading-edge notch to effectively control flow separation and improve wing buffeting.</li> </ul>

<p>1993, Ashill &amp; Riddle</p>	<p>Tests on a wing with leading edge sweep of <math>60^{\circ}</math>; investigate use of sub boundary-layer vortex generators (SBVGs) to control leading-edge separation. SBVGs in the form of thin wires (diameter of <math>0.00051c</math> &amp; length of <math>0.023c</math>); known as wire vortex generators (WVGs). Mach number based on freestream, <math>M_{\infty} = 0.18</math> and Reynolds number, based on geometric mean chord, <math>Re_c = 3.9 \times 10^6</math>.</p>	<p>Test results show that:</p> <ul style="list-style-type: none"> <li>▪ WVGs reduced the extent of leading-edge separation and delayed light buffeting criterion to higher lift coefficients.</li> </ul> <p>SBVGs effectively controlled upper surface separation of highly-swept, cambered wings for supersonic combat aircraft significantly improving performance at subsonic manoeuvre conditions.</p>
<p>1994, Ashill et al</p>	<p>Test on model and SBVG configuration of Ashill et al<sup>6</sup> (1993); study parameters affecting performance of WVGs, such as angle of incidence, position, geometry and number, to control three-dimensional separation on highly swept wings.</p>	<p>Effectiveness of WVGs determined by amount of increased attached flow length at the leading edge. Results demonstrated that effectiveness of WVGs is dependent on:</p> <ul style="list-style-type: none"> <li>▪ Position of WVG in relation to the upper surface separation line; optimum performance when it is upstream and close to the separation line.</li> <li>▪ Angle between WVG axis and leading edge; optimum angle is <math>16^{\circ}</math> for <math>13^{\circ} &lt; \alpha &lt; 15^{\circ}</math>.</li> <li>▪ WVG height or diameter; effective height range between 3 and 6 times maximum height of viscous sub-layer.</li> </ul>
<p>1997, Broadley &amp; Garry</p>	<p>Tests on a <math>40^{\circ}</math> swept parallel leading- and trailing-edge wing; study mechanisms by which separation can be controlled and prevented via vortex generators. Vortex generator in the form of cropped delta vanes with height of <math>0.016c</math>. Mach number based on freestream, <math>M_{\infty} = 0.17</math> and Reynolds number based on chord, <math>Re_c = 4 \times 10^6</math>.</p>	<p>At wing sweep, <math>\Lambda</math>, of <math>40^{\circ}</math> and <math>50^{\circ}</math> best reduction of lift-dependent drag factor obtained for VVGs positioned at 65% chord and toed out at an angular deflection of <math>+25^{\circ}</math>, relative to oncoming freestream. Performance of VVG is improved for:</p> <ul style="list-style-type: none"> <li>▪ VVG height equal to local height of boundary layer.</li> <li>▪ Angular deflection between <math>+18^{\circ}</math> and <math>+30^{\circ}</math> relative to the local freestream.</li> <li>▪ Positions upstream and close to separation position/line.</li> </ul>

<b>Periodic addition of momentum/Oscillatory blowing</b>		
1994, McManus et al	<p>Tests to determine effectiveness of pulsed vortex generator jets (VGJs) to control boundary layer separation.</p> <p>Turbulent boundary layer on wind tunnel floor is forced to separate by a <math>20^{\circ}</math> divergence.</p> <p>3 pulsed jet orifices (<math>D_j = 0.67\delta_j</math>) positioned upstream of the divergence. Jet pitch, <math>\phi = 45^{\circ}</math> and skew, <math>\psi = 90^{\circ}</math> relative to the oncoming freestream.</p> <p>Reynolds number based on tunnel height of 6.4cm, <math>Re_h = 2 \times 10^4</math> and <math>4 \times 10^4</math>.</p>	<p>Streamwise velocity measurements and flow visualisations demonstrated that pulsed AJVGs inhibit the flow from separating. Flow visualisation showed that pulsed AJVGs create a periodic disturbance in the flowfield by forming vortex structures during each pulsing cycle. Phase-locking the image acquisition with the jet pulse control signal showed a vortex is formed as a result of the jet pulse and convects downstream adjacent to the tunnel floor. It is suggested that the vortex formation and evolution is responsible for enhanced cross-stream mixing in the boundary layer.</p> <p>Mass flow requirements for effective separation control using pulsed AJVGs are greatly reduced compared to the requirements for steady AJVGs.</p>
1995, McManus et al	<p>Tests on two-element flat-plate aerofoil model with overall chord of 15.24cm and flap chord of 3.2cm; investigate effectiveness of pulsed VGJs to delay stall onset.</p> <p>Test incidence range <math>6^{\circ} \leq \alpha \leq 20^{\circ}</math> and flap deflection <math>15^{\circ}</math>.</p> <p>One jet (<math>D_j = 0.016c</math>) positioned at flap leading edge and orientated at <math>\phi = 45^{\circ}</math> and <math>\psi = 90^{\circ}</math> relative to the oncoming freestream.</p> <p>Reynolds number based on chord, <math>Re_c = 5.1 \times 10^5</math>.</p>	<p>Experiments revealed that:</p> <ul style="list-style-type: none"> <li>▪ Pulsed jet effectiveness is strongly dependent on jet to cross-stream velocity ratio, VR, and total mass flow rate through the jet. Maximum separation control effectiveness achieved with high VR and high mass flow rate.</li> </ul> <p>Pulsed jet actuator concept is suited for aircraft applications because of:</p> <ul style="list-style-type: none"> <li>▪ Its potential compact size and low power requirement.</li> <li>▪ Its relatively low air mass flow requirements compared with steady blowing techniques.</li> </ul>
1996, McManus et al	<p>Test model of McManus et al<sup>86</sup> (1995); modified to investigate effect of varying pulse VGJ characteristics, such as pulsing frequency, to delay stall.</p>	<p>Effective pulsing to increase lift and decrease drag; <math>F^+ = 0.5</math> for <math>VR \leq 2</math> and <math>F^+ = 0.4</math> for <math>VR &gt; 2</math>.</p>

<p>1996, McManus &amp; Magill</p>	<p>Tests on flapped NACA 4412 aerofoil with overall chord of 11.6cm and flap chord of 2.32cm; determine effectiveness of pulsed VGJs to reduce flow separation and augment lift.</p> <p>Two jets (<math>D_j = 0.027c</math>) positioned at flap leading edge and orientated at <math>\phi = 45^\circ</math> and <math>\psi = 90^\circ</math> relative to the oncoming freestream.</p> <p>Reynolds number based on chord, <math>Re_c = 2.0 \times 10^5</math></p>	<p>Maximum lift enhancements occur at pulsing frequency of 0.6, 30% higher than optimum value of McManus et al (1996) suggesting that optimum pulsing frequency is geometry dependent.</p>
<p>2001, Magill &amp; McManus</p>	<p>Test on generic tailless fighter configuration with swept lambda wings; investigate pulsed VGJs to control separation on aircraft wings.</p> <p>Four jets positioned at wing leading edge and orientated at <math>\phi = 45^\circ</math> and <math>\psi = 90^\circ</math> relative to the oncoming freestream.</p> <p>Reynolds number based on chord (per ft), <math>Re_c = 0.86 \times 10^6</math> and <math>1.72 \times 10^6</math>.</p>	<p>Tests showed that pulsed VGJs delayed stall by up to <math>4^\circ</math>, increased maximum lift by up to 11% and decreased drag by up to 17%; offering improved post-stall manoeuvre performance.</p> <p>Pulsed VGJs can be operated asymmetrically to provide lateral manoeuvring control in regions where conventional control surfaces is deemed ineffective.</p> <p>Therefore, pulsed VGJs actuators could <u>enhance aerodynamic performance</u> and <u>manoeuvrability</u> of advanced fighters.</p>

## 2.2 Viscous Flow Control with Air-Jet Vortex Generators (AJVGs)

The main aims of viscous flow control on wings are the enhancement of lift, the reduction of drag and the prevention of the development of extensive wakes thereby improving the overall stalling characteristics. These objectives are achieved when the energy dissipated by viscosity is either minimised or restored efficiently by passive or active means. The most popular method currently employed to delay boundary-layer separation in a variety of external and internal aerodynamic flows is the installation of protuberance-type vortex generators. These devices work by inducing the local boundary-layer and freestream flow to form well-organised vortical structures. Increased mixing is promoted as high momentum fluid from the freestream is swept along a helical path towards the surface. Likewise, the low momentum fluid is rapidly convected away from the surface by the vortical motion. As a result, the mean streamwise momentum of the fluid within the boundary layer is increased and flow separation is delayed. This is a continuous process and thus provides a continuous source of boundary-layer re-energisation to counter the natural boundary layer retardation and growth caused by surface friction, viscosity and adverse pressure gradients. Steeper adverse pressure gradients can then be adequately negotiated by viscous flow on aerodynamic surfaces suitably configured with vortex generators. Useful drag reductions may also result from properly employing vortex generators, as the persistent effects of the vortical motion are able to limit the growth of the wake downstream of the trailing edge, even when there has been flow departure from the surface.

Using the above principles, Taylor (1950) of the United Aircraft Corporation was able to demonstrate boundary layer control by solid Vane Vortex Generator (VVG). Such systems consist of a row of small plates or cropped delta-wing vanes that project normal from the surface with each one set at an angle of incidence to the local freestream flow to produce a single trailing vortex. Setting each VVG, in a spanwise array, to the same height and skew angle across the surface enables the generation of a set of co-rotating identical vortices as shown in Figure 2.1. Pearcey (1961) also showed that the devices could be arranged at alternate positive and negative yaw angles to generate a counter-rotational vortex system, as illustrated in Figure 2.2.

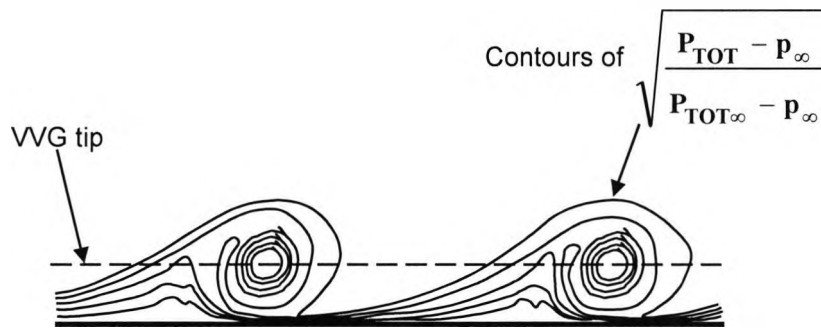


Figure 2.1: Co-rotating vortex arrays from equi-spaced vortex generators indicated by contours of velocity [reproduced from Pearcey (1961)]

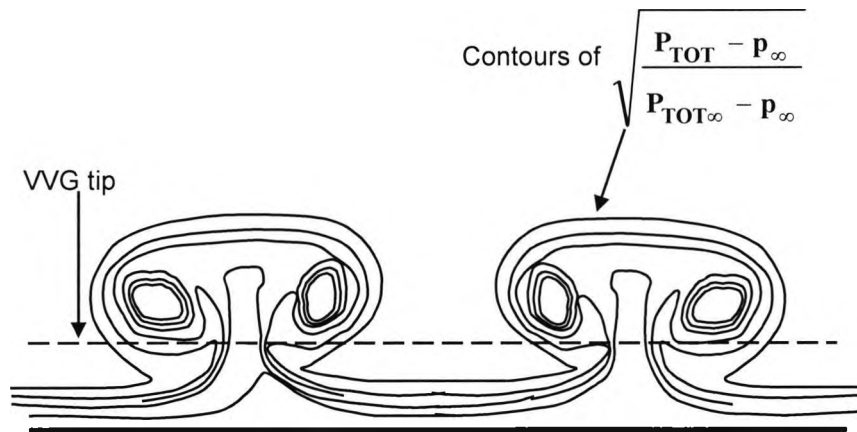


Figure 2.2: Counter-rotating vortex arrays from equi-spaced vortex generators indicated by contours of velocity [reproduced from Pearcey (1961)]

Because VVGs are permanent installations on the airframe, they cause an additive parasite drag contribution. The positioning of the vanes needs to be precise to ensure adequate revitalisation of retarded flow downstream. Hence, the vanes are usually single point design attributes. Elimination of the installed drag effects of the flow control devices themselves leads to the idea of ‘active’ devices, where the device can be turned on and off, as the flow field dictates. Wallis (1952) conceived the idea of using air-jets as a replacement for VVGs. Initial tests were carried out on a NACA 2214 aerofoil with a chord of 0.45m at chord Reynolds number of  $Re_c = 4 \times 10^6$  to demonstrate the potential

application of AJVGs to suppress turbulent boundary-layer separation. AJVGs consist of a spanwise row of small holes (diameter = 7.5% chord) normal to the surface installed at 50% chord. Each AJVG consists of a jet of air squirting from the aerodynamic surface, to interact with and mix with the oncoming freestream and viscous flows. This interaction increases the rate of momentum transfer between high speed freestream flow and low speed boundary-layer flow adjacent to the surface. This results in the reduction of the momentum deficit in the boundary layer as well as the likelihood of boundary-layer separation. Although, air-jets issuing normal to the surface only partially suppressed turbulent boundary-layer separation when compared to VVGs, the application of a pneumatic device to increase momentum transfer within the turbulent boundary layer was nonetheless successfully demonstrated.

Building upon the success of the initial study by Wallis (1952), Wallis (1956) attempted to develop a type of AJVG capable of producing persistent vorticity for the purpose of delaying turbulent boundary-layer separation similar to that of a VVG. Tests were conducted on a 0.3m chord, 12% thick, low drag type aerofoil at a chord Reynolds number of  $Re_c = 5 \times 10^6$ . Two types of circular AJVG (diameter = 0.01c) were studied (a), jets issuing normal to the surface and (b), jets inclined at  $45^\circ$  to the aerofoil surface and yawed  $90^\circ$  to the oncoming freestream flow. The height of the rectangular metal vanes (VVG) used was 0.011c each angled  $20^\circ$  relative to the local freestream direction. A co-rotating array of either vanes or AJVGs was installed on the aerofoil at 25% chord. Air-jets issuing normal to the surface were ineffective in suppressing turbulent boundary-layer separation because the pair of counter-rotating vortices produced acted as a flow spoiler and it decayed rapidly downstream. Boundary-layer separation control was successfully achieved by orientating the AJVG at a pitch and skew angles relative to the oncoming freestream. The net result was that the relatively weak pair of counter-rotating vortices formed by the normal jet was replaced with one main, strong and persistent vortex while weakening the influence of the other. These longitudinal vortices are known to trail far downstream close to the surface similar to those, which trail from VVGs. Even with low mass fluxes inclined jets provided useful suppression of boundary-layer separation and performed as good as VVGs. Later tests by Pearcey (1961) confirmed that circular co-rotating AJVGs, inclined at  $45^\circ$  to the local freestream flow, performed comparably to VVGs to delay shock-induced boundary layer separation.

A preliminary experimental investigation by Freestone (1985) demonstrated that for a given plenum pressure rectangular orifice AJVGs could increase the magnitude of vorticity generation downstream compared with the VVGs and circular orifice AJVGs. Study of the experimental test set-up, however, revealed that the rectangular and circular AJVGs tested were completely different, as shown in the Table 2.1 below.

<u>Circular AJVG</u>	<u>Rectangular AJVG</u>
Pitch angle, $\phi = 45^0$	Pitch angle, $\phi = 30^0$
Skew angle, $\psi = 60^0$	Skew angle, $\psi = 60^0$
Jet exit area $\approx 380\text{mm}^2$	Jet exit area $\approx 255\text{mm}^2$

Table 2.1: Comparison of rectangular and circular AJVG utilised by Freestone (1985)

Hence, any comparison highlighting the benefit of rectangular AJVGs over circular AJVGs, shown by this study, has to be treated with care. Measurement of the streamwise vorticity produced by the VVGs and AJVGs in a downstream cross-flow plane does, however, show that AJVGs are capable of generating streamwise vortices similar to those produced by VVGs. Further tests of varying mass flow rates and pitch and skew angles as well as investigating the flow development at various streamwise locations downstream of the jet exit are required to better ascertain the mechanism behind vortex generation of these devices.

Johnston and Nishi (1990) conducted experiments investigating the ability of AJVGs to generate longitudinal streamwise vortices and concluded that these vortices are capable of controlling stall in strong adverse pressure gradients. Tests were conducted on a flat plate with an array of co-rotating and counter-rotating circular AJVGs inclined at  $45^0$  and skewed  $\pm 90^0$  relative to the local freestream flow at Reynolds number based on jet diameter of 6350. Skin friction and mean velocity profile measurements at two downstream locations of the AJVGs exhibited features associated with longitudinal vortices embedded in a boundary layer. Good examples are provided by Pauley and Eaton (1988), who made detailed studies of the vortices generated by VVGs in a turbulent boundary layer. Johnston and Nishi (1990) also demonstrated that streamwise

vortices generated by AJVGs with jet-to-freestream velocity ratios (VR) above 0.8 are strong enough to reduce or eliminate turbulent boundary-layer separation. Further tests by Compton and Johnston (1992) utilising the experimental set-up of Johnston and Nishi (1990) showed that the maximum vorticity levels, measured in the transverse planes downstream of the vortex arrays, are strongly dependent on VR and skew angle, with the optimal skew angle between  $45^{\circ}$  and  $90^{\circ}$  relative to the local freestream flow.

Despite the evident potential of low jet momentum, active-control AJVGs, to suppress boundary-layer separation it was not until Henry and Pearcey (1994) performed a systematic programme of interactive experimental and computational AJVG research at City University that the AJVG system capabilities of enhancing not only single element aerofoil but multi-element aerofoil performance has emerged. The programme was built upon the AJVG parametric design studies of Pearcey et al (1993) [see also Rao (1988)] investigating the effectiveness of AJVGs to suppress shock-induced boundary-layer separation. Tests were conducted on a half-aerofoil/bump with a chord of 0.31m at a Mach number range between  $1.0 < M_{\infty} < 1.7$ . A co-rotating array of rectangular AJVGs positioned at 35% chord was inclined at  $30^{\circ}$  and  $45^{\circ}$  and yawed between  $45^{\circ} \leq \psi \leq 90^{\circ}$  relative to the local freestream direction. These transonic wind-tunnel experiments showed that the optimum AJVG pitch and skew angles required to effectively suppress shock-induced boundary-layer separation lies between  $30^{\circ} \leq \phi \leq 45^{\circ}$  and  $45^{\circ} \leq \psi \leq 90^{\circ}$  respectively.

Water tunnel flow visualisation tests by Rao (1988) illustrated the formation a streamwise vortex from a single yawed and pitched rectangular air-jet exiting from a surface to mix with the local boundary-layer and freestream flow. As shown in Figure 2.3, it was demonstrated that the fluid issuing from the jet exit formed the vortex core and the vortex itself is established by the freestream flow, initially wrapping itself around this core before becoming entrained with it. The flow interaction rapidly produces a well-organised system of a helical vortex structure that penetrates downstream to influence the development of the wall viscous layers.

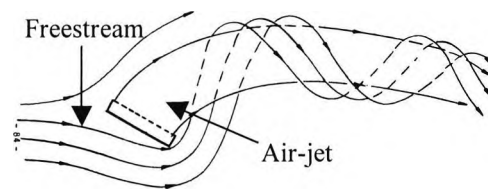


Figure 2.3: Sketch of typical vortex formation as observed in water tunnel tests ( $\phi = 30^0$  and  $\psi = 45^0$ ) [courtesy of Rao (1988)]

Henry and Pearcey (1994) conducted numerical tests on a flat plate in zero- and adverse-pressure gradient refining the AJVG geometric configuration proposed by Pearcey et al (1993). These numerical tests were conducted with a co-rotating array of rectangular AJVGs with the pitch varied between  $15^0$  and  $90^0$  and the skew varied between  $0^0$  and  $60^0$  at a Reynolds number based on flat plate length of  $Re = 5 \times 10^6$ . The performance of the AJVGs was assessed by monitoring the predicted axial skin friction and the maximum vorticity decay at two spanwise locations downstream of the AJVG. These numerical tests showed that AJVGs orientated at  $\phi = 30^0$  and  $\psi = 60^0$  were the most effective in delaying the onset of turbulent boundary-layer separation. Akanni and Henry (1995) utilised the numerical model of Henry and Pearcey (1994) to conduct a numerical study comparing the effectiveness of co-rotating and counter-rotating AJVGs to suppress turbulent boundary-layer separation. Comparing the wall shear stress distribution at spanwise locations downstream of the AJVG arrays Akanni and Henry (1995) demonstrated that (a), counter-rotating vortices increased skin friction over a large area immediately downstream of the jet exit before moving away from the surface at further downstream locations; and (b), co-rotating vortices remained closer to the surface and increased skin friction over a longer downstream distance.

Based on the results of Henry and Pearcey (1994) and Akanni and Henry (1995), Oliver (1997) conducted low speed wind-tunnel experiments at City University on a 17% thick single-element aerofoil to study the ability of AJVGs to suppress trailing-edge separation. The tests were conducted on the NACA 63<sub>2</sub>-217 aerofoil with a chord of 0.5m at a Reynolds number based on chord of  $Re_c = 1.1 \times 10^6$ . A co-rotating array of rectangular AJVGs orientated at  $\phi = 30^0$  and  $\psi = 60^0$  relative to the local freestream

flow were installed on the aerofoil model at 10% chord. Each AJVG, spaced at  $0.10c$  intervals, had dimension of length,  $l = 0.025c$  and width,  $w = 0.003c$  as shown in Figure 2.4. Utilising only small amounts of blowing ( $C_{\mu} \leq 0.010$ ) Oliver (1997) demonstrated that aerofoil stall could be delayed by up to  $6^{\circ}$  and maximum normal force ( $C_{Nmax}$ ) increased by up to 50%.

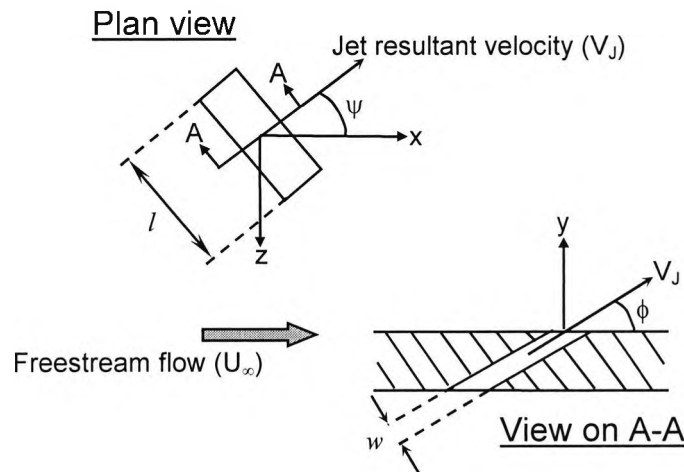


Figure 2.4: Air-jet slot configuration of Oliver (1997)

The effectiveness of the AJVG configuration utilised by Oliver (1997) to delay the onset of trailing-edge separation was also investigated by Vronsky<sup>\*</sup> (1999) on a collaborative experimental programme between Aerolaminates Ltd. (now NEG Micon) and City University. The aim of the low-speed wind tunnel tests conducted at City University ( $Re_c = 1.1 \times 10^6$ ,  $M_{\infty} = 0.1$ ) were to evaluate the feasibility of using AJVG as a cost-effective device for aerodynamic performance improvements of large stall regulated wind turbine blades. Operating the AJVGs, installed at 10% chord on a 21% thick (NACA 63-421) aerofoil, at low amounts of blowing ( $C_{\mu} \leq 0.010$ ) successfully delayed the onset of stall by up to  $6^{\circ}$ , whilst generating a  $C_{Nmax}$  40% above that of the unblown aerofoil. Even for an aerofoil section with thickness/chord ratio as high as 30% (NACA 63-430), AJVGs installed at 10% chord successfully suppressed trailing-edge

<sup>\*</sup> Consultancy work for Aerolaminates Ltd by City University and funded by the Energy Technology Support Unit (ETSU) on behalf of the Department of Trade and Industry (DTI) and published under the report number ETSU W/41/00541/REP. Mr Vronsky on behalf of Aerolaminates managed the test programme whilst Mr Singh (the author) conducted the tests supervised by Prof Peake at City University.

separation and hence delayed stall by up to  $4^\circ$ , increased  $C_{N_{max}}$  by up to 20% and reduced drag at  $C_{N_{max}}$  by up to 40%. The experimental and numerical research programmes at City University culminating with the experiments by Oliver (1997) and Vronsky (1999) have successfully demonstrated that a spanwise array of co-rotating rectangular AJVGs is capable of delaying trailing-edge separation and limiting the growth of the wake downstream of the trailing edge. The recommended AJVG geometry and spacing is given in the Table 2.2 below.

<u>Parameter</u>	<u>Configuration</u>
Pitch angle, $\phi$	$30^\circ$
Skew angle, $\psi$	$60^\circ$
Jet exit length, $l$	$0.025c$
Jet exit width, $w$	$0.003c$
Jet spacing, $s$	$0.10c$

Table 2.2: Summary of recommended AJVG parameters

The successful application of spanwise AJVGs to deter stall commencement on a series of aerofoils of increasing thickness/chord ratio from 17% to 30% led to the initiation of a seed, collaborative, experimental research programme between City University and Westland Helicopters Ltd. (WHL). The aim of the research programme was to study the potential application of AJVGs to helicopter aerofoils in order to expand the rotor envelope, limited by blade stall, and to reduce the power associated with the drag rise occurring prior to blade stall. A series of tests were carried out at City University's T2 low speed wind-tunnel on a modified NACA 23012 aerofoil under quasi-steady flow conditions at a Mach number of 0.10 and Reynolds number based on chord of  $1.1 \times 10^6$  [see Lewington et al (2000)] The geometry, spacing and orientation of the AJVGs installed on the upper surface of the aerofoil at 12% chord were based on the outcome of investigations by Oliver (1997) and Vronsky (1999) (see Table 2.2). Results of these tests showed that the application of spanwise AJVGs on a thinner aerofoil section more representative of rotorcraft applications delayed the onset of stall by up to  $6^\circ$  and increased  $C_{N_{max}}$  by up to 25%, all at the expense of relatively low momentum feed air supplying the AJVGs ( $C_\mu \leq 0.010$ ).

The results of the seed experimental programme showed that AJVGs could deliver large improvements in performance for helicopter aerofoil sections with low jet mass flow rates ( $C_{\mu} \leq 0.010$ ). The incorporation of an array of AJVGs into the rotor blade are of importance because demands for improvements in the performance of helicopter rotors continue to increase while the magnitude of improvements available from the design of conventional aerofoils is diminishing. Further investigations are required in order to establish the feasibility of incorporating AJVGs into a full-scale rotor blade to potentially control the entire viscous flow, from subsonic along the blade, to transonic at the tip. These investigations include:

- a) Assessing the impact of AJVGs to control or suppress dynamic stall on a pitching aerofoil section blade.
- b) Studying the effect of aerodynamic sweep on the geometric requirements of the AJVGs. This is due to the fact that the retreating rotor blade is only instantaneously unswept at azimuth angle  $\Psi = 270^{\circ}$ , whilst retreating blade stall occurs primarily between azimuth angles  $230^{\circ} < \Psi < 310^{\circ}$ .

### **2.3 Control of dynamic stall**

With a view to improve the cost effectiveness and the performance of helicopters, the French National Aerospace Research Establishment (ONERA), German Aerospace Center (DLR) and Defence Science and Technology Laboratory (DSTL) have initiated research programmes with the intent of increasing the efficiency of rotor blades in hover and forward flight. One of the most important contributions towards the effort of improving the aerodynamics of helicopters in order to increase high-speed forward flight and manoeuvrability is the advent of composite materials. Replacing metal rotor blades with composite rotor blades (as done on the PUMA) allowed the optimisation of the blade twist distribution and the use of multi-aerofoil sections along the rotor blade radius, whereby the blade disc loading is distributed efficiently [see Thibert and Gallot (1980) and Horstmann et al (1984)].

Concurrently, research programmes have also focussed on developing new-generation, advanced helicopter rotor blade aerofoils. An aerofoil with good aerodynamic

characteristics, i.e. low drag at high Mach numbers and high lift capability at lower Mach numbers as well as a small pitching moment, forms the basis of a successful rotor blade design [see Johnson (1980)]. The development of more efficient aerofoils for helicopter rotor blades is, therefore, an essential task for improving helicopter performance and extending the flight envelope of helicopters. The first generation of helicopter rotors were equipped with symmetrical aerofoils, such as the NACA 0012 aerofoil, which have the advantage of a zero pitching moment at zero lift. An early wind-tunnel investigation by McCloud and McCullough (1958) demonstrated the superiority of cambered aerofoil sections compared to symmetrical aerofoil sections in increasing rotor blade lifting capacity for a given forward speed. The design of cambered aerofoils, such as the NACA 23012, was the most significant progress for the development of the second generation of rotor blades. The growing understanding of transonic flow and the progress in the field of numerical methods, especially for the computation of transonic flow and in the coupling of inviscid flow and boundary layer calculations, allowed the introduction of supercritical aerofoils, into the development of the third generation of rotor blades [see Thibert and Gallot (1980) and Horstmann et al (1984)].

High performance future rotorcraft will require significant improvements in a number of attributes, such as increased speed and performance for fast, agile missions, increased payload and reduced vibration. Since the implementation of traditional passive design techniques appears incapable of producing simultaneous improvements in these attributes, active systems for controlling rotor loads and performance are being extensively studied.

Current research activities are focused on flow control techniques such as leading-edge deformation, leading- or trailing-edge flaps and tangential wall blowing/suction. Yu et al (1995) reviewed the possible implementation of these flow control techniques to control dynamic stall and, hence, improve the aerodynamic characteristics of the helicopter rotor blade. An interactive experimental and computational programme was established to study the effect of aerofoils that deform, aerofoils with slats and slots, and aerofoils with flow energizers to control dynamic stall. These experimental and numerical studies were conducted at a Reynolds number based on (basic aerofoil) chord of  $0.2 \times 10^6$  using (i), a basic VR-7 aerofoil section and with the addition of a drooped

leading-edge aerofoil; and (ii), a basic VR-12 aerofoil section and an extended leading-edge portion forming a slat aerofoil. The aerofoil oscillation motion was described by ( $\alpha = 15 + 10 \sin \omega t$ ) deg and reduced frequency,  $k$ , of 0.1. Results from the experimental and numerical studies showed:

a) Slatted Aerofoils – significant improvement in the aerodynamic characteristics of the aerofoils could be achieved with a slat configuration. However, the superior behaviour of the slatted VR-7 aerofoil when compared with the VR-12 aerofoil indicated the need to (i), rotate and droop the slat rather than simply extend the slat element forward; and (ii), have upper surface curvature on the main element for some distance behind the slat.

b) Deformable Aerofoil – the deformable leading-edge (DLE) aerofoil concept is a variation of the leading-edge slat where it is only employed when needed. Two parameters that specify the DLE aerofoil is the centre of rotation and droop angle ( $\alpha_{droop}$ ). The DLE aerofoil decreased lift hysteresis and drag and pitching moment magnitude compared with the basic aerofoil. An alternative is the variable-droop leading-edge (VDLE) aerofoil where the droop angle is varied with angle of attack, e.g.  $\alpha_{droop} = \alpha^0 - 13^0$  for  $\alpha^0 \geq 13^0$ . Employing the variable-droop leading-edge concept further decreased lift hysteresis and drag and pitching moment magnitude compared with the DLE aerofoil.

Experimental and numerical tests of the surface-blown aerofoils, as suggested by Yu et al (1995), were conducted at a Reynolds number based on chord of 30,000 using a NACA 0012 aerofoil. The aerofoil oscillation motion was described by ( $\alpha = 15 + 10 \sin \omega t$ ) deg at a reduced frequency,  $k$ , of 0.1. A spanwise slot located at the aerofoil quarter-chord provided tangential steady blowing to the aerofoil upper surface for  $0 \leq C_{\mu} \leq 0.45$ . These tests showed that upper-surface blowing, of  $C_{\mu} = 0.45$ , prevented the trailing-edge separation from moving upstream, which in turn delayed the formation of the dynamic stall vortex. An in-depth discussion and analysis of the methods outlined by Yu et al (1995) as well as its potential applicability to a full-scale helicopter rotor is provided in the following sections.

### 2.3.1 Dynamic stall control by geometric alteration

Numerous investigations utilising geometry altering devices, as outlined by Yu et al (1995), are attributed to technological advances in materials, piezoelectrics and actuators. For instance, Carr and McAllister (1983) successfully demonstrated the potential of an oscillating aerofoil fitted with a leading-edge slat to eliminate dynamic stall. A VR-7 aerofoil with chord of 0.6m and equipped with a leading-edge slat was tested at Mach number of approximately 0.2 and a chord Reynolds number of  $2.5 \times 10^6$ . The aerofoil sinusoidal pitching motion is denoted by  $(\alpha = 15 + 10 \sin \omega t)$  deg oscillating at reduced frequencies  $0.0006 < k < 0.35$ . Instantaneous normal force, pitching moment and surface pressure distributions demonstrated that the oscillating aerofoil equipped with a leading-edge slat eliminated dynamic stall for all frequencies tested. The effects of the slat/aerofoil combination were determined by analysis of the flow behaviour (such as boundary-layer transition, flow reversal, separation and reattachment) near the surface of the aerofoil, using a variety of surface hot films and hot-wire sensors. The boundary layer behaviour for the basic VR-7 aerofoil oscillating at a reduced frequency of 0.10 showed flow reversal moving upstream from the trailing edge and reaching the leading edge by  $\alpha = 22^\circ$ . However, with the slat/aerofoil combination the flow reversal barely reaches the aerofoil quarter-chord at the maximum angle of attack ( $\alpha_{max} = 25^\circ$ ).

A combined numerical and experimental investigation carried out by Geissler and Raffel (1993) studied the influence of dynamic aerofoil deformation on the control of dynamic stall. Dynamic aerofoil deformation is achieved when the aerofoil is allowed to deform its shape dynamically during the oscillatory motion. The aerofoil sinusoidal pitching motion was defined by  $(\alpha = 15 + 10 \sin \omega t)$  deg oscillating at a reduced frequency,  $k$ , of 0.3. Numerical tests were conducted at a Mach number of 0.28 and a chord Reynolds number of  $3 \times 10^6$ ; whereas the experimental tests were conducted under incompressible flow conditions at Mach number of 0.1 and Reynolds number of  $0.4 \times 10^6$ . Experimental tests were initially conducted under incompressible flow conditions to first verify the ability to deform an oscillating aerofoil in a wind-tunnel test. For both the numerical and experimental tests, the aerofoil deformed from NACA 0012 at low angles of attack to NACA 0016 or NACA 0018 at high angles of attack. Although the numerical and experimental tests were carried out under different flow

conditions, they both exhibited similar dynamic stall control characteristics. For the basic, un-deformed aerofoil a laminar separation bubble formed in the vicinity of the leading edge at  $\alpha \approx 18^\circ$ . As the angle of attack was increased, the bubble broke down and a vortical structure appeared indicating that the dynamic stall process has begun. When the aerofoil was deformed, the formation of the leading-edge bubble is delayed to a higher angle of attack,  $\alpha \approx 25^\circ$ . This, in turn, delayed the formation and shedding of the dynamic stall vortex and consequently shifted the lift- and moment stall to a higher incidence and reduced the lift-curve hysteresis loop.

Reuster and Baeder (2001) supplemented the work of Geissler and Raffel (1993) by studying the ability of a deflected leading-edge aerofoil to control dynamic stall in pitching and plunging motions. The numerical simulations were conducted using a NACA 0012 aerofoil at a Mach number of 0.3 and a chord Reynolds number of  $6 \times 10^6$ . A continuous leading-edge deformation was achieved throughout the entire aerofoil motion, i.e. no deformation at  $0^\circ$ , increasing to maximum deformation at maximum angle of attack. For the aerofoil pitching motion, leading-edge deformation prevented the onset of dynamic stall by reducing the adverse pressure gradients in the vicinity of the leading edge. Dynamic stall for the aerofoil plunging motion was attributed to the apparent increase of aerofoil thickness at the trailing edge, thereby rendering any leading-edge flow control device ineffective.

Chan and Brocklehurst (2001) conducted an analytical evaluation investigating the ability of rotor blades fitted with trailing-edge flaps to expand the flight envelope of a helicopter by suppressing retreating blade stall. The analysis was carried out using the coupled rotor-fuselage model (CRFM). It is a comprehensive rotorcraft analysis package capable of predicting aircraft performance, rotor loads, rotor stability and aircraft vibration, in both steady level and manoeuvring flight conditions. It was written, jointly by the Defence Evaluation and Research Agency (DERA) of Farnborough and Westland Helicopters Ltd. (WHL), to accommodate a wide range of rotorcraft configurations. The effects of the trailing-edge flap or performance enhancement flap (PEF) were theoretically demonstrated on a Lynx helicopter. The PEF was found to be effective in suppressing retreating blade stall, and hence offers an expansion of the flight envelope by some 20kt.

Building on the success of the analytical evaluation of Chan and Brocklehurst (2001) which demonstrated the effectiveness of a trailing-edge flap to suppress retreating blade stall, Feszty et al (2003) carried out a numerical investigation illustrating the improved aerodynamic performance of a trailing-edge flapped aerofoil over a basic aerofoil with no flap motion. Improvement of the aerofoil aerodynamic performance was denoted by the eradication of the large pitching moments associated with dynamic stall. A NACA 0012 aerofoil with a trailing-edge flap oscillating at  $(\alpha = 15 + 10 \sin\omega t)$ deg with a reduced frequency,  $k$ , of 0.173 was numerically tested at a Mach number of 0.117 and a chord Reynolds number of  $1.46 \times 10^6$ . Feszty et al (2003) hypothesised that the large pitching moment observed on the basic oscillating aerofoil is attributed to the shedding of a trailing-edge vortex (TEV) and not the shedding of the dynamic stall vortex. They found that in order to reduce the large nose-down pitching moments on an oscillating aerofoil, it made good sense to attempt to influence the behaviour of the TEV rather than that of the dynamic stall vortex. This was done using an active trailing-edge flap. They found that the upward deflection of the trailing-edge flap displaced the TEV to a much higher position above the aerofoil upper surface than when the trailing-edge flap was not deflected. Because of the higher TEV position, the large nose-down pitching moments associated with the shedding of the TEV were reduced. However, given the fact that dynamic stall is essentially a leading edge phenomenon, the trailing-edge actuator is only limited to mitigating the effects of the dynamic stall process rather than to suppress the formation of dynamic stall vortex.

The leading-edge slat method proposed by Carr and McAllister (1983) seems to be the most promising flow control mechanism as the slat/aerofoil combination delays the forward movement of the flow reversal from the aerofoil trailing edge and hence suppresses the formation of the dynamic stall vortex. Although the leading-edge slat has shown the benefit of suppressing the dynamic stall vortex akin to steady upper-surface blowing [see Yu et al (1995)], it remains an unattractive option for helicopter rotor blade designers due to the added mechanical complexities and weight associated with installing and operating a leading-edge slat. Consideration must also be focussed on the effects of high centripetal accelerations on actuators.

The aerofoil deformation method proposed by Geissler and Raffel (1993) and Reuster and Baeder (2001) as well as the trailing-edge flap method proposed by Chan and

Brocklehurst (2001) and Feszty et al (2003) is considered undesirable because these methods only mitigate the effects of the dynamic stall rather than suppress the formation of dynamic stall vortex. Furthermore, apart from the issue of mechanical complexity and weight, design of a practical actuation mechanism to deform the aerofoil and/or move the trailing-edge flap, which have not yet matured beyond a preliminary stage, also makes these devices unfavourable with rotor blade designers.

### 2.3.2 Dynamic stall control by boundary-layer blowing or suction

A full-scale wind-tunnel test of a 13.5m diameter, three-bladed helicopter rotor examining the delay of retreating blade stall by means of steady blowing from rotor blade leading edge or mid-chord was reported by McCloud et al (1960). The rotor blades used had a cambered NACA 0012 aerofoil section with a chord of 0.42m. Tangential leading edge and mid-chord blowing was only provided between 60% and 95% of the rotor radius,  $r$ , as shown in Figure 2.5 below.

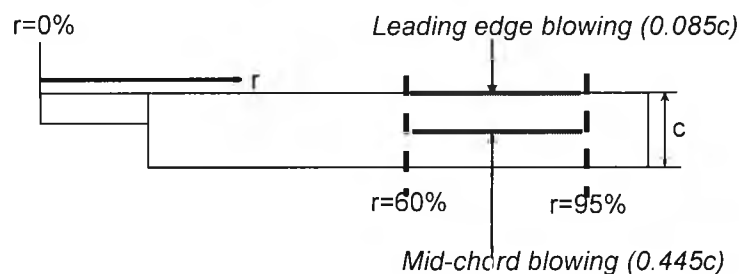


Figure 2.5: Location of leading edge and mid-chord blowing along the rotor radius

The leading-edge boundary-layer control consists of a slot (width of  $0.004c$ ) positioned at 8.5% chord; whereas the mid-chord boundary-layer control consists of 32 slots (length  $\approx 0.15c$  and width  $\approx 0.006c$ ) positioned at 44.5% chord and spaced about  $0.03c$  apart. The blowing momentum coefficient utilised for both the leading edge and mid-chord blowing ranged between  $0.0 \leq C_{\mu} \leq 0.06$ . Results of the investigations carried out to determine the effects of blowing boundary-layer control applied to a helicopter rotor with cambered blades showed that retreating blade stall can be significantly delayed in the advance ratio,  $\mu$ , range of 0.3 to 0.46 by blowing near the leading edge of the rotor

blades. Blowing from the mid-chord of the rotor blade did not have any effect on retreating blade stall for the range of flow rates investigated.

An experimental study by Weaver et al (1996) was performed to further examine the effects of steady upper-surface blowing on an aerofoil's dynamic-stall behaviour. The test was conducted in the U.S. Army Aeroflightdynamics Directorate (AFFD) closed-circuit water tunnel at the NASA Ames Research Center water tunnel. Measurements for the test were made on a Boeing-Vertol VR-7 aerofoil, with chord of 0.1m, at a Reynolds number based on chord of  $0.1 \times 10^6$ . Steady addition of momentum,  $0 \leq C_{\mu} \leq 0.57$ , was provided to the aerofoil upper surface boundary layer via a spanwise slot (width =  $0.00075c$ ) positioned at the aerofoil quarter-chord. Flow visualisation of the unblown aerofoil oscillating at ( $\alpha = 10 + 10 \sin \omega t$ ) with a reduced frequency,  $k$ , of 0.05 showed that dynamic stall only occurs over a small portion of the oscillation cycle. Flow visualisation results showed that employing steady upper-surface blowing prevents the forward movement of the trailing edge separation. Yu et al (1995) suggested that preventing the forward movement of the trailing edge separation resulted in the suppression of the dynamic stall process. Measurements of the oscillating aerofoil demonstrated that steady upper surface blowing (i), eliminated moment and lift stall; (ii), significantly enhanced lift; (iii), substantially reduced lift curve slope hysteresis; and (iv), reduced the severity of load fluctuations. Flow visualisation of the unblown aerofoil showed that increasing the oscillation frequency from  $k = 0.05$  to  $k = 0.15$  resulted in dynamic stall occurring over a larger portion of the oscillation cycle. Measurements of the oscillating aerofoil demonstrated that although steady blowing at  $k = 0.15$  reduced the lift curve slope hysteresis and the severity of load fluctuations; the reductions were not as large as they were for the lower reduced frequency.

Alrefai and Acharya (1995) conducted an experimental investigation examining the effect of leading-edge suction on the evolution of the unsteady surface pressures and flow development over the suction surface of a dynamically stalling aerofoil. The study was conducted on a NACA 0012 aerofoil with chord of 30cm for a wide range of dimensionless pitch rates  $0.01 < \alpha^+ < 0.15$  at a Reynolds number based on chord of  $1.1 \times 10^5$ . Boundary layer suction, for dimensionless suction flow rates of  $0 < Q < 0.024$ , was achieved via a spanwise suction slot (width =  $0.0017c$ ) positioned at 2% chord. Results of the tests showed that at a given pitch rate, e.g.  $\alpha^+ = 0.15$  and angle of attack,

e.g.  $\alpha = 35^\circ$ , complete suppression of the dynamic stall vortex could be achieved by utilising the optimum value of controlled suction,  $Q_{opt} = 0.0074$ . Suction rates higher than the optimum value had no effect on the flow field or pressure distribution whereas decreasing the suction rate below the optimum value resulted in the presence of a dynamic stall vortex.

McCloud et al (1960) has shown that steady upper-surface blowing from the leading edge of the rotor blade successfully delayed retreating blade stall. However, they did not offer an explanation on how upper-surface blowing delays the onset of dynamic stall. Following the tests of McCloud et al (1960), Weaver et al (1996) utilised steady upper-surface blowing from the vicinity of the leading edge to effectively suppress the formation of a dynamic stall vortex on an oscillating aerofoil. Flow visualisation carried out by Weaver et al (1996) showed that steady upper-surface blowing prevents any significant trailing-edge separation from occurring [see also Yu et al (1995)]. Referring to Figures 1.7 (b) to 1.7(e) in Table 1.1 (see Chapter 1), it can be shown that on an unblown oscillating aerofoil the occurrence and forward movement of trailing-edge separation leads to the formation of a dynamic stall vortex. Therefore, preventing the occurrence and/or forward movement of trailing-edge separation would potentially control or eliminate the formation of the dynamic stall vortex. Employing steady upper surface blowing on an oscillating aerofoil controlled dynamic stall akin to the slat/aerofoil combination of Carr and McAllister (1983), but without the problem of added weight and mechanical complexities. Conversely, Alrefai and Acharya (1995) has shown the possibility of using leading-edge suction to control or eliminate the dynamic stall vortex, but this method is considered undesirable and uneconomical due to the complexity of the ducting involved to transport the ingested boundary layer [Cheeseman (1967)].

Whilst, the potential of using steady upper-surface blowing to control the retreating blade boundary layer has been successfully demonstrated by McCloud et al (1960), Weaver et al (1996) and Yu et al (1995), the amount of blowing utilised to suppress the formation of the dynamic stall vortex is considered very high. The prospect of using an active flow control system utilising low amounts of blowing to control or eliminate the formation of the dynamic stall vortex on an oscillating aerofoil offers a way forward. The evaluation of an innovative concept at City University to capitalise on this approach

was demonstrated for a range of single-element and multi-element aerofoils [see Innes (1995), Oliver (1997), Vronsky (1999) and Lewington (2000)]. The concept involves studying the utilisation of low momentum AJVGs ( $C_{\mu} \leq 0.010$ ) to enhance the natural mixing in the shear layers above a dynamically stalling aerofoil; with the aim of delaying the forward movement of trailing edge separation and controlling or eliminating the dynamic stall vortex.

## **2.4 Control of separation over swept wings by passive means**

Investigations of the dynamic stall vortex shedding around the azimuth of the rotor disk by Bousman (1997) showed that dynamic stall occurs primarily between the azimuth angles  $230^{\circ} \leq \Psi \leq 310^{\circ}$ . Because the retreating rotor blade is only instantaneously unswept at the azimuth angle  $\Psi = 270^{\circ}$ , the effect of sweep becomes an important criterion when deciding the geometric configuration of the flow control devices required to improve the aerodynamic performance of the rotor blade. A series of experimental and numerical tests reported in the following section reviews the application of potential flow control devices to control flow separation on wings with moderate to high sweepback angles.

Mabey et al (1989) carried out experiments to develop leading-edge notches to improve the subsonic performance of moderate sweep wings. The model, a large half model of the RAE High Incidence Research Model (HIRM), was tested at a Reynolds number based on mean chord of  $3.6 \times 10^6$ . Leading-edge notches were provided at six positions along the span of the model wing, which had a leading-edge sweep of  $60^{\circ}$ . Mabey et al (1989) concluded that carefully designed leading-edge notches placed at carefully selected positions could inhibit the growth of leading-edge separation bubbles. This will reduce the wing buffeting and provide small improvements in overall force characteristics. Badly designed leading-edge notches positioned in sensitive positions can increase wing buffeting whilst seemingly improving overall force characteristics. It was also found that short leading-edge fences, as well as ‘vestigial’ fences, could also inhibit the growth of leading-edge separations and thus improve wing buffeting.

Ashill and Riddle (1993) investigated the potential of using 'vestigial' or small fences as a means of controlling boundary layer separation on a swept wing. The tests were carried out on a cambered wing with a  $60^\circ$  leading-edge sweep wing at a Mach number of 0.18 and Reynolds number, based on geometric mean chord ( $\hat{c}$ ), of  $3.9 \times 10^6$ . Sub boundary layer vortex generators (SBVGs) were thin wires of circular cross section, length =  $0.023\hat{c}$  and diameter =  $0.00051\hat{c}$  and primarily inclined at  $16.3^\circ$  (orientation angle measured between the axis of the VG and the wing leading edge). Tests showed that the small fences or SBVGs provided an effective control of flow separation on the upper surface of a highly swept, cambered wing, designed primarily for efficient supersonic manoeuvres. The wire devices used were much smaller in size as a proportion of the wing mean chord compared with the fences used by Mabey et al (1989).

Utilising the same model of Ashill and Riddle (1993), Ashill et al (1994) experimentally determined parameters affecting the effectiveness of SBVGs at controlling three-dimensional separation on a swept wing. The effectiveness of SBVGs is dependent on the following parameters:

- a) *Position of SBVG in relation to the upper surface separation line.* Optimum performance was achieved when the SBVG was positioned close to the separation line.
- b) *Orientation angle between the SBVG axis and the leading edge.* For these tests, the optimum angle of a single SBVG is about  $16^\circ$ , independent of axial position, for angles of incidence between  $13^\circ$  and  $15^\circ$ .
- c) *SBVG height or SBVG diameter.* The most effective height or diameter of the SBVG is between 3 to 6 times the maximum height of the viscous sub-layer.

Although the flow control mechanism studied by Mabey et al (1989), Ashill and Riddle (1993) and Ashill et al (1994) successively controlled three-dimensional separation, it mainly concentrated on highly swept leading-edge wings with leading-edge separation. Low speed wind tunnel tests conducted by Broadley and Garry (1997) utilised a swept leading- and trailing-edge wing capable of being swept aft from  $\Lambda = 0^\circ$  to  $\Lambda = 60^\circ$  to study the effectiveness of controlling trailing-edge separation using vane vortex generators (VVGs). The experiments were conducted at a Mach number of 0.17 and a chord Reynolds number of  $4 \times 10^6$ . The characteristics of the wing were constant cross section with a chord of 0.61m and a semi-span of 1.83m at  $0^\circ$  sweep and

thickness/chord ratio of 14%. The VVGs utilised were cropped delta-wing vanes with a height of  $0.016c$ . Experimental results showed that vortex generators positioned at  $0.65c$  and toed out at an angular deflection to the freestream flow direction of  $+25^{\circ}$  provided the best reduction in the lift-dependent drag factor for the  $\Lambda = 40^{\circ}$  and  $\Lambda = 50^{\circ}$  wings. Corresponding numerical analysis showed that the VVGs enhanced aerodynamic performance if the height of the VVG was equal to the local height of the boundary layer and angled between  $+18^{\circ}$  and  $+30^{\circ}$  relative to the local freestream direction. The vanes were more effective in controlling separation when positioned upstream of the clean wing separation position. However, the height of the VVG was the more important parameter compared with its chordwise positioning. When the height of the VVG was greater than the local boundary-layer thickness, the longitudinal streamwise vortex produced was not close enough to the wing surface to control the separation effectively.

Mabey et al (1989), Ashill and Riddle (1993), Ashill et al (1994) and Broadley and Garry (1997) have successfully demonstrated the ability of passive flow control devices to control separation on wings with moderate to high sweepback angles. However, Carr and McAllister (1983) reported that although passive vortex generators significantly delayed static stall, dynamic loads of an oscillating aerofoil fitted with passive vortex generators were not measurably improved when compared with a basic oscillating aerofoil. Furthermore, employing passive vortex generators is not without cost, as the devices protrude from the aerodynamic surface generating additional parasitic drag. An innovative active pneumatic flow control device originated with the work of Wallis (1952), at the Aeronautical Research Laboratory, Melbourne, and researched extensively at City University, provides an alternative to passive vortex generators in an attempt to reduce the adverse effects of parasitic drag. This is because the pneumatic device can be switched on and off to suit the aerodynamic need. The concept involves injecting air-jets through holes or slots in the aerodynamic surface, which are pitched and yawed relative to the local freestream flow direction to generate longitudinal streamwise vortices. The application of these Air Jet Vortex Generators (AJVGs), at City University, to delay aerofoil stall was mainly conducted on **unswept** single-element and multi-element aerofoils [see Innes (1995), Oliver (1997), Vronsky (1999) and Lewington (2000)]. Experimental tests were, therefore, devised to study the effect of aerodynamic sweep on the geometry requirements of the AJVGs.

## 2.5 Periodic addition of momentum (Periodic blowing)

Research at City University has concentrated upon the application of steady addition of momentum into the boundary-layer via steady AJVGs on a variety of external and internal flows providing useful skin friction enhancement with noticeable suppression of flow separation in both subsonic and transonic flows [see Rao (1998), Innes (1995), Oliver (1997), Küpper (1999) and Lewington (2001)]. The AJVG consists of a small air jet emerging from an aerodynamic surface with the jet pitched and skewed relative to the local freestream flow. The longitudinal vortices generated by an array of AJVGs re-energise the retarded boundary layer by entrainment of high momentum freestream air, enabling it to negotiate severe adverse pressure gradients as the longitudinal vortices penetrate downstream.

McManus et al (1995 and 1996) have successfully demonstrated the potential of reducing the feed air supplying the AJVGs, whilst maintaining aerofoil aerodynamic performance attributed to steady AJVGs, by periodically injecting air-jets into the flow. The spanwise AJVGs incorporated into the test models did not, however, utilise the optimum configuration suggested by Oliver (1997), Vronsky (1999) and Lewington et al (2001). Instantaneous surface pressure measurements on an aerofoil, by Seifert et al (1996), with oscillatory blowing introduced at the leading edge illustrated the presence of at least two large scale coherent structures at every phase of imposed oscillations. The ability of periodic blowing to accelerate and regulate the generation of these large scale coherent structures or eddies is believed to be the underlying physical mechanism responsible for the delay of aerofoil stall. This is because the large eddies generated by the periodic perturbations transports momentum, swept from the freestream to the surface allowing the boundary layer to withstand severe adverse pressure gradients than otherwise possible. McManus et al (1995) and Seifert et al (1996) have suggested that the effectiveness of pulsed blowing in suppressing stall is due to the enhanced crosstream mixing relative to steady blowing as well as the reduction in mass flow because the pulsed jet is only active for some portion of the pulse cycle. One detriment to the technique, however, is increased electrical or mechanical power to drive the pulsed actuators.

McManus et al (1994) conducted a low speed wind-tunnel test utilising circular pulsed AJVGs to control turbulent boundary-layer separation over a  $20^\circ$  divergent lower wall. The tests were conducted at a Reynolds number, based on boundary layer thickness at the jet exit ( $\delta_j$ ), of 2300. The AJVG array was composed of 3 jet orifices (jet diameter,  $D_j = 0.67\delta_j$ ) positioned, off-centreline, approximately  $8\delta_j$  upstream of the divergent floor. The jets were spaced  $4\delta_j$  apart and orientated at  $\phi = 45^\circ$  and  $\psi = 90^\circ$  relative to the oncoming freestream. Test results showed that for a fixed mass flow rate, pulsed AJVGs were more effective in suppressing separation when compared with steady AJVGs.

McManus et al (1994) also recorded flow visualisation images in order to document and study the flowfield topology with and without the AJVGs operating. The flow visualisation technique involves seeding the flow with acetone vapour and using a pulse-laser light source to produce electronic excitation of the acetone molecules, which then fluoresce. The fluorescence was detected using a gated CCD camera to obtain instantaneous images of the acetone vapour distribution. The instantaneous image of the baseline flow, i.e. with AJVGs switched off, clearly show that the boundary layer separates near the upstream end of the divergent wall (see Figure 2.6). In this grey scale image along with those following, dark and light acetone vapour regions correspond to high and low concentrations of boundary layer fluid respectively.

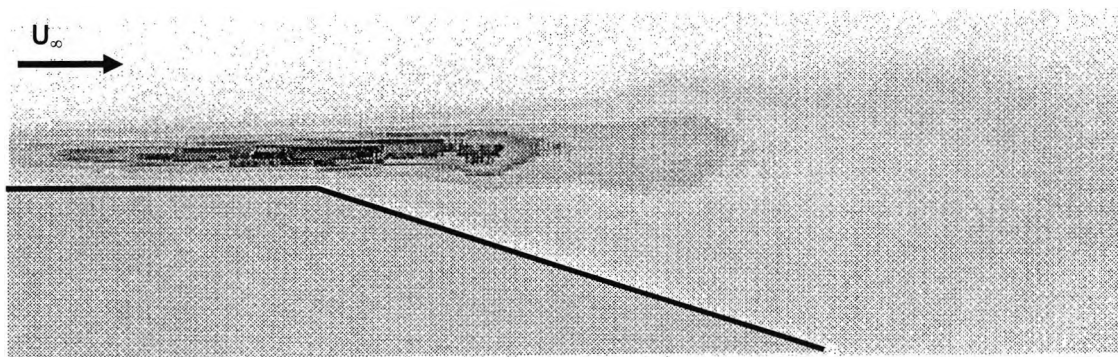


Figure 2.6: Instantaneous image of the flow without AJVGs operating;  $20^\circ$  divergence [courtesy of McManus et al (1994)]

Figure 2.7 shows a set of four images taken at phase angles ( $\theta$ ) of  $0^\circ$ ,  $90^\circ$ ,  $180^\circ$  and  $270^\circ$  with respect to the jet pulse control signal, illustrating the effects of pulsed AJVGs on

the separated flow. This image set shows that a vortex structure or eddy is formed as a result of the jet pulse and then convects downstream adjacent to the lower wall. It was hypothesised that the formation and evolution of the large eddy, generated by the pulsed AJVG, transports (via entrainment) high momentum flow from the freestream to the low momentum boundary layer flow adjacent to the aerofoil surface. This hypothesis is the underlying mechanism of why pulsed AJVGs are superior to steady AJVGs at suppressing separation.

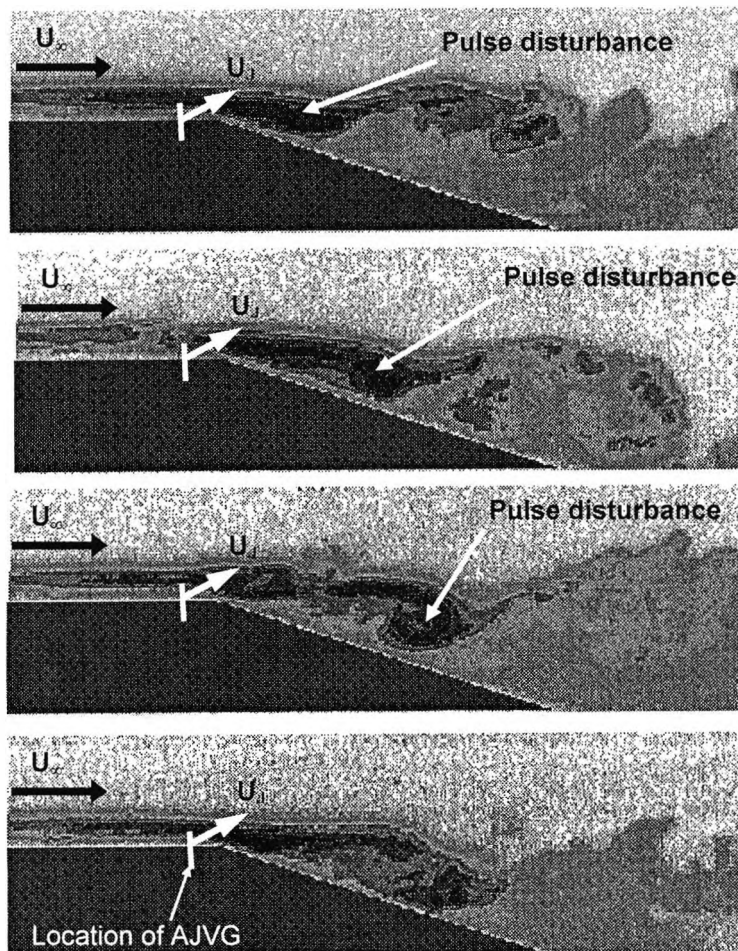


Figure 2.7: Instantaneous images taken at different phase angles ( $\theta$ ) during a pulse cycle;  $\theta = 0^\circ, 90^\circ, 180^\circ$  and  $270^\circ$  (top to bottom) [courtesy of McManus et al (1994)]

The success of the experiments by McManus et al (1994) demonstrating the ability of pulsed AJVGs to control separation over a  $20^\circ$  divergent lower wall led McManus et al (1995) to experimentally assess the effectiveness of pulsed AJVGs to control stall on an

aerofoil model. The tests were conducted at a chord Reynolds number of  $5.0 \times 10^5$ , using a two-element flat-plate aerofoil with a chord of 15.24cm. The leading-edge flap had a length of approximately 21% of the overall chord and is deflected at  $\alpha_f = 15^\circ$ . A single circular AJVG ( $D_J = 0.016c$ ), inclined at  $45^\circ$  and yawed at  $90^\circ$  to the local freestream flow, was positioned at the flap leading edge. Results of these tests showed that the pulsed AJVG successfully delayed aerofoil stall from  $12^\circ$  to  $16^\circ$ . The effectiveness of pulsed AJVGs in inhibiting separation was strongly dependent on the jet-to-freestream velocity ratio (VR) and also on the total mass flow rate through the jet. Maximum separation control was achieved with the pulsed AJVGs operating at jet to freestream velocity ratios,  $VR > 2$ . The dependence on VR may be used advantageously to reduce the total jet mass flow rate by simply reducing the fraction of pulse period over which the jet is flowing.

McManus et al (1996) utilising the test model of McManus et al (1995) found that the optimum pulse frequency for separation control can be calculated using the freestream velocity and aerofoil chord. The pulsing frequency is given in a non-dimensional term as:

$$F^+ = \frac{f * c}{U_\infty}$$

where:

$F^+$  = non-dimensional pulsing frequency

$f$  = dominant pulsing frequency (Hz)

$c$  = aerofoil chord (m)

$U_\infty$  = freestream velocity (m/s)

The optimum pulse frequency is dependent on VR, where for  $VR \leq 2$  the optimum pulsing frequency is  $F^+ = 0.5$  and for  $VR > 2$  the optimum pulsing frequency is  $F^+ = 0.4$ .

The effects of the pulsed AJVGs on the separated flow over the upper surface of the flat plate model were studied by McManus et al (1996) using smoke flow visualisation. Figure 2.8 shows a sequence of images taken with the pulsed AJVGs operating. The images were taken at different phase angles ( $\theta$ ) relative to the pulse cycle to illustrate

the formation and convection of large eddies over the upper surface of the aerofoil model [see McManus et al (1994)]. The image taken at phase angle  $\theta = 180^\circ$  shows the presence of a small eddy over the forward region of the aerofoil and another larger eddy downstream of the aerofoil trailing edge. The small eddy near the aerofoil leading edge convects along the upper surface and grows in size. The structure may be tracked as it convects downstream before shedding from the trailing edge into the aerofoil wake, in the images corresponding to  $\theta = 270^\circ$ ,  $360^\circ$  and  $390^\circ$ .

An additional test, by McManus and Magill (1996), utilising the AJVG configuration of McManus et al (1996) on a 11.6cm chord NACA 4412 aerofoil equipped with a leading-edge flap of 20% chord length, showed that optimum aerodynamic enhancements were obtained at a jet-to-freestream velocity ratio of  $VR = 7.4$  and pulsing frequency  $F^+ = 0.6$ . This value is approximately 30% higher than the optimum value found by McManus et al (1996) suggesting that the optimum pulsing frequency required to enhance aerodynamic performance is geometry dependent.

Magill and McManus (2001) reviewed the feasibility of utilising pulsed AJVGs to control separation on a generic aircraft wing. They used a model of a generic tailless fighter configuration with swept lambda wings. It had a span of approximately 83cm with mean aerodynamic chord of 38cm inboard and 22.5cm outboard. It was equipped with leading-and trailing-edge flaps corresponding to 9% and 18% inboard and 16% and 31% outboard of the mean aerodynamic chord respectively. Four jets were positioned at the leading edge of each wing. The jets were directed toward the tip of the wing and pitched at  $45^\circ$  relative to the oncoming freestream. The inboard jets had a diameter of  $0.008c$  while the outboard jets had a diameter of  $0.011c$ . The lambda wing tests showed that pulsed jets delayed stall by up to  $4^\circ$ , increased  $C_{Nmax}$  by up to 11% and decreased drag at high angles of attack by up to 17%, offering improved post-stall aerodynamic performance. Concurrently, the test results also showed that pulsed jets could be operated asymmetrically to provide lateral manoeuvring control in the region where conventional control surfaces are deemed ineffective. Hence, pulsed jet actuators could conceivably enhance both the aerodynamic performance as well as the manoeuvrability of advanced fighters.

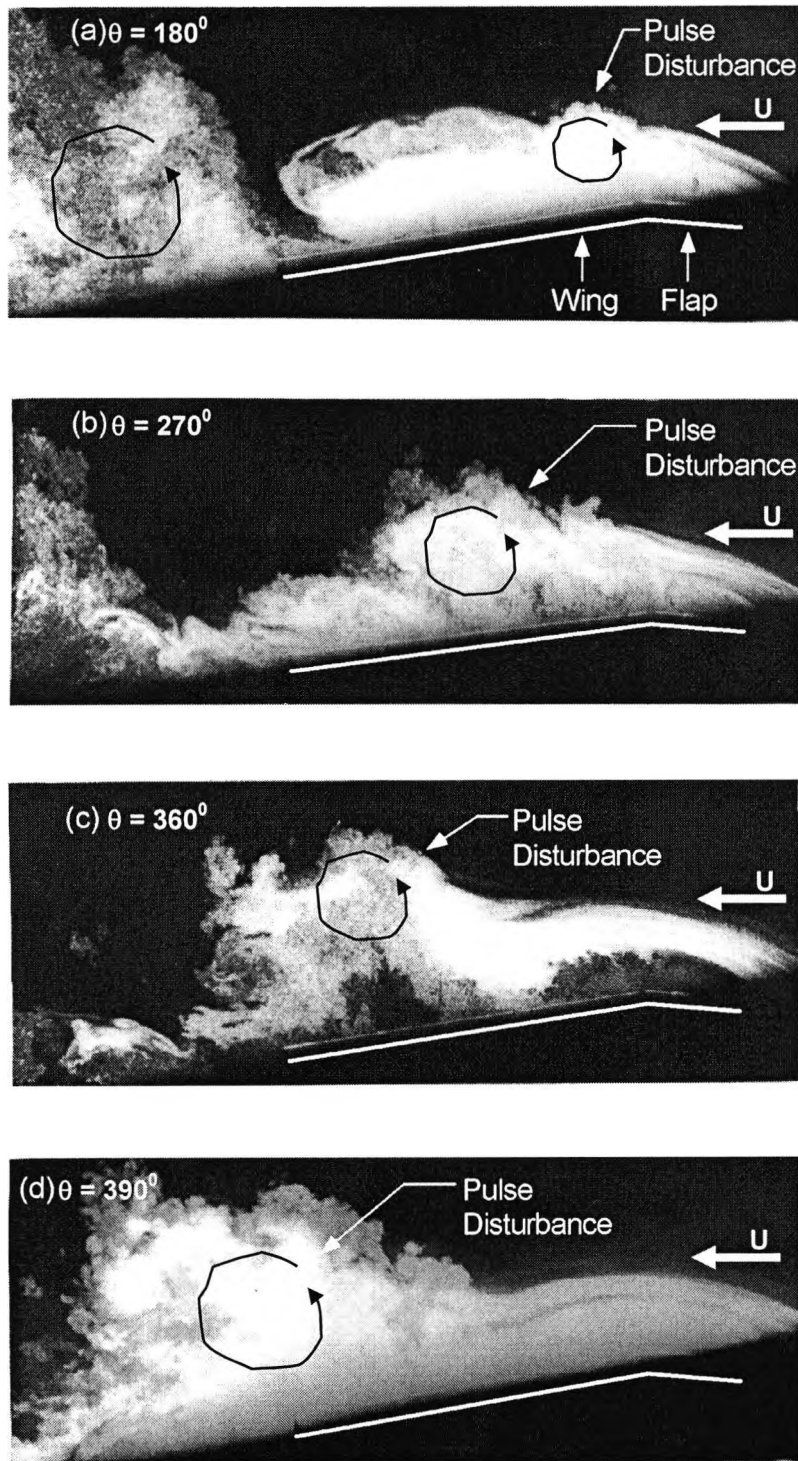


Figure 2.8: Phase conditioned images of the formation and convection of large eddies over the upper surface with pulsed AJVG on;  $\alpha = 12^\circ$ ,  $\alpha_f = 15^\circ$  [courtesy of McManus et al (1996)]

The comprehensive studies of McManus et al (1994, 1995 and 1996) and Magill and McManus (2001) have shown that pulsed AJVGs are more effective in controlling separation with substantially lower jet-mass flow requirements than when the jets were

operated with steady flow. The effectiveness of pulsed AJVGs is dependent on the jet-to-freestream velocity ratio, which can be exploited to reduce the total jet mass flow rate by simply reducing the fraction of pulse period over which the jet is flowing. The optimum pulsing frequency required for effective stall delay is geometry dependent. Magill and McManus (2001) also found that pulsed jet actuators, apart from improving the aerodynamic performance, could also be used to improve manoeuvrability of advanced fighters.

Flow visualisations by McManus et al (1994 and 1996) have demonstrated that the effectiveness of AJVGs to suppress stall was enhanced when the jet flow was made unsteady or pulsed. This is because in addition to streamwise vortices, large-scale coherent structures or eddies are generated in the flow when the jets are pulsed. Both the streamwise vortices and large-scale coherent structures can substantially increase cross-stream mixing and lead to stall suppression in adverse pressure gradients.

Research at City University has successfully demonstrated the application of low momentum AJVGs to single-element and multi-element aerofoil configurations to either improve the skin friction distribution downstream of the jet entry into the flow or enhance the mixing in the aerofoil upper-surface boundary layer to delay separation and hence improve lift/drag performance [see Innes (1995), Oliver (1997), Vronsky (1999) and Lewington (2000)]. McManus et al (1996) has shown that increments of the aerofoil aerodynamic performance attributed to steady AJVGs could be maintained, but with the prospect of further reducing the jet mass momentum fluxes, when the jet flow is made unsteady, i.e. pulsed AJVGs. Tests were, therefore, conducted on a single-element aerofoil, representative of a rotor blade section, with the intent of comparing the effectiveness of steady and pulsed AJVGs to improve aerofoil aerodynamic performance.

## 2.6 Summary of the current state of the art for control of helicopter retreating blade stall

Improving the aerodynamic performance of the rotor blade continues to be a major area where helicopter vehicle performance improvements can be generated. Currently, improvements rely on conventional shape design techniques such as optimising the blade twist distribution along the rotor radius and careful blade planform design allowing the blade loading to be distributed efficiently along the rotor radius. The use of mechanical devices (such as leading- or trailing-edge flaps) and pneumatic (such as tangential wall blowing or suction) flow control devices has been demonstrated to potentially improve rotor blade aerodynamic performance by controlling or eliminating dynamic stall [see McCloud et al (1960), Weaver et al (1996), Alrefai and Acharya (1995), Chan and Brocklehurst (2001) and Feszty et al (2003)]. Boundary-layer blowing provided the most attractive option for installation into a full-scale rotor blade to improve its aerodynamic performance. This is because this active flow control method exhibited the ability to suppress the formation of the dynamic stall vortex without either, the added weight and mechanical complexities associated with operating a leading- or trailing-edge flap or the complexity of the ducting involved to transport the ingested boundary layer associated with boundary-layer suction. However, the tangential wall blowing method proposed by McCloud et al (1960) and Weaver et al (1996) utilised a relatively high amount of blowing ( $C_{\mu} > 0.020$ ) to control dynamic stall.

An experimental seed programme at City University (with funding from Westland Helicopters Ltd.) has successfully demonstrated the potential application of an active flow control device utilising low energy systems to provide large improvements in performance for helicopter aerofoil section. The concept involves employing AJVGs to generate streamwise vortices to enhance mixing between the retarded flow in the viscous shear layers and the high momentum fluid in the freestream. As a result, the momentum deficit in the boundary layer is reduced, as is the likelihood of boundary-layer separation. Improvements in the performance of an unswept modified NACA 23012 aerofoil, representative of a helicopter rotor section, up to 25%  $C_{Nmax}$  and  $6^{\circ}$   $\alpha_{max}$  have been demonstrated when employing low mass momentum fluxes to power the AJVG system ( $C_{\mu} \leq 0.010$ ) [see Lewington et al (2000)].

The proposal of incorporating a spanwise array of AJVGs into a full-scale rotor blade to potentially control retreating blade stall is the leading item of research in the recently awarded Rotorcraft Aeromechanics DARP. The collaborative experimental programme between City University and University of Glasgow is aimed at demonstrating that:

- a) A spanwise array of AJVGs installed into the upper surface of an unswept oscillating aerofoil section is capable of suppressing trailing edge separation and delaying or eliminating the dynamic stall vortex.
- b) AJVGs can replace protuberance-type vortex generators (e.g. VVGs) to effectively control separation on a wing with moderate to high sweepback angles. The potential application of spanwise AJVGs to control dynamic stall on a swept oscillating aerofoil section is important because an unswept retreating rotor blade can experience a  $\pm 30^\circ$  variation in sweep.
- c) Pulsing discrete jets, that are inclined and yawed to the local freestream flow, are capable of delaying aerofoil stall with lower jet-mass flow requirements than when the jets are operated with steady flow. The concept of pulsed AJVGs injecting time-controlled air-jets into the flow would permit the installation of an active, very-low-blowing, pneumatic device on a full-scale rotor blade to control dynamic stall.

### **3. Experimental arrangement – Dynamic Stall Control**

#### **3.1 Introduction**

In the first Rotorcraft Aeromechanics DARP, a collaborative experimental programme between City University and University of Glasgow was initiated to investigate the effects of incorporating spanwise arrays of AJVGs into the upper surface of an oscillating rotor section. The tests were aimed at investigating the effectiveness of AJVGs to delay the forward movement of trailing edge separation and to control or eliminate the dynamic stall vortex [see Yu et al (1995) and Weaver et al (1996)]. The proposed collaboration enabled City University's expertise in AJVG technology to be utilised on an oscillating aerofoil tested at University of Glasgow's dynamic stall test facility.

#### **3.2 Wind tunnel set-up**

The experiments were conducted in the University of Glasgow's Handley Page low-speed closed-return wind tunnel as shown in Figure 3.1. The model was mounted vertically in its octagonal working section of width of 2.13m and height of 1.61m and was pivoted about the quarter-chord position on two tubular steel shafts. These shafts were connected to the main support via two self aligning bearings, with the weight being taken by a single thrust bearing on the top support beam. The dynamic and aerodynamic loadings from the aerofoil were carried to the wind tunnel framework by two transversely mounted beams as shown in Figure 3.2. The angular movement of the model was obtained using a linear hydraulic actuator and crank mechanism. The actuator was mounted horizontally below the wind tunnel working section on the supporting structure, with the crank rigidly connected to the tubular part of the spar by a welded sleeve and keyway. The actuator was a UNIDYNE 907/1 type with a normal dynamic thrust of 6.1kN operated from a supply pressure of 7.0Mpa. A MOOG 76 series 450 servo valve was used via a UNIDYNE servo controller unit to control the movement of the actuator. A suitable feedback signal for the controller was provided by a precision linear angular displacement transducer geared to the main spar of the model.

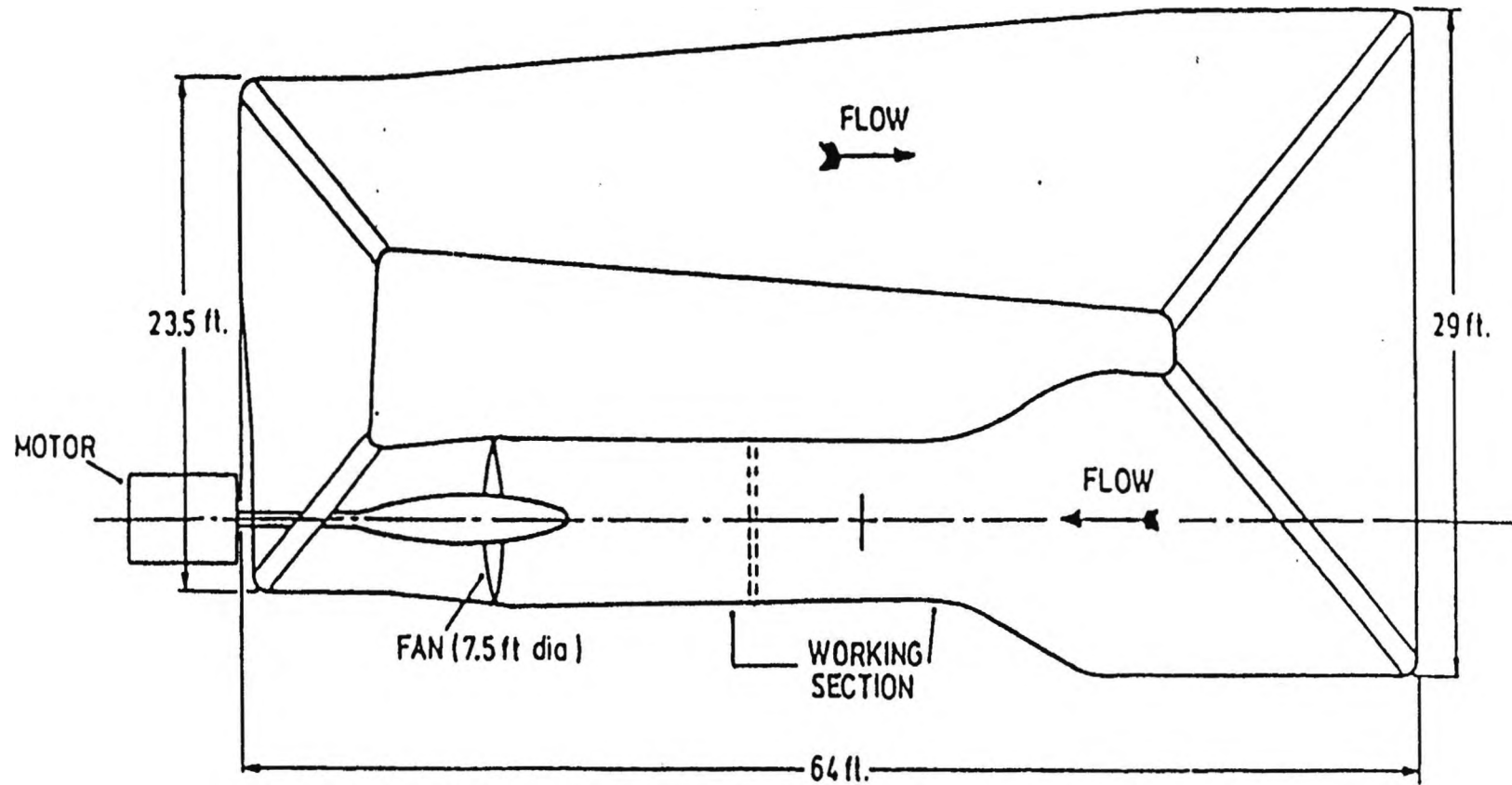


Figure 3.1: Plan view of the University of Glasgow's "HANDLEY PAGE" 7ft X 5ft 3in wind tunnel

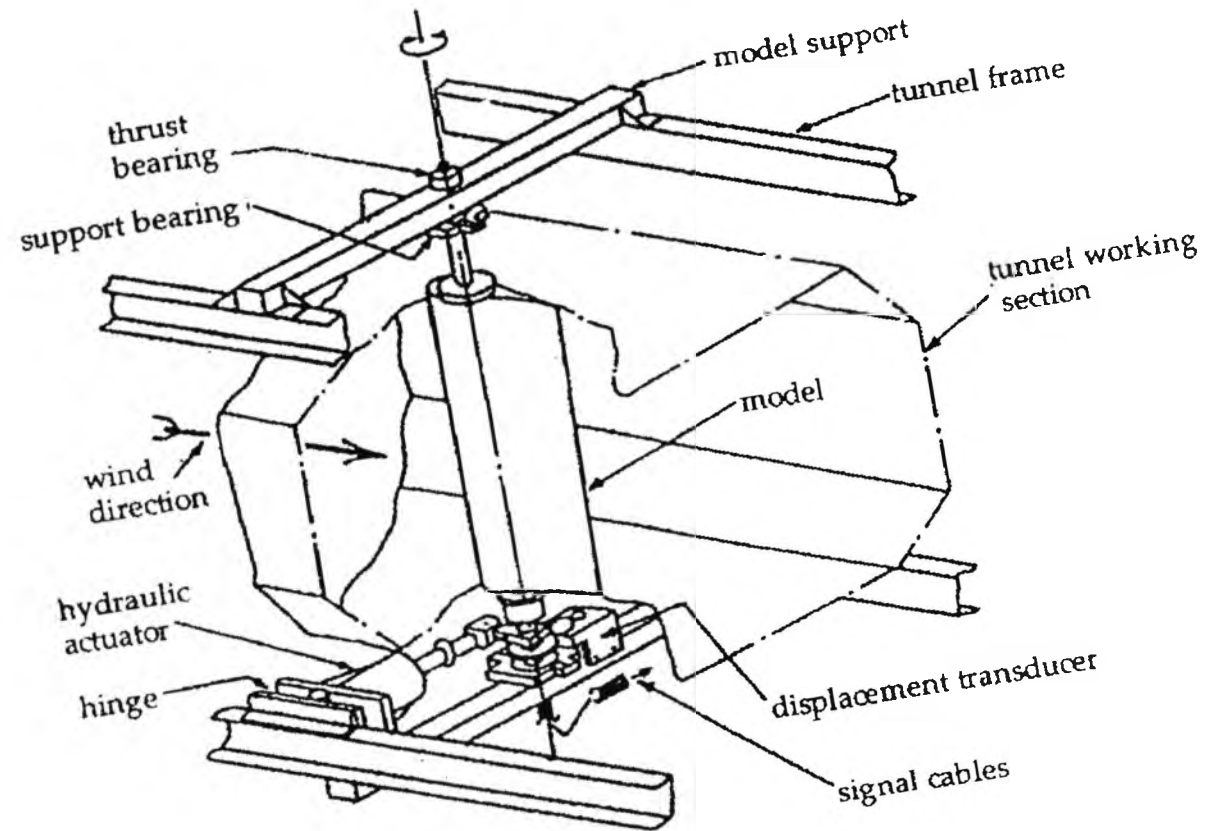


Figure 3.2: University of Glasgow's Dynamic Stall Rig

### 3.3 Wind tunnel model

The single-element RAE 9645 aerofoil section has a chord of 0.5m and a span of 1.35m. This aerofoil profile was designed especially for use as a helicopter rotor blade section at the Royal Aircraft Establishment (RAE) Farnborough. It was designed to delay the onset of retreating blade stall and thereby permit a rotor of given size to generate more lift (in forward flight), without detriment to control loads [see Wilby (1980)]. The design of the RAE 9645 incorporated a combination of nose droop and reflex camber so that separation initiates at the trailing edge. This is because aerofoils which exhibit a trailing-edge separation under quasi-steady flow conditions often display a greater stall delay in unsteady or dynamic conditions than do aerofoils with a leading-edge separation [see Beddoes (1978) and Wilby (1984)]. The model was fitted with two chordwise sets of AJVG arrays located at 12% and 62% chord (see Figures 3.3 through 3.6). Each of the two chordwise positions has a total of 28 AJVGs equally spaced along the span of the model.

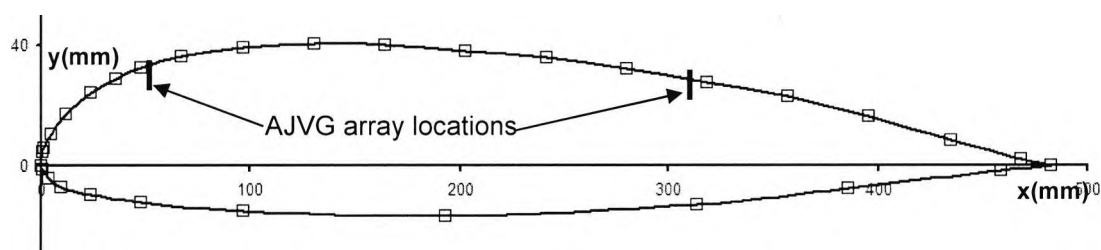


Figure 3.3: Profile of the RAE 9645 aerofoil section showing AJVG locations at 12% and 62% chord

The model was constructed with an internal aluminium framework of ribs and stringers and covered with an outer epoxy glass fibre skin. The geometrical design and spacing of the AJVG installed in the RAE 9645 aerofoil were obtained from research conducted by Henry and Percy (1994), Akanni and Henry (1995), Oliver (1997) and Lewington (2000) at City University (*see also page 150*). Air is supplied to the AJVG arrays via a pressure regulated plenum chamber located within the aerofoil section. The plenum chamber was comprised of an aluminium C-section, having a width of 40mm, height of 20mm, thickness of 2mm and a length approximating the span of the aerofoil model (see Figures 3.4 and 3.5).

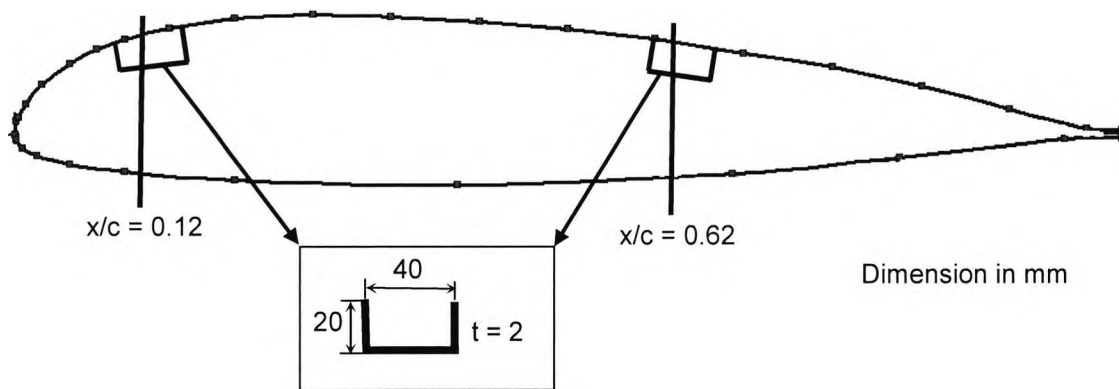


Figure 3.4: RAE 9645 aerofoil illustrating the two plenum chambers

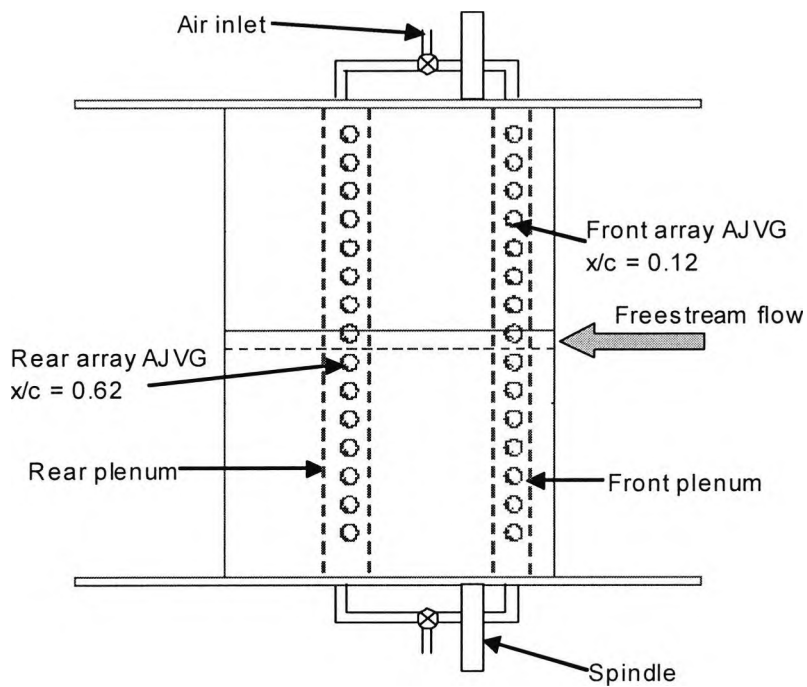


Figure 3.5: Plan view of the RAE 9645 aerofoil installation (see page 150 for AJVG configuration)

### 3.4 Experimental arrangement, instrumentation and analysis

The experimental regime was divided into quasi-static and oscillatory (unsteady) tests for the unblown and blown aerofoil. The blown aerofoil tests included continuous blowing from either the front AJVG array or the rear AJVG array or both the front and rear AJVG arrays operating together (see Table 3.1). The unsteady tests were performed whereby the oscillatory motion could be defined by:

$$\alpha = (\alpha_m + \alpha_a \sin \omega t) \text{deg}$$

where:

$\alpha$  = angle of attack (deg)

$\alpha_m$  = mean angle of attack (deg)

$\alpha_a$  = amplitude of aerofoil oscillation (deg)

$k = \frac{\omega c}{2U_\infty}$  = reduced oscillation frequency

$\omega$  = angular velocity (rad/s)

Experiment	$Re_c$	$\alpha$ range			$C_\mu$	AJVG
Quasi-static	$1.5 \times 10^6$	$-5^0$ to $26^0$			0.0 to 0.010	fb, rb, frb
Oscillatory	$1.5 \times 10^6$	$\alpha_a = 15^0$	$\alpha_m = 10$	$k = 0.01$ to $0.18$	0.0 to 0.010	fb, rb, frb

Table 3.1: Quasi-static and oscillatory tests for unblown and blown RAE 9645

The test procedure for the pressure measurement under quasi-static conditions involves running the wind tunnel up to the desired flow speed with the aerofoil angle of attack set at  $\alpha = 0^0$  and the flow control devices activated if required. This procedure ensures that the AJVGs are employed to influence boundary-layer growth prior to separation rather than reattaching a separated boundary layer. Once a uniform test flow is established, the desired angle of attack is set and the measurements taken. Correspondingly, the execution of the oscillatory tests also necessitated a uniform test flow to be established

at the desired wind tunnel speed with the angle of attack set at  $\alpha = 0^0$  and the flow control devices activated if required. Then, the mean angle of attack was set, i.e.  $\alpha_m = 15^0$ , and an effective oscillation motion set up prior to the acquisition of pressures.

Quasi-static tests were conducted for an angle of attack range of  $-5^0$  to  $26^0$ , in  $1^0$  steps, utilising 32 sampling blocks each collecting 1000 samples per angle of attack. Alternatively, the oscillatory tests were conducted over 4 continuous cycles with each cycle utilising one sampling block giving a total of 4 sampling blocks collecting 8000 samples per sampling block (or cycle). The results over the 4 cycles were then averaged to obtain a representative or gross feature of the dynamic stall process. This was done in order to avoid misinterpreting the data if there were a (slight) difference between two cycles.

#### Surface pressure measurement

The model was instrumented with 36 dynamic pressure sensors measuring the aerofoil surface pressures and the front and/or rear plenum chamber pressures (see Table 3.2 and Figures 3.6 and 3.7).

<b>Pressure orifice position</b>	<b>Quantity</b>
Around the aerofoil at $z/b = 0.50$	30
Front plenum chamber	3
Rear plenum chamber	3

Table 3.2: RAE 9645 surface pressure sensors. Their position and quantity

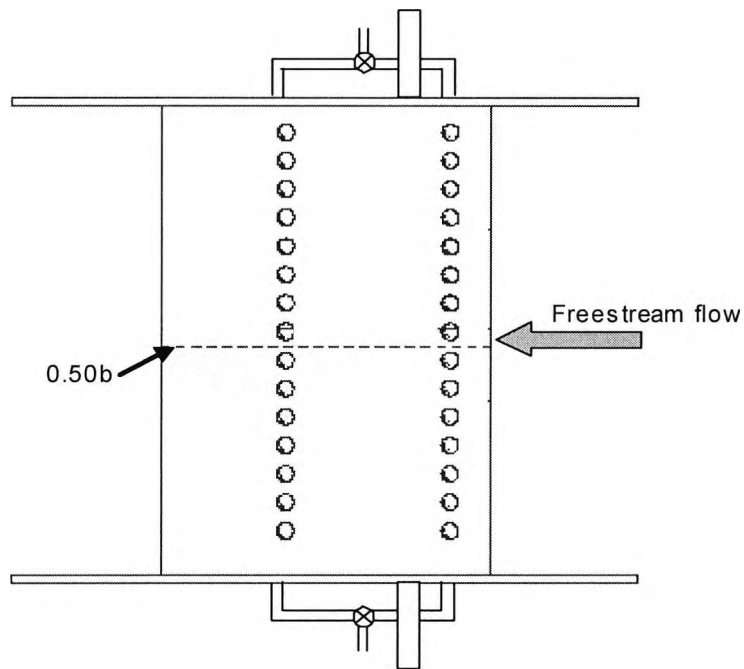


Figure 3.6: Surface dynamic pressure transducer locations at  $z/b = 0.50$  compared with AJVG position

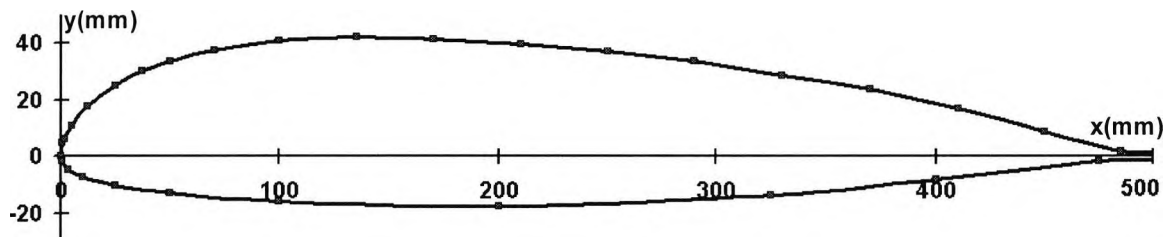


Figure 3.7: Locations of dynamic pressure transducers along aerofoil chord at  $z/b = 0.50$  (20 pressure sensors on upper and 10 pressure sensors on lower surfaces)

The sensors used to measure the aerofoil surface pressure were the differential Sensortech SCC05GSMT(P) rated at 5psid whilst the plenum chamber pressures were measured with the differential Sensortech SCC100(A,G)SMT rated at 100psid. Output signals from the transducers were taken to a specially designed signal-conditioning unit with its own control board. On instruction from the computer, the

control board automatically removed all offsets to below the A-D converter resolution and adjusted all gains as necessary. During a test, the computer sampled the maximum and minimum of each transducer output and adjusted the gains accordingly to improve the data acquisition resolution. The data acquisition was carried out by a PC microcomputer interfaced with proprietary Bakker Electronics BE256 modules that provided the necessary analogue to digital conversion. The software used for data acquisition was TEAM 256. A schematic of the experimental instantaneous pressure acquisition system is provided in Figure 3.8. The measurement system has a capability of measuring up to 200 channels with each A-D channel having a maximum sampling rate of 50kHz. Such a high sampling rate was required to capture the fine detail of the dynamic stall process, especially at the relatively high oscillatory frequencies tested.

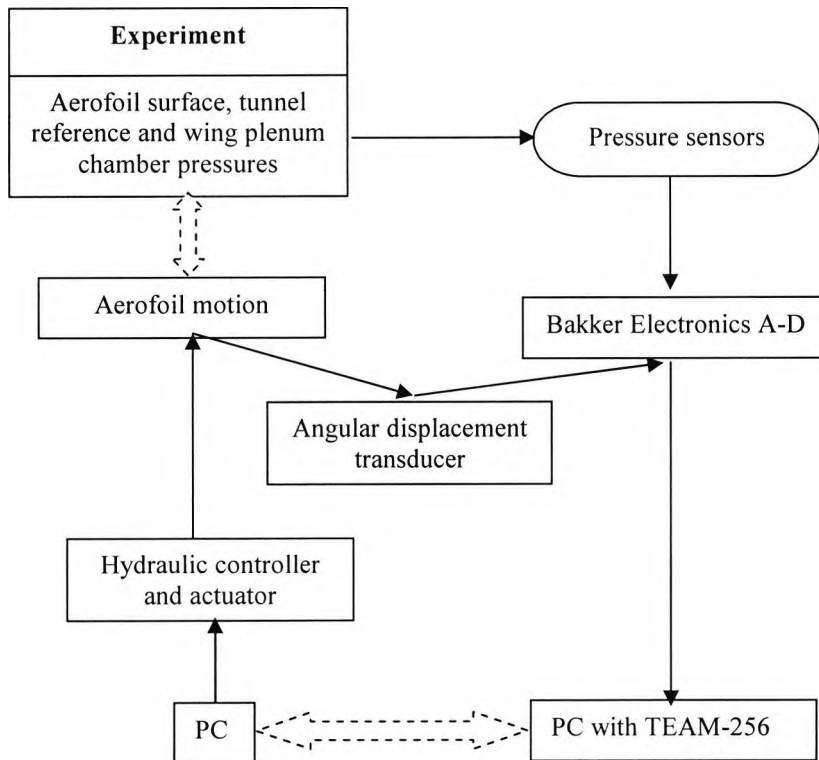


Figure 3.8: Schematic of the experimental instantaneous pressure acquisition system

The following expression is used to calculate the surface pressure coefficients,  $C_{ps}$ ,

$$C_p = \frac{(p - p_\infty)}{\frac{1}{2} \rho U_\infty^2} = \frac{(p - p_s)}{\frac{1}{2} \rho U_\infty^2} \quad (3.1)$$

where:

$p$  = local static pressure on aerofoil surface (N/m<sup>2</sup>)

$p_\infty, U_\infty$  = freestream static pressure and velocity (upstream of the model) (N/m<sup>2</sup>)

$p_s$  = tunnel working section static pressure (N/m<sup>2</sup>)

Assuming  $\frac{1}{2}\rho U_\infty^2 = K(p_t - p_s)$ , where  $(p_t - p_s)$  is the difference between the static pressure in the settling chamber ( $p_t$ ) and the static pressure in the working section ( $p_s$ ).

Substituting this relationship into Eqn. (3.1) gives:

$$C_p = \frac{(p - p_s)}{K(p_t - p_s)} \quad (3.2)$$

Calibrating the wind tunnel prior to installing the RAE 9645 aerofoil yielded the value 1.1392 for the constant K. This expression is then used to calculate the surface pressure coefficients.

## 4. Results and Discussion – Dynamic Stall Control

### 4.1 Introduction

Dynamic stall can be encountered when an aerofoil is rapidly pitched beyond the incidence of static stall. It is characterised by the formation, migration and shedding of a leading-edge vortex or dynamic stall vortex. The movement of this vortical structure across the aerofoil chord as it migrates from the leading edge and sheds at the trailing edge contributes to large lift and moment overshoots in excess of static values. As a consequence, there is significant non-linear hysteresis in the behaviour of aerofoil forces and moments [see Johnson (1980)].

Rotor blade dynamic stall substantially limits the overall performance of rotorcraft in forward flight [see Bousman (1997)]. The understanding and the suppression of the dynamic stall vortex, that is formed under dynamic stall conditions, is a major research area of interest in rotorcraft [see Yu et al (1995)]. Suppressing or eliminating the formation of the dynamic stall vortex will enhance the performance of the helicopter rotor and, hence, expand the helicopter flight envelope and vehicle utility.

Control of the dynamic stall process may be realised using an active flowfield-altering device such as AJVGs. Continuous blowing AJVGs have been successfully utilised at City University to suppress separation on single-element and multi-element aerofoils under **quasi-steady flow conditions** [see Innes (1995), Oliver (1997), Vronsky (1999) and Lewington et al (2000)]. The need to control dynamic stall and the success of quasi-static stall control using continuous blowing AJVGs, led to the idea of integrating them into the RAE 9645 aerofoil and testing it under **dynamic stall conditions**. The objective of this initial experimental research programme was to investigate the feasibility and effectiveness of utilising steady blowing AJVGs to control the dynamic stall process.

## 4.2 Quasi-steady tests

### Surface pressure distributions

First experiments were conducted to assess the aerodynamic performance of the unblown and blown RAE 9645 aerofoil under quasi-steady flow conditions. This included varying the AJVG blowing configuration and pressure, which consisted of blowing from the, (a), front array ( $x/c = 0.12$ ); (b), rear array ( $x/c = 0.62$ ); and (c), simultaneously from front and rear arrays ( $x/c = 0.12 + 0.62$ ), for the low-blowing momentum coefficient range of  $0 \leq C_\mu \leq 0.01$ .

The sensitivity of the chordwise surface static pressures to angle of attack, with AJVGs installed but quiescent, is shown on Figure 4.1. Examination of this test data shows that at  $\alpha = 10^\circ$ , the flow is fully attached over the entire aerofoil upper surface, with full pressure recovery at the trailing edge. As the angle of incidence is increased to  $\alpha = 15^\circ$ , flow separation leaps forward from the aerofoil trailing edge to approximately  $x/c = 0.80$ , where now the trailing-edge pressure coefficient ( $C_{pte}$ ) has turned negative. Increasing the angle of incidence further moves the separation point upstream towards the aerofoil leading edge and thus increases the region of separated flow on the aerofoil. At  $\alpha = 18^\circ$ , flow separation encompasses almost the entire aerofoil upper surface, with the separation point located at about  $x/c = 0.27$ . The region of flow separation is indicated by the plateau in the upper surface static pressure, which is due to the low, nearly constant velocity in the separated flow region adjacent to the aerofoil top surface (dead-air region). At  $\alpha = 15^\circ$  a plateau in the upper surface static pressure is observed from about 80% chord up to the trailing edge and at  $\alpha = 18^\circ$  it is from about 27% chord up to the trailing edge (see Figure 4.1). The onset of trailing-edge separation is indicated when the trailing-edge pressure coefficient,  $C_{pte}$ , goes from a positive value ( $\alpha < 10^\circ$ ) to zero at about  $\alpha = 10^\circ$ .

Employing AJVGs over the upper surface of the aerofoil modifies substantially the surface pressure distributions. Figures 4.2 to 4.7 illustrate the influence of varying the blowing pressure for a given AJVG array configuration. Surface static pressure and leading edge peak suction distributions at  $\alpha = 18^\circ$  are presented in these figures. Blowing continuously from the front AJVG array at  $C_\mu = 0.005$  reattaches the stalled

flow. Figure 4.2 shows that this low amount of blowing delays the upstream movement of separation from the trailing edge and increases suction pressure over the upper surface of the aerofoil, with the benefit of flow control further emphasised by the considerable improvement in leading-edge peak suction (see Figure 4.3). Notwithstanding, progressively increasing the blowing amount from the front AJVG array produces no further significant improvement in the upper surface pressure distribution and leading-edge peak suction.

A range of AJVG blowing pressures was also applied to the rear AJVG array in isolation as well as combined front and rear AJVG array blowing (see Figures 4.4 to 4.7). Blowing from the rear AJVG array alone provides a small suction pressure enhancement around the leading edge region; but fails to fully reattach the highly separated flow at this high incidence angle (see Figures 4.4 and 4.5). Pearcey (1961) has shown that for the AJVG to effectively suppress separation it has to be positioned upstream of the separation line; but at  $\alpha = 18^\circ$ , the separation line is located at 27% chord whilst the rear AJVG array is installed at 62% chord. AJVGs work by inducing the local boundary-layer and freestream flow to form a well-organised, turbulent, helical structure that re-energises the “tired” boundary layer enabling it to negotiate severe adverse pressure gradients. Because the rear AJVG array is immersed in the separated flow region it is unable to induce the formation of a strong vortical structure to suppress separation or promote reattachment of the separated flow.

Blowing from the combined front and rear AJVG arrays effectively restores and increases peak suction around the leading edge; but it is not as effective as blowing from the front AJVG array alone, to control the flow at the trailing edge. When using multiple AJVG arrays, the position of the second array have to be placed far enough downstream to allow the vortices from the front array to pass over the top; if this is not done the vortices from both arrays will be weaker than they would otherwise have been from the position of the second row onwards [see Pearcey (1961)]. Therefore, the inability of the combined front and rear AJVG blowing to sustain the strong, well-organised streamwise vortices capable of negotiating the adverse pressure gradient limits its control over the flow at the trailing edge. Utilising only the front AJVG array at the low blowing momentum coefficient of  $C_{\mu} = 0.005$  is sufficient to enhance the aerodynamic performance of the RAE 9645 aerofoil.

## Performance characteristics of the RAE 9645 aerofoil section

Figures 4.8 to 4.10 show the effect of blowing continuously from the front AJVG array on the normal force and quarter-chord pitching moment performance. Utilising the low blowing momentum coefficient of  $C_{\mu} = 0.005$  increases  $C_{N_{max}}$  by about 16% and delays  $\alpha_{stall}$  by about  $4^{\circ}$ . Examination of the normal force curve slope reveals that blowing at  $C_{\mu} > 0.005$  delays the stall angle of attack,  $\alpha_{stall}$ , by only a further  $1^{\circ}$ . Comparably the maximum normal force coefficient,  $C_{N_{max}}$  creeps up by only 0.1 (see Figure 4.8).

Figure 4.9 represents the stability of the aerofoil in terms of the pitching moment at the quarter-chord for the quiescent and operating front AJVG array. At  $C_{\mu} = 0.005$ , the pitching moment break is delayed, by about  $4^{\circ}$ , to  $\alpha \approx 19^{\circ}$ . Increasing the amount of blowing to  $C_{\mu} = 0.008$  and  $C_{\mu} = 0.01$  further delays the pitching moment break, by another  $2^{\circ}$  and  $4^{\circ}$ , to  $\alpha = 21^{\circ}$  and  $\alpha = 23^{\circ}$  respectively. The delay of the aerofoil pitching moment break is proportional to the increase of AJVG blowing. This is in contrast to the normal force performance as previously noted.

A better and more accurate measure of the AJVG blowing efficiency can be obtained from Figure 4.10, which shows the incremental normal force,  $DC_N$ , per unit  $C_{\mu}$  increasing substantially as angle of attack exceeds  $\alpha_{stall}$ . This plot enables the effectiveness of the AJVG to be assessed relative to the momentum requirements of the flow control system. Blowing at  $C_{\mu} = 0.005$  provides the most enhancement per unit  $C_{\mu}$  for  $\alpha > 14^{\circ}$ ; but blowing at  $C_{\mu} > 0.005$  is clearly less effective.

The effect of AJVG array location at  $C_{\mu} = 0.005$  on the normal force and quarter-chord pitching moment performance of the aerofoil is shown in Figures 4.11 and 4.12. Blowing from the front AJVG array at  $C_{\mu} = 0.005$  increases  $C_{N_{max}}$  by approximately 16% and delays the stall angle of attack and pitching moment break, by about  $4^{\circ}$ , to  $\alpha \approx 19^{\circ}$ . There is no substantial enhancement in the normal force and quarter-chord pitching moment performance when the jet blowing is switched from the front AJVG array to the rear AJVG array. Blowing from the rear AJVG array increases  $C_{N_{max}}$  by about 9%, but delays the stall angle of attack and pitching moment break by only a negligible amount.

Blowing from the front and rear AJVG arrays simultaneously, delayed stall by  $3^\circ$ , to  $\alpha_{stall} \approx 18^\circ$  (see Figure 4.11). It also shows that the aerofoil experiences a sudden and drastic loss in normal force after  $\alpha_{stall}$ , as opposed to the gradual decrease in normal force observed when utilising blowing from the front AJVG array. Similar observations can be noted in the quarter-chord pitching moment curves, where the moment break angle is delayed by about  $3^\circ$  only, to  $\alpha \approx 18^\circ$  (see Figure 4.12). The inability of the combined front and rear AJVG blowing, at a total  $C_\mu$  of 0.005, to negotiate the adverse pressure gradient associated with high incidence angles ( $\alpha > \alpha_{stall}$ ) significantly limits its ability to sustain performance enhancements for the higher range of angle of attack.

#### **4.3 Dynamic stall tests, oscillating aerofoil at $\alpha = (15 + 10 \sin \omega t)$ deg**

The objective of the dynamic stall tests was to explore the potential of utilising continuous blowing AJVGs to control or eliminate the dynamic stall vortex on an oscillating aerofoil. Because the quasi-steady stall angle for the unblown aerofoil was found to be  $\alpha_{stall} = 15^\circ$ , sinusoidal-pitching motion tests were conducted at  $\alpha = (15 + 10 \sin \omega t)$ deg, for the reduced oscillation frequency range of  $0.01 \leq k \leq 0.181$ . The amplitude of  $10^\circ$  was chosen to ensure the formation and shedding of a fully developed dynamic stall vortex as a result of the breakdown of the boundary layer during the pitch-up of the oscillating aerofoil, rather than one that is shed at the top of the cycle [see McAllister and Carr (1979)]. With the tests of Section 4.2 in hand, there is optimism that the upstream AJVG array (located at  $x/c = 0.12$ ) will influence the formation of the dynamic stall vortex [see also McCloud et al (1960)].

### 4.3.1 Reduced frequency, $k = 0.05$ with front AJVG operating, $0 \leq C_{\mu} \leq 0.01$

#### Curves of normal force and quarter-chord pitching moment coefficients versus angle of attack

The force and moment coefficients, for the case of a spanwise AJVG array installed at  $x/c = 0.12$ , with the aerofoil oscillating at  $k = 0.05$  are shown in Figures 4.13 to 4.18. This reduced frequency was chosen based on the suggestion of McCroskey (1981), where for an aerofoil with the sinusoidal-pitching motion defined by  $\alpha = (15 + 10 \sin \omega t)$  deg the reduced frequency required to develop the vortex-shedding phenomenon associated with the dynamic stall process is  $k \geq 0.05$  [see also Chapter 1, Table 1.1]. Oscillating the aerofoil at  $\alpha = (15 + 10 \sin \omega t)$  deg and  $k = 0.05$  will, therefore, ensure the formation, migration and shedding of a dynamic stall vortex before the aerofoil has reached the maximum angle of attack.

#### ***Zero-blowing reference***

The effect of dynamic stall on the aerodynamic loads of the unblown RAE 9645 aerofoil is illustrated in Figures 4.13 and 4.14. Figure 4.13-(a) shows that the aerofoil overshoots the quasi-steady stall angle and generates more normal force or lift than it normally would in a quasi-steady environment. This phenomenon is called “*lift overshoot*”. Past experiments by Carr et al (1977) show that a pitching aerofoil tolerates large regions of reversed flow on its surface before experiencing large-scale, boundary-layer separation. This tolerance allows the aerofoil to rotate well beyond the quasi-static stall angle and produces a much higher normal force that it would normally be capable of.

As the angle of incidence continues to increase, the normal force increases monotonically up to  $\alpha \approx 20^\circ$  after which the slope increases non-linearly ( $C_{N\text{rise}}$ ) due to the vortex lift of the dynamic stall vortex [Figure 4.13-(b)]. The stall vortex grows as the aerofoil continues to rotate upward, and it eventually begins to migrate toward the trailing edge at a speed of roughly  $0.4U_\infty$  [see McCroskey (1981) and Green et al (1992)]. When the stall vortex reaches the aerofoil mid-chord the normal force ceases to increase with angle of attack and the aerofoil is said to be experiencing “*lift stall*”. Figure 4.13-(c) shows this occurs at approximately  $\alpha \approx 22^\circ$ .

The rearward movement of the dynamic stall vortex, from the leading-edge region, considerably alters the pressure distribution that results in a noticeable negative divergence in the quarter-chord pitching moment curve ( $C_{M\text{break}}$ ), i.e. at  $\alpha \approx 20^\circ$  [Figure 4.14-(d)]. This phenomenon is known as “*moment stall*” and usually occurs prior to lift stall. The negative divergence in the aerodynamic pitching moment curve continues as the vortex migrates rearwards. The quarter-chord pitching moment curve reaches a maximum negative value ( $C_{M\text{max}}$ ) as the stall vortex reaches the aerofoil trailing edge, i.e. at  $\alpha \approx 23^\circ$  [Figure 4.14-(e)].

The dynamically pitching aerofoil encounters full stall when the vortex sheds from the aerofoil trailing edge. The shedding of the dynamic stall vortex from the aerofoil trailing edge is represented by the sudden and severe break in the lift-curve slope, which in this case occurs at  $\alpha \approx 23^\circ$  as shown in Figure 4.13-(f). The additional or secondary increase and break observed in the aerodynamic normal force- and pitching moment-curve, as depicted in Figures 4.13 and 4.14, is attributed to the presence of a secondary vortical structure [see McCroskey (1981)].

On the downstroke motion of the oscillating aerofoil, boundary-layer reattachment is initiated at the leading edge, and moves downstream towards the trailing edge as shown in Figure 4.13-(g) [see Ahmed and Chandrasekhara (1994) and Green and Galbraith (1995)]. The boundary-layer reattachment process is only completed towards the end of the downstroke motion, i.e. at approximately  $\alpha \approx 7^\circ$  [Figure 4.13-(h)]. When the boundary layer is completely re-established, the forces and moments return to their former, approximately linear, behaviour. The large amount of hysteresis observed in the aerodynamic loads is due to the fact that the boundary layer is attached for nearly all of the “*upstroke*” motion whereas it is separated for most of the “*downstroke*” motion.

#### ***Blowing from front array of AJVGs $0 < C_\mu \leq 0.01$***

Figures 4.15 to 4.18 show the effect of utilising blowing from the front array of AJVGs in isolation on the aerodynamic loads of the RAE 9645 aerofoil oscillating at  $\alpha = (15 + 10 \sin \alpha) \text{deg}$  and  $k = 0.05$ . Carr et al (1977) [see also **Figures 1.7 (b) to 1.7(e)** in Table 1.1, Chapter 1] has shown that the occurrence and forward movement of trailing-edge

separation on an unblown oscillating aerofoil eventually leads to the formation of a dynamic stall vortex. Therefore, the aim of introducing blowing from the front array of AJVGs is to delay the forward movement of the trailing-edge separation and subsequently control or eliminate the dynamic stall vortex. Figure 4.15 shows that steady blowing at  $C_{\mu} = 0.005$  delays the inception of normal force non-linear increase ( $C_{N_{rise}}$ ) by about  $2^{\circ}$ , to  $\alpha \approx 23^{\circ}$ . The normal force slope then increases non-linearly up to  $\alpha \approx 24.5^{\circ}$  after which the normal force decreases abruptly. The observed change in the gradient of the normal force curve is attributed the formation, migration and shedding of a dynamic stall vortex [see Figure 4.13-(b), (c) & (f)]. Correspondingly, the moment break and the peak nose-down moment of the quarter-chord pitching moment curve is also considerably altered when employing blowing from the front AJVG array, as shown in Figure 4.16. Steady blowing at  $C_{\mu} = 0.005$  delays the pitching moment break ( $C_{M_{break}}$ ) by about  $3.5^{\circ}$ , to  $\alpha \approx 22.5^{\circ}$  and reduces the magnitude of the maximum negative moment ( $C_{M_{max}}$ ) by about 7%. It can, therefore, be suggested that blowing at  $C_{\mu} = 0.005$  suppresses the upstream movement of trailing-edge separation and delays the formation, migration and shedding of the dynamic stall vortex. The delayed development of the dynamic stall vortex on the oscillating aerofoil with blowing at  $C_{\mu} = 0.005$  is highlighted by the delay of  $C_{N_{rise}}$  and  $C_{M_{break}}$ .

When the amount of blowing from the front array of AJVGs is increased to  $C_{\mu} = 0.008$  and then to  $C_{\mu} = 0.01$ , there is no non-linear increase followed by the abrupt decrease in the gradient of the normal force-curve (as seen in Figures 4.13 and 4.15) to indicate the existence of a dynamic stall vortex (see Figure 4.17). Figure 4.18 illustrates the effect of increasing blowing on the quarter-chord pitching moment curve. Blowing at  $C_{\mu} = 0.008$  and  $C_{\mu} = 0.01$  only delays the pitching moment break ( $C_{M_{break}}$ ) by about  $4^{\circ}$  and  $5^{\circ}$ ; but the magnitude of the maximum negative moment ( $C_{M_{max}}$ ) is significantly reduced, by about 14%. When utilising blowing, at  $C_{\mu} > 0.005$ , from the front array of AJVGs, the aerodynamic loads do not exhibit the change in gradients associated with the initiation, development and shedding of a dynamic stall vortex (see Figures 4.17 and 4.18). For that reason it can be suggested that blowing at  $C_{\mu} > 0.005$  successfully eliminates trailing-edge separation and consequently the dynamic stall vortex. When the pitching aerofoil reaches the top of the oscillation cycle and begins to pitch-down, the attached boundary layer detaches completely from the aerofoil and the flow no longer follows the shape of the surface [see Figure 4.17-(i) and (j)]. The sudden break and peak nose

down moment observed in the normal force- and pitching moment-curve slope respectively is, therefore, not due to the shedding of the dynamic stall vortex but to the change in the direction of the pitch at the top of the oscillation cycle [see Carr et al (1977) and McAllister and Carr (1979)].

The introduction of steady blowing also progressively reduces the magnitude of hysteresis in the aerodynamic loads. Weaver et al (1996) suggested that the main factor affecting the hysteresis amplitude is the extent of the separation present throughout the downstroke portion of the oscillation cycle. Figure 4.18 show that the progressive increase of blowing from the front array of AJVGs reduces the magnitude of hysteresis in the normal force curve, thus increasing the usable normal force in the cycle. This is due to the increased rate of boundary-layer reattachment, via entrainment, during the downstroke portion of the oscillation cycle.

#### Instantaneous upper surface pressure distribution

The dynamic aerodynamic loads (see Figures 4.13 through to 4.18) are manifestations of the unsteady pressure distributions on the oscillating aerofoil. Therefore, it is instructive to look at the upper surface pressure distribution ( $C_p$ ) as a function of space ( $x/c$ ) and time ( $\alpha$ ) as shown in Figures 4.20 to 4.23. The instantaneous chordwise pressure distributions for the unblown aerofoil oscillating at  $k = 0.05$ , depicted in Figure 4.20, shows that with increasing angle of attack, the aerofoil peak suction increases, up to P1. This value is well in excess of the quasi-steady peak suction as a result of the dynamic suppression of trailing-edge separation. Also, just prior to the achievement of this peak, a localised increase in suction appears in the vicinity of the aerofoil quarter-chord. This secondary suction feature is produced by the formation of the dynamic stall vortex in this region [see McCroskey (1981) and Carr (1988)]. A further increase in angle of attack leads to the collapse of the leading edge suction peak and the migration of the dynamic stall vortex downstream towards the trailing edge. The suction pressure ridge observed in Figure 4.20 illustrates the passage of the dynamic stall vortex over the upper surface of the aerofoil.

As the dynamic stall vortex reaches the trailing-edge region, it induces the formation of a vortical system of opposite circulation, known as *trailing-edge vortex*. The trailing-edge vortex is formed as a result of the mass influx from the high-pressure region on the aerofoil lower surface to the upper surface, which at this stage is dominated by the dynamic stall vortex suction in the vicinity of the trailing edge as illustrated in Figure 4.19. It has been suggested, that the trailing-edge vortex is responsible for the suction peak, P3, observed over the trailing edge of the aerofoil [see Robinson et al (1986) and Shih et al (1992)]. It was mentioned earlier that the peak nose-down moment ( $C_{Mmax}$ ) observed in Figure 4.14 is attained when the dynamic stall vortex reaches the aerofoil trailing edge. However, Feszty et al (2003) suggests that the dynamic stall vortex only indirectly influences  $C_{Mmax}$ . This is because the dynamic stall vortex induces the formation of a trailing-edge vortex and the shedding of this trailing-edge vortex is responsible for the maximum negative moment,  $C_{Mmax}$ .

Continuing, the instantaneous pressure distribution of Figure 4.20 shows the presence of a secondary suction peak, P2, in the vicinity of the leading edge, which is associated with the development of a secondary vortical structure. Likewise, the migration of the secondary vortex from the aerofoil leading edge downstream towards the trailing edge results in:

- a) The collapse of the leading edge peak suction.
- b) The formation of a secondary trailing-edge vortex that consequently induces a secondary suction peak, P4, in the vicinity of the trailing edge.

The initiation, convection and shedding of this secondary vortical structure results in the additional increase and break observed in the normal force- and pitching moment-curves (see Figures 4.13 and 4.14).

As mentioned previously, the introduction of blowing from a spanwise array of AJVGs located at  $x/c = 0.12$  is aimed at delaying the forward movement of trailing edge separation and controlling or eliminating the dynamic stall vortex. In general, the instantaneous pressure distribution for the oscillating aerofoil with the front AJVG operating, exhibits higher leading-edge suction pressures than the unblown pressure distributions. This is a consequence of the delay in the forward movement of trailing-edge separation. Closer examination of Figures 4.21 to 4.23 reveals that blowing from the front array of AJVGs at  $C_{\mu} = 0.01$  considerably enhances the leading-edge suction

pressure leading to the assumption that this level of steady blowing better suppresses the forward movement, or maybe even eliminates, trailing-edge separation.

An in-depth examination of Figure 4.21, depicting the instantaneous pressure distribution for front AJVG array operating at  $C_{\mu} = 0.005$ , shows the existence of a vortex suction pressure ridge associated with the passage of the stall vortex over the upper surface of the aerofoil. This observation is consistent with the presence of vortex lift followed by the sudden and severe break in the aerodynamic loads attributed to the development of the dynamic stall vortex as shown in Figures 4.15 and 4.16. The existence of a dynamic stall vortex reinforces the suggestion that blowing at  $C_{\mu} \leq 0.005$  is insufficient to effectively prevent the dynamic stall process. Conversely, when blowing is increased to either  $C_{\mu} = 0.008$  or  $C_{\mu} = 0.01$ , the instantaneous pressure distribution does not exhibit any noticeable localised suction build-up that could be attributed to the formation and migration of the dynamic stall vortex. This implies that steady blowing from the front array of AJVGs at  $C_{\mu} > 0.005$  has successfully suppressed the formation of the dynamic stall vortex.

### **4.3.2 Effects of increasing reduced frequency**

#### Curves of normal force and quarter-chord pitching moment coefficients versus angle of attack

Figures 4.24 to 4.27 depict the development of these coefficients with the front array of AJVGs installed but quiescent ( $C_{\mu} = 0.0$ ) and operating at  $C_{\mu} = 0.01$ , with the RAE 9645 aerofoil oscillation frequency increased from  $k = 0.05$  to  $k = 0.1$ . During one rotation a helicopter rotor blade pitches through an approximately sinusoidal variation in angle of attack. The speed of the rotation of the rotor determines the pitch rate of the blade, i.e. the higher the rotational speed, the faster the blade has to pitch to complete the pitch cycle if the amplitude of the cycle does not change. The latter reduced oscillation frequency was chosen because it corresponds to a once per revolution variation on a typical full scale rotor [see Wilby (1980) and (1984)]. That is to say that the pitch amplitude and rotational speed of a typical helicopter rotor blade is such that the reduced frequency at which the blade pitches is about 0.1.

### *Zero-blowing reference – Effects of increasing frequency*

On an unblown oscillating aerofoil, the type of boundary-layer separation, stall and resultant aerodynamic force behaviour is determined not only by aerofoil geometry but also reduced frequency,  $k$  [see Carr et al (1977) and Carr (1988)]. The effects of varying the oscillation frequency on the aerodynamic loads of the unblown RAE 9645 aerofoil, with a sinusoidal-pitching motion defined by  $\alpha = (15 + 10 \sin \omega t)$ deg, are shown in Figures 4.24 and 4.25. Increasing the oscillation frequency from  $k = 0.05$  to  $k = 0.1$  delays the inception of non-linear normal force increase ( $C_{N\text{rise}}$ ) from  $\alpha \approx 20^\circ$  to  $\alpha \approx 23.5^\circ$  and the pitching moment break ( $C_{M\text{break}}$ ) from  $\alpha \approx 20^\circ$  to  $\alpha \approx 22.5^\circ$  [Figure 4.24-(b) and (c)]. The delay of  $C_{N\text{rise}}$  and  $C_{M\text{break}}$  are attributed to the delay of trailing-edge separation moving upstream towards the aerofoil leading edge, which subsequently delays the formation and rearward movement of the dynamic stall vortex [see Carr et al (1977) and Weaver et al (1996)].

Figure 4.24 shows that at the higher reduced oscillation frequency,  $k = 0.1$ , the build up of normal force associated with the formation of the dynamic stall vortex and the subsequent break in the normal force curve is much more severe compared to  $k = 0.05$ . Correspondingly, Figure 4.25 shows that the aerofoil oscillating at  $k = 0.1$  increases the magnitude of peak nose-down moment ( $C_{M\text{max}}$ ) by about 13%. These observations suggest that the dynamic stall vortex increases in strength with increasing oscillation frequency. At  $k = 0.05$ , the non-linear increase followed by the abrupt break in the gradient of the normal force-curve before the aerofoil has reached the maximum angle of attack indicates that the dynamic stall vortex forms, develops and sheds on the upstroke portion of the oscillation cycle (Figures 4.13 and 4.24). Conversely, for the aerofoil oscillating at  $k = 0.1$  the vortex lift followed by the abrupt break in normal force gradient is attributed not only to the existence of a stall vortex but also to the change in the direction of pitch at the top of the oscillation cycle, as illustrated in Figure 4.24-(f).

It was mentioned in Section 4.3.1 that the secondary increase and break observed in the aerodynamic normal force- and pitching moment-curve, for the unblown aerofoil oscillating at  $k = 0.05$ , is attributed to the presence of a secondary vortical structure (Figures 4.13 and 4.14). Additional changes in the gradient of the aerodynamic loads were also observed at the higher reduced frequency,  $k = 0.1$  indicating the presence of a

secondary vortical structure. For  $k = 0.05$  the secondary vortical structure initiates and sheds prior to the aerofoil reaching the maximum angle of attack, but for  $k = 0.1$  this process occurs on the downstroke portion of the oscillation cycle (Figures 4.24 and 4.25).

Increasing the oscillation frequency from  $k = 0.05$  to  $k = 0.1$  results in the increased magnitude of hysteresis in the normal force curve as shown in Figure 4.24. Figure 4.13-(h) shows that for  $k = 0.05$  the boundary layer completely re-establishes itself over the aerofoil surface at  $\alpha \approx 7^\circ$  during the aerofoil pitch-down motion. However, at the higher oscillation frequency boundary-layer reattachment only completes at the end of the downstroke portion of the oscillation cycle, i.e.  $\alpha \approx 5^\circ$  [Figure 4.24-(h)]. The forces and moments only return to their former, approximately linear, behaviour at the beginning of the upstroke portion of the oscillation cycle. For  $k = 0.1$ , boundary-layer separation persists for most of the downstroke due to the time it takes for the wake fluid to convect away from the aerofoil allowing the separated region to close [see Carr et al (1977) and Green and Galbraith (1995)].

#### ***Blowing from front array of AJVGs ( $C_\mu = 0.01$ ) with aerofoil oscillating at $k = 0.1$***

The effects of employing spanwise AJVGs on the aerodynamic loads of the RAE 9645 aerofoil oscillating at  $\alpha = (15 + 10 \sin \omega t)$  deg and  $k = 0.1$  is shown in Figures 4.26 and 4.27. Blowing continuously from the front array of AJVGs at  $C_\mu = 0.01$  is seen to eliminate the non-linear increase and abrupt decrease of the normal force gradient associated with the existence of a dynamic stall vortex (see Figure 4.26). Moreover, utilising AJVG at  $C_\mu = 0.01$  delays the moment break ( $C_{M\text{break}}$ ) by about  $\alpha \approx 2.5^\circ$  to the maximum angle of attack as well as substantially reducing the maximum negative moment ( $C_{M\text{max}}$ ), by about 20% (see Figure 4.27). Because the aerodynamic loads do not exhibit the change in gradients associated with the initiation, development and shedding of a dynamic stall vortex, it can be suggested that blowing at  $C_\mu = 0.01$  successfully eliminates trailing-edge separation and consequently the dynamic stall vortex. It can, therefore, be concluded that the sudden break and peak nose-down moment observed in the normal force- and pitching moment-curve slopes is not due to the shedding of the dynamic stall vortex but to the change in the direction of the pitch at the top of the oscillation cycle [see Carr et al (1977) and McAllister and Carr (1979)].

However, closer examination of the normal force curve reveals that at the beginning of the pitch-down motion the gradient of the normal force-curve increase and decrease indicating the possible existence of a dynamic stall vortex [Figure 4.26-(A)]. With the AJVGs switched on, the boundary layer of the pitching aerofoil remains attached to the surface for the entire pitch-up motion [Figure 4.26-(i)]. As the aerofoil begins to pitch-down, the boundary layer detaches completely from the aerofoil and the flow no longer follows the shape of the surface. It is hypothesised that at the beginning of the pitch-down motion, a dynamic stall vortex is shed from the aerofoil contributing to the increase and decrease observed in the normal force gradient [Figure 4.26-(j)]. The magnitude of the change in the gradient of the normal force indicates that the dynamic stall vortex is weak.

The leading cause of hysteresis amplitude is the extent of the separation present throughout the downstroke portion of the oscillation cycle [see Weaver et al (1996)]. Figure 4.26 shows that spanwise blowing ( $C_{\mu} = 0.01$ ) from AJVGs at  $x/c = 0.12$  reduces the hysteresis loop of the normal force curve by promoting reattachment, via entrainment, of the separated boundary layer on the downstroke portion of the oscillation cycle.

#### Instantaneous upper surface pressure distribution

As mentioned in Section 4.3.1, a popular method of displaying unsteady pressure data is to stack the chordwise pressure distribution to form a pseudo-three dimensional surface; the manifestations of the aerodynamic phenomena then appear as pressure peaks, ridges, etc. Figures 4.28 and 4.29 show the instantaneous pressure distributions for the RAE 9645 aerofoil oscillating at  $k = 0.1$  with the spanwise AJVGs turned off and on, respectively. In general, the characteristics of the instantaneous pressure distribution for the unblown aerofoil oscillating at  $k = 0.1$  correspond to those of the  $k = 0.05$  case. Figure 4.28 shows that the aerofoil peak suction increases, up to P1, with increasing angle of attack. Also, just prior to reaching this peak (P1), a localised increase in suction pressure appears in the vicinity of the aerofoil quarter-chord. This secondary suction feature is produced by the formation of the dynamic stall vortex in this region. Figure 4.24 demonstrates that before the dynamic stall vortex can fully develop, the aerofoil

has reached the top of the oscillation cycle. As the aerofoil begins to pitch-down, the leading edge suction peak collapses and the dynamic stall vortex migrates downstream towards the trailing edge. The suction pressure ridge, observed in Figure 4.28, illustrates the passage of the dynamic stall vortex over the upper surface of the aerofoil.

As the dynamic stall vortex reaches the trailing-edge region it induces the formation of a trailing-edge vortex, which is responsible for the suction peak, P3, observed over the trailing edge of the aerofoil as suggested by Robinson et al (1986) and Shih et al (1992) (see Section 4.3.1 and Figure 4.19). The shedding of the trailing-edge vortical structure is responsible for the peak nose-down moment observed in Figure 4.24 [see Feszty et al (2003)]. Comparing the unblown instantaneous pressure distribution for the aerofoil oscillating at  $k = 0.05$  (Figure 4.20) and  $k = 0.1$  (Figure 4.28) revealed that the dynamic stall vortex and the trailing-edge vortex for the latter oscillation frequency is considerably stronger. This is indicated by the higher suction pressure on the aerofoil surface, as the dynamic stall vortex travels downstream, and the increased suction pressure (P3) at the trailing edge. This effect coincides with the higher vortex lift and the increased peak nose-down moment observed in the normal force- and pitching moment-curves (see Figures 4.24 and 4.25).

Similar to the instantaneous pressure distribution of the unblown aerofoil oscillating at  $k = 0.05$  (see Figure 4.20), Figure 4.28 shows the presence of a secondary suction peak, P2, in the vicinity of the leading edge, which is associated with the development of a secondary vortical structure. The migration downstream of this vortex results in the collapse of the leading edge peak suction and the formation of a secondary trailing-edge vortex that consequently induces the secondary suction peak, P4, in the vicinity of the trailing edge. The initiation, convection and shedding of this secondary vortical structure results in the additional increase and break observed in the normal force- and pitching moment-curves (see Figures 4.24 and 4.25).

Figure 4.29 depicts the instantaneous pressure distribution for the spanwise blowing from AJVGs located at  $x/c = 0.12$ . Employing steady blowing at  $C_{\mu} = 0.01$  considerably enhances the leading-edge suction pressure leading to the assumption that this level of blowing successfully suppressed the forward movement, or maybe even eliminated, trailing-edge separation. An in-depth examination of Figure 4.29 shows the existence of

a vortex suction pressure ridge associated with the passage of a stall vortex over the upper surface of the aerofoil. The low-level suction pressure indicates that the stall vortex is weak. This observation is consistent with the small increase and decrease of the normal force curve at the beginning of the pitch-down motion [Figure 4.24-(A)].

Based on the observations of the normal force- and pitching moment-curves as well as the instantaneous pressure distributions, it is postulated that the formation of the dynamic stall vortex has been successfully eliminated, for the RAE 9645 aerofoil oscillating at  $k = 0.05$  and  $k = 0.1$ , with steady blowing from the front array of AJVGs at  $C_{\mu} = 0.01$  (see Figures 4.13 through to 4.29).

### **4.3.3 Effects of varying AJVG blowing location**

Upon establishing the minimum amount of blowing required ( $C_{\mu} = 0.01$ ) to suppress the formation of the dynamic stall vortex on an oscillating aerofoil, subsequent tests were carried out to ascertain the chordwise location of the spanwise AJVGs to effectively control or eliminate the dynamic stall process. Figures 4.30 and 4.31 demonstrate the effect of varying the AJVG chordwise location on the aerodynamic loads of the RAE 9645 aerofoil oscillating at  $\alpha = (15 + 10 \sin \omega t)$ deg and  $k = 0.1$ .

#### ***Blowing from AJVG located at $x/c = 0.12$***

The ability of blowing from the front array of AJVGs to control dynamic stall has been demonstrated in Section 4.3.2, where blowing at  $C_{\mu} = 0.01$  has successfully suppressed the forward movement of the trailing-edge separation and hence eliminated the dynamic stall vortex. Figures 4.26 and 4.31 show that there is no obvious change in the gradient of the normal force curve, such as the non-linear increase followed by the abrupt break of the normal force, to indicate the existence of a dynamic stall vortex. As a result, the abrupt break in the normal force curve and the peak nose-down moment in the pitching moment curve are attributed to the change in pitching direction at the top of the oscillation cycle (see Figures 4.26, 4.27, 4.31 and 4.32). On the downstroke portion of the oscillation cycle, blowing from the front array of AJVGs at  $C_{\mu} = 0.01$  promotes

reattachment to occur earlier, via increased upstream boundary layer entrainment, thus reducing the hysteresis loop and increasing the useable normal force in the cycle.

### ***Blowing from AJVG located at $x/c = 0.62$***

Changing the AJVG blowing location from  $x/c = 0.12$  (front array) to  $x/c = 0.62$  (rear array), whilst maintaining blowing at  $C_{\mu} = 0.01$ , substantially diminishes the capability of steady blowing to control the dynamic stall process on an oscillating aerofoil. Figure 4.31 shows that the normal force, with the rear AJVG operating, increases almost linearly up to  $\alpha \approx 24^{\circ}$  after which its gradient sharply increases followed by the sudden and severe break in the normal force- and pitching moment-curves. The non-linear increase in the gradient of the normal force is indicative of vortex lift associated with the presence of a dynamic stall vortex (see Section 4.3.1 – *Zero-blowing reference*). Defining the maximum normal force ( $C_{Nmax}$ ) as when the stall vortex ceases to non-linearly increase normal force with angle of attack, Figure 4.31 shows that with the rear AJVG operating  $C_{Nmax}$  is increased by about 7% over that of the unblown aerofoil. This suggests that the dynamic stall vortex, formed when utilising the rear array of AJVGs, is much stronger than that of the unblown aerofoil. Similar to the unblown case, the abrupt break in normal force curve is attributed not only to the existence of a dynamic stall vortex but also to the change in the direction of pitch at the top of the oscillation cycle (see Figures 4.24 and 4.31). Figure 4.32 shows that the peak nose-down moment ( $C_{Mmax}$ ) attained when utilising the rear AJVG blowing is almost as high as that of the unblown aerofoil. There are two possible explanations for this phenomenon. First, the increased strength of the dynamic stall vortex, when compared to the unblown case, probably induces a stronger vortical structure of opposite circulation at the trailing edge (see Figure 4.19). Alternatively, it is hypothesised that the presence of the stall vortex in the vicinity of the trailing edge induces the formation of a secondary vortical structure and blowing from the AJVGs located at 62% chord feeds this vortical structure and thus increases its strength, as illustrated in Figure 4.30. The eventual shedding of this stronger trailing-edge vortex results in the increased maximum negative moment, by about 14%, when compared with the front AJVG blowing (see Figure 4.32).

The ineffectiveness of utilising blowing from the rear AJVG array is further highlighted by its inability to reduce the hysteresis of the aerodynamic loads. Because boundary-

layer reattachment begins at the leading region and moves downstream, the promotion of boundary-layer reattachment can only begin when it approaches the location of the rear AJVG array ( $x/c = 0.62$ ), which occurs at the latter stages ( $\alpha \approx 14^\circ$ ) of the downstroke motion (see Figure 4.31). This may be why blowing from the rear AJVG array is incapable of reducing the hysteresis of the aerodynamic loads.

#### ***Combined blowing from AJVG located at $x/c = 0.12$ and $x/c = 0.62$***

Utilising the combined front and rear AJVG arrays at a total  $C_\mu$  of 0.01 only partially suppresses the dynamic stall process. Analysis of Figure 4.31 shows that the normal force increases almost linearly up to  $\alpha \approx 24^\circ$  after which its gradient sharply increases followed by the sudden and severe break in the normal force- and pitching moment-curves, akin to utilising the rear AJVG array in isolation. As mentioned in section 4.3.1, the non-linear increase in the gradient of the normal force is usually attributed to the presence of a dynamic stall vortex over the aerofoil upper surface. The abrupt break observed in the normal force gradient is, therefore, attributed to the change of the aerofoil pitching motion, as well as the shedding of the dynamic stall vortex, at the top of the oscillation cycle (see Figures 4.24 and 4.31). Using the combined blowing from the front and rear AJVG arrays delays, slightly, the initiation of the stall vortex when compared with blowing from the rear array of AJVGs, which is highlighted by the  $\alpha \approx 0.4^\circ$  delay in  $C_{N_{rise}}$  (see Figure 4.31). This in turn causes the stall vortex to shed at the top of the oscillation cycle before it could fully develop. The maximum negative moment ( $C_{M_{max}}$ ) is, nonetheless, almost as high as when the rear array of AJVGs is operated in isolation (see Figure 4.32). This observation would confirm the hypothesis that the presence of the stall vortex in the vicinity of the trailing edge induces the formation of a vortical structure and blowing from the AJVGs located at 62% chord feeds the vortical structure and thus increases its strength (see Figure 4.30). The shedding of this vortex from the aerofoil trailing edge contributes to the increased  $C_{M_{max}}$ , by about 14%, observed in Figure 4.32. During the pitch-down motion blowing from the front and rear AJVG arrays simultaneously promotes boundary-layer reattachment to occur earlier compared with blowing from the rear array of AJVGs; but it is still not as good as blowing from the array of AJVGs. The hysteresis loop for blowing at  $C_\mu = 0.01$  from the combined front and rear AJVG arrays is, therefore,

slightly smaller than when blowing is employed from the rear AJVG array at  $C_{\mu} = 0.01$  but bigger than with front array of AJVG operating (see Figure 4.31).

## Summary of utilising continuous blowing AJVGs under quasi-steady and unsteady flow conditions

The above discussions detail the experimental results, demonstrating the effects of various AJVG blowing pressures and configurations on the aerodynamic performance of the quasi-static and oscillating RAE 9645 aerofoil. Experiments were conducted at the University of Glasgow's Handley Page low speed wind tunnel at a Reynolds number based on chord of  $Re_c = 1.5 \times 10^6$  and a freestream Mach number of  $M_\infty = 0.13$ . The sinusoidal pitching motion of the oscillating aerofoil is described by  $\alpha = (15 + 10 \sin \omega t)$  deg, for the reduced oscillation frequency of  $k = 0.05$  and  $k = 0.1$ . The AJVG blowing configuration employed was (a), with the front AJVG array only; (b), with the rear AJVG array only; and (c), with both the front and rear AJVG arrays operating in tandem; while the blowing momentum coefficient employed was in the range of  $0.0 \leq C_\mu \leq 0.01$ .

The key findings from the investigations are as follows:

- i) Blowing only from the front AJVG array, operating as a pseudo slat flow, provides the best increase in aerodynamic performance of the unblown RAE 9645 aerofoil under quasi-steady flow conditions.
- ii) Similar to the quasi-steady tests, it is shown that blowing from the front AJVG array considerably enhanced the aerodynamic performance of the oscillating RAE 9645 aerofoil compared with blowing from either the rear AJVG array or from both the front and rear AJVG arrays simultaneously (with the same total mass flux).
- iii) Blowing from the front AJVG array at  $C_\mu = 0.01$  successfully eliminates the formation of the dynamic stall vortex on the RAE 9645 aerofoil oscillating at  $\alpha = (15 + 10 \sin \omega t)$  deg for the reduced oscillation frequency  $k = 0.05$  and  $k = 0.1$ .

Further tests are required to investigate the effectiveness of steady blowing via AJVGs to control or eliminate the dynamic stall vortex at other oscillation frequencies and angles of attack:

- i) On an aerofoil experiencing constant pitch rate motions (ramps). The motion of a sinusoidally pitching aerofoil affects the detail of the stalling sequence, where on the pitch-up, the boundary layer is mostly attached whilst on the pitch-down it is mostly separated. Therefore, by concentrating on either the pitch-up or pitch-down motion the

stalling process can be clearly distinguished [see Coton and Galbraith (1999)]. This is because once the dynamic stall process has been initiated, the subsequent development is insensitive to the effective motion of the aerofoil [see McCroskey (1981)].

ii) On an aerofoil undergoing a sinusoidal pitching motion or constant pitch rate motions under compressible flow conditions. This is because above the threshold Mach number of 0.3, the effect of compressibility is more pronounced and it accelerates the initiation of the dynamic stall vortex as well as changing the mechanism of dynamic stall onset from that observed at low-speed experiments, such as trailing-edge stall becomes leading-edge stall [see Chandrasekhara and Carr (1990) and (1995)]. Moreover, on most modern helicopters the retreating blade works at a Mach number of about 0.4 [see St. Hilaire et al (1979)].

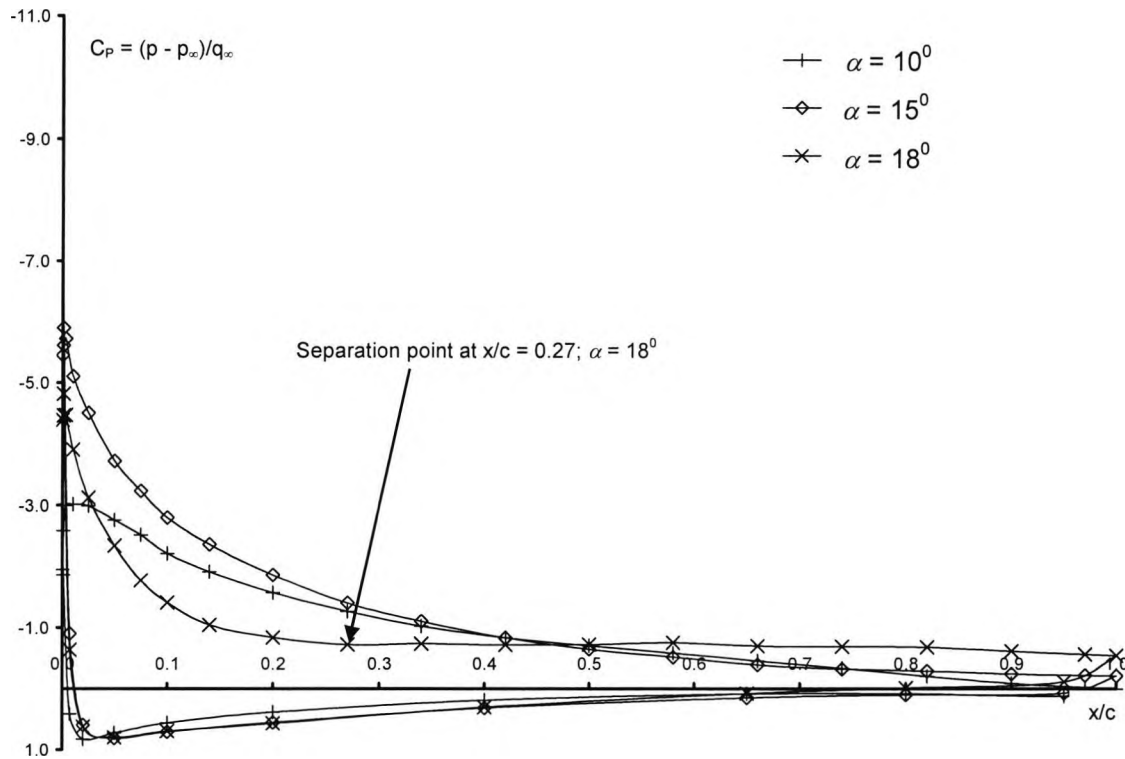


Figure 4.1: Sensitivity of chordwise surface pressure distribution for unblown RAE 9645 at  $\alpha = 10^\circ$ ,  $15^\circ$  and  $20^\circ$ ,  $Re_c = 1.5 \times 10^6$  and  $M_\infty = 0.13$

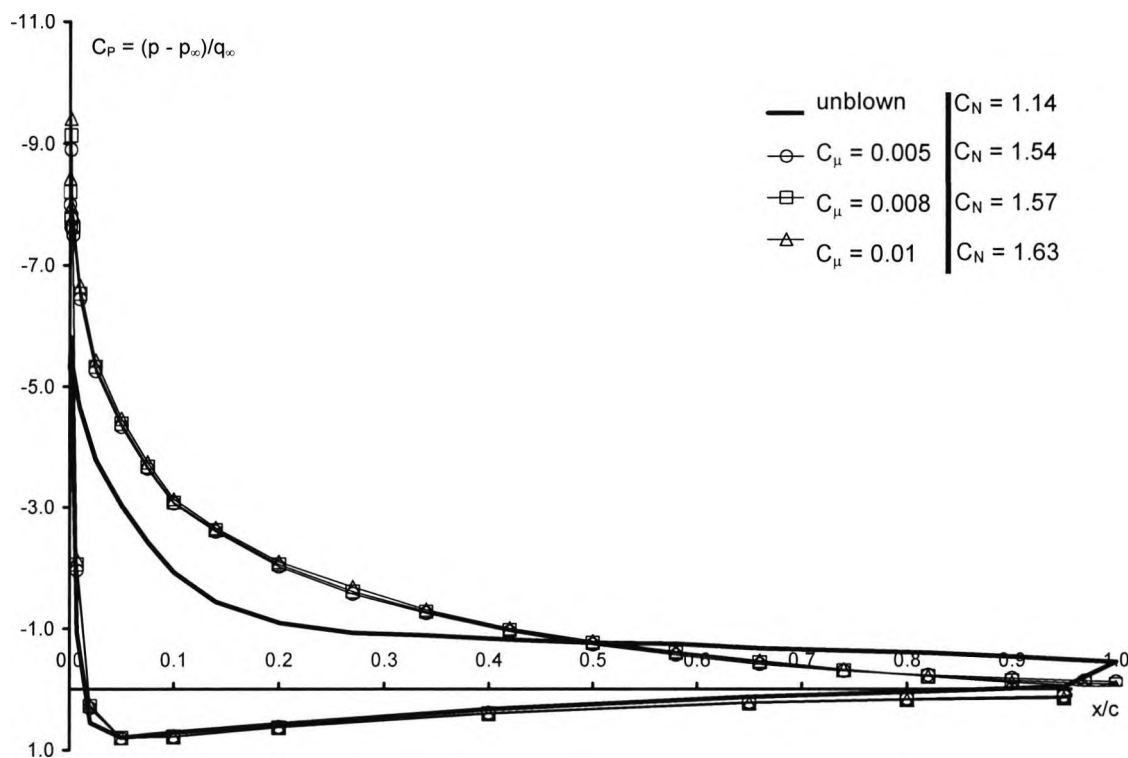


Figure 4.2: Sensitivity of chordwise surface pressure distribution to front AJVG operating for RAE 9645 at  $\alpha = 18^\circ$ ,  $Re_c = 1.5 \times 10^6$  and  $M_\infty = 0.13$

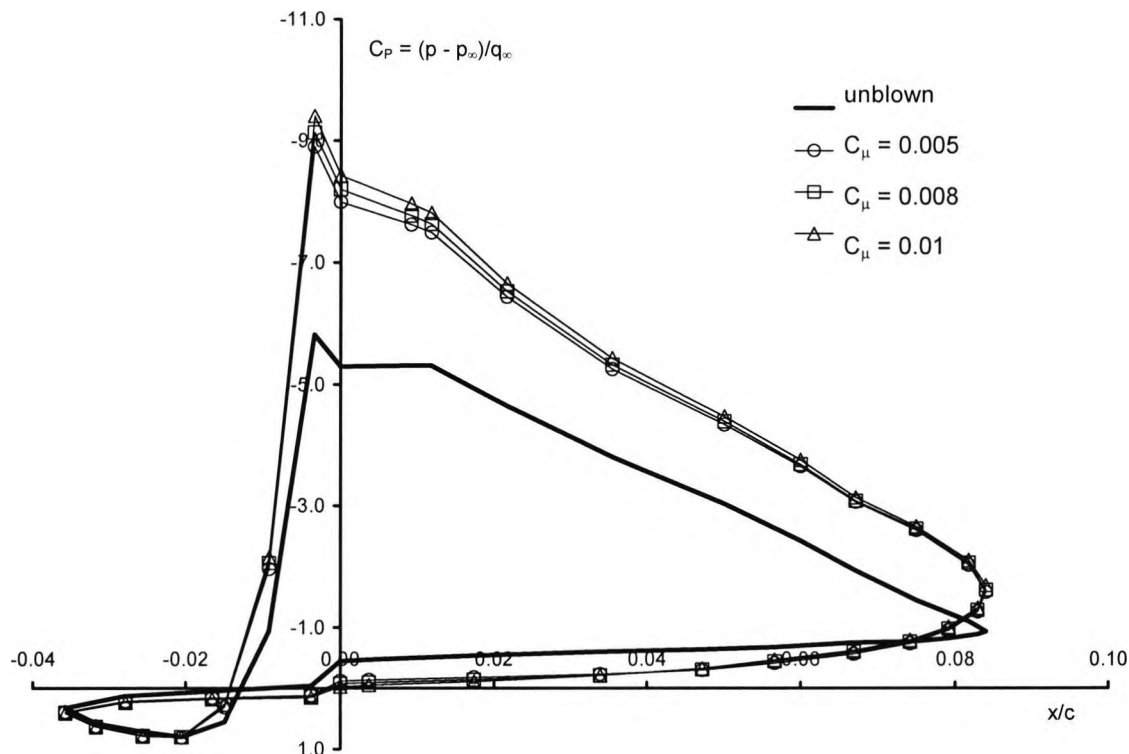


Figure 4.3: Sensitivity of leading edge suction to front AJVG operating for RAE 9645 at  $\alpha = 18^\circ$ ,  $Re_c = 1.5 \times 10^6$  and  $M_\infty = 0.13$

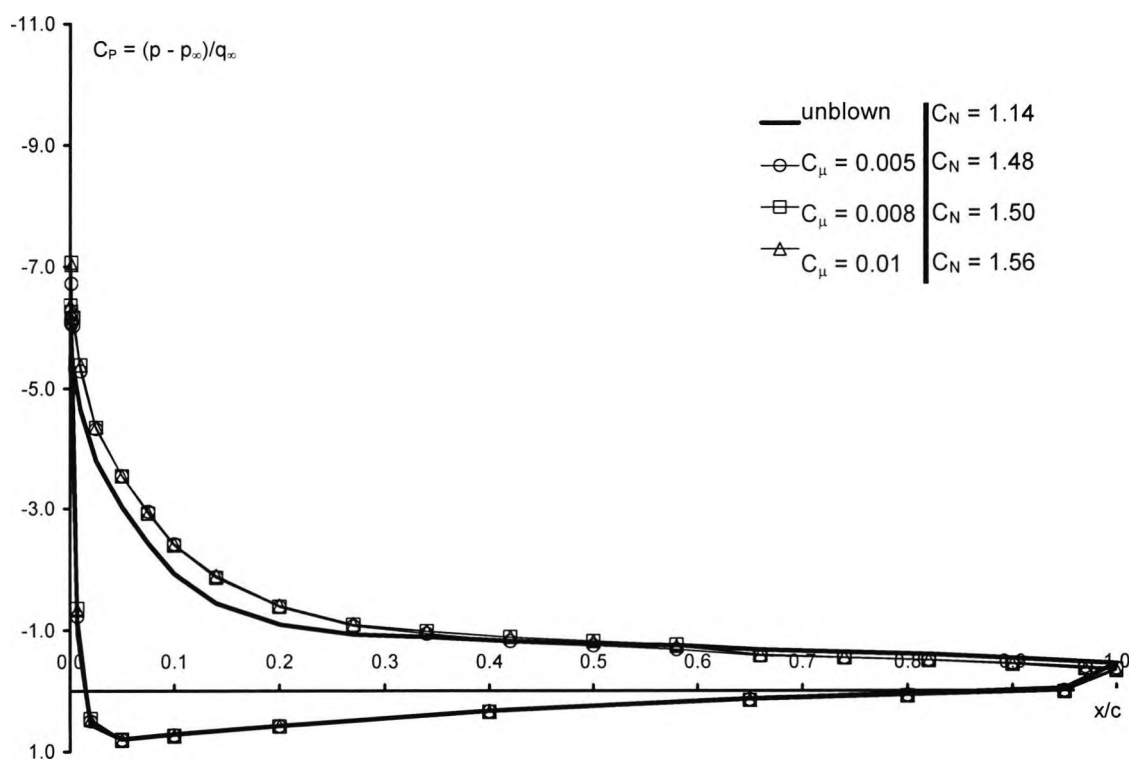


Figure 4.4: Sensitivity of chordwise surface pressure distribution to rear AJVG operating for RAE 9645 at  $\alpha = 18^\circ$ ,  $Re_c = 1.5 \times 10^6$  and  $M_\infty = 0.13$

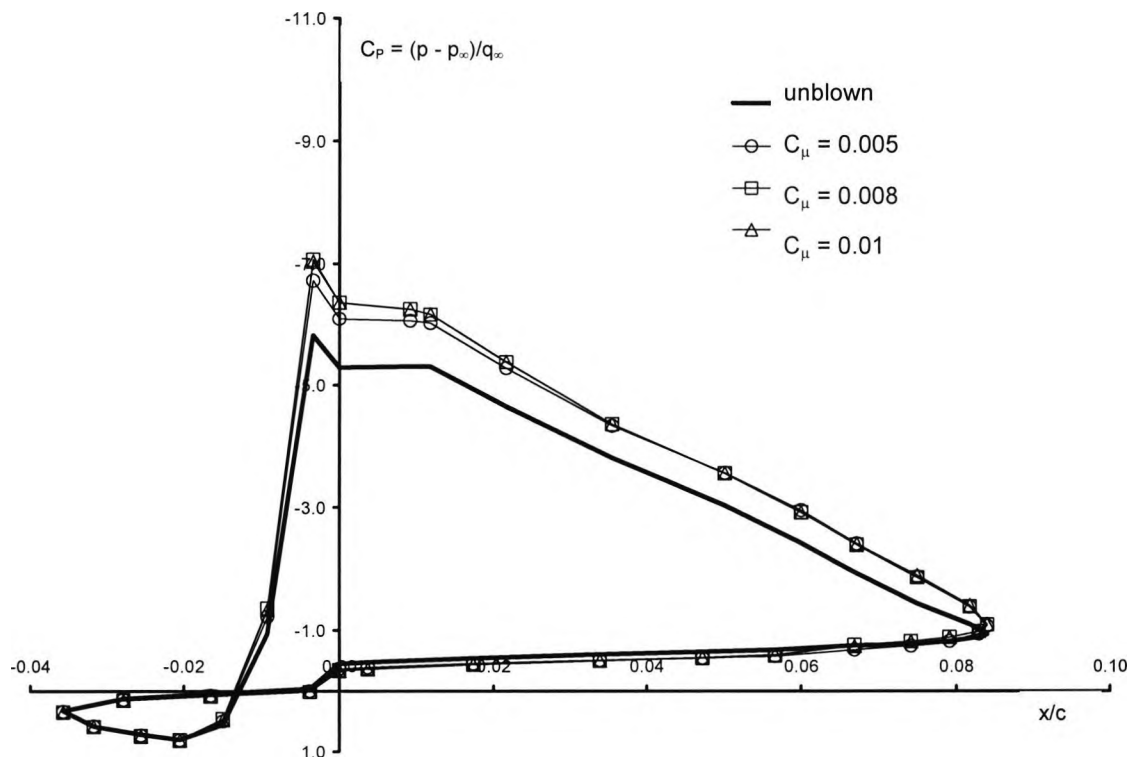


Figure 4.5: Sensitivity of leading edge suction to rear AJVG operating for RAE 9645 at  $\alpha = 18^\circ$ ,  $Re_c = 1.5 \times 10^6$  and  $M_\infty = 0.13$

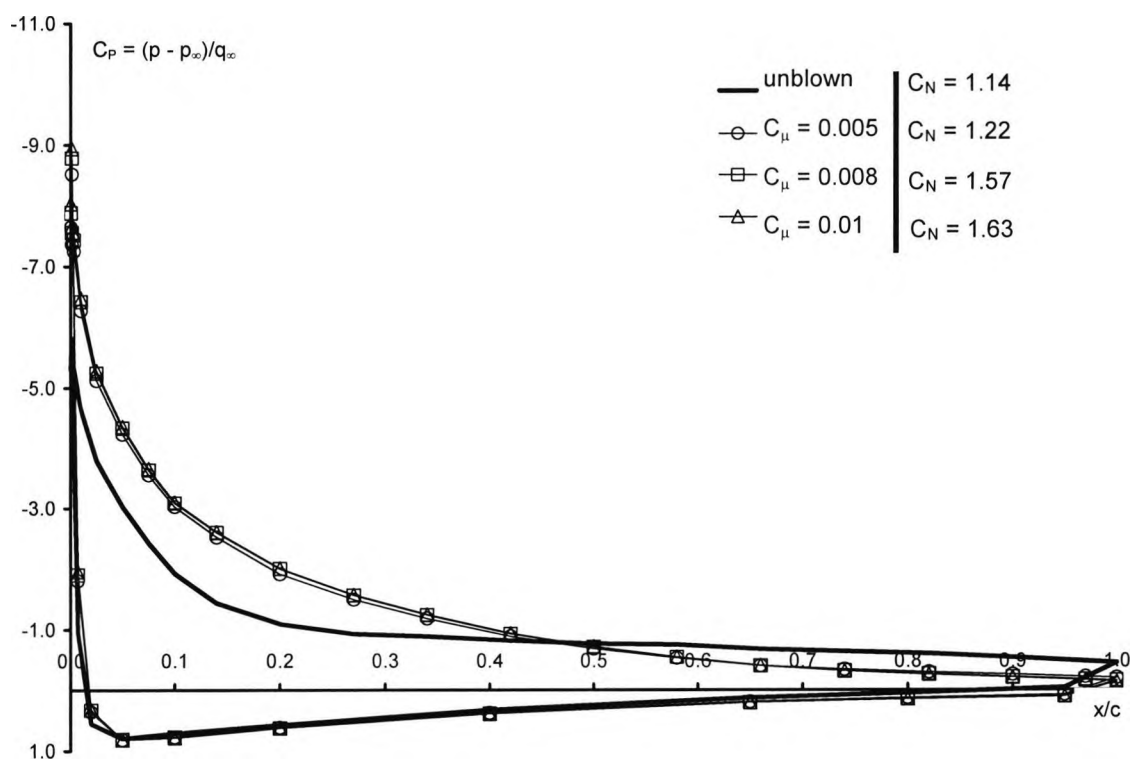


Figure 4.6: Sensitivity of chordwise surface pressure distribution to combined front and rear AJVG operating for RAE 9645 at  $\alpha = 18^\circ$ ,  $Re_c = 1.5 \times 10^6$  and  $M_\infty = 0.13$

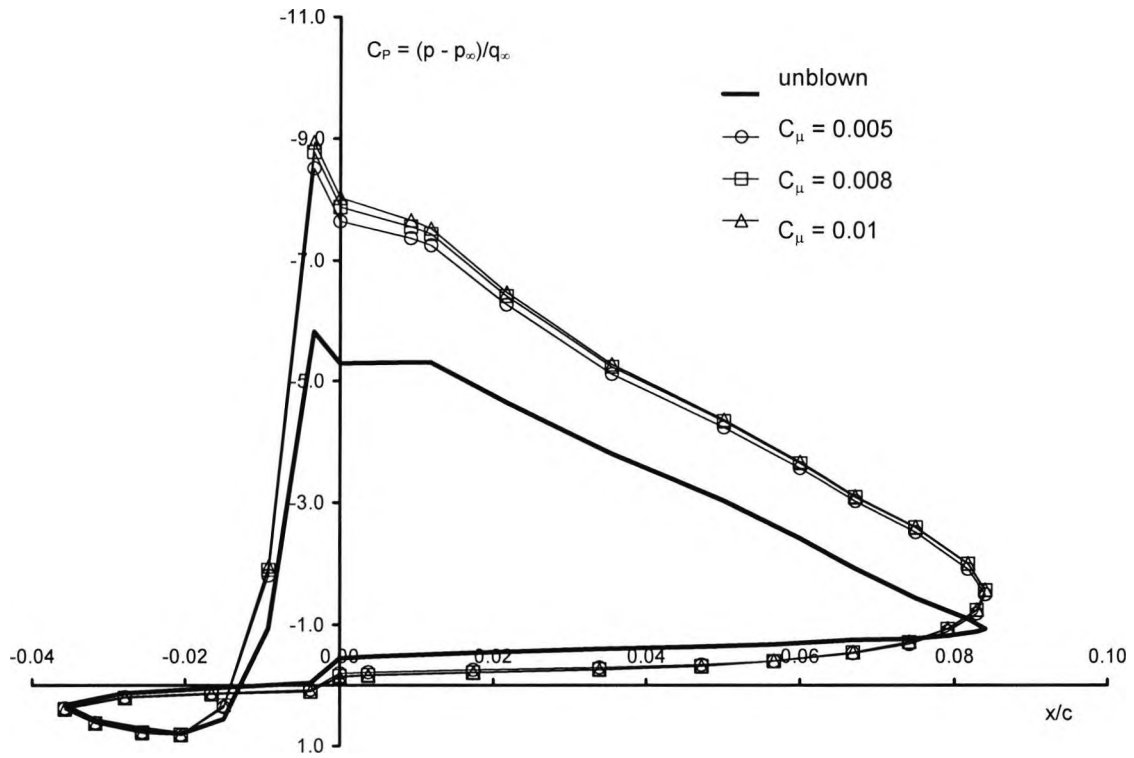


Figure 4.7: Sensitivity of leading edge suction to combined front and rear AJVG operating for RAE 9645 at  $\alpha = 18^\circ$ ,  $Re_c = 1.5 \times 10^6$  and  $M_\infty = 0.13$

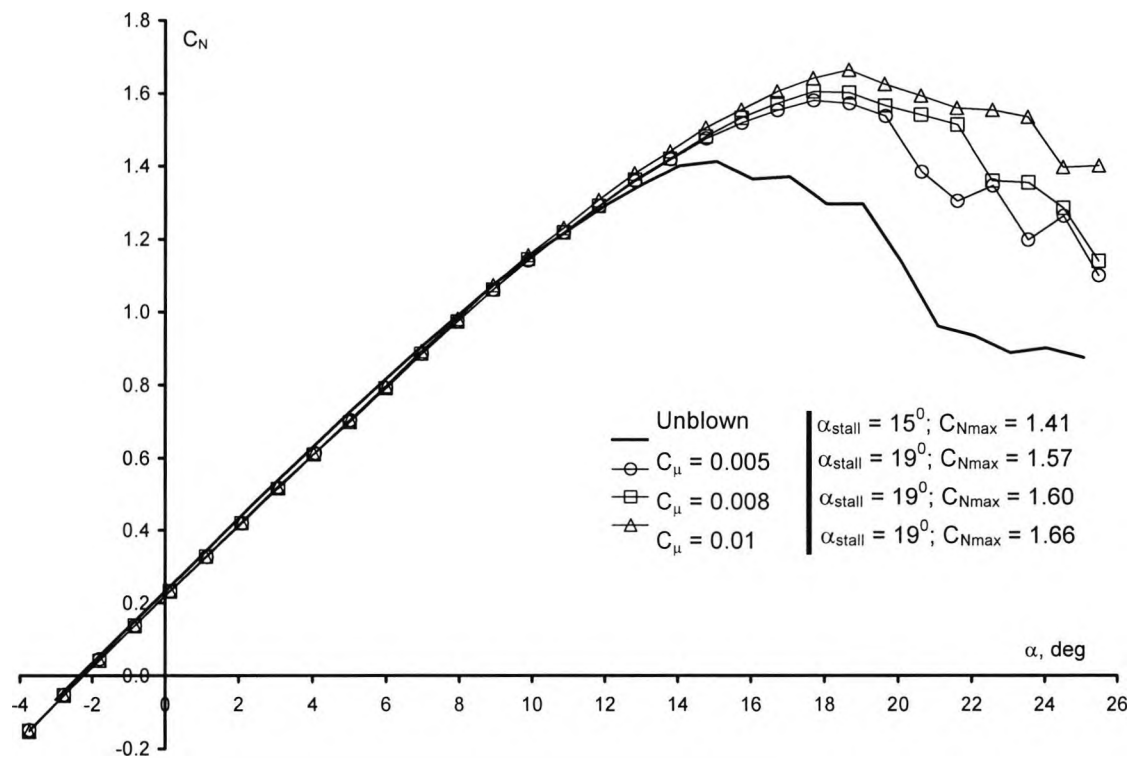


Figure 4.8: Variation of normal force coefficient with angle of attack for RAE 9645 with front AJVG operating,  $Re_c = 1.5 \times 10^6$  and  $M_\infty = 0.13$

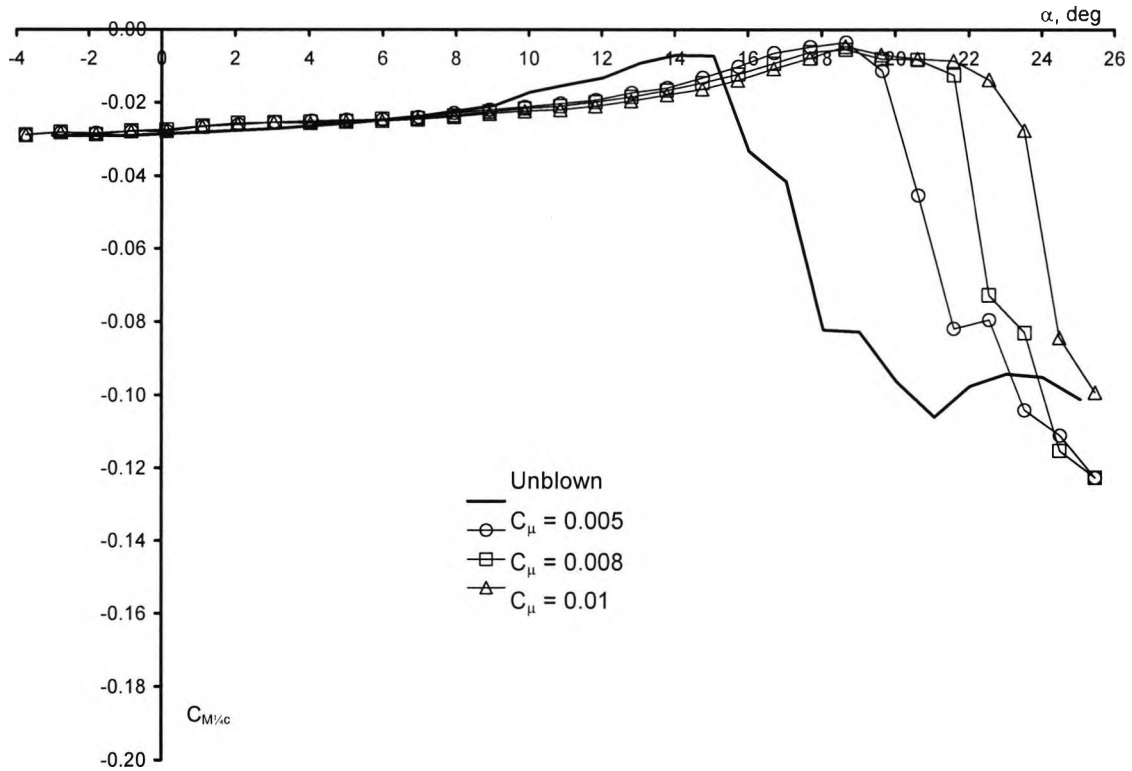


Figure 4.9: Variation of  $1/4$ -chord pitching moment coefficient with angle of attack for RAE 9645 with front AJVG operating,  $Re_c = 1.5 \times 10^6$  and  $M_\infty = 0.13$

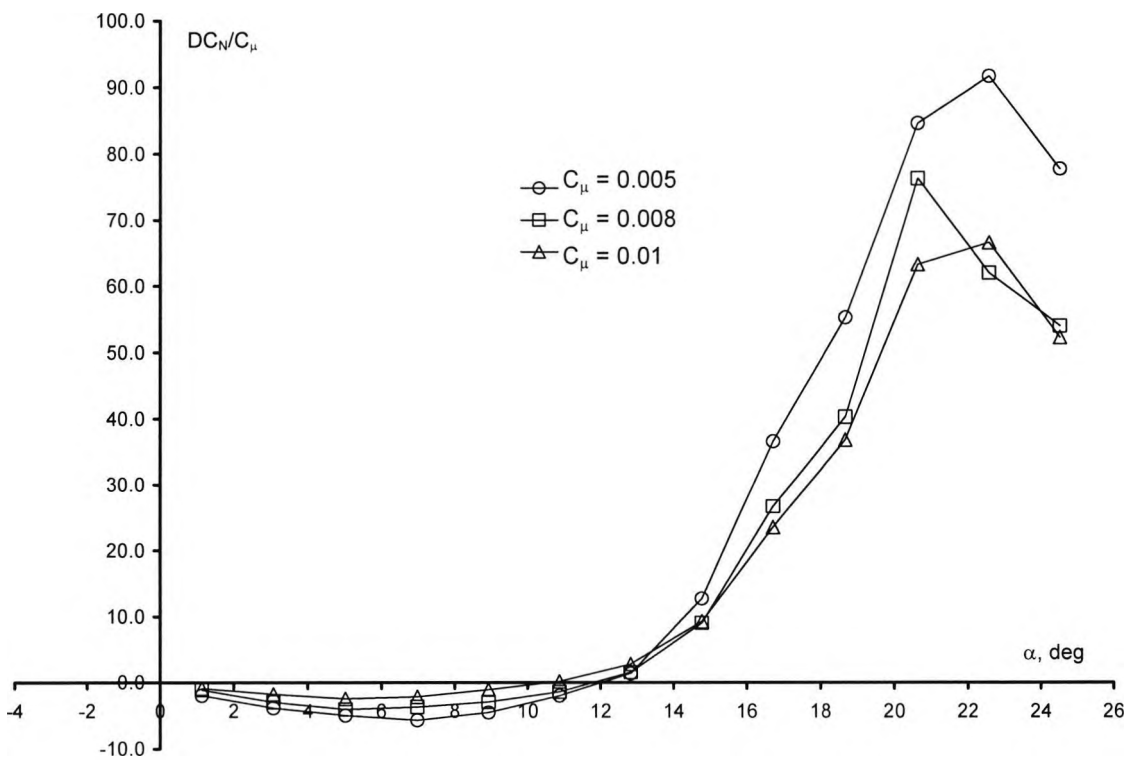


Figure 4.10: Variation of incremental normal force coefficient with angle of attack for RAE 9645 with front AJVG operating,  $Re_c = 1.5 \times 10^6$  and  $M_\infty = 0.13$

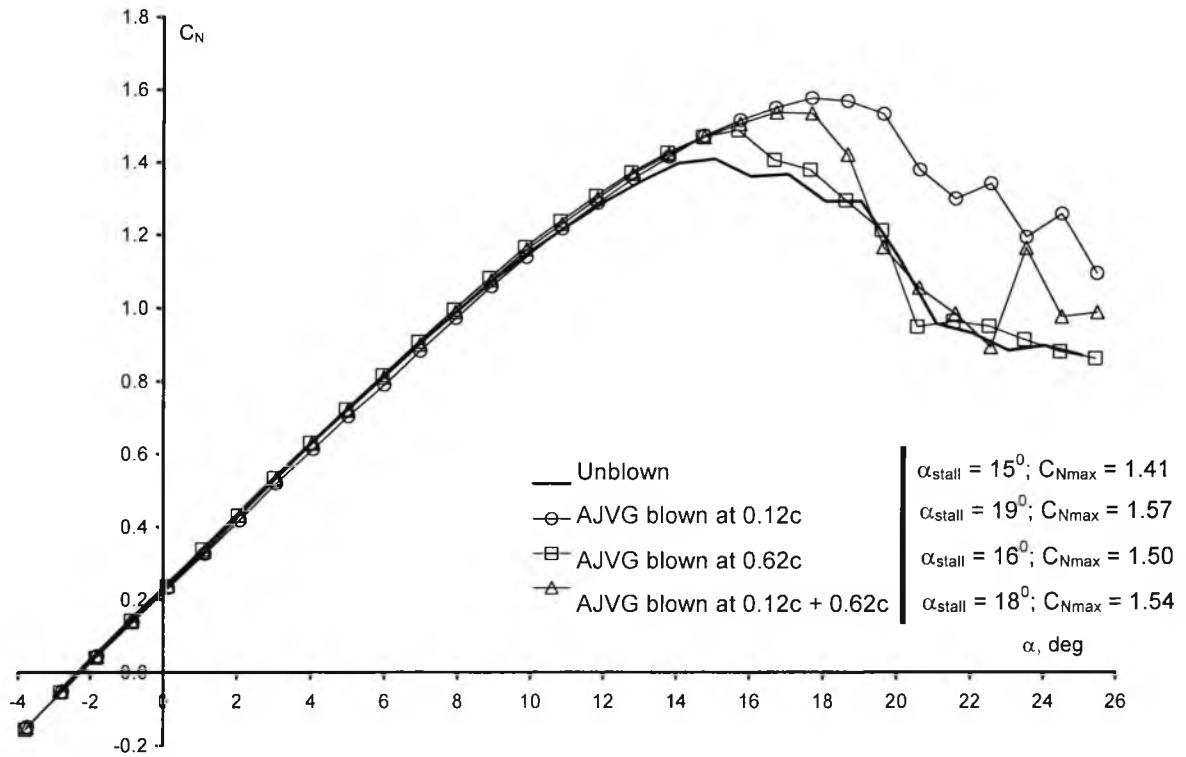


Figure 4.11: Variation of normal force coefficient with angle of attack for RAE 9645 with  $C_\mu = 0.005$ ,  $Re_c = 1.5 \times 10^6$  and  $M_\infty = 0.13$

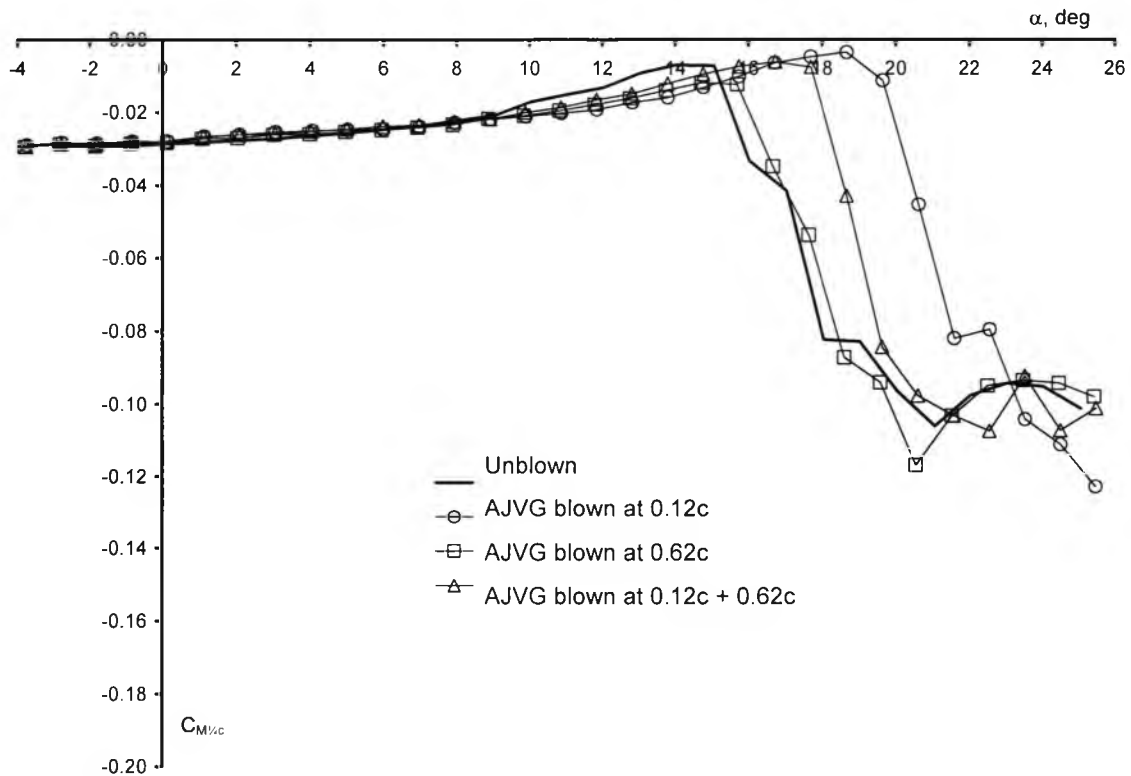


Figure 4.12: Variation of  $1/4$ -chord pitching moment coefficient with angle of attack for RAE 9645 with  $C_\mu = 0.005$ ,  $Re_c = 1.5 \times 10^6$  and  $M_\infty = 0.13$

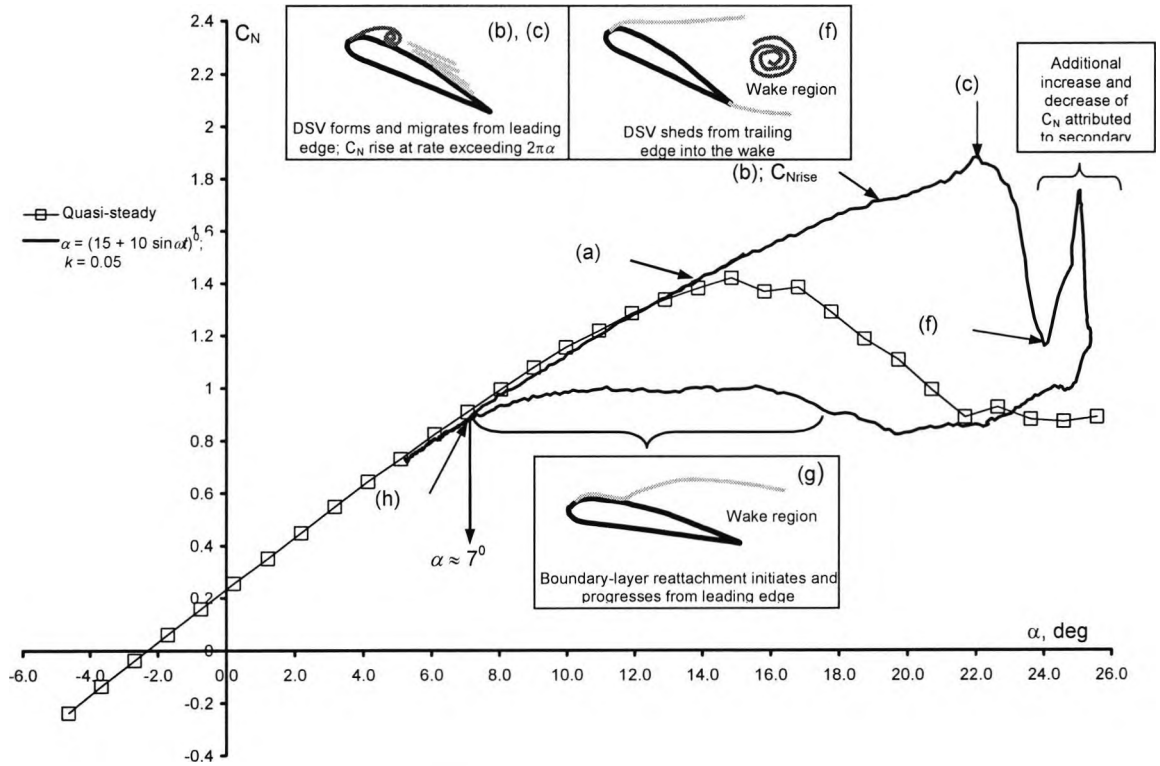


Figure 4.13: Normal force coefficient variation with angle of attack for unblown RAE 9645 at  $Re_c = 1.5 \times 10^6$  and  $M_\infty = 0.13$

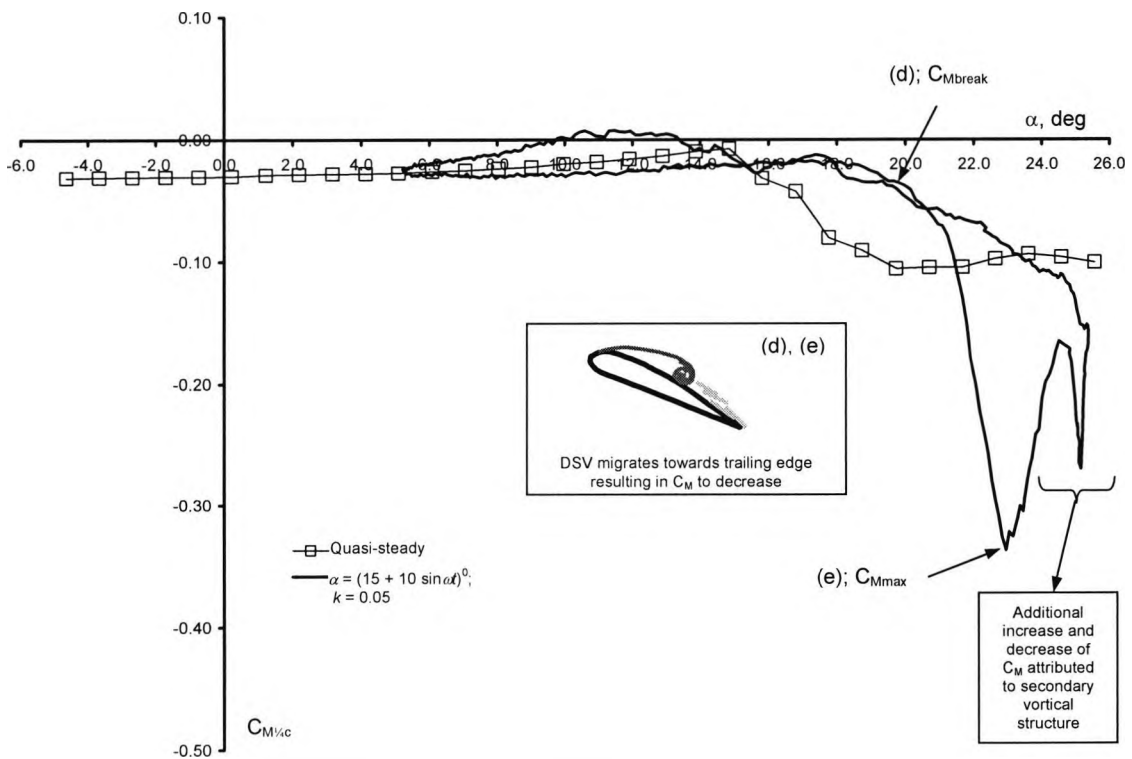


Figure 4.14:  $1/4$ -chord pitching moment coefficient variation with angle of attack for unblown RAE 9645 at  $Re_c = 1.5 \times 10^6$  and  $M_\infty = 0.13$

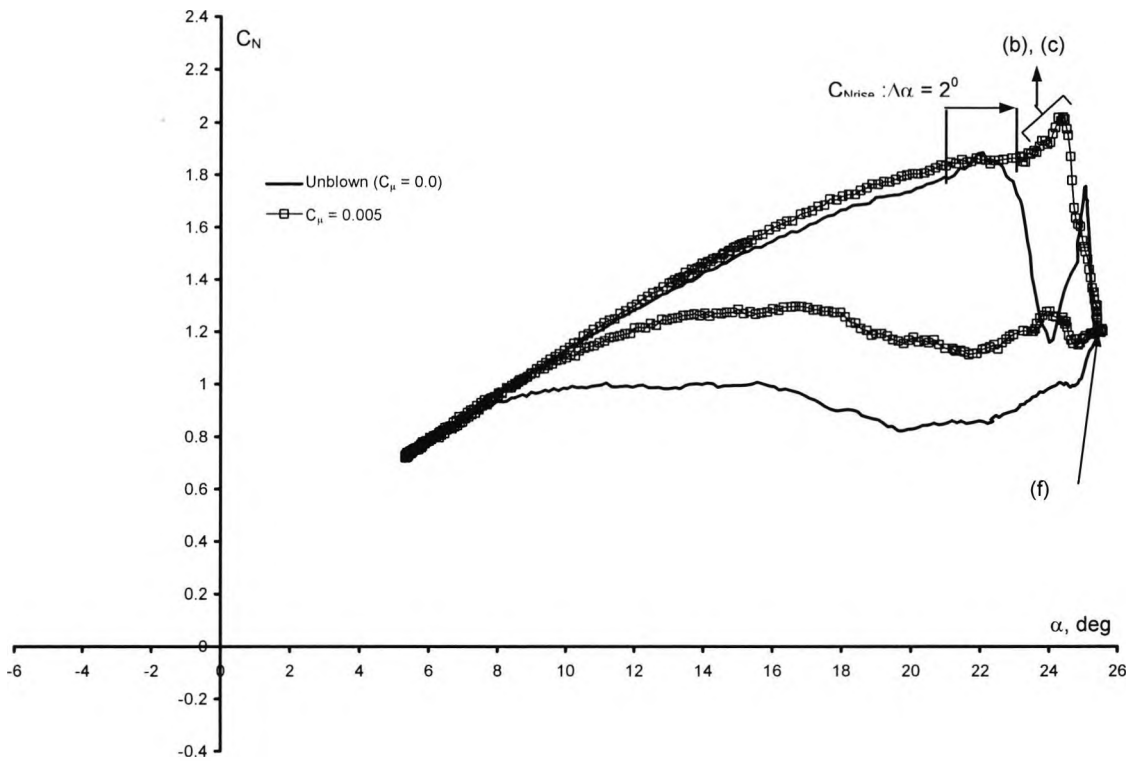


Figure 4.15: Normal force coefficient variation with angle of attack for RAE 9645 at  $\alpha = (15 + 10 \sin \omega t)$  deg,  $k = 0.05$ ,  $Re_c = 1.5 \times 10^6$  and  $M_\infty = 0.13$  with front AJVG operating

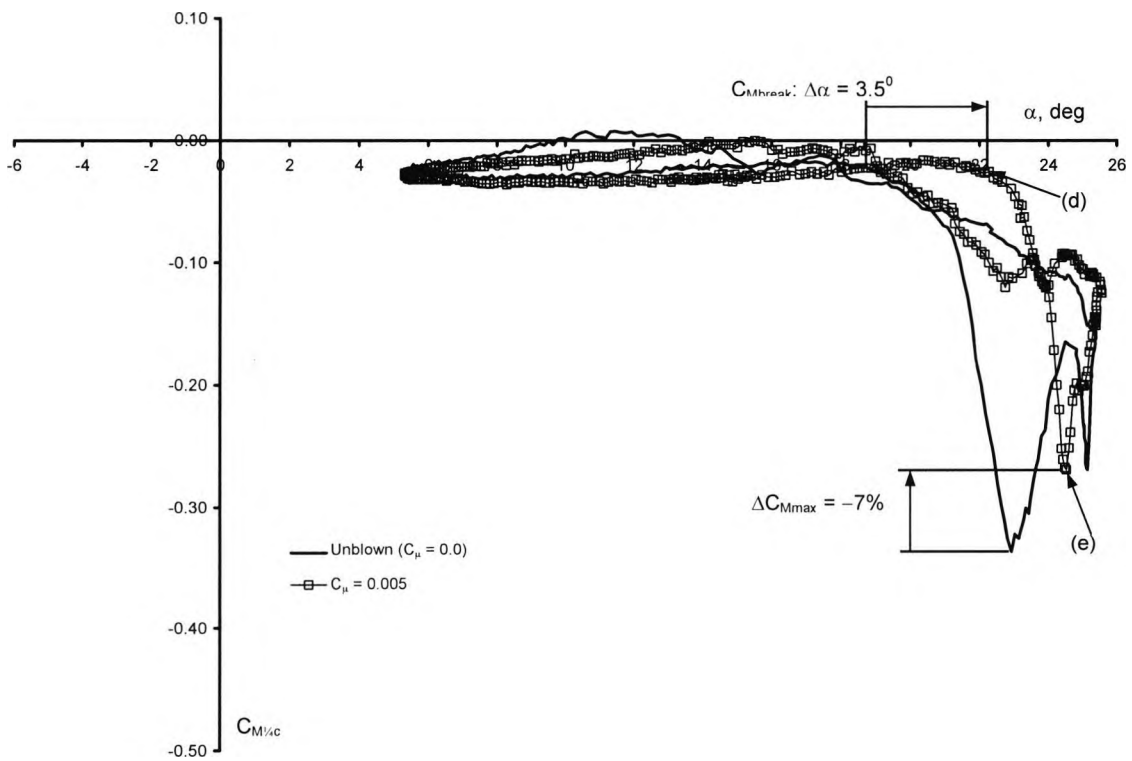


Figure 4.16:  $1/4$ -chord pitching moment coefficient variation with angle of attack for RAE 9645 at  $\alpha = (15 + 10 \sin \omega t)$  deg,  $k = 0.05$ ,  $Re_c = 1.5 \times 10^6$  and  $M_\infty = 0.13$  with front AJVG operating

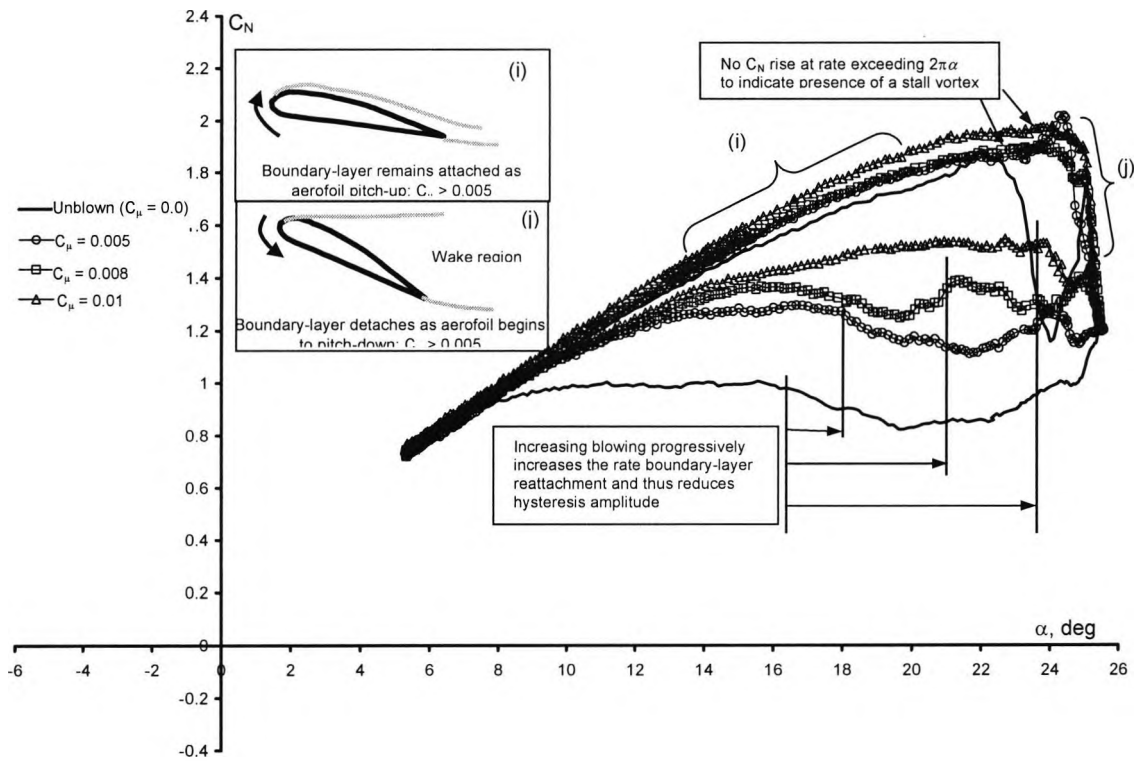


Figure 4.17: Normal force coefficient variation with angle of attack for RAE 9645 at  $\alpha = (15 + 10 \sin \omega t)$  deg,  $k = 0.05$ ,  $Re_c = 1.5 \times 10^6$  and  $M_\infty = 0.13$  with front AJVG operating

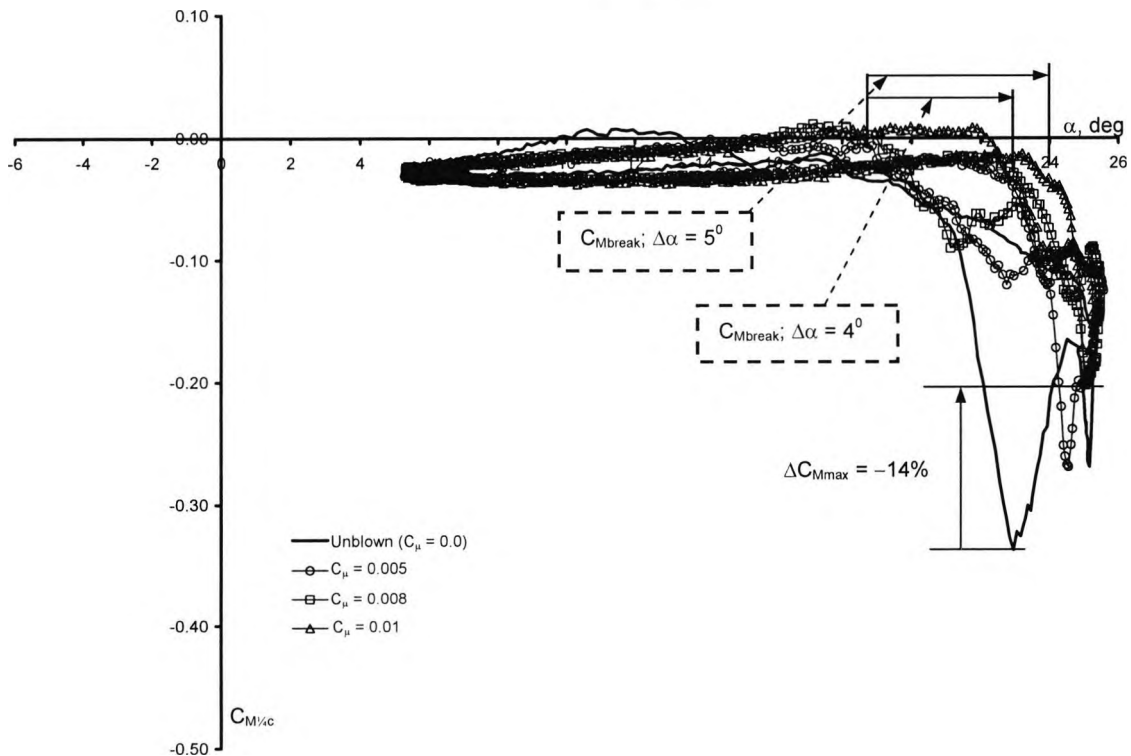


Figure 4.18:  $1/4$ -chord pitching moment coefficient variation with angle of attack for RAE 9645 at  $\alpha = (15 + 10 \sin \omega t)$  deg,  $k = 0.05$ ,  $Re_c = 1.5 \times 10^6$  and  $M_\infty = 0.13$  with front AJVG operating

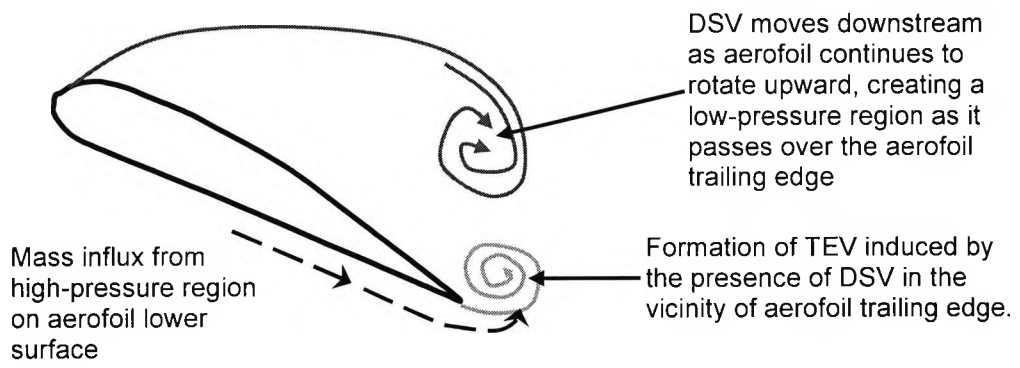


Figure 4.19: Illustration of the formation of the trailing-edge vortex

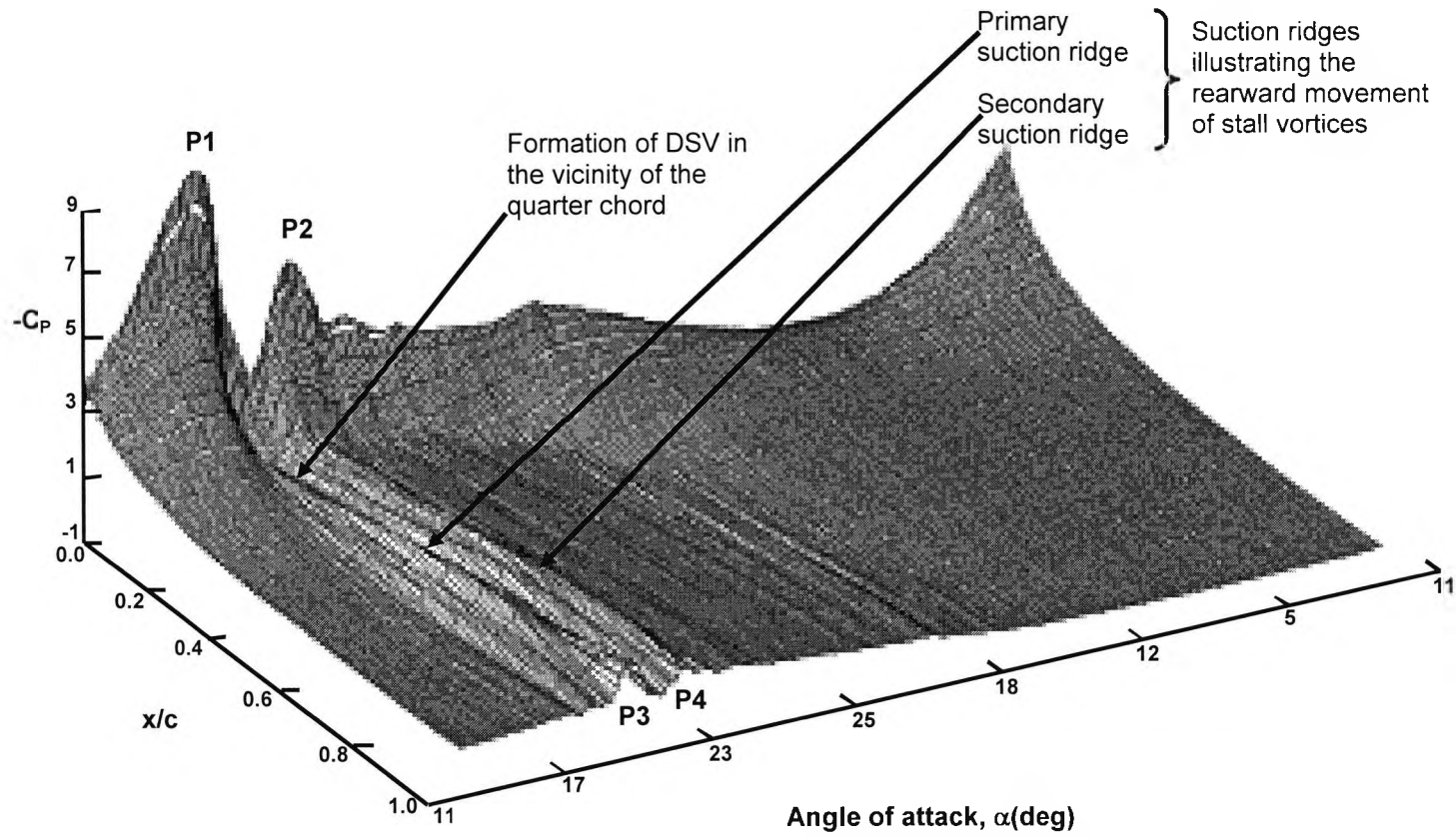


Figure 4.20: Instantaneous chordwise pressure distribution for the unblown RAE 9645 oscillating at  $\alpha = (15^0 + 10^0 \sin \omega t)$ ,  $k = 0.05$ ,  $Re_c = 1.5 \times 10^6$  and  $M_\infty = 0.13$

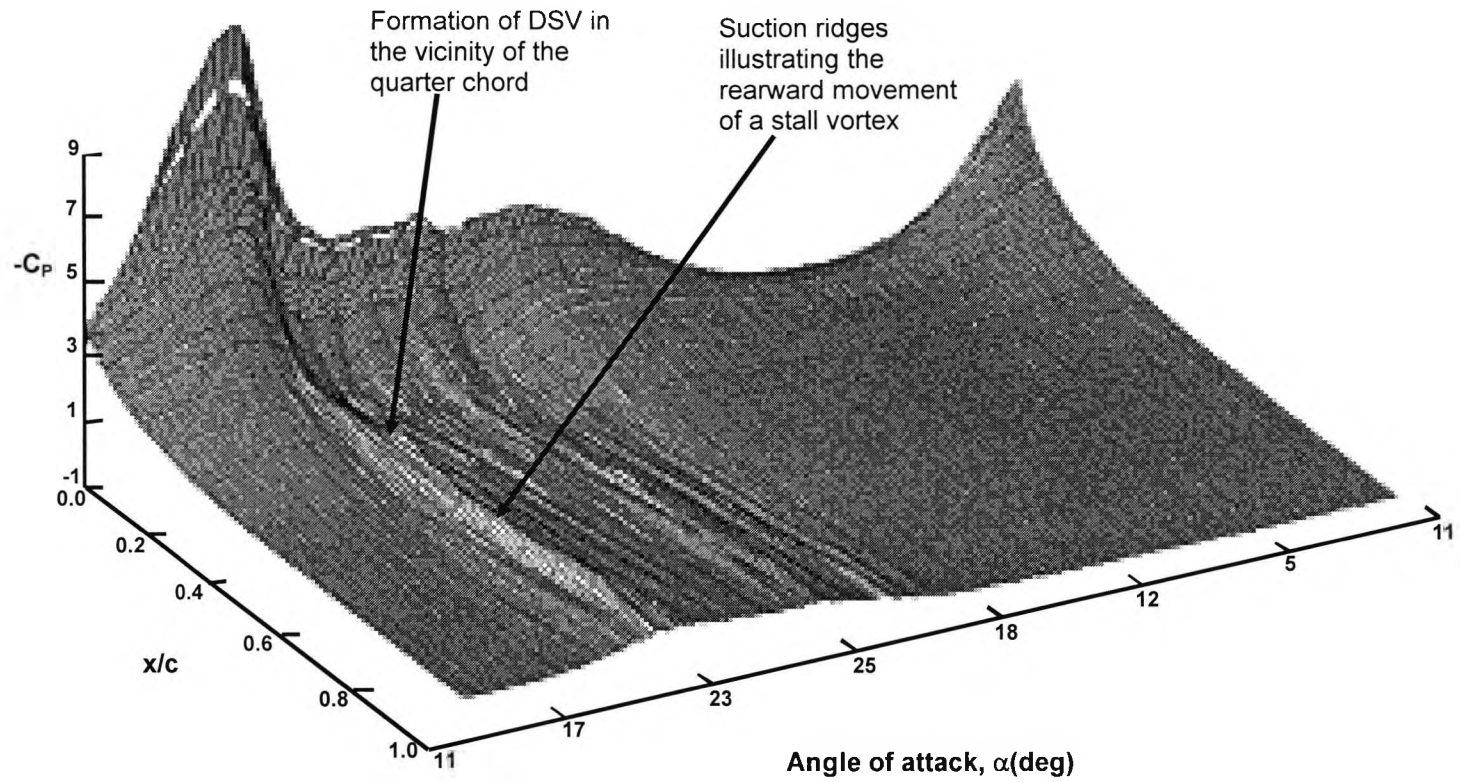


Figure 4.21: Instantaneous chordwise pressure distribution for RAE 9645 oscillating at  $\alpha = (15 + 10 \sin \omega t)$  deg,  $k = 0.05$ ,  $Re_c = 1.5 \times 10^6$  and  $M_\infty = 0.13$  with front AJVG array operating at  $C_{\mu} = 0.005$

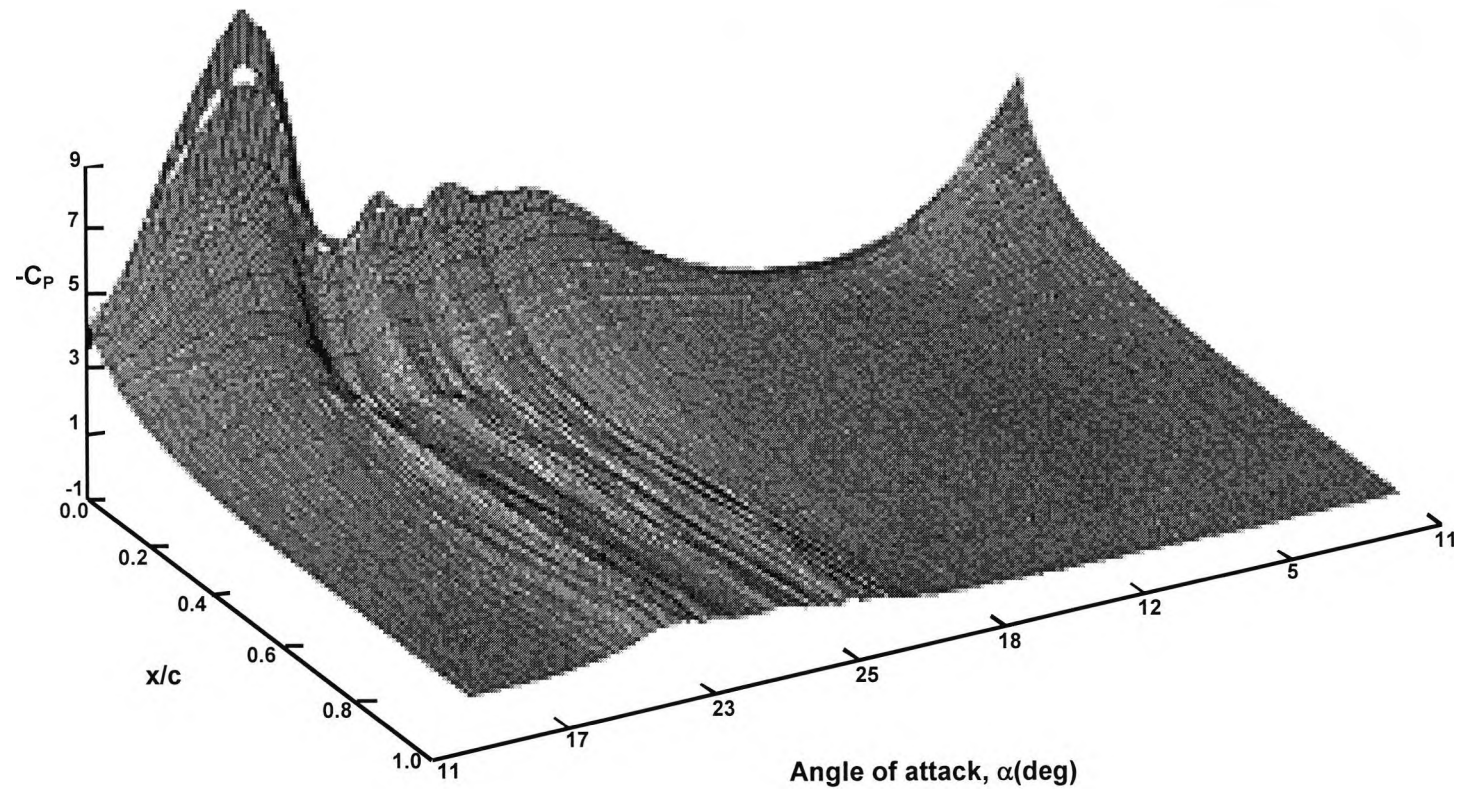


Figure 4.22: Instantaneous chordwise pressure distribution for RAE 9645 oscillating at  $\alpha = (15 + 10 \sin \alpha)$ deg,  $k = 0.05$ ,  $Re_c = 1.5 \times 10^6$  and  $M_\infty = 0.13$  with front AJVG array operating at  $C_\mu = 0.008$

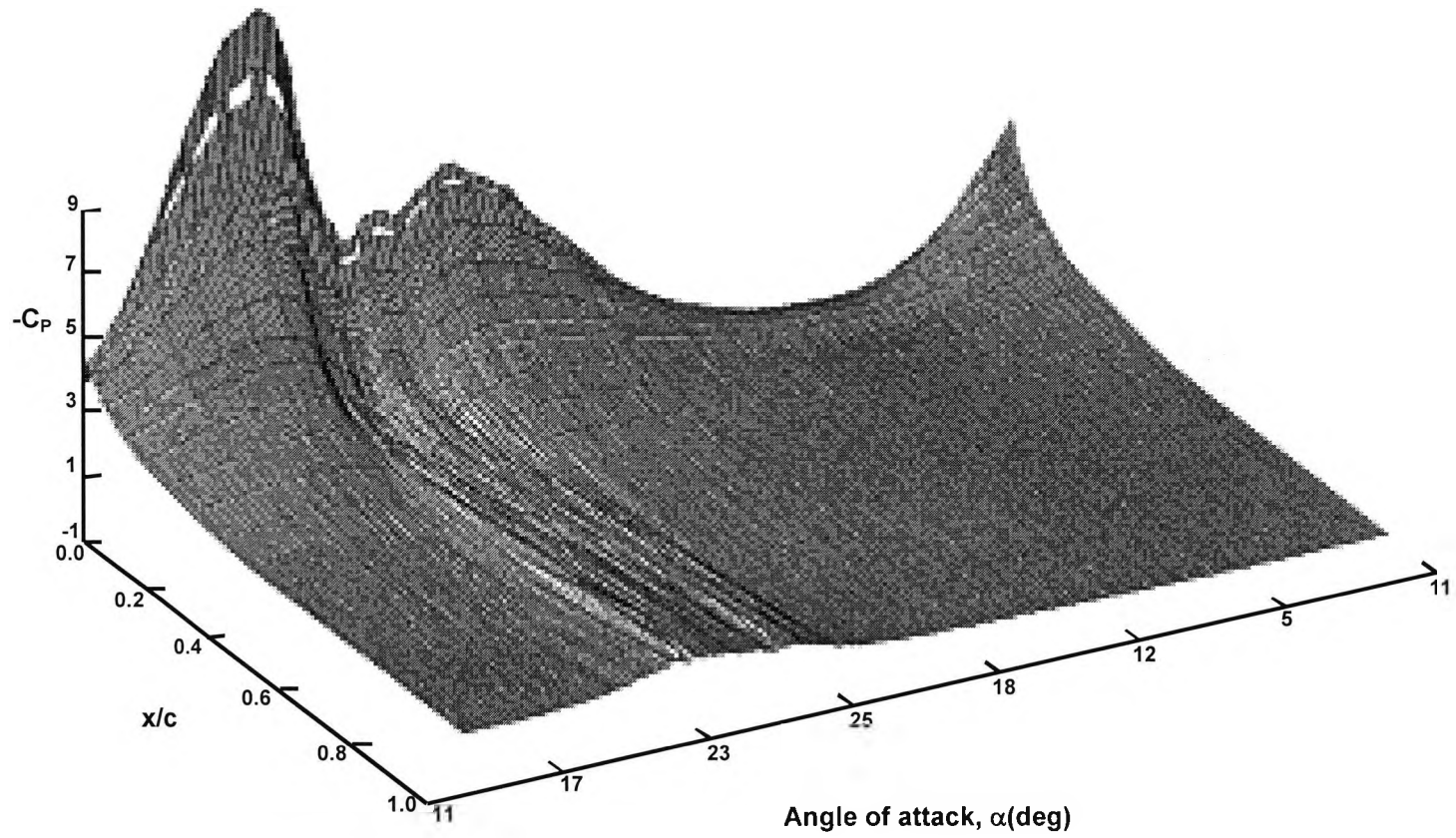


Figure 4.23: Instantaneous chordwise pressure distribution for RAE 9645 oscillating at  $\alpha = (15 + 10 \sin \omega t)$  deg,  $k = 0.05$ ,  $Re_c = 1.5 \times 10^6$  and  $M_\infty = 0.13$  with front AJVG array operating at  $C_\mu = 0.01$

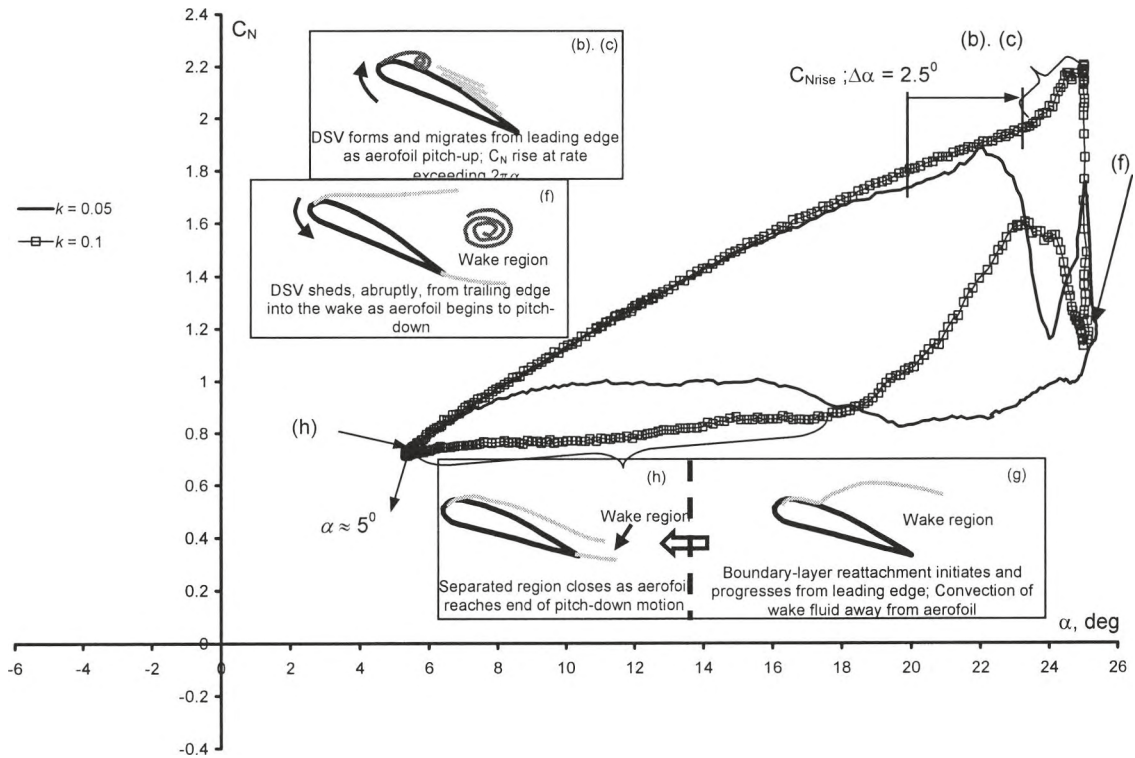


Figure 4.24: Normal force coefficient variation with angle of attack for unblown RAE 9645 oscillating at  $\alpha = (15 + 10 \sin \omega t)$  deg,  $Re_c = 1.5 \times 10^6$  and  $M_\infty = 0.13$

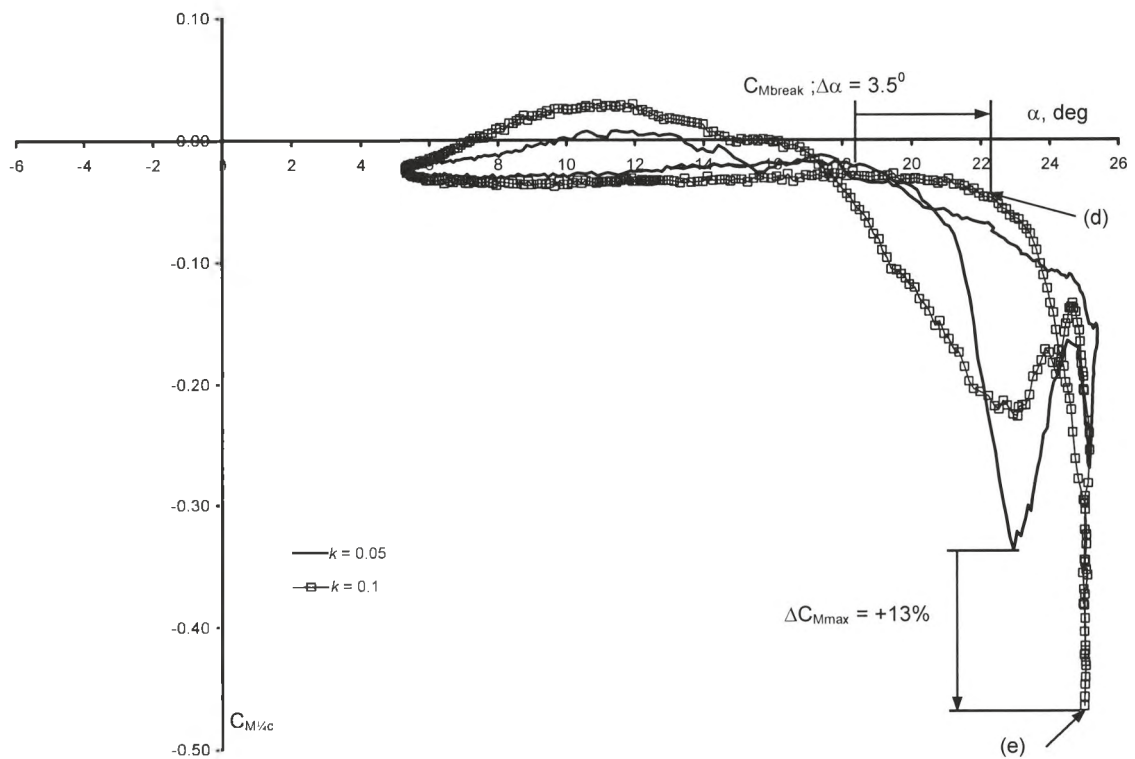


Figure 4.25:  $1/4$ -chord pitching moment coefficient variation with angle of attack for unblown aerofoil oscillating at  $\alpha = (15 + 10 \sin \omega t)$  deg,  $Re_c = 1.5 \times 10^6$  and  $M_\infty = 0.13$

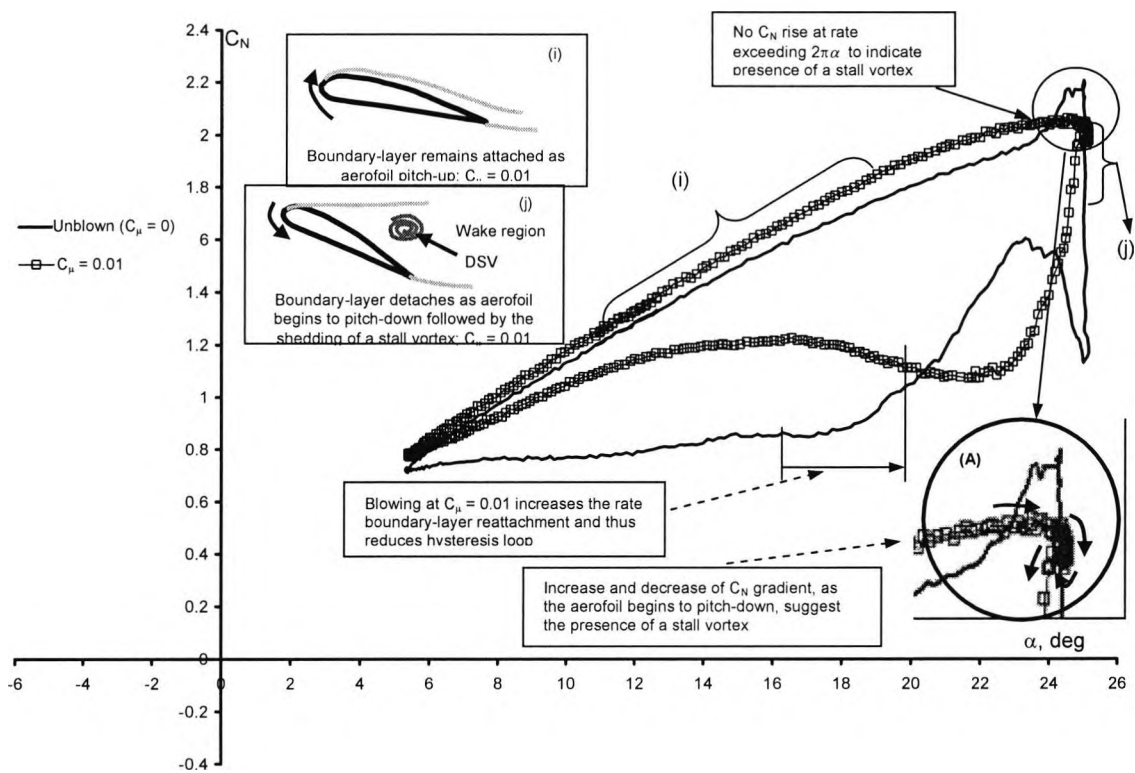


Figure 4.26: Normal force coefficient variation with angle of attack for RAE 9645 at  $\alpha = (15 + 10 \sin \omega t)$  deg,  $k = 0.1$ ,  $Re_c = 1.5 \times 10^6$  and  $M_\infty = 0.13$  with front AJVG operating

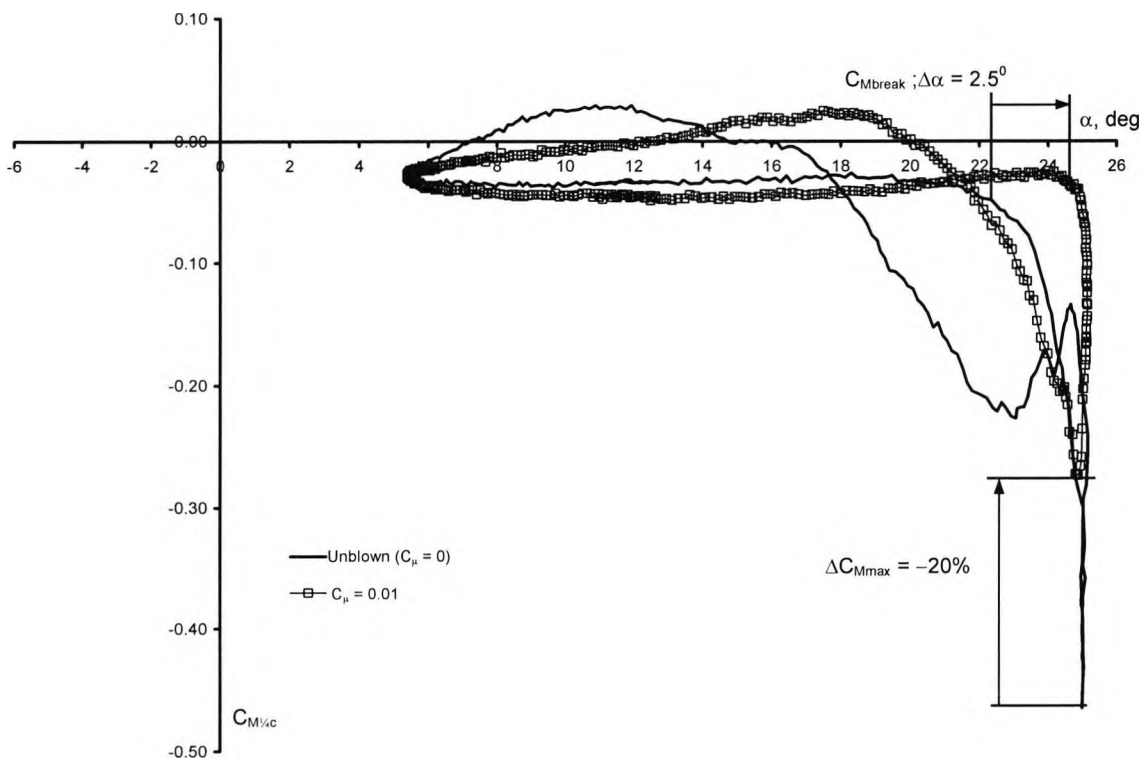


Figure 4.27:  $\frac{1}{4}$ -chord pitching moment coefficient variation with angle of attack for RAE 9645 at  $\alpha = (15 + 10 \sin \omega t)$  deg,  $k = 0.1$ ,  $Re_c = 1.5 \times 10^6$  and  $M_\infty = 0.13$  with front AJVG operating

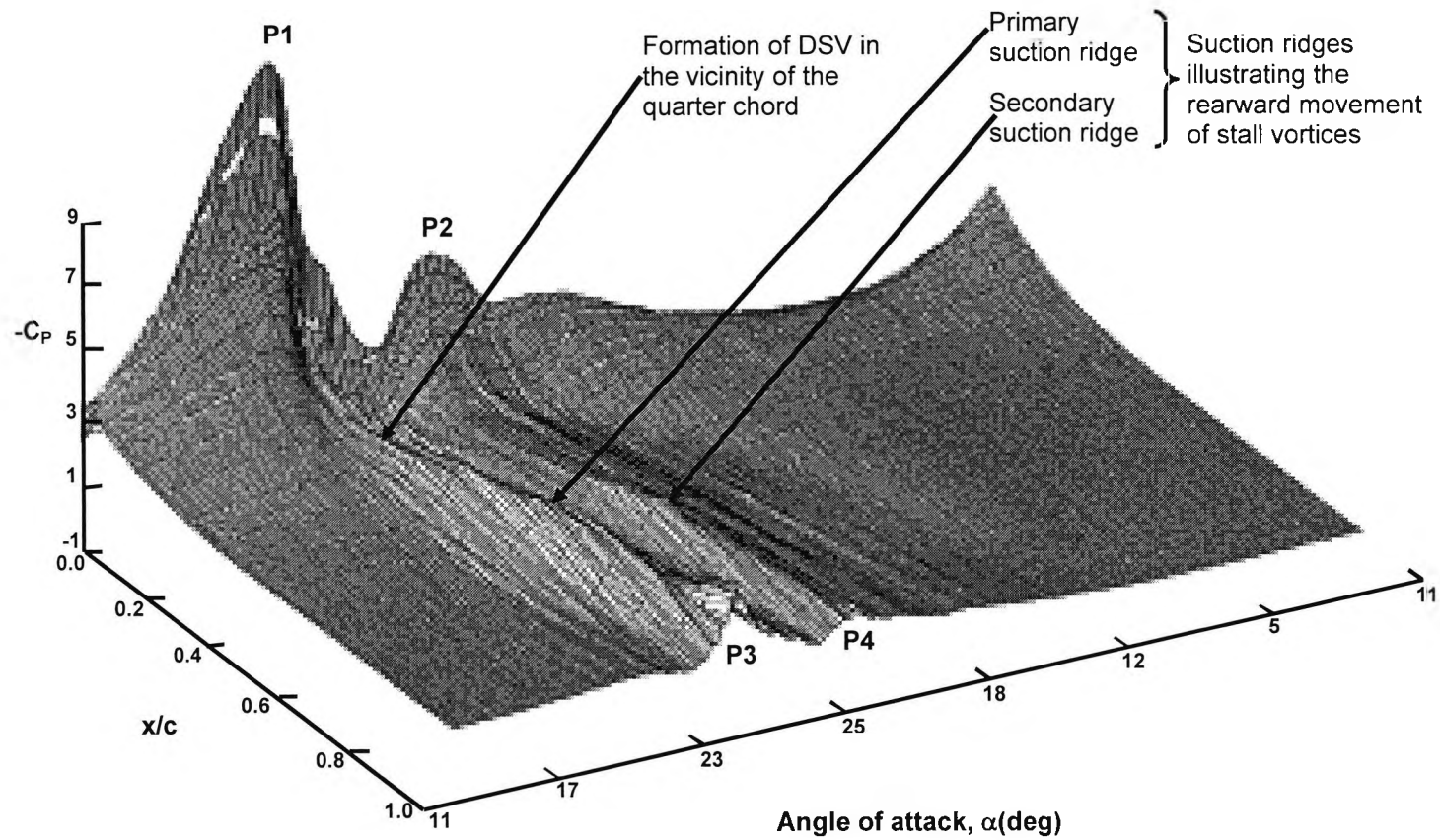


Figure 4.28: Instantaneous chordwise pressure distribution for unblown RAE 9645 oscillating at  $\alpha = (15 + 10 \sin \omega t)$  deg,  $k = 0.1$ ,  $Re_c = 1.5 \times 10^6$  and  $M_\infty = 0.13$

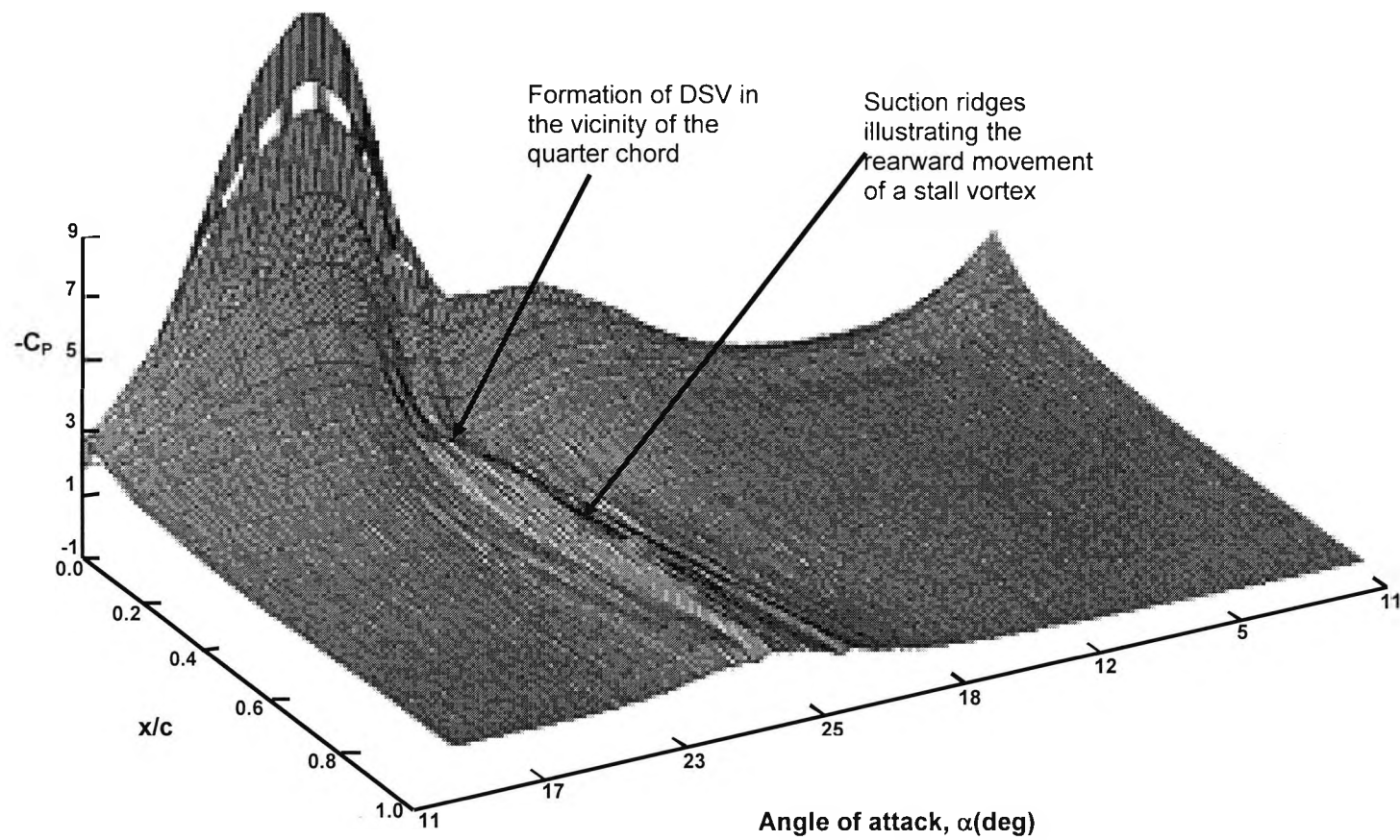


Figure 4.29: Instantaneous chordwise pressure distribution for RAE 9645 oscillating at  $\alpha = (15 + 10 \sin \omega t)$  deg,  $k = 0.1$ ,  $Re_c = 1.5 \times 10^6$  and  $M_\infty = 0.13$  with front AJVG array blowing at  $C_{\mu} = 0.01$



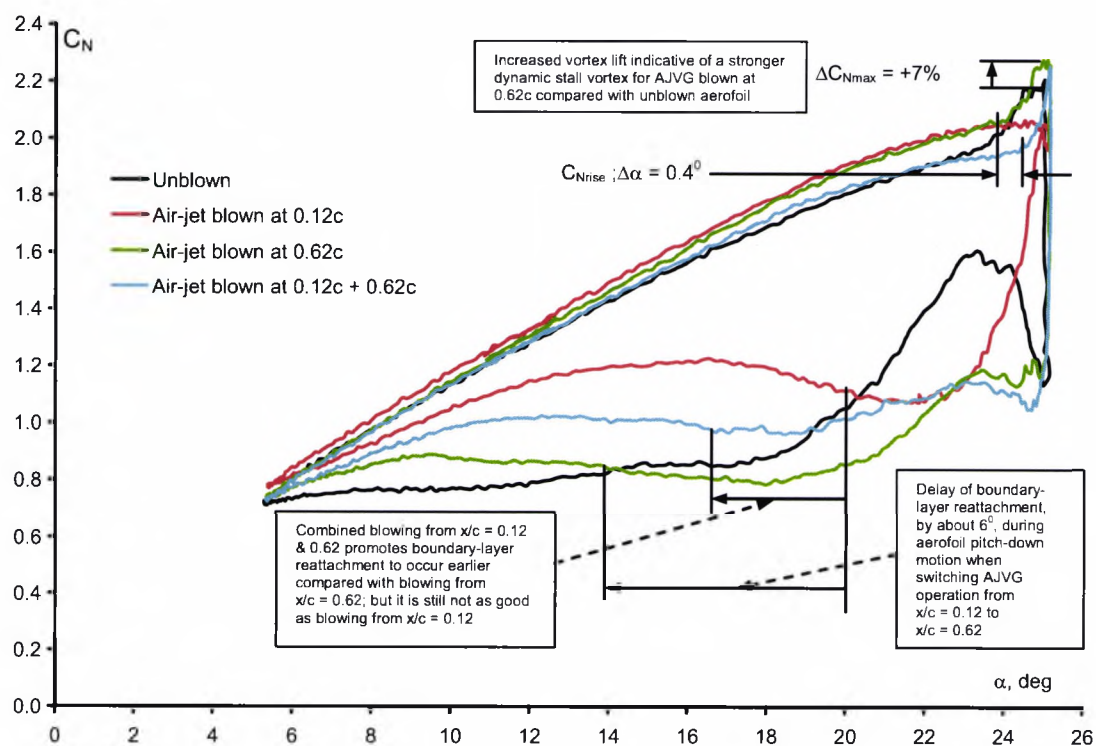


Figure 4.31: Normal force coefficient variation with angle of attack for RAE 9645 at  $\alpha = (15 + 10 \sin \omega t)$  deg,  $k = 0.1$ ,  $Re_c = 1.5 \times 10^6$  and  $M_\infty = 0.13$  with  $C_\mu = 0.01$

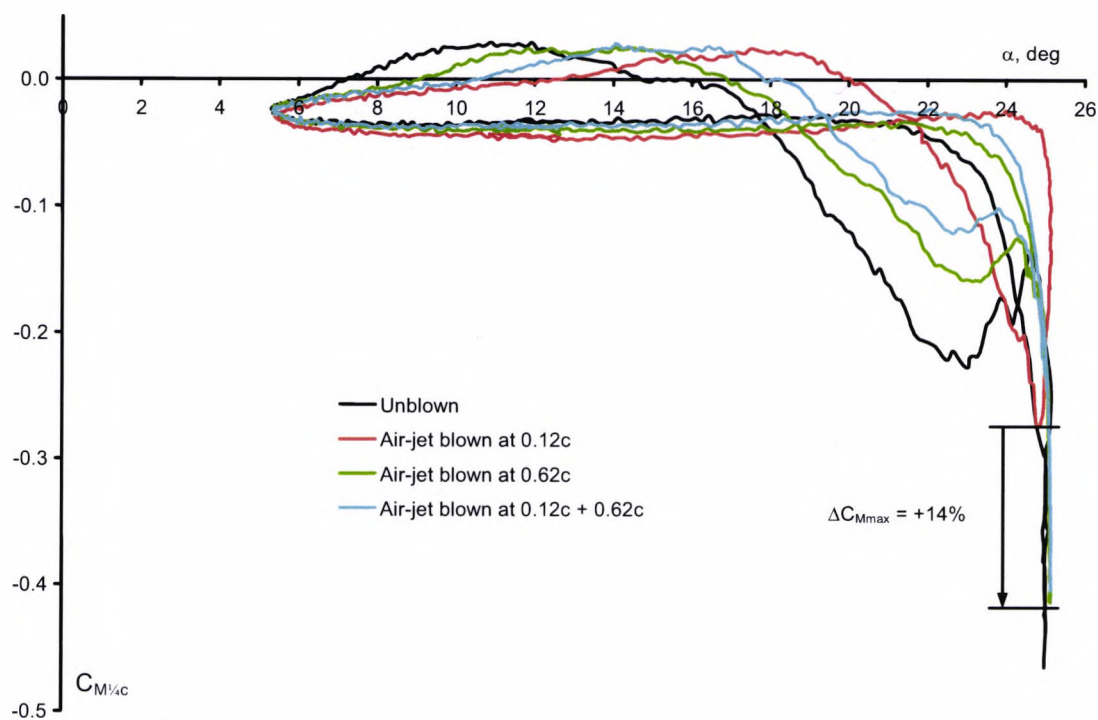


Figure 4.32:  $1/4$ -chord pitching moment coefficient variation with angle of attack for RAE 9645 at  $\alpha = (15 + 10 \sin \omega t)$  deg,  $k = 0.1$ ,  $Re_c = 1.5 \times 10^6$  and  $M_\infty = 0.13$  with  $C_\mu = 0.01$

## 5. Swept-Wing Experiments

### 5.1 Introduction

Thus far, research on steady blowing AJVGs at City University have been successfully utilised to suppress flow separation on **unswept**, single-element and multi-element aerofoils under quasi-steady flow conditions [see Innes (1995), Oliver (1997) and Lewington (2000)]. A number of researchers, such as Johnston and Nishi (1990) and Compton and Johnston (1992), have also studied the use of AJVGs to control boundary layers over flat plates, but as far as is known, there is no other work on the novel concept of using powered vortices to enhance mixing in the complex non-steady shear layers surrounding rotor blade sections.

The effect of sweep is of importance in helicopter aerodynamics because even under the simplest of inflow conditions, a helicopter blade in forward flight is instantaneously unswept in only two positions, i.e. at azimuth angles  $\Psi = 90^0$  and  $\Psi = 270^0$ . A schematic of the retreating blade stall region on the azimuth of the rotor disc, as suggested by Carr (1988), is illustrated in Figure 5.1. This schematic compares quite well with dynamic stall flight test data for manoeuvring and steady, level flight conditions reported by Bousman (1997).

It is apparent from Figure 5.1 that because the dynamic stall process occurs predominantly in the third and fourth quadrant of the helicopter azimuth, the effect of sweep on an oscillating aerofoil has to be taken into consideration. This deduction would suggest that conventional, unswept, two-dimensional aerodynamic testing might not be completely adequate for helicopter rotor blade applications. This is true because a helicopter blade section undergoes wide variations in Mach number, sweep angle and incidence angle while traversing the azimuth plane [see Leishman (1989)]. Figure 5.2 depicting typical contours of constant sweep angle on the rotor disk plane; show that blade sweep angle is  $15^0$  or greater over 60% of the rotor disk plane (as shown by the shaded region in Figure 5.2). Additionally, experiments carried out by Carta (1985) demonstrate that the dynamic stall process for an oscillating swept-wing differs from that of an unswept wing.

This chapter reports on a series of exploratory tests conducted in collaboration with DERA Bedford (now Qinetiq) aimed at determining the optimum AJVG geometrical configuration to control three-dimensional quasi-steady separation on a  $35^\circ$  swept-back wing. The results from this study have cross over application to rotor blade designers to decide the most effective AJVG set-up to be incorporated into a full-scale rotor blade.

## 5.2 Swept wing flows

The development of the jet engines for use in aircraft towards the end of the Second World War necessitated the advent of swept wings and the development of super critical wing sections to sustain high speed flight. A fundamental feature of swept wing boundary layers is that the combined influences of wing sweep and pressure gradient produce curved streamlines at the boundary-layer edge. Within the boundary layer, the loss of momentum through viscosity results in a secondary flow that is directed perpendicular to the external streamline (see Figure 5.3). The secondary flow is called crossflow [see Jones (1947) and Küchemann (1953)]. The crossflow observed on the surface of the swept-back wing should not be mistaken for a sign of flow separation; this type of flow is different from that with a separation from the trailing edge where a free boundary is formed, as will be discussed in Figures 5.5 and 5.6.

Measurements of the turbulent boundary layer on an infinite swept wing ( $\Lambda = 35^\circ$ ) by Van den Berg and Elsenaar (1972) indicate that the boundary-layer adheres to two-dimensional theory up to the point of separation or separation line after which a two-layer structure develops [see also Jones (1947)]. They found that there is a region close to the wall with a flow mainly in spanwise direction, parallel to the trailing edge, and on top of this a second layer can be observed with a structure similar to the upstream boundary layer. This type of separation is known as "*three-dimensional boundary-layer separation*". Boundary layer measurements by Esmile et al (1953) on a  $45^\circ$  swept wing showed the boundary layer to be thicker towards the trailing edge and out towards the wing tip than that on an unswept wing due to the spanwise flow along the trailing edge. These results also showed the angle between the boundary layer flow and the freestream

flow increase with distance from the leading edge, with incidence and with closeness to the wing surface.

Maskell (1955) provided an example of three-dimensional boundary-layer separation on a swept wing, as illustrated in Figure 5.4. Separation occurs along the line of P1-P2, forward of the trailing edge, with the leading edge the only line of attachment. Two distinct sets of limiting streamlines, A1-P1-P2-A2 and A1-P1-P2-A3, meet at the line P1-P2 from which a surface of separation originates, while the limiting streamlines inboard of A3-P2 separate from the trailing edge.

Broadley and Garry (1997) carried out surface pressure measurements and oil flow visualisations on a finite,  $40^\circ$  swept-back wing model, with parallel leading and trailing edges. The flows are characterised by a combination of oil flows and pressure distributions, which indicate a complex three-dimensional separation, with the separation line moving forward with increasing angle of attack. Figure 5.5 shows a sketched interpretation to illustrate the flow development on the model once separation has occurred. The surface flow direction over the forward part of the wing is almost normal to the leading edge with the angle of surface streamlines decreasing over the rear section, where the pressure gradients (and therefore crossflows) are most severe, until the streamlines are almost parallel to the trailing edge. Downstream of this line the flow separates, with separation line indicated by line 'S'.

This separated flow rolls into a vortex (see Figure 5.6) aligned in the spanwise direction and, due to the low pressure generated behind the vortex, draws air from the trailing edge region resulting in a reverse flow towards the separation line.

### 5.3 Experimental arrangement

A swept-wing, half model section was tested, in an angle of attack range of  $0^{\circ} < \alpha < 20^{\circ}$ , in City University's T2 low speed wind tunnel. The swept-wing model was mounted vertically in the working section and connected to the tunnel six-component balance on top of the wind tunnel working section via a spindle fixed at mid-chord of the model root. The balance was used to vary the angle of attack of the model. Tests were conducted at a chord Reynolds number,  $Re_c$ , of  $0.5 \times 10^6$  and a freestream Mach number,  $M_{\infty}$ , of 0.1. Further details of the experimental set-up and data analysis can be found in Chapter 6.

The half-model section, with parallel leading and trailing edges, has a sweepback angle of  $\Lambda = 35^{\circ}$ . The wing section (normal to sweep) is derived from the supercritical aerofoil RAE 5225 and has a 15% thickness/chord ratio. The half span ( $s = 0.958\text{m}$ ) model has a constant chord of 0.232m and an aspect ratio of 4.5. The model is fitted with a spanwise array of 18 AJVGs located at 10% chord. The geometry and orientation of the AJVG configuration utilised is shown in Figures 5.7 and 5.8. These AJVGs were operated at steady, low blowing momentum coefficients in the range of  $0.0 < C_{\mu} < 0.01$ , with the air being supplied to the AJVG array via a pressure regulated plenum chamber located within the wing section.

The initial AJVG geometrical design and spacing, *Config A*, installed on the top surface of the swept wing model was based on the recommendations outlined by Pearcey et al (1993), Henry and Pearcey (1994) and Akanni and Henry (1995) and optimised by Oliver (1997). The co-rotating, rectangular AJVG, spaced  $0.2c$  apart, had a slot aspect ratio of approximately 8 and was pitched and skewed at  $30^{\circ}$  and  $60^{\circ}$  relative to the local surface tangent and the oncoming freestream respectively (see Figure 5.7).

The yaw angle of the AJVG is denoted as  $\psi = 0^{\circ}$  when it is blowing downstream in the direction of the freestream flow, whilst it is  $\psi = 180^{\circ}$  when blowing upstream opposing the direction of the freestream flow. The AJVG skew angle is positive when rotated in the counter-clockwise direction (CCW) and negative in the clockwise direction (CW).

The swept wing model was instrumented with a total of 90 static pressure orifices comprising three spanwise arrays of (i), 35 pressure orifices at  $z/b = 0.50$  and (ii) 26 pressure orifices at  $z/b = 0.25$  &  $0.75$ ; with the remaining 3 in the plenum chamber. This allows for pressure measurement on the wing surface as well as monitoring the plenum chamber pressure for AJVG blowing momentum coefficient assessment (see Figure 5.9).

#### **5.4 Effect of varying AJVG configuration on the aerodynamic performance of the swept wing**

The experimental tests were carried out with the aim of studying the effects of varying the AJVG geometries, such as pitch and skew angles, on the aerodynamic performance of a  $35^\circ$  swept-back wing. The sensitivity of the chordwise surface static pressures at spanwise positions  $s/b = 0.25, 0.50$  and  $0.75$  to angle of attack, with AJVGs installed but quiescent, is shown on Figures 5.10 to 5.12. Examination of the test data at  $s/b = 0.25, 0.50$  and  $0.75$  shows that at  $\alpha = 10^\circ$ , the flow is fully attached over the entire upper surface of the wing, with full pressure recovery at the trailing edge. As the angle of incidence is increased to  $\alpha = 12^\circ$ , there is still no evidence of flow separation near the wing root ( $s/b = 0.25$ ), with the flow fully attached over the entire top surface. But at the wing mid-span ( $s/b = 0.50$ ) and the wing tip ( $s/b = 0.75$ ), flow separation has leapt forward from the wing trailing edge to approximately  $x/c = 0.70$ , where now the trailing-edge pressure coefficient ( $C_{P_{te}}$ ) has turned negative. The onset of trailing-edge separation is indicated when the trailing-edge pressure coefficient,  $C_{P_{te}}$ , goes from a positive value to zero at about  $\alpha \approx 11^\circ$ .

At  $\alpha = 15^\circ$ , the peak suction in the vicinity of the wing root has collapsed; but  $C_{P_{te}}$  still has a positive value indicating that boundary-layer separation has not yet occurred. However, at  $z/b = 0.50$  and  $0.75$  the collapse of the peak suction is accompanied by the increased negative divergence of the pressure at the trailing edge suggesting that the wing has stalled from the mid-span region outboard. Although the boundary layer in the wing root region is influenced by the boundary layer on the splitter plate, reducing the spanwise velocity component in this region and moving the separation position further downstream [see Broadley and Garry (1997)]; the observation of stall in the outboard

region of the swept wing is, however, characteristic of an untwisted swept wing where stall occurs in the outboard region first before spreading inboard [Shortal and Margin (1946)]. Flow separation and loss of lift over parts of the wing usually result in a pronounced nose-up pitching moment. This is usually referred to as “*tip-stall*”.

Flow visualisations carried out using fluorescent tufts, which is a light flexible material made of monofilament nylon that has been treated with fluorescent dye, illustrates the development of the flow with incidence over the top surface of the unblown wing (see Figure 5.13). At  $\alpha = 10^\circ$  the tufts are aligned predominantly in the streamwise direction suggesting that the boundary-layer is still attached to the top surface of the wing. Increasing the angle of incidence to  $\alpha = 12^\circ$ , the tufts over the forward part of the wing are aligned parallel with the local freestream direction which then unsweeps over the rearward part of the wing to flow spanwise, almost parallel to the trailing edge, to form a separation line [see Van den Berg and Elsenaar (1972)]. The separation line moves upstream with increasing angle of attack and at  $\alpha = 15^\circ$  the wing has stalled, indicated by the dominant spanwise flow, outboard of about 50% span.

Employing AJVGs over the upper surface of the swept wing modifies the surface pressure distributions. Figures 5.14 to 5.16 demonstrate the influence of varying the AJVG configuration for a given blowing momentum coefficient. Surface static pressure distributions at  $\alpha = 12^\circ$  for the spanwise positions  $s/b = 0.25, 50$  and  $0.75$  are presented in these figures. Blowing continuously ( $C_{\mu} = 0.003$ ) from the spanwise AJVG array, set-up as **Config A** ( $\phi = 30^\circ, \psi_1 = 60^\circ$ ), located at  $x/c = 0.10$  did not improve the surface pressure distributions of the swept wing, where at  $s/b = 0.50$  and  $0.75$  boundary-layer separation is still present on the upper surface of the wing in the vicinity of the trailing edge, i.e. downstream of  $x/c = 0.70$ .

Pearcey (1961) demonstrated the usefulness of installing an array of co-rotating vane vortex generators (VVGs) on swept wings to suppress trailing-edge separation. The VVG has the ability to maintain a transverse shear at the surface of constant sign (by virtue of the circulation in the vortices and of the transverse displacement of the whole array), which if orientated correctly could be used to oppose the natural spanwise boundary-layer drift and thus reduce wing pressure drag that is due to boundary-layer

growth. Pearcey (1961) found that on swept-back wings the vanes should be “toed-out” with respect to the local flow direction, as illustrated in Figure 5.17.

It is, therefore, important to ensure that the yaw angle of the AJVG is correct with respect to the local flow direction. Based on the suggestion of Pearcey (1961) the yaw angle of the AJVG was re-orientated so that it produces an array of co-rotating longitudinal streamwise vortices that oppose the spanwise flow, which develops after the line of separation, on the upper surface of the swept wing. Figure 5.18 illustrates the AJVG set-up on the  $35^\circ$  swept-back wing with the skew angle measured with respect to the freestream flow (see also Figure 5.7).

Installing the AJVG with the geometric arrangement of **Config B** into the top surface of the swept wing and operating it at  $C_\mu = 0.003$  recovers the stalled flow. Figures 5.14 to 5.16 show that this low amount of blowing delays the upstream movement of separation from the trailing edge and increases suction pressure over the entire upper surface of the wing. Increasing the amount of blowing from the spanwise AJVG array to  $C_\mu = 0.006$  further enhances the upper surface pressure distributions over the top surface of the wing. These observations are substantiated by surface flow visualisations that show the introduction and increase of the blowing amount progressively delays trailing-edge separation. This is indicated by the increased region of streamwise flow over the top surface of the wing with blowing rate as illustrated in Figure 5.19.

The incremental normal force,  $DC_N$ , per unit  $C_\mu$  along the span of the swept wing is shown in Figures 5.20 to 5.22. These plots enable the effectiveness of the AJVG to be assessed relative to the momentum requirements of the flow control system. The results from the series of investigations demonstrated that utilising the spanwise array of AJVGs configured as **Config A** deteriorates the aerodynamic performance of the unblown swept wing. Changing the AJVG arrangement to **Config B** immediately restores and enhances the aerodynamic performance of the unblown wing, where at  $\alpha = 12^\circ$ , close to stall, AJVG operating at  $C_\mu = 0.003$  considerably enhances the sectional normal force especially at the outboard section, with  $DC_N/C_\mu \approx 40$ .

An explanation as to why **Config A** and **Config B** has significantly different influences on the aerodynamic performance of the swept wing could be obtained by examining the

influence of the longitudinal streamwise vortices generated by these AJVG configurations on the separated flow. The spanwise flow observed on swept wings aft of the line of separation is induced by the transverse pressure gradient forcing the low momentum boundary layer to drift towards the wing tip. It is believed that the secondary spanwise flow induced by a longitudinal streamwise vortex can, if properly skewed with respect to the local flow direction, acts to oppose and decelerate the spanwise movement of the flow towards the wing tip [see Pearcey (1961)]. Figure 5.23 shows that the spanwise array of AJVGs set-up as *Config B* induces longitudinal streamwise vortices rotating clockwise that were able to oppose the spanwise flow towards the wing tip and to prevent trailing-edge separation by re-energising the low momentum boundary layer over the rear of the wing section.

### 5.5 Possible full-scale rotor blade AJVG configuration for dynamic stall control

Dynamic stall occurs predominantly in the third and fourth quadrant of the rotor disc azimuth; in particular between  $\Psi = 240^\circ$  and  $\Psi = 310^\circ$  and is dependent on various factors such as forward speed, aircraft weight and flight conditions. Collating the results of the dynamic stall tests and the swept wing experiments, it is envisaged that the AJVG configuration incorporated into a full-scale rotor blade would consist of:

- i) An array of co-rotating, rectangular AJVGs with the slot aspect ratio of about 8 positioned between 6% and 12% of the aerofoil chord. The AJVGs would be equispaced at  $0.1c$  apart and operating continuously at  $C_\mu = 0.01$ .
- ii) AJVGs pitched at  $\phi = 30^\circ$ , with the pitch angle measured relative to the local surface tangent (see Figure 5.7).
- iii) AJVGs skewed at  $\psi = 60^\circ$ , with the skew angle measured relative to the tangential velocity component,  $u_T$ , and the jet efflux directed towards the wing root, as illustrated in Figure 5.24.

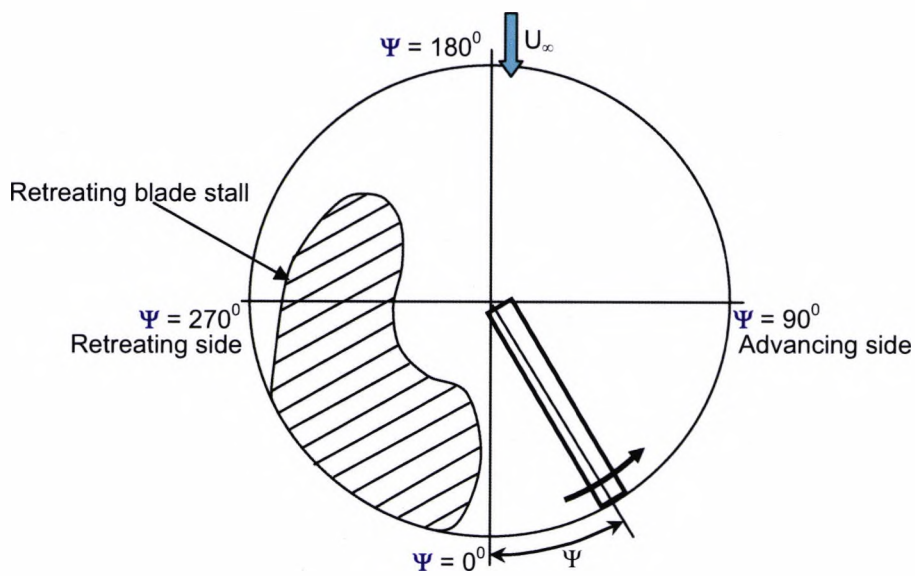


Figure 5.1: Schematic of the retreating blade stall region [Carr (1988)]

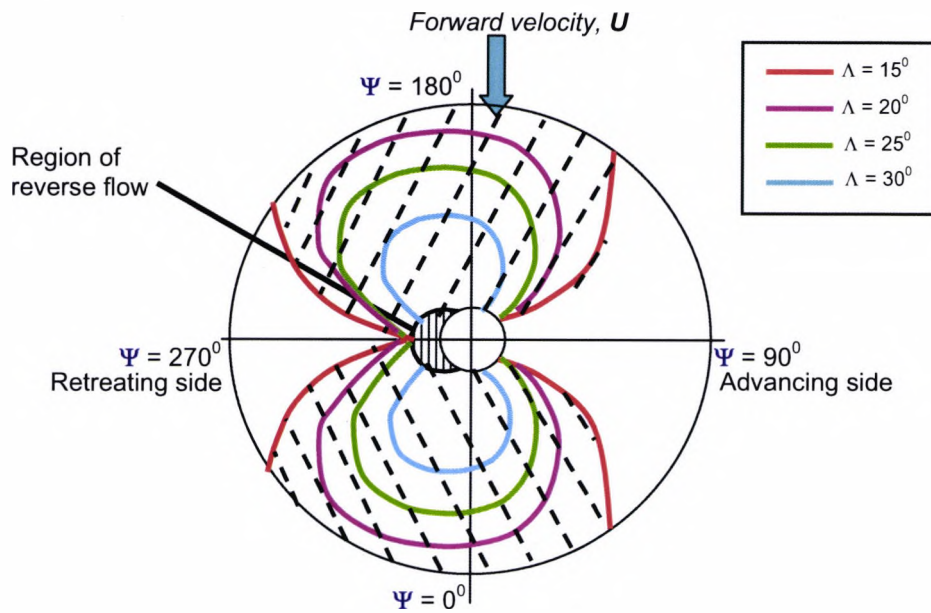


Figure 5.2: Contours of local sweep angle on rotor disc in forward flight at  $\mu = 0.33$  [Leishman (1989)]

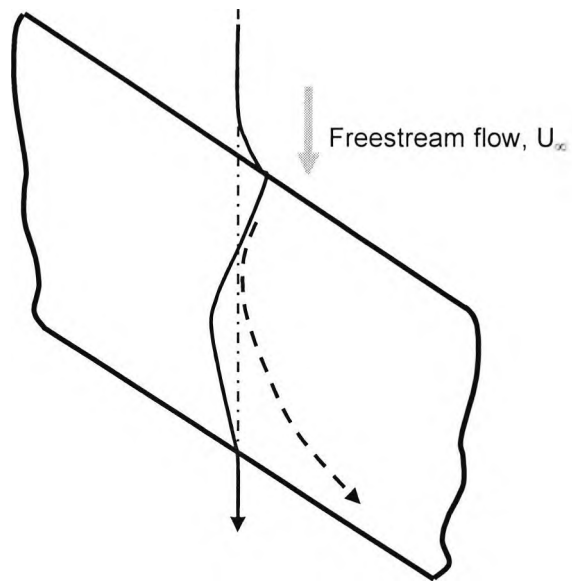


Figure 5.3: Path of a particle outside the boundary layer (full line) and inside (broken line) on a swept-wing [Küchemann (1953)]

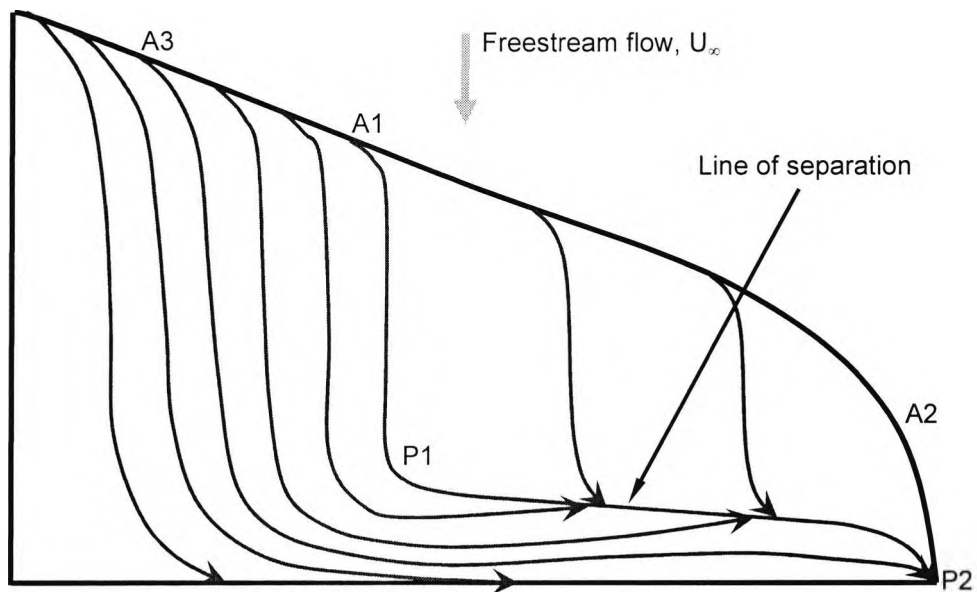


Figure 5.4: Surface flow pattern for a type of rear separation on a swept-wing [Maskel (1955)]

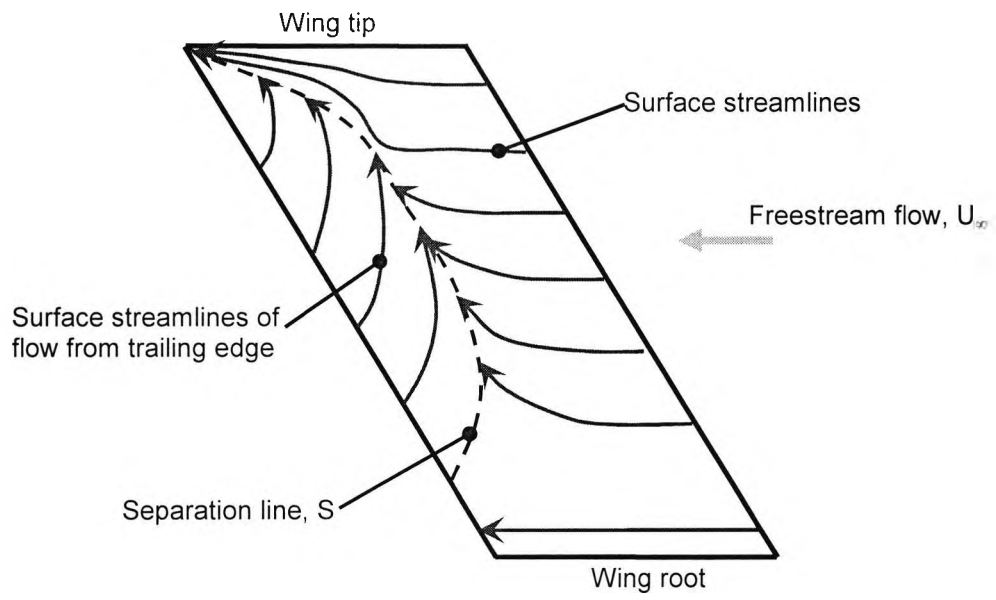


Figure 5.5: Sketched interpretation of the surface flow once separation has occurred [Broadley and Garry (1997)]

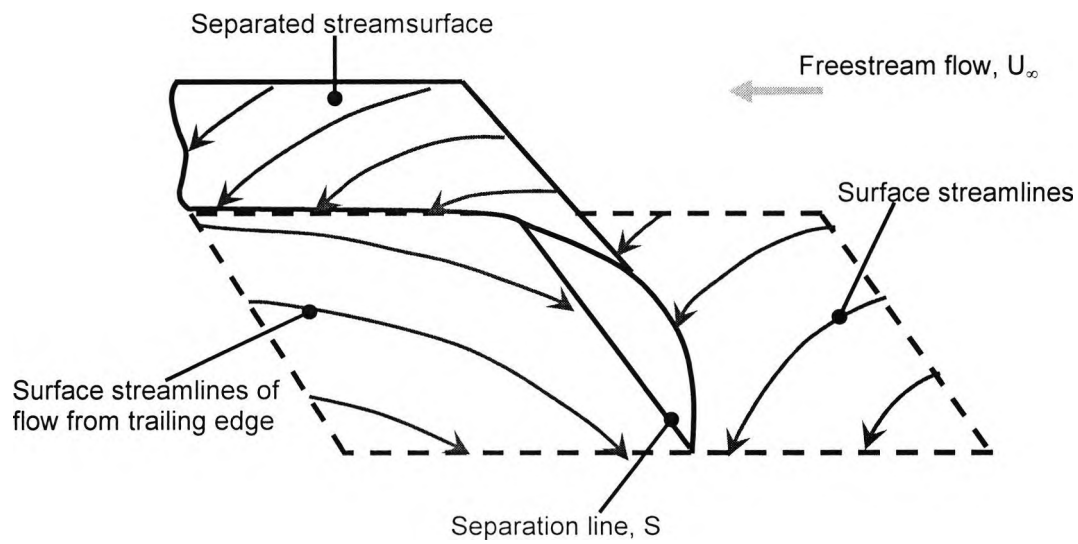


Figure 5.6: Surface flow streamlines in the separation region [Broadley and Garry (1997)]

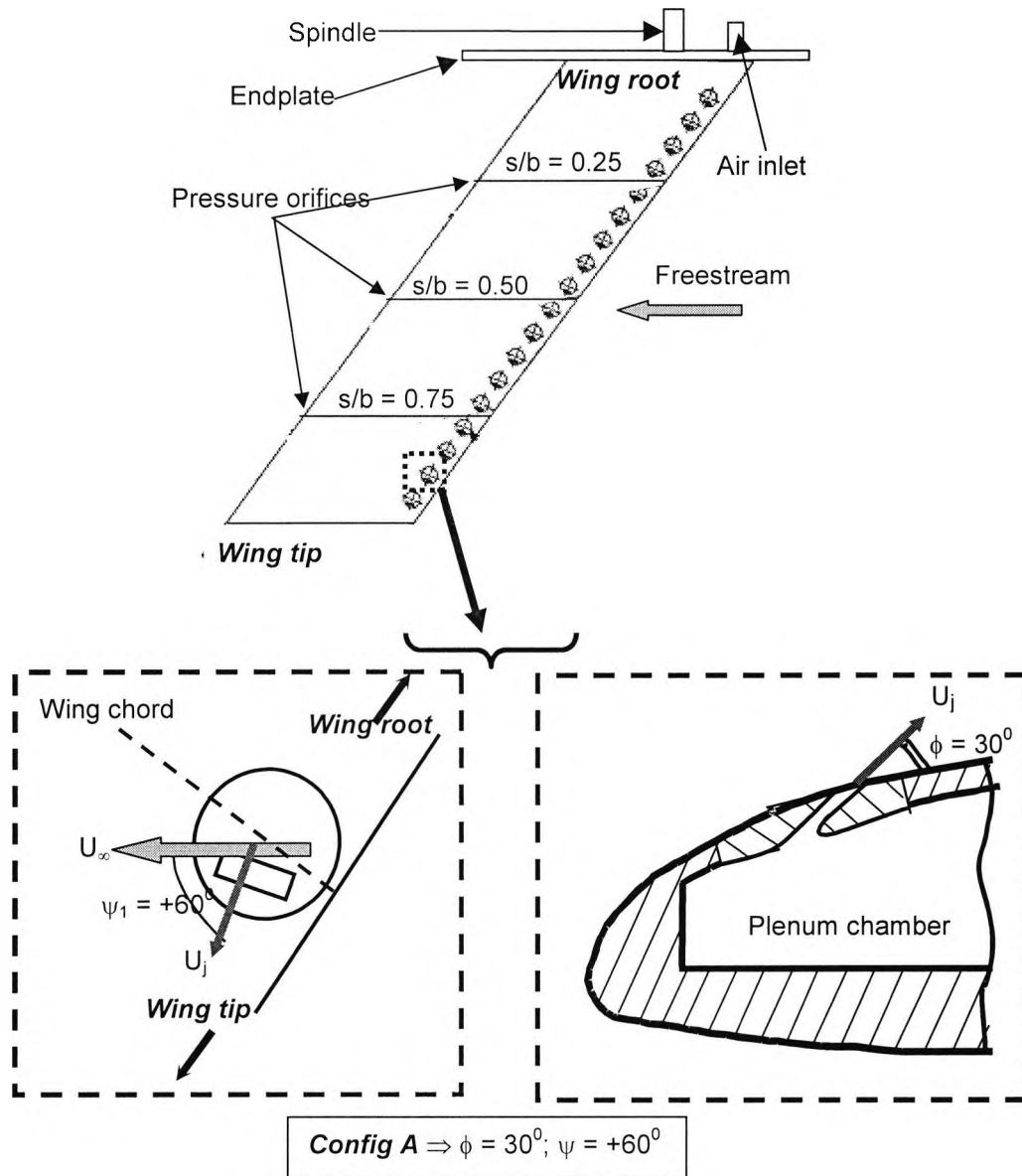


Figure 5.7: Schematic diagram of the swept wing illustrating (a), test model set-up, (b), surface static pressure orifices and (c), AJVG geometries

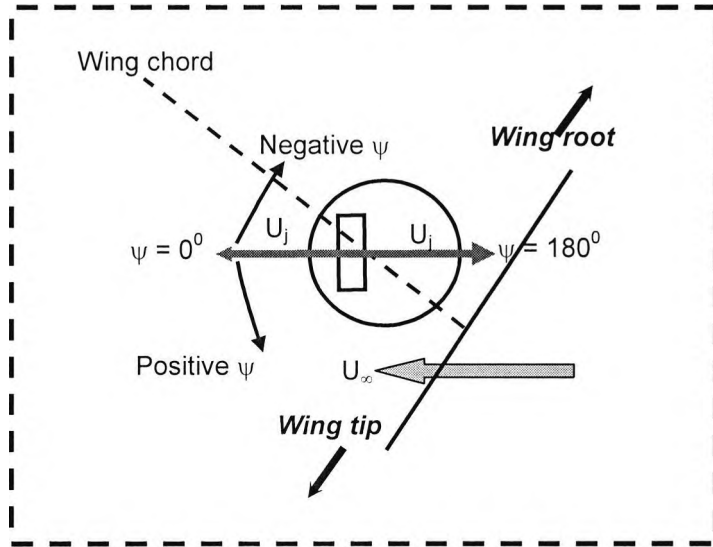


Figure 5.8: Orientation of AJVG skew angle

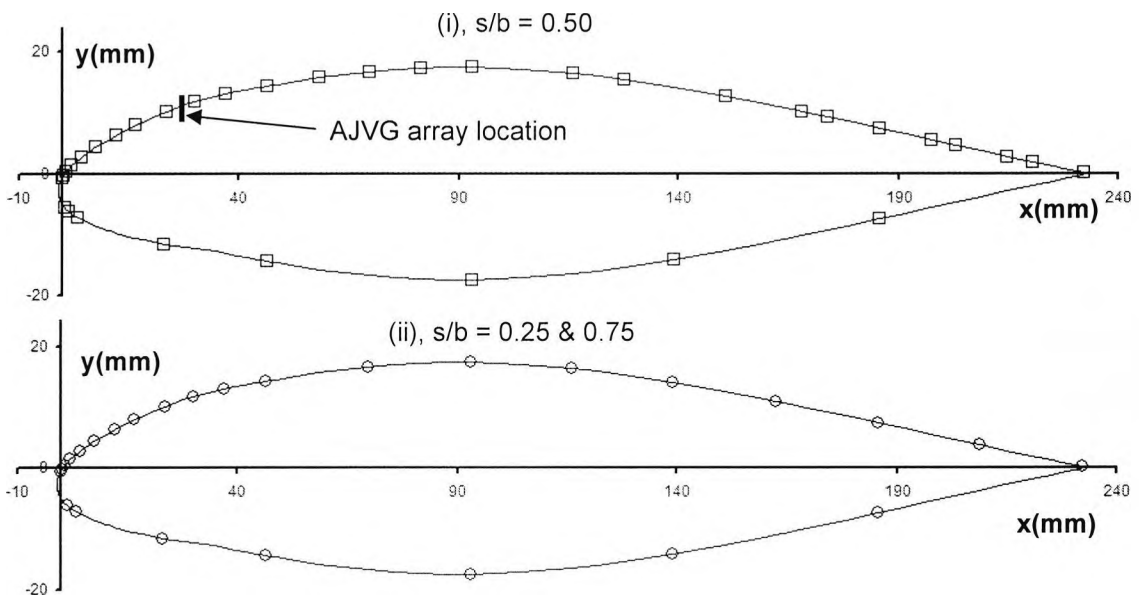


Figure 5.9: Chordwise profiles of the RAE 5225 aerofoil section showing (a), AJVG location at  $x/c = 0.10$  and (b), surface static pressure orifices along the chord at spanwise locations of  $z/b = 0.25, 0.50$  and  $0.75$

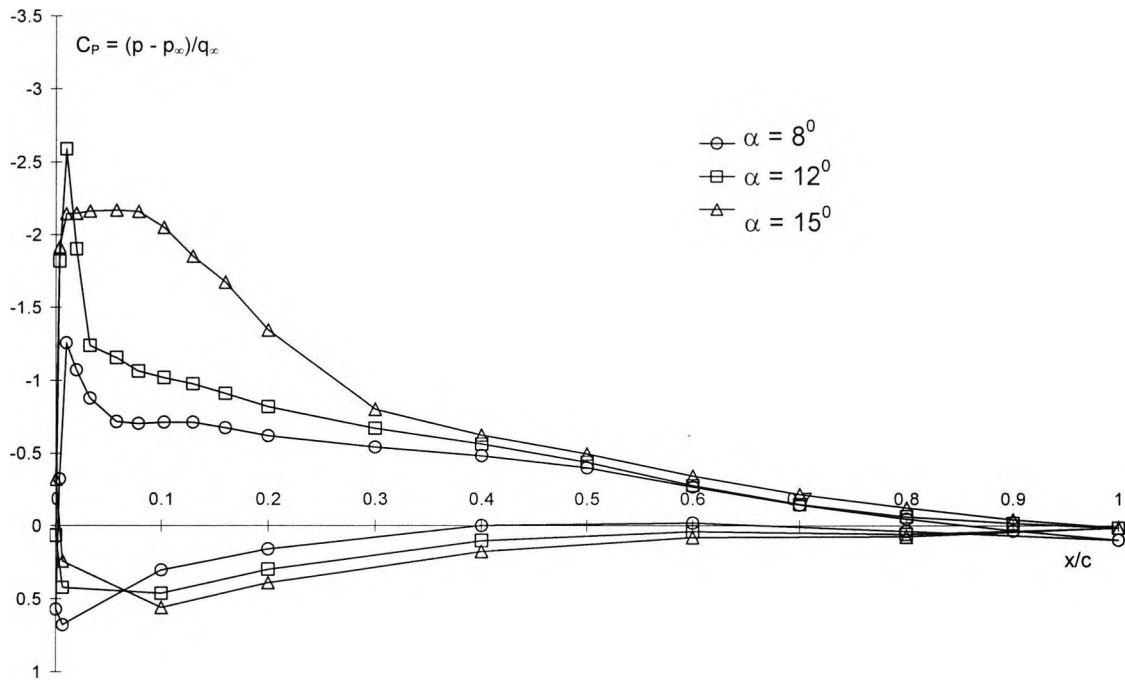


Figure 5.10: Sensitivity of chordwise surface pressure distribution for the unblown swept-wing at  $s/b = 0.25$ ,  $Re_c = 0.5 \times 10^6$  and  $M_\infty = 0.1$

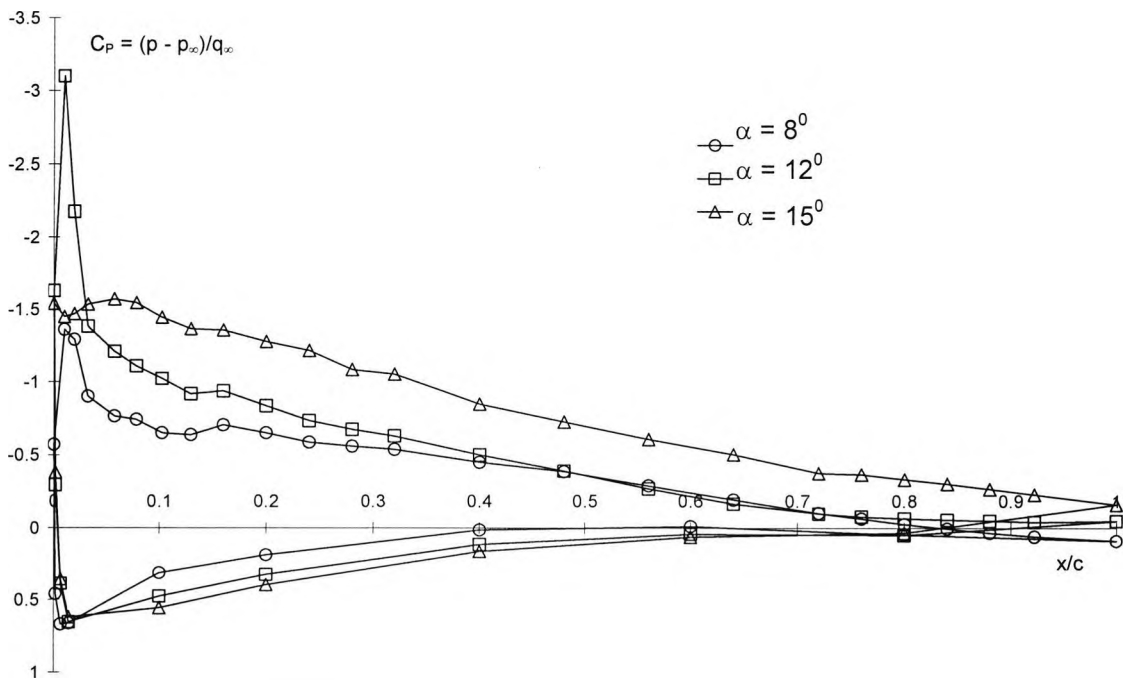


Figure 5.11: Sensitivity of chordwise surface pressure distribution for the unblown swept-wing at  $s/b = 0.50$ ,  $Re_c = 0.5 \times 10^6$  and  $M_\infty = 0.1$

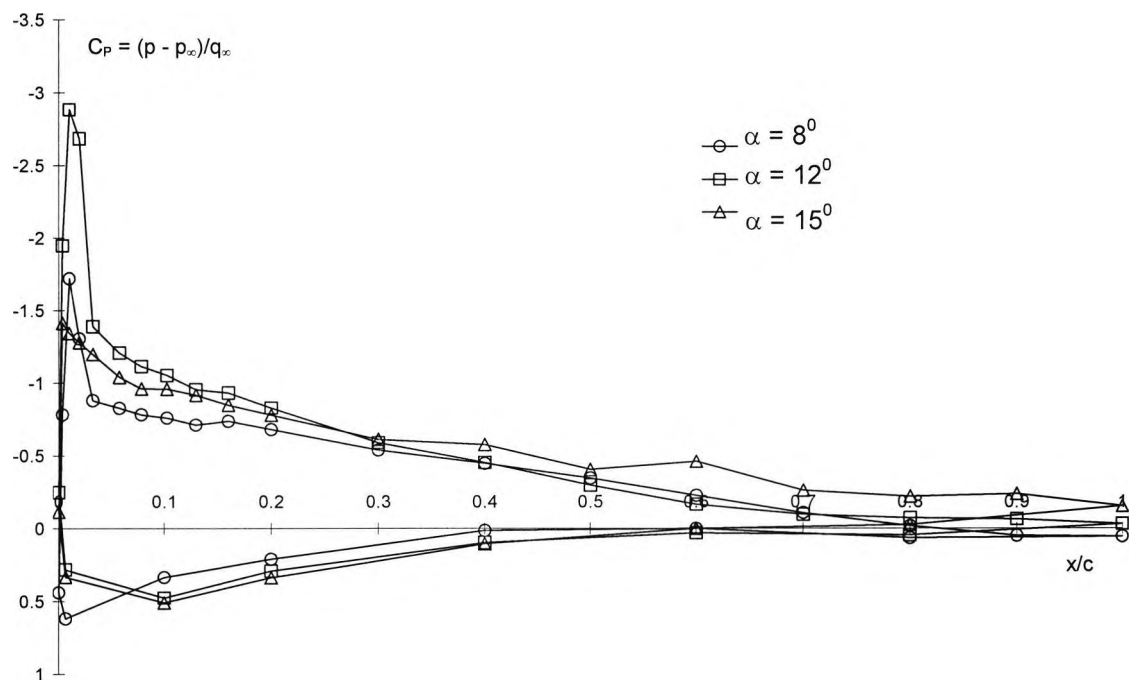


Figure 5.12: Sensitivity of chordwise surface pressure distribution for the unblown swept-wing at  $s/b = 0.75$ ,  $Re_c = 0.5 \times 10^6$  and  $M_\infty = 0.1$

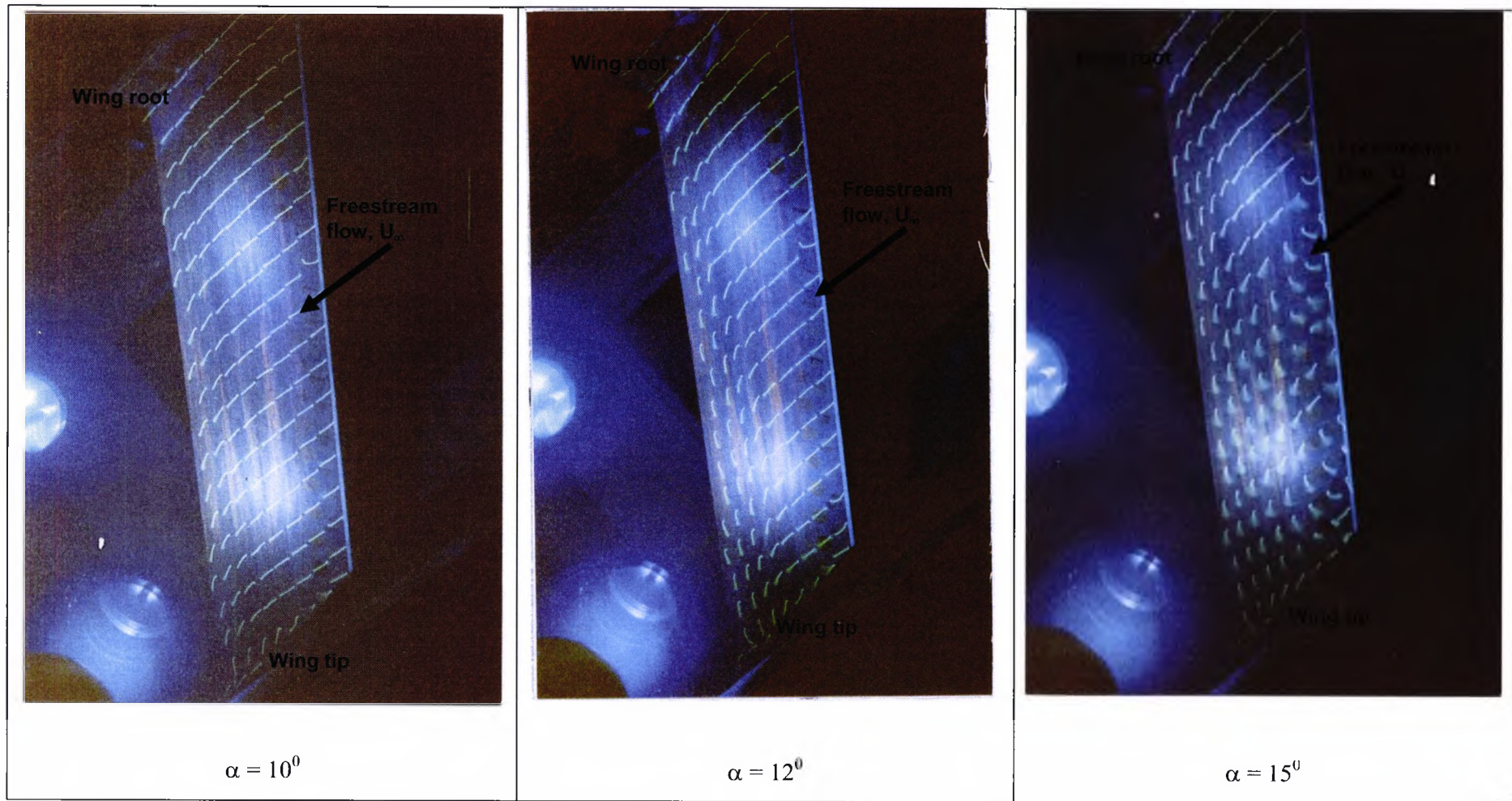


Figure 5.13: Flow visualisation using fluorescent tufts for the unblown swept wing increasing angle of attack at  $Re_c = 0.5 \times 10^6$  and  $M_\infty = 0.1$

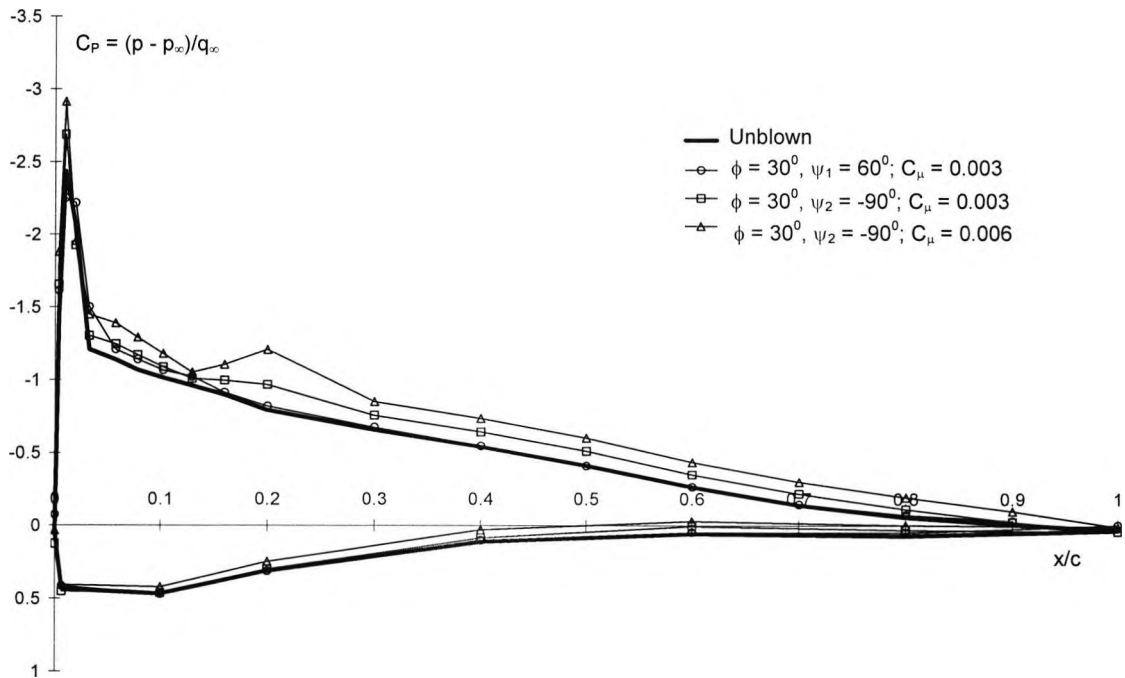


Figure 5.14: Sensitivity of chordwise surface pressure distribution with AJVG operating at  $\alpha = 12^\circ$ ,  $s/b = 0.25$ ,  $Re_c = 0.5 \times 10^6$  and  $M_\infty = 0.1$

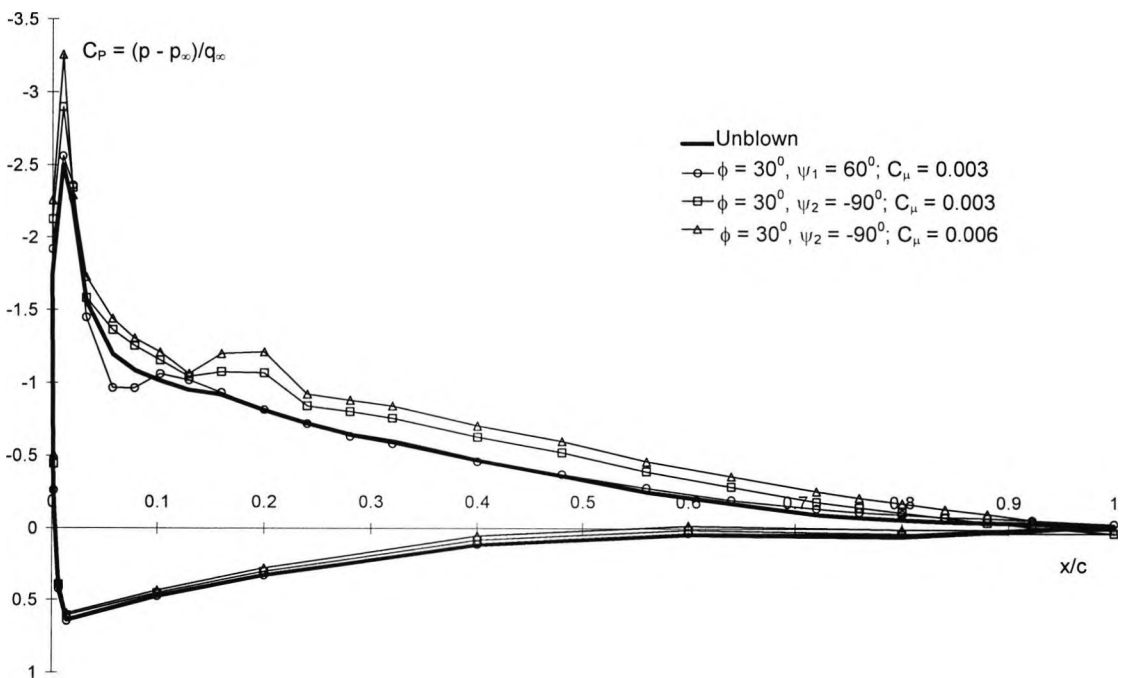


Figure 5.15: Sensitivity of chordwise surface pressure distribution with AJVG operating at  $\alpha = 12^\circ$ ,  $s/b = 0.50$ ,  $Re_c = 0.5 \times 10^6$  and  $M_\infty = 0.1$

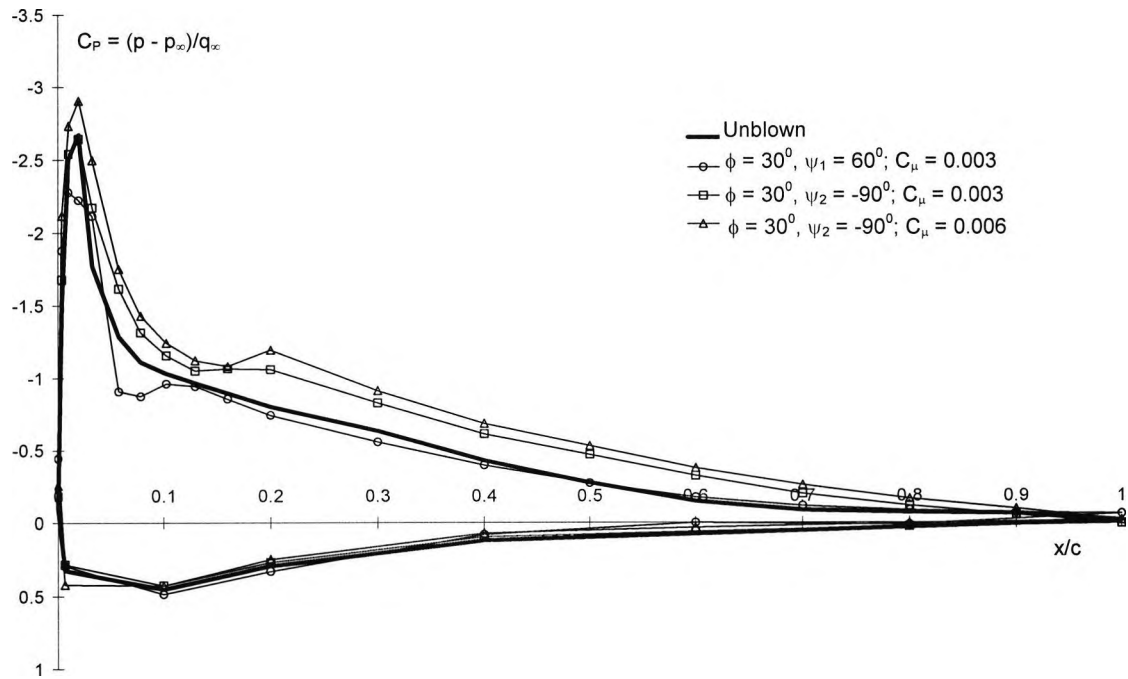


Figure 5.16: Sensitivity of chordwise surface pressure distribution with AJVG operating at  $\alpha = 12^\circ$ ,  $s/b = 0.75$ ,  $Re_c = 0.5 \times 10^6$  and  $M_\infty = 0.1$

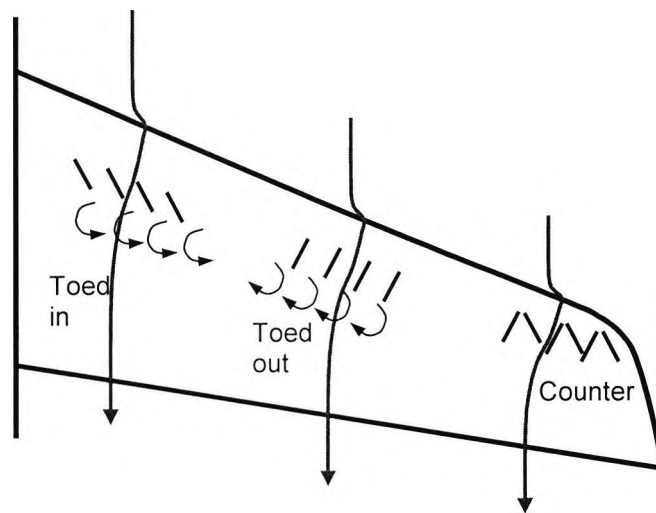


Figure 5.17: The orientation of various VVG systems for a swept-back wing with respect to wing sweep and local flow direction [Pearcey (1961)]

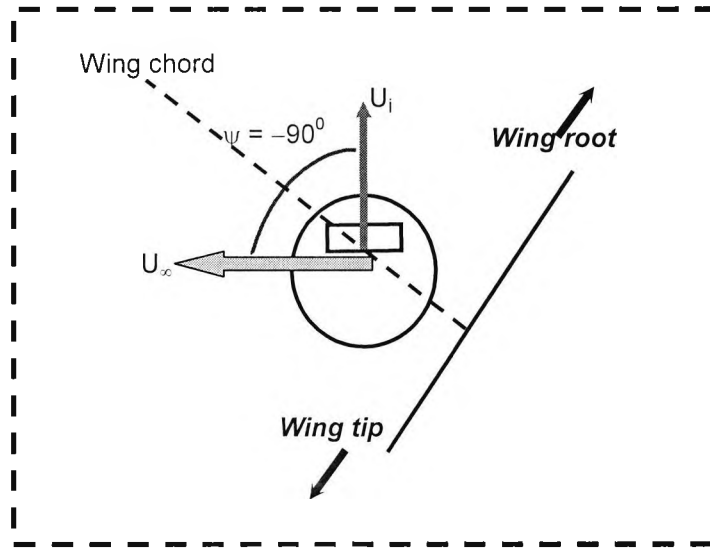


Figure 5.18: Orientation of the AJVG yaw angle based on recommendations of Pearcey (1961); **Config B** with  $\phi = 30^\circ$  and  $\psi = -90^\circ$

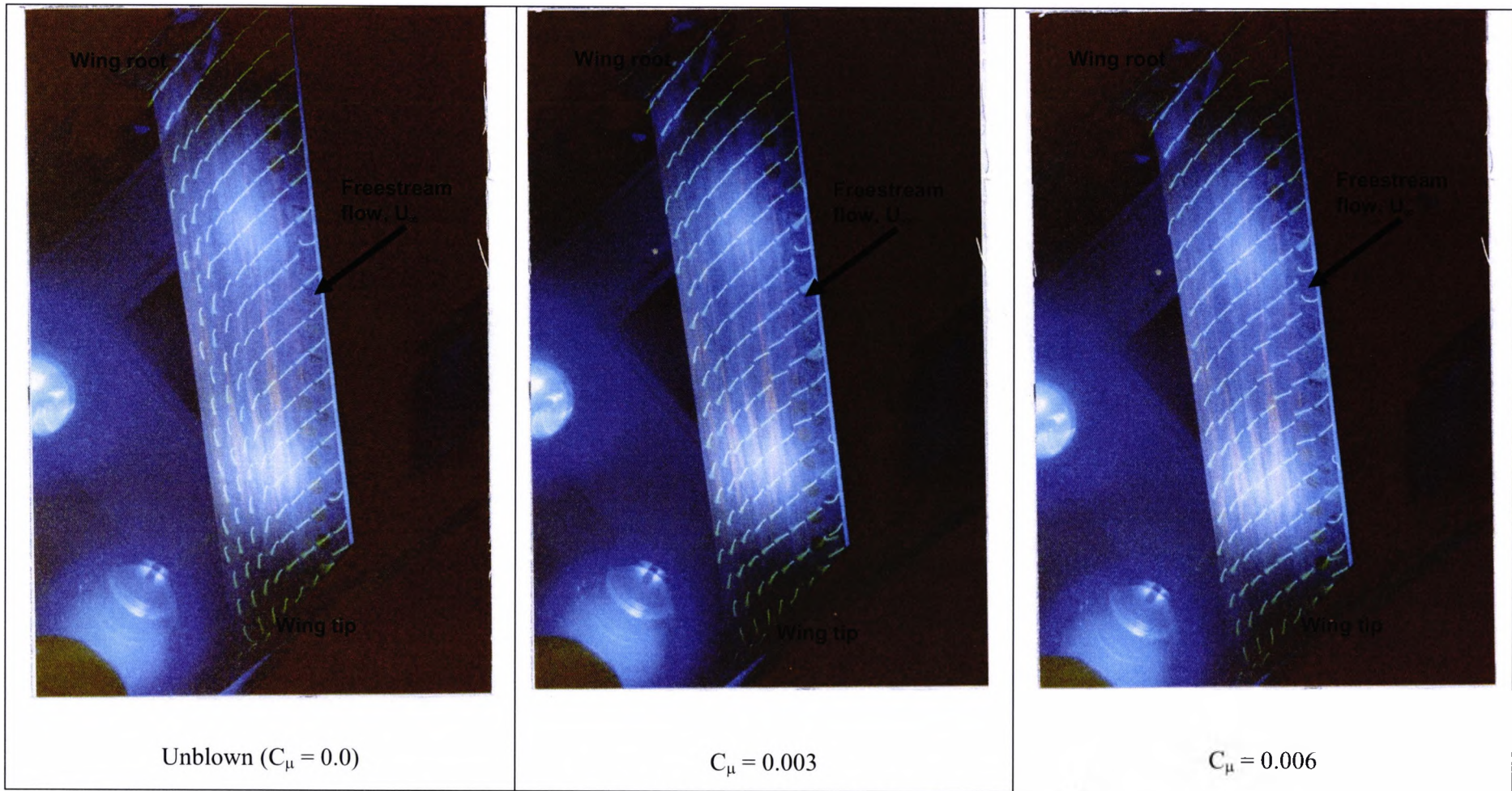


Figure 5.19: Flow visualisation using fluorescent tufts for *Config B* AJVG at  $\alpha = 12^\circ$ ,  $Re_c = 0.5 \times 10^6$  and  $M_\infty = 0.1$

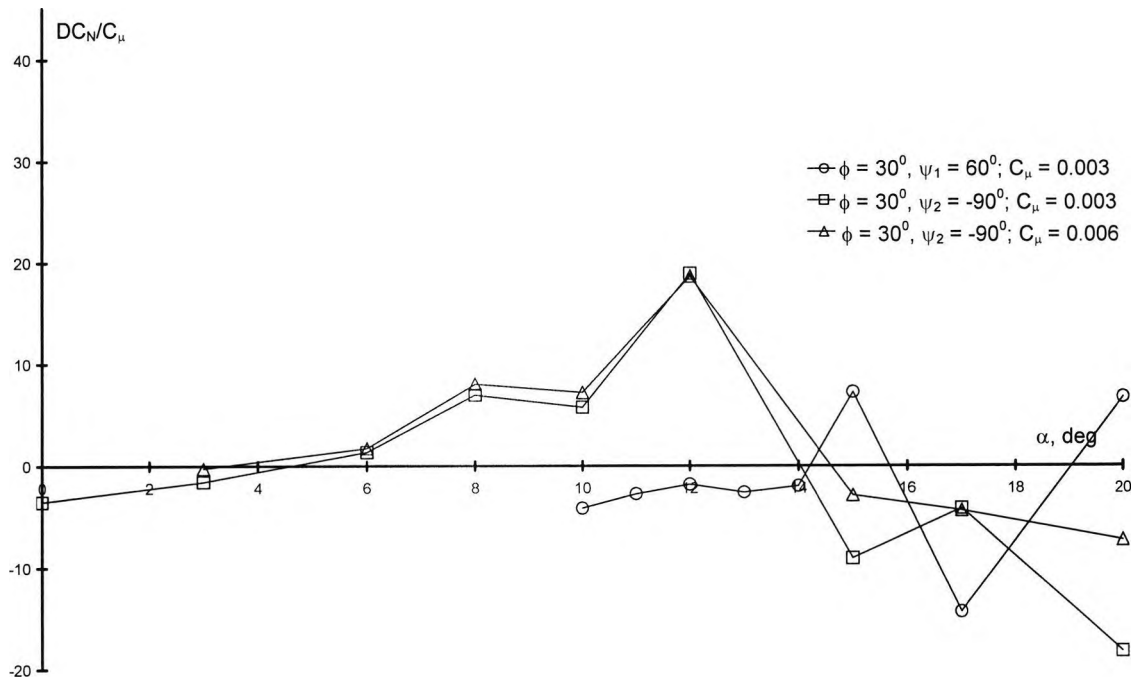


Figure 5.20: Variation of incremental normal force coefficient with angle of attack for the  $35^\circ$  swept-back wing with AJVG operating at  $z/b = 0.25$ ,  $Re_c = 1.5 \times 10^6$  and  $M_\infty = 0.1$

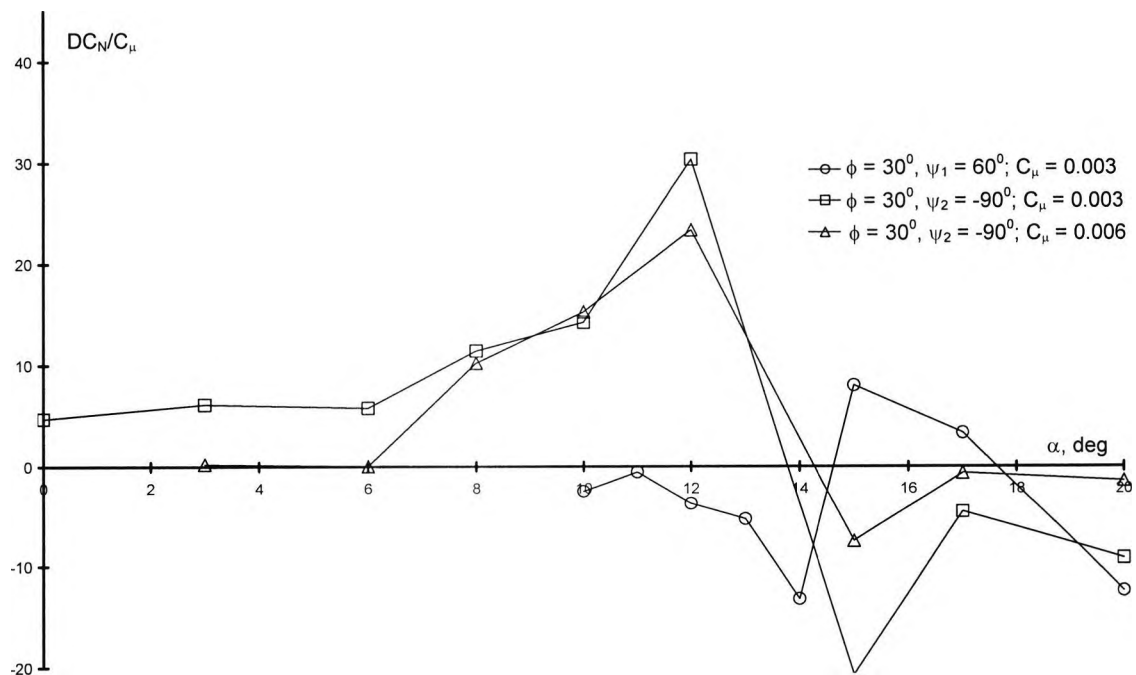


Figure 5.21: Variation of incremental normal force coefficient with angle of attack for the  $35^\circ$  swept-back wing with AJVG operating at  $z/b = 0.50$ ,  $Re_c = 1.5 \times 10^6$  and  $M_\infty = 0.1$

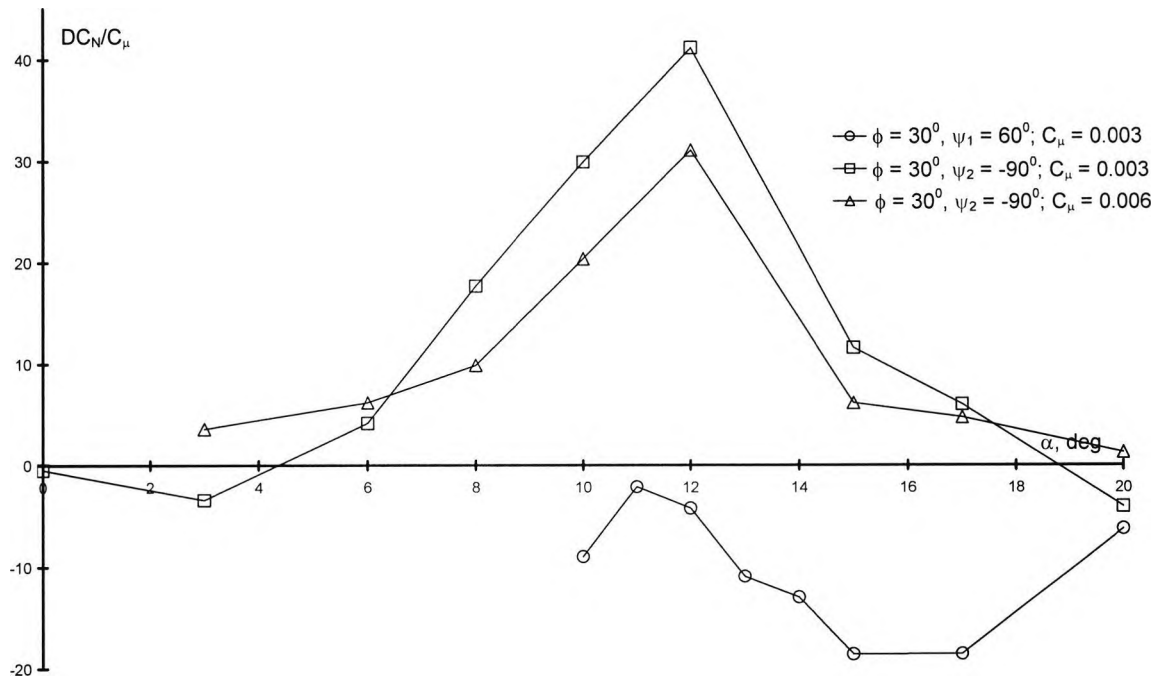


Figure 5.22: Variation of incremental normal force coefficient with angle of attack for the  $35^\circ$  swept-back wing with AJVG operating at  $z/b = 0.75$ ,  $Re_c = 1.5 \times 10^6$  and  $M_\infty = 0.1$

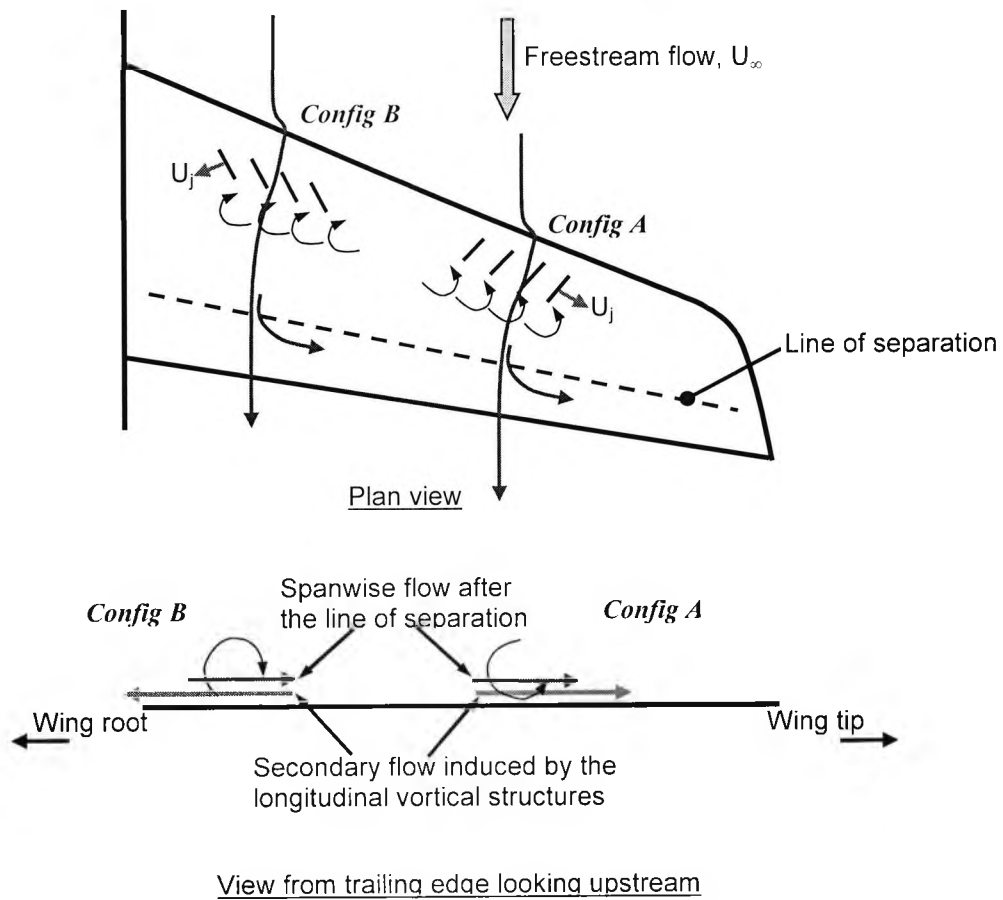


Figure 5.23: The AJVG set-up as *Config A* and *Config B* and its influence on swept wing boundary-layer separation

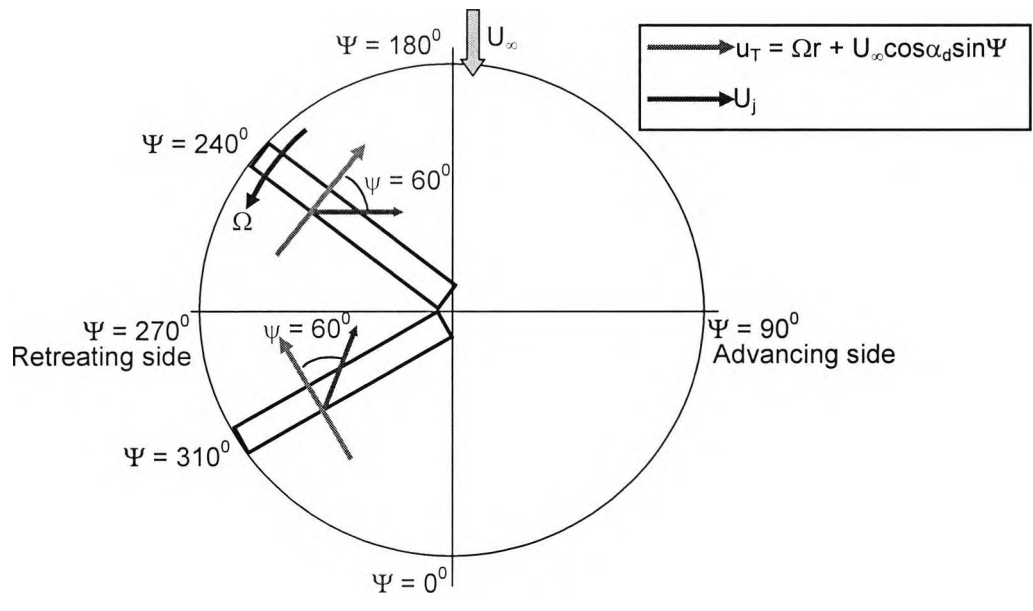


Figure 5.24: Schematic of the AJVG skew angle when incorporated into a full-scale rotor blade

## 6. Experimental arrangement – Pulsed Blowing Experiment

### 6.1 Introduction

Hitherto, research at City University has concentrated on utilising continuous blowing AJVGs to enhance the aerodynamic performance of single-element and multi-element aerofoils under quasi-steady flow conditions [see Innes (1995), Oliver (1997) and Lewington (2000)]. McManus et al (1994) and Seifert et al (1996) have shown that the steady-state blowing mass flow required for effective separation control can be reduced by up to 50% by means of periodic blowing. The research programme carried out at City University concentrates on wind tunnel tests investigating the potential of maintaining the aerodynamic performance of a single-element aerofoil attributed to AJVGs operated at steady, low blowing momentum coefficients, but with the prospect of reducing the jet mass momentum fluxes, when the jet flow is made unsteady, i.e. pulsed AJVGs.

### 6.2 Wind tunnel set-up

The experiments were conducted in City University's T2 low speed, closed-circuit wind tunnel (see Figure 6.1). The model, described in the next section, was mounted vertically in its octagonal working section of width = 1.12m, height = 0.81m and length = 1.68m. The rear of the working section is vented to atmosphere, whilst at the entry to the tunnel contraction are low turbulence meshes, used to achieve test section flow uniformity and a turbulence level of 0.7%. The model is supported about the mid-chord at either end by spindles mounted to the side of the model (see Figure 6.2). The spindles are held in place by base plates, which are connected to the top and bottom walls of the wind tunnel. Angle of attack is set by rotating the model about the spindle axis on two sets of thrust roller bearings and locking them in position. A pointer attached to the model top spindle permits measurement of the angle of attack to within  $\pm 0.1\%$ . Experiments were conducted at an equivalent chord Reynolds number,  $Re_c$ , of  $1.1 \times 10^6$  and freestream Mach number,  $M_\infty$ , of 0.10.

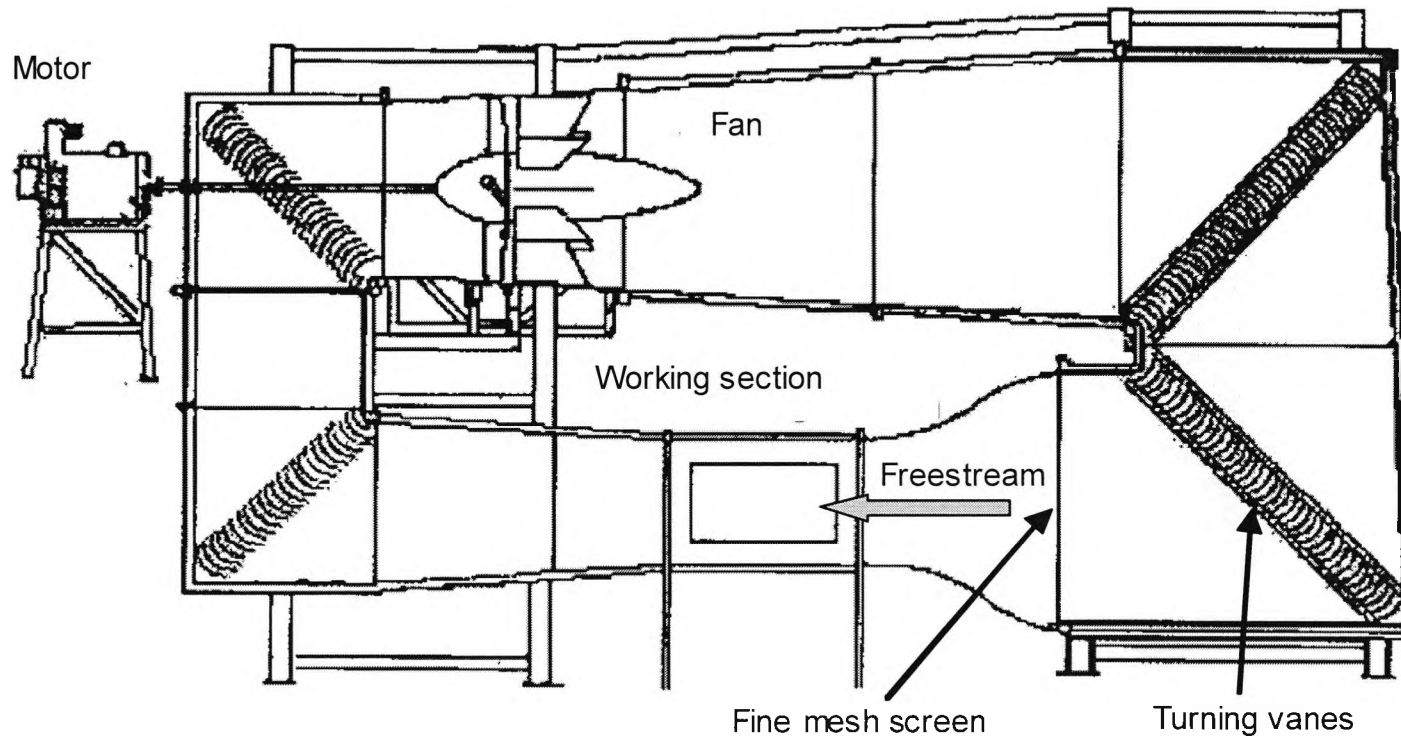


Figure 6.1: Schematic of T2 low speed wind tunnel

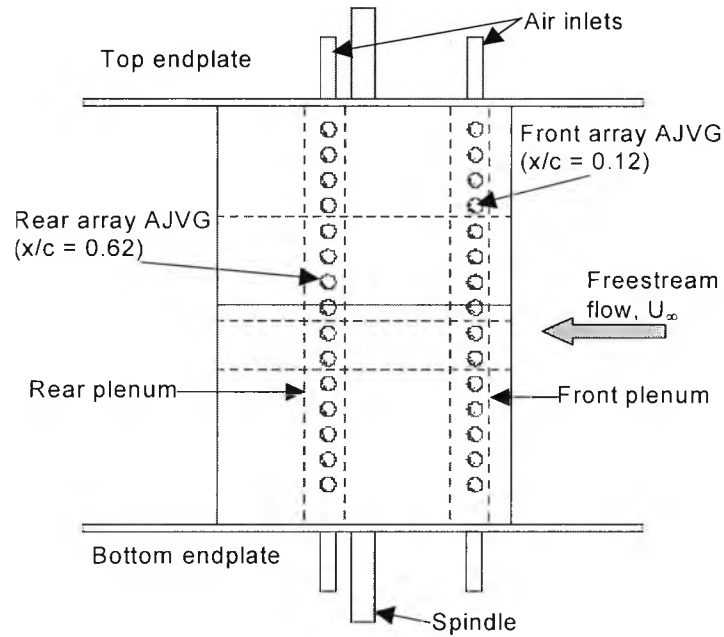


Figure 6.2: Plan view of the NACA 23012C aerofoil mounted vertically in T2 wind tunnel

### 6.3 Wind tunnel model

The model is a modified single element aerofoil, NACA 23012C, with a chord of 480mm and a span of 740mm. This aerofoil, designed as a test case to study low  $\alpha$  trailing edge stall development, is a modification of the NACA 23012 with increased camber and modified trailing edge to promote trailing edge separation. The model is fitted with two chordwise sets of AJVG arrays located at 12% and 62% chord as shown in Figure 6.3. Each of the two chordwise positions has a total of 15 AJVGs equally spaced along the span of the model.

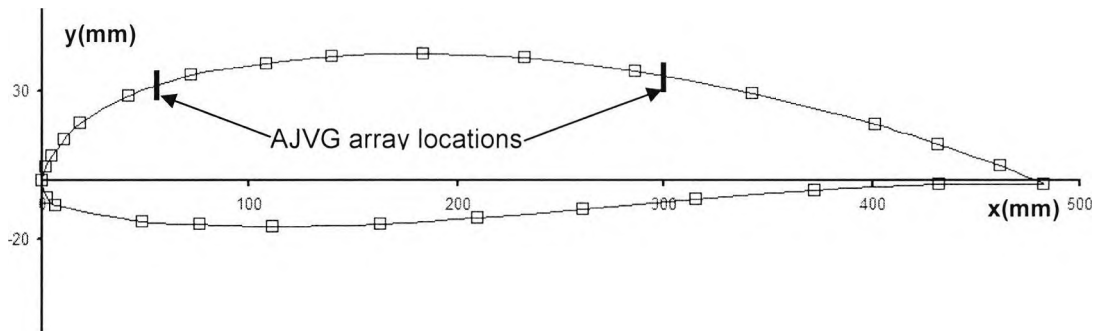


Figure 6.3: Profile of the NACA 23012C aerofoil section showing AJVG locations at 12% and 62% chord

The model was fabricated in upper and lower sections out of white beech wood allowing the construction of the plenum chamber and the fitting of brass tubing used to attach to static pressure orifices in the wing surface (see Section 6.4.1). Air is supplied to the AJVG array(s) via a pressure regulated plenum chamber located within the aerofoil section. Intermittent blowing was attained via a pulsing device consisting of a rotor disc sandwiched between two stator discs, each with 8 equispaced radial slots (see also Section 6.6). The pulsing system was situated outside of the test section and supplied the plenum via a short interlink. Tangential blowing on the endplates was used to control the boundary layer growth at the aerofoil/endplate junctions. Thus, a nominally two-dimensional flow across the span over the entire angle of attack range (up to stall) tested was reasonably maintained. Adequacy of nominal two-dimensional flow was verified by monitoring parallelism of mini-tufts in the endplate/aerofoil junctions at all angle of attack settings. Innes (1995) suggested that the minimum tangential blowing pressure of 4.0psig is required to control boundary layer growth and separation on the endplates.

#### 6.4 Experimental arrangement, instrumentation and analysis

The experimental procedure involved running the wind tunnel up to the desired speed with the aerofoil at  $\alpha = 0^0$  and activating the flow control devices when required. Once a uniform test flow field is established, the desired angle of attack is set and the measurements taken. This procedure minimises the effects of hysteresis on the experimental results and ensures that when the AJVGs are employed they are influencing boundary-layer growth prior to reaching the unblown aerofoil stall angle of attack; rather than employing the AJVGs to restore the attached flow after the unblown aerofoil has stalled. Quasi-steady tests were conducted in the angle of attack range of  $6^0 \leq \alpha \leq 21^0$ . For these tests, AJVGs were operated at low blowing momentum coefficients, both mean and root-mean-square (RMS), of between  $0.0 < C_{\mu} < 0.01$  over a range of dimensionless pulsing frequencies of  $0.0 \leq F^+ \leq 2.0$ .

Measurement of the chordwise static surface pressure distribution and wake properties were obtained via pressure transducers. These pressure transducers were connected to a multi-tasking CED 1401, which enables conversion of data from analogue to digital and vice versa. A PC, equipped with a 486 processor, is configured and interfaced with the CED 1401 from which a Data Acquisition program is used to execute the acquisition and storing of data (see Figure 6.4). The system is capable of measuring up to 4 scanivalve systems (4×48 ports) on a single experimental run. Further information about the program can be obtained from Innes (1995). The only difference between the current data acquisition set-up and that of Innes (1995) is that a new transducer amplifier unit with built-in low pass filter (Fylde FE-379-TA) replaces the bridge conditioning, Fylde FE-492-BBS, and differential amplifier, Fylde FE-254-GA, unit. A schematic of the experimental data acquisition procedure is outlined in Figure 6.4.

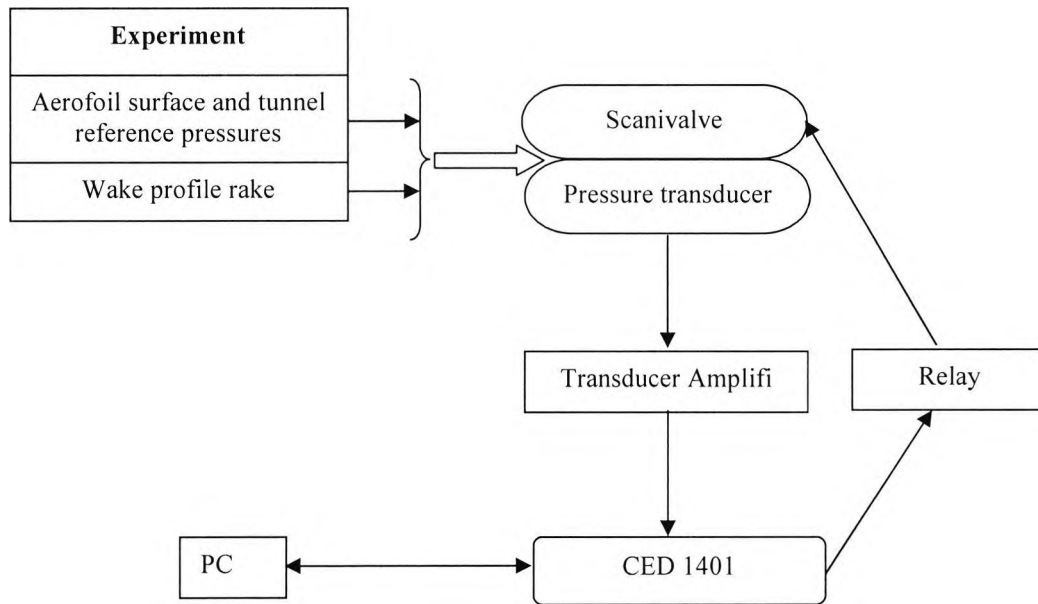


Figure 6.4: Schematic diagram of experimental data acquisition

#### 6.4.1. Surface static pressure measurements

The model was instrumented with 90 pressure orifices measuring (a), surface static pressure; and (b), plenum chamber pressure. Table 6.1 shows the distribution of the pressure orifices across the model span and plenum(s). Figures 6.5 and 6.6 illustrate the chordwise pressure orifice distribution with respect to the position of the AJVG and distribution of the pressure orifices on the upper and lower surface of the aerofoil section, respectively.

Pressure orifice position	Quantity
Around the aerofoil at $z/b = 0.26$	28
Around the aerofoil at $z/b = 0.52$	28
Around the aerofoil at $z/b = 0.62$	28
Front plenum chamber	3
Rear plenum chamber	3

Table 6.1: NACA 23012C surface and plenum static pressure orifices. Their position and quantity

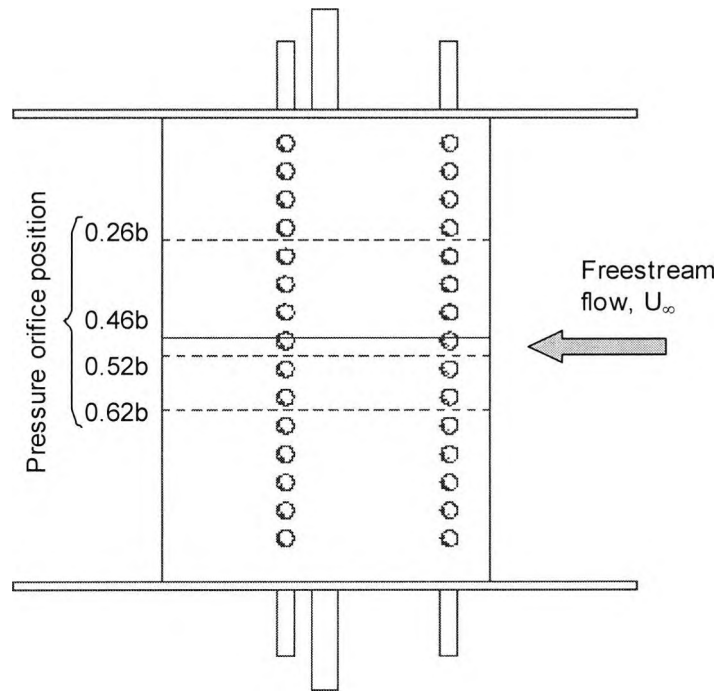


Figure 6.5: Surface static pressure orifice and dynamic pressure sensor locations compared with AJVG position (see also page 123)

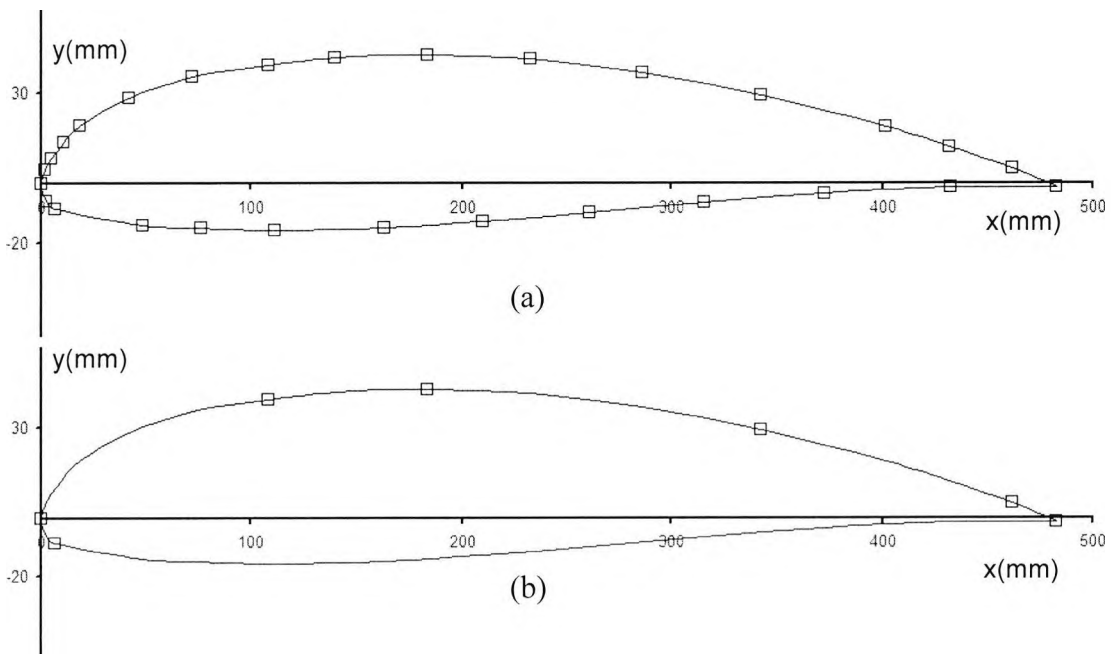


Figure 6.6: (a) Locations of static pressure orifices along the aerofoil chord at  $z/b = 0.26, 0.52$  and  $0.62$  (17 pressure orifices on upper and 11 pressure orifices on lower surfaces); (b) Locations of dynamic pressure sensors along aerofoil chord at  $z/b = 0.46$  (6 pressure sensors on upper and 1 pressure sensors on lower surfaces)

The surface static pressure coefficients,  $C_p$ , around the chord of the aerofoil section were measured by connecting the aerofoil surface pressure tappings (and the tunnel reference pressure tappings) to pressure transducers via 48 port scanivalves. For this experiment two 48-port scanivalve systems (Type 48S3), each housing a 2.5psid range DRUCK PDCR22 differential pressure transducer, were utilised. Inclusion of the tunnel reference pressure tappings on the scanivalve enabled calculation of the pressure coefficients directly from the transducer output voltages, without the need for an absolute calibration; provided the pressure outputs are proportional to their inputs. A differential mercury manometer, with a 10psid range, was used to monitor the plenum chamber pressure, thereby allowing assessment of the AJVG blowing momentum coefficient (see Section 6.7).

Referring to Innes (1995), the calculation procedure for the experimental pressure coefficients is outlined as follows:

$$C_p = \frac{p - p_\infty}{\frac{1}{2} \rho U_\infty^2} = \frac{(p - p_a) - (p_\infty - p_a)}{\frac{1}{2} \rho U_\infty^2} \quad (6.1)$$

where:

$p$  = static pressure on the aerofoil surface

$p_a$  = atmospheric pressure

$p_\infty, U_\infty$  = freestream static pressure and velocity (upstream of the model)

Assuming:

$$\begin{aligned} \frac{1}{2} \rho U_\infty^2 &= K_1 (p_1 - p_2) \\ (p_1 - p_3) &= K_2 (p_1 - p_2) \\ (p_2 - p_3) &= K_3 (p_1 - p_2) \end{aligned} \quad (6.2)$$

where:

$(p_1 - p_2)$  is the tunnel static pressure drop along the tunnel contraction and  $p_3$  is the averaged pressure measured along the tunnel working section centreline;

Substituting Eqn. 6.2 into Eqn. 6.1 gives:

$$C_p = \frac{(p - p_a) - (p_2 - p_a)}{K_1(p_1 - p_2)} + \frac{K_3}{K_1} \quad (6.3)$$

Calibrating the wind tunnel produced the following values for the  $K_1$ ,  $K_2$  and  $K_3$  constants 1.1034, 0.9839 and 0.0161 respectively.

The method above requires certain ports on each scanivalve to be reserved for the pressure differences. These ports include (a), port 0 assigned as the atmospheric pressure reference; (b), port 24 measuring the tunnel stagnation pressure ( $p_1 - p_a$ ); and (c), port 25 measuring the tunnel static pressure ( $p_2 - p_a$ ). The remainder of the ports read ( $p - p_a$ ).

#### 6.4.2. Wake momentum deficit measurements

A wake rake was used to measure the aerofoil wake momentum deficit approximately one chord length downstream of the aerofoil trailing edge (see Figure 6.7). The wake rake consists of 40 stainless steel pitot probes and 5 static probes (OD 1.05mm and ID 0.81mm). The pitot pressure probes are spaced at 7mm intervals in the centre and at 15mm intervals towards each spanwise extremity (see Figure 6.8), giving a total span of 350mm. The static pressure tubes were used to measure any static pressure gradient across the wake.

Measuring the pitot and static pressures across the wake, via a 48-port scanivalve system housing a 0.25psi range SETRA 237 differential pressure transducer, permits the assessment of the aerofoil wake using the B.M.Jones expression [Houghton & Boswell (1969)] :

$$C_{Dw} = 2 \int_{Wake} \sqrt{\frac{H_1 - p_1}{H_\infty - p_\infty} \left( 1 - \sqrt{\frac{H_1 - p_\infty}{H_\infty - p_\infty}} \right)} d\left(\frac{y}{c}\right) \quad (6.4)$$

where:

$H_\infty$  = total head in the freestream

$p_\infty$  = static pressure in the freestream

$H_1$  = local total head one chord length downstream of the aerofoil

$p_1$  = local static pressure across the wake

$y$  = distance normal to the aerofoil wake

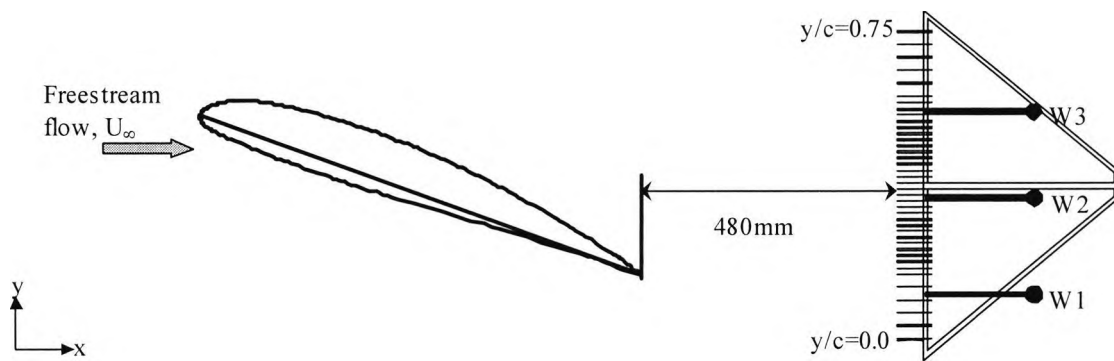


Figure 6.7: Top view showing the NACA 23012C aerofoil and wake rake arrangement

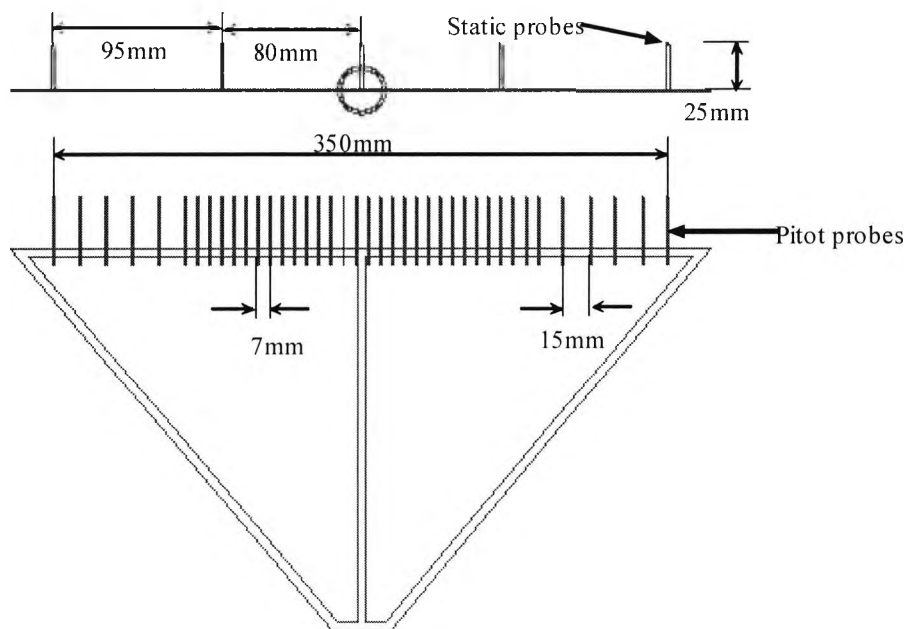


Figure 6.8: Schematic of the wake rake

The accuracy of the measured surface pressure and wake properties is dependent upon the resolution of the data channels in the CED 1401 data acquisition system. Voltage signals from the pressure transducers ( $\pm 5$  volt range) were handled with 12-bit accuracy, i.e. 2.4mV. At a constant tunnel speed of 40m/s where  $(p_1 - p_2) = 950\text{mV}$ , a resolution better than  $\pm 0.25\%$  can be achieved in determining  $C_p$ .

### 6.4.3 Dynamic pressure measurements

The aerofoil section is also instrumented with (a), 9 surface pressure sensors capable of measuring (mean and fluctuating) static pressures (see Figures 6.5 and 6.6); (b), two pressure sensors measuring plenum chamber (mean and fluctuating) total pressures; and (c), 3 pressure sensors measuring wake (mean and fluctuating) total pressures (see Table 6.2 and Figure 6.7).

Pressure sensor position	Qty
Around the aerofoil at mid-span, $z/b = 0.46$	7
Front plenum chamber	2
Wake rake (W1 at $y/c = 0.12$ ; W2 at $y/c = 0.47$ and W3 at $y/c = 0.65$ )	3

Table 6.2: NACA 23012C surface, plenum and wake rake dynamic pressure sensors. Their position and quantity

The pressure sensors were connected, via flexible vinyl tubing, to brass tubing positioned at the measuring locations. Care must be taken not to exceed the length/diameter ratio of 25 to avoid data aliasing and biasing, which occurs when a pressure sensor is connected to the measuring location with long tubing. The pressure sensors are Kulite's CTQH187 series with a rated pressure of 5psid operating in a differential mode. These pressure sensors were connected to a multi-tasking CED 1401*plus*, which enables conversion of data from analogue to digital and vice versa. A PC, equipped with a Pentium II processor, is configured and interfaced with the CED

1401plus where the data were stored for analysis (using the Spike2 v4 software) (see Figure 6.9). The system has a maximum sampling rate of 166kHz and has the capability of measuring up to 16 channels of data.

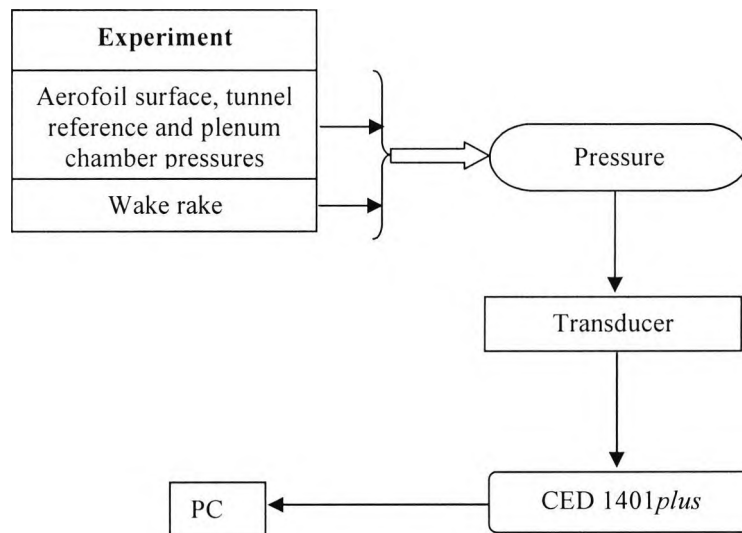


Figure 6.9: Schematic of the experimental dynamic pressure data acquisition

The physical data can be described as a combination of a time-invariant or *static* component and a fluctuating or *dynamic* component. The static component may be described by as an average of all values i.e. *mean value*. The software Spike2, used for data analysis, describes the mean value between predefined time ranges, *Start Time* and *End Time*, of a waveform as,

$$\mu_x = \sum_{StartTime}^{EndTime} \frac{x(t)}{N}$$

where:

$\mu_x$  = mean value

$x(t)$  = sample value

$N$  = number of samples

The dynamic component is described by a *variance*, which is simply the mean square value about the mean. The positive square root of the variance is known as *standard deviation*. In the Spike2 software the standard deviation has a value only for a waveform and is calculated by,

$$SD = \sqrt{\frac{\sum_{StartTime}^{EndTime} [x(t) - \mu_x]^2}{N - 1}}$$

where:

$SD$  = standard deviation

The standard deviation can also be termed as the true root-mean-square (RMS) of waveform data. An example of the pressure pulse signal measured inside the plenum chamber for a supplied mean pressure of 0.1psig and dimensionless pulsing frequency  $F^+ = 0.7$  is shown in Figure 6.10.

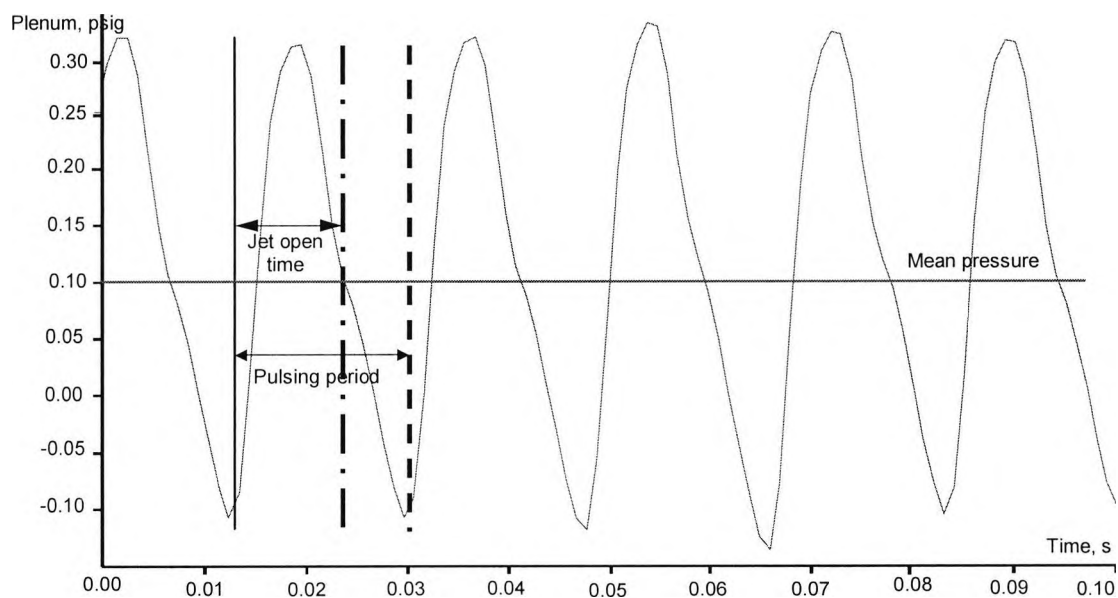


Figure 6.10: Example of pulse signal in the aerofoil plenum chamber at mean and unsteady levels of 0.1psig and 0.16psig (RMS amp = 0.18) at  $F^+ = 0.7$  and DC = 0.65

Additionally the Spike2 software describes the general intensity of waveform data as a root-mean-square amplitude or mean square value. Root-mean-square amplitude is given by:

$$RMSamp = \sqrt{\frac{\sum_{StartTime}^{EndTime} x(t)^2}{N}}$$

where  $RMSamp$  = root-mean-square amplitude

The pressure fluctuation coefficient as suggested by Fricke (1971) and Mabey (1972) can, therefore, be defined as:

$$\langle C_p \rangle = \frac{\langle p \rangle}{q_\infty} \quad (6.9)$$

where:

$\langle p \rangle$  = RMS pressure fluctuation (total/static) (N/m<sup>2</sup>)

$q_\infty$  = freestream dynamic pressure (N/m<sup>2</sup>)

Amongst the parameters associated with the pressure pulse signal are:

i) The dimensionless pulsing frequency,  $F^+ = \frac{fL}{U_\infty}$  (6.10)

where characteristic length,  $L$ , is defined as the distance between the jet exit and the aerofoil trailing edge.

ii) Duty cycle, DC, of the pressure signal is defined as the ratio of the jet open time compared with the pulse period (see Figure 6.10).

## 6.5 Air-jet vortex generator design

The geometrical design and spacing of the AJVG installed on the NACA 23012C were based on the wind tunnel tests of Oliver (1997) on a single-element aerofoil (NACA 63<sub>2</sub>-217). Oliver (1997) successfully demonstrated the ability of a spanwise array of co-rotating, rectangular AJVGs positioned at 10% chord to suppress trailing-edge separation. For the current tests on the NACA 23012C aerofoil the co-rotating AJVG system is positioned at 12% and 62% chord and spaced  $0.1c$  apart. The rectangular jet slot passage and exit has a slot aspect ratio of approximately 8 and is pitched,  $\phi$ , and skewed,  $\psi$ , at  $30^\circ$  and  $60^\circ$  respectively. The AJVG pitch angle is measured relative to the aerofoil local surface tangent whilst the skew angle is measured relative to the freestream direction (see Figure 6.11).

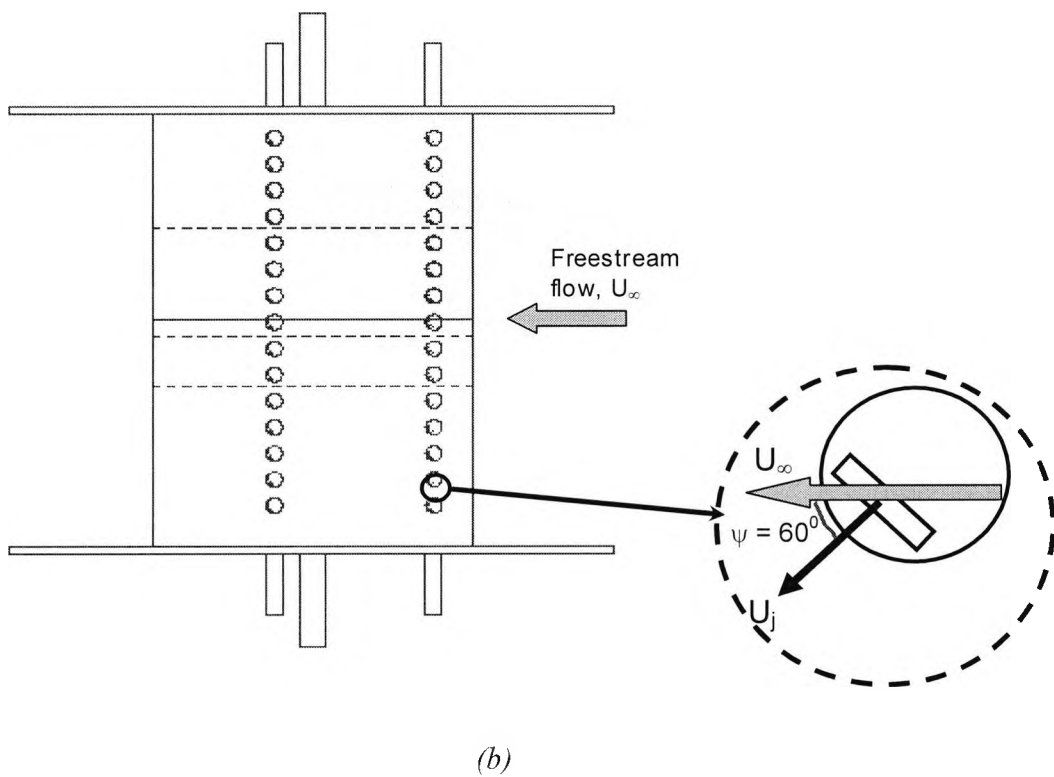
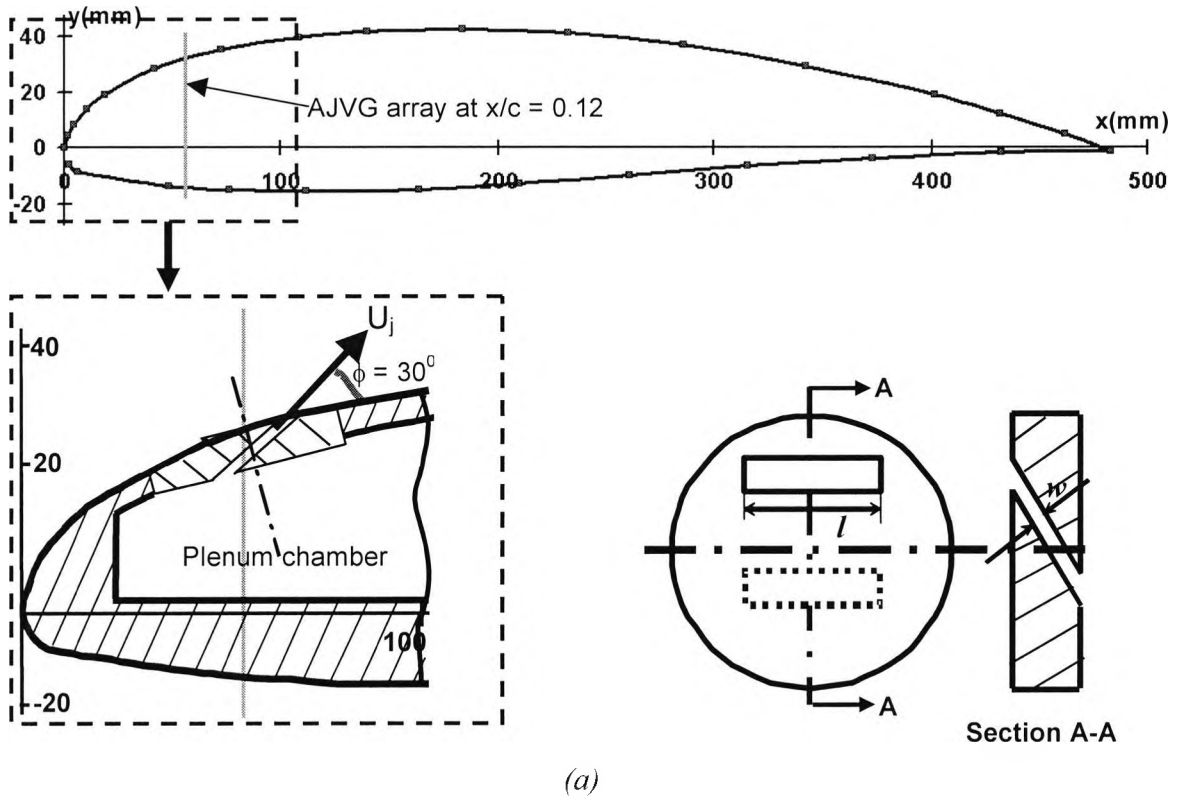


Figure 6.11: AJVG geometry configuration (a), pitch angle,  $\phi = 30^\circ$  ( $l = 0.025c$ ;  $l/w = 8$ ) and (b), yaw angle  $\psi = 60^\circ$

## 6.6 Pulsing device

Periodic AJVG blowing was realised with a pulsing device, as shown in Figure 6.12, designed at City University capable of producing frequencies,  $f$ , in excess of 500Hz. The device consists of a rotor disc sandwiched between two stator discs, each with 8 equispaced radial slots (see Figure 6.13). These discs were fabricated out of steel whilst the rest of the pulsing assembly was fabricated out of aluminium alloy (Duralmin). The rotor disc is mounted on a drive shaft and coupled to an electric motor. It is supported at either end by SKF matched precision thrust bearings (71905 CDGA/T4A). A Mitsubishi FR E540-0.2K-EC inverter was used to control the speed of the (ABB M3000) motor. The contraction of the pulsing device was carefully designed to insure uniform, low-turbulence flow exiting the system [see Mikhail (1976)]. Steady blowing, on the other hand, was achieved with the slots of the rotor and stator discs aligned with the rotor disc stopped.

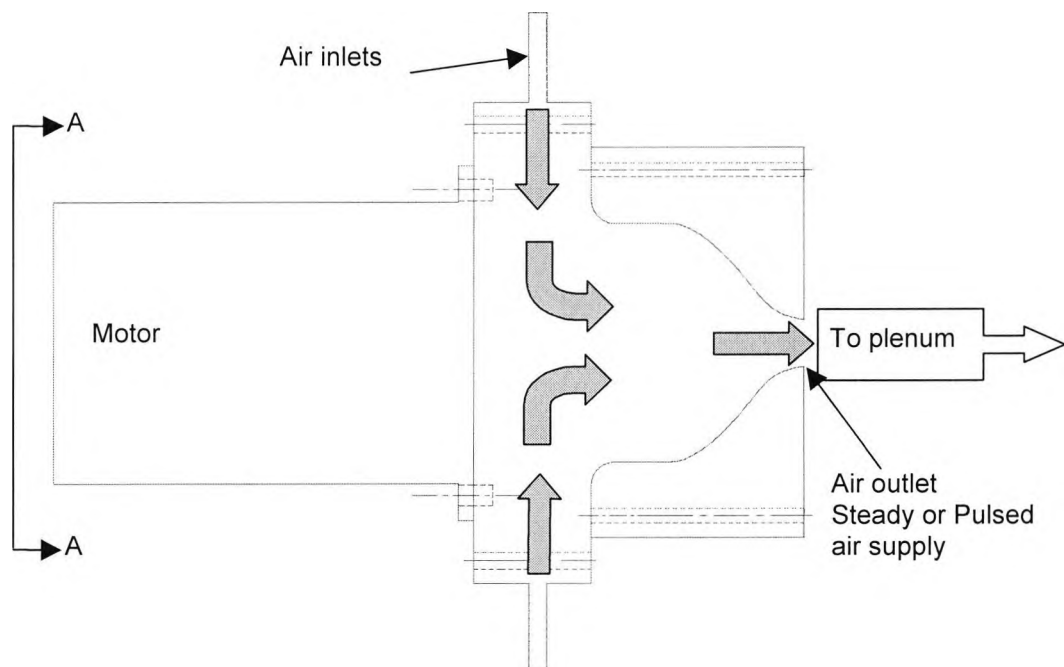


Figure 6.12: Side view schematic of the pulsing device

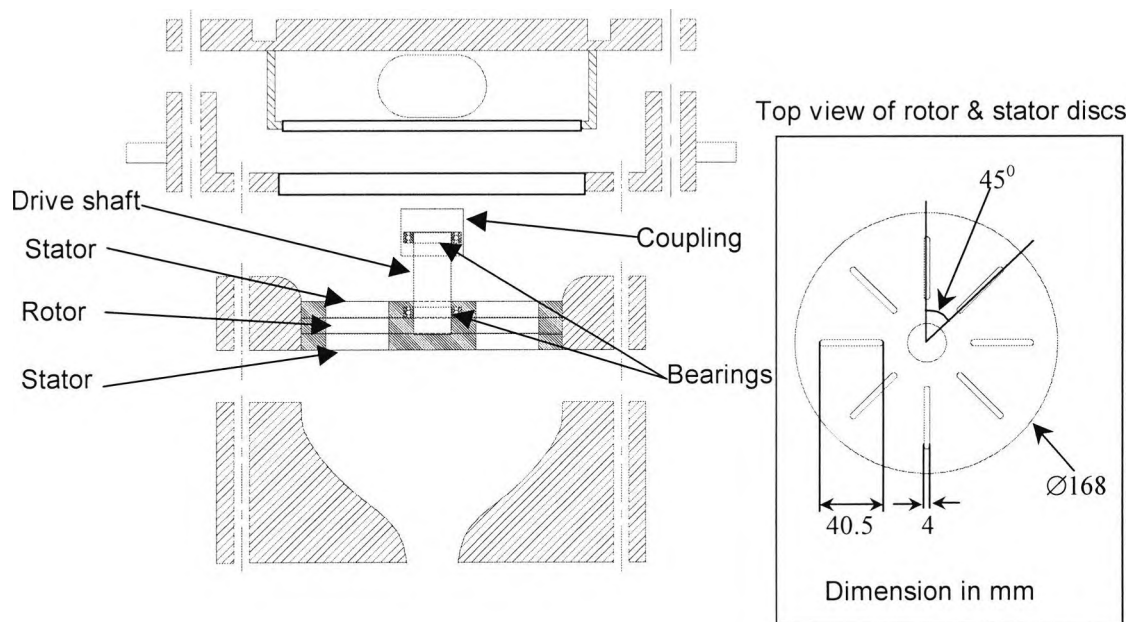


Figure 6.13: "Exploded" cross section (A – A) of the pulsing device

### 6.7 Measurement of nominal mass flow rate supply via BS orifice plate rig

The energy required to power the AJVG system in terms of added momentum is defined as the steady and pulsed AJVG blowing momentum coefficient,  $C_\mu$  and  $\langle C_\mu \rangle$ , emerging from the aerofoil surface:

$$C_\mu = \frac{\dot{m} U_j}{\frac{1}{2} \rho U_\infty^2 S}$$

$$\langle C_\mu \rangle = \frac{\dot{m} \langle U_j \rangle}{\frac{1}{2} \rho U_\infty^2 S}$$

where:

$\dot{m}$  = total mass flow rate through the AJVG system (kg/s)

$U_j, \langle U_j \rangle$  = mean and RMS fluctuating jet exit velocity (m/s)

Hence, the total blowing momentum coefficient can be formulated as  $C_{\mu total} = [C_{\mu} + \langle C_{\mu} \rangle]$  as suggested by Seifert et al (1993). The steady and fluctuating component of the jet exit velocity is deduced by re-arranging Bernoulli's equation:

$$U_j^2 = \frac{(p_T - p_s)}{\frac{1}{2}\rho_j} \text{ and } \langle U_j^2 \rangle = \frac{(\langle p_T \rangle - \langle p_s \rangle)}{\frac{1}{2}\langle \rho_j \rangle}$$

$$\rho_j = \frac{\dot{m}}{A_j U_j} \text{ and } \langle \rho_j \rangle = \frac{\dot{m}}{A_j \langle U_j \rangle}$$

where:

$p_T, \langle p_T \rangle$  = mean and RMS fluctuating AJVG total pressure (N/m<sup>2</sup>)

$p_s, \langle p_s \rangle$  = mean and RMS fluctuating AJVG static pressure (N/m<sup>2</sup>)

$\rho_j, \langle \rho_j \rangle$  = mean and RMS fluctuating AJVG density (N/m<sup>3</sup>)

$A_j$  = total jet exit area (m<sup>2</sup>)

The 'effective' drag of the NACA 23012C with AJVG operating is then deduced by expressing it as the sum of the measured wake profile drag  $C_{De} = C_{Dp} + C_{\mu total}$ , which in turn would provide an idea of the energy required to power the AJVG system.

The mass flow rate through the AJVG system was measured using an orifice plate in the supply pipeline. The device was manufactured and installed in accordance with BS ISO 5167(1). The technique uses an iterative method that yields a value for  $C_{\mu}$  accurate to within  $\pm 3\%$ . Readings were taken of the static pressure upstream of the orifice plate, the static pressure drop across the plate and the total temperature in the blowing supply line. The discharge coefficient,  $C_D$ , for the plate is given by Stolz's equation:

$$C_D = 0.5959 + 0.0312\beta^{2.1} - 0.184\beta^8 + 0.0029\beta^{2.5} \left( \frac{10}{Re} \right) + \frac{0.09L_1\beta^4}{(1-\beta^4)} - 0.0337L_2\beta^3$$

where:

$\beta$  = ratio of the orifice diameter to the pipe diameter

$L_1$  = the quotient of the distance of the upstream tapping from the upstream face of the plate and the pipe diameter (= 1)

$L_2$  = the quotient of the distance of the downstream tapping from the downstream face of the plate and the pipe diameter (= 0.47)

The mass flow rate is then deduced using the following expression:

$$\dot{m} = \frac{C_D}{\sqrt{(1-\beta^4)}} \varepsilon \frac{\pi}{4} d^2 \sqrt{2\Delta p \rho_1}$$

where:

$d$  = internal pipe diameter upstream of the orifice plate (=0.072m)

$\varepsilon = 1 - (0.41 + 0.35\beta^4)\Delta p / \kappa p_1$

$\kappa$  = pipe relative roughness (= 0.075)

$p_1$  = pressure upstream of orifice plate (N/m<sup>2</sup>)

$\rho_1$  = density upstream of orifice plate (kg/m<sup>3</sup>)

$\Delta p$  = pressure drop across the orifice plate (N/m<sup>2</sup>)

For the pulsed AJVG experiments a common expression of the blowing momentum coefficient representing both steady and unsteady jets is given in the form of [ $C_{\mu S/US} =$  (Mean steady level, RMS unsteady level),  $F^+$ ] or [ $C_{\mu S/US} = (C_{\mu}, <C_{\mu}>)\%$ ,  $F^+$ ]. For these experiments the oscillatory blowing is superimposed on the steady blowing level. A pure oscillatory blowing could not be achieved due to the limitations of the pulsing device.

## 7. Results and Discussion – Pulsed Blowing Experiment

### 7.1 Introduction

To recap, the tendency of the helicopter retreating blade to experience dynamic stall limits the helicopter flight envelope and vehicle utility. Dynamic stall is characterised by the formation of a dynamic stall vortex in the leading edge region, which propagate over the aerofoil upper surface and eventually sheds at the trailing edge. The movement of the stall vortex as it migrates and sheds from the aerofoil trailing edge contributes to large lift and moment overshoots in excess of static values, and leads to significant non-linear hysteresis in the aerofoil force and moment behaviour. In Chapter 4 it has been demonstrated that employing steady, low momentum blowing AJVGs ( $C_{\mu} \leq 0.01$ ) successfully controlled or eliminated the dynamic stall vortex on an unswept RAE 9645 aerofoil oscillating at  $\alpha = (15 + 10 \sin \omega t)$  deg, for the reduced oscillation frequency,  $k$ , of 0.05 and 0.1.

The rotor blade undergoes wide variations in sweep angle as it travels around the azimuth of the rotor disk and Figure 5.2 (see Chapter 5) shows that the blade sweep angle is  $15^{\circ}$  or more for at least 60% of the rotor disk plane [see Leishmann (1989)]. Because the retreating rotor blade is only instantaneously unswept at the azimuth angle  $\Psi = 270^{\circ}$ , the effect of sweep becomes an important criterion when deciding the AJVG geometric configuration required to control the dynamic stall process. In Chapter 5 quasi-steady tests carried out on a  $35^{\circ}$  swept-back wing showed that a spanwise array of AJVGs operated continuously at low blowing momentum coefficients of  $C_{\mu} < 0.01$ , with the jet efflux directed towards the wing root, successfully suppressed three-dimensional quasi-steady separation.

McManus et al (1994) and Seifert et al (1996) have experimentally demonstrated the effectiveness of utilising either unsteady AJVGs or tangential wall jets to reduce the steady-state blowing mass flow required for effective separation control by up to 50%. The potential of utilising unsteady AJVGs to reduce the blowing mass flux requirements of steady AJVGs has led to a pilot study at City University assessing the effectiveness of steady and unsteady AJVGs, in terms of the induced lift obtained per unit mass flux.

The quasi-steady tests of the unsteady AJVGs were conducted on the unswept NACA 23012C aerofoil, where Lewington et al (2000) have demonstrated that steady AJVGs utilising low amount of blowing ( $C_{\mu} = 0.01$ ) successfully delayed the onset of stall by about  $6^{\circ}$ , whilst generating a  $C_{N_{\max}}$  25% above that of the unblown aerofoil.

## 7.2 Preliminary unblown NACA 23012C aerofoil surface pressure investigation

Initial tests of the unblown aerofoil chordwise surface pressure distribution for the angle of attack range of  $6^{\circ} \leq \alpha \leq 21^{\circ}$  showed the presence of a “hump” in the vicinity of the leading edge (see Figure 7.1). It was postulated that the “hump” indicates the presence of a laminar separation bubble. The bubble formed seems to be of very small chordwise extent and its existence does not significantly affect the forces and moments on the aerofoil [see Küchemann (1953)]. The occurrence of this “hump” on the surface pressure distribution was not pursued further because it does not affect the overall aerofoil aerodynamic performance within the  $\alpha$  range investigated.

## 7.3 Spanwise surface pressure variation

A quick check into the spanwise variation of chordwise surface pressure distributions was conducted by monitoring the pressure distribution at 26%, 52% and 62% of the model span. Figure 7.2 shows the normal force coefficients, obtained from integrating the chordwise pressure distributions, at the three spanwise locations for the unblown aerofoil. Corresponding with the observations of Lewington et al (2000), there is good comparability of the normal force-curve slopes at all three stations prior to stall, indicating that a nominally two-dimensional flow across the span was reasonably maintained. After stall, the flow is obviously three-dimensional contributing to the spanwise variance in the normal force coefficients. The following results and discussions are based on the chordwise surface pressure distribution measured at the 52% span.

## 7.4 Steady and Unsteady AJVG tests

### Mechanisms of turbulent boundary-layer separation control

The mechanism of blowing continuously through discrete, yawed jets to forestall flow separation is well documented [see Johnston and Nishi (1990), Henry and Pearcey (1994), and Küpper and Henry (2001)]. The interaction between the airjets exiting a slot/hole on an aerodynamic surface and the freestream flow forms longitudinal streamwise vortices that promote mixing between high-speed flow from the freestream with the lower-speed flow in the boundary layer. Through this mixing action, the retarded boundary layer adjacent to the (aerofoil) surface is re-energised enabling it to withstand especially severe adverse pressure gradients as the AJVGs penetrate downstream. This in turn delays separation, increases maximum lift and extends the useful angle-of-attack range as demonstrated by Selby et al (1992), Innes (1995), Oliver (1997) and Lewington (2000).

On the other hand, Seifert et al (1993) and McManus et al (1996) envisaged that the underlying principle of unsteady blowing, either by tangential wall jets or AJVGs, to delay separation is to accelerate and regulate the generation of large coherent structures in the shear layer. These coherent structures are effective in transporting momentum across the shear layer from the freestream to the surface enabling the flow to withstand especially severe adverse pressure gradients without separating. Narayanan and Banaszuk (2003) have demonstrated that unsteady forcing creates large, energetic vortices that transports (via entrainment) high momentum flow from the high speed core flow to the region closer to the lower wall of a planar diffuser. This is schematically displayed in Figure 7.3, where an inflectional velocity profile at the diffuser inlet is shown to evolve into a more stable channel flow-like mean velocity profile at the diffuser exit.

Various techniques have been successfully used for generating and/or controlling the large eddies in turbulent boundary layers. Viets et al (1981) used an asymmetrical rotating cam embedded in the wall to produce large eddies with zero and adverse-pressure gradients. By using this device in a wide-angle diffuser, they were able to reduce the separation region and improve the diffuser's performance. Alternatively, thin

ribbons could be placed in the boundary layer to act as large-eddy breakup devices. Bushnell (1983) and Anders and Watson (1985) have shown that, at zero angle of attack, two thin ribbons, one placed above a flat plate and one parallel to it, lead to a reduction in the skin friction of the boundary layer. Oscillating these devices could produce a series of large and smaller eddies in the boundary layer. However, it is felt that the pulsating jet, such as that utilised by Seifert et al (1993) and McManus et al (1996), has greater practical advantage because it is easier to control and has no external moving parts. In addition, by properly synchronising the jet's amplitude, angle and acceleration, a greater degree of controllability would appear to be achievable with the proposed jet [see Gad-el-Hak and Blackwelder (1985), McManus et al (1994) and Amitay and Glezer (2002)].

#### Surface pressure and wake profile distributions

Wu et al (1997) has suggested that the shear layer must be well developed and *free* to be modulated by the periodic addition of momentum, such as when  $\alpha > \alpha_{stall}$ , for effective momentum transport across the shear layer. For angles of attack prior (and near) to  $\alpha_{stall}$ , the shear layer is too close to the aerofoil surface and, hence, reduces its ability of being modulated by unsteady blowing to effectively transport momentum across the shear layer. The sensitivity of the chordwise surface static pressures, for the unblown NACA 23012C, to angle of attack, for  $\alpha \geq \alpha_{stall}$ , is shown in Figure 7.4. At the stall angle of attack,  $\alpha_{stall} = 15^\circ$ , the boundary layer is separated over the rear 40% chord of the aerofoil upper surface with pressure loss at the trailing edge. As the angle of incidence is increased to  $\alpha = 18^\circ$ , boundary-layer separation moves upstream to approximately  $x/c = 0.40$ , where now the trailing-edge pressure coefficient ( $C_{P_{te}}$ ) becomes more negative. Increasing the angle of incidence further moves the separation point upstream towards the aerofoil leading edge and thus increases the region of boundary-layer separation on the aerofoil. At  $\alpha = 20^\circ$ , boundary-layer separation encompasses almost the entire aerofoil upper surface, with the separation point located at about  $x/c = 0.15$ . The region of boundary-layer separation is indicated by the plateau in the upper surface static pressure, which is due to the low, nearly constant velocity in the separated flow region adjacent to the aerofoil upper surface (dead-air region). For example at  $\alpha = 20^\circ$  a

plateau in the surface static pressure is observed from about 15% chord up to the trailing edge on the aerofoil upper surface (see Figure 7.3).

The trailing-edge separation progresses upstream towards the aerofoil leading edge with increasing angle of attack, as a consequence of the increased adverse pressure gradient over the rear of the aerofoil section. In the simplified sketch of Figure 7.5, it is imagined that a free boundary springs from the top surface of the aerofoil at the point of separation. This separates a dead-air region adjacent to the aerofoil surface from the freestream flow. The dead-air or shear-layer region grows in size as boundary-layer separation moves upstream, which in turn results in the increase of the total pressure loss (or momentum defect) across the wake downstream of the aerofoil trailing edge, i.e. size of the wake increases (see Figure 7.5). Figure 7.6 shows the wake profile distributions for the unblown NACA 23012C, measured one chord length downstream of the NACA 23012C aerofoil trailing edge, with increasing angle of attack, at  $\alpha \geq \alpha_{stall}$ . This figure shows that the size of the wake profile distributions for the unblown aerofoil increase with increasing angle of attack suggesting the growth of the shear layer region. Based on the surface static pressure and wake profile distributions of the unblown NACA 23012C as well as the illustration of Figure 7.5, it is hypothesised that the shear layer region for the unblown aerofoil at  $\alpha \geq 18^\circ$  is sufficiently well developed to be modulated by the introduction of unsteady blowing as suggested by Wu et al (1997).

Figures 7.7 to 7.9 show the effect of utilising an array of AJVGs located at 12% chord either continuously or intermittently on the aerofoil chordwise surface pressure and wake profile distributions for  $\alpha = 18^\circ$ . Operating the AJVGs continuously at  $C_\mu = 0.0027$  successfully reattaches the separated flow, where the steady blowing performance improvements over that of the unblown aerofoil, as shown in Figures 7.7 to 7.9, highlights:

- i) The increased suction pressure over upper surface of the aerofoil.
- ii) The considerable improvement in leading-edge peak suction.
- iii) The significant reduction of the momentum defect across the wake traverse, i.e. reduction of wake size.

Pulsing the AJVGs at  $F^+ = 0.7$  or  $F^+ = 1.3$  whilst maintaining the mean steady blowing at  $C_\mu = 0.0027$  showed that there is virtually no change in the surface pressures, leading-

edge peak suction and wake profile distributions when compared with steady AJVGs at  $C_{\mu} = 0.0027$  (see Figures 7.7 to 7.9).

At  $\alpha = 20^{\circ}$ , it can be seen that blowing steadily at  $C_{\mu} = 0.0027$  failed to exert any control over the stalled flow (most probably) due to its inability to generate longitudinal streamwise vortices capable of withstanding the especially severe adverse pressure gradients at this angle of incidence, as they penetrate downstream (see Figures 7.10 to 7.12). Conversely, the superposition of steady blowing on the imposed oscillations resulted in a considerable recovery of the stalled flow. Figure 7.10 demonstrates that operating the AJVGs at the dimensionless pulsing frequencies,  $F^{+}$ , of 0.7 and 1.3 enhances suction pressure on the aerofoil surface as well as impels boundary-layer separation downstream from  $x/c \approx 0.15$  to  $x/c \approx 0.75$ . The effectiveness of unsteady AJVGs at  $F^{+} = 0.7$  and  $F^{+} = 1.3$  is further highlighted by the increase of the leading-edge suction pressure and decrease of the size and turbulence in the wake (see Figures 7.11 and 7.12).

Increasing the pulsing frequency to  $F^{+} = 2.0$  diminishes the benefit attained when pulsing the AJVGs at either  $F^{+} = 0.7$  or  $F^{+} = 1.3$  and separation has once again leapt forward from  $x/c \approx 0.75$  to  $x/c \approx 0.45$ . This is accompanied by the collapse of the leading-edge suction pressure and the increase of the momentum defect across the wake traverse (see Figures 7.10 to 7.12). The failure of the pulsed AJVGs operating at  $F^{+} = 2.0$  is most probably due to the dissipation of the imposed oscillations before reaching the locality of separation [see Nishri and Wygnanski (1998)].

Figures 7.13 to 7.15 show that the stalled flow at  $\alpha = 20^{\circ}$  can only be mitigated by steady AJVGs when the amount of blowing is increased from  $C_{\mu} = 0.0027$  to  $C_{\mu} = 0.004$ . The longitudinal streamwise vortices generated, with steady blowing increased to  $C_{\mu} = 0.004$ , re-energise the retarded boundary layer enabling it to negotiate the severe adverse pressure gradient as the AJVGs penetrate downstream. As a result, a significant portion of the separated boundary layer is reattached contributing to (a), the increase of suction pressure over the upper surface of the aerofoil; (b), the downstream movement of the separation point, i.e. from  $x/c \approx 0.15$  to  $x/c \approx 0.71$ ; and (c), the decrease of momentum defect across the wake traverse.

The superposition of pulsing on steady blowing provides an effective means of turbulent boundary-layer separation control, where operating the AJVGs intermittently at either  $[C_{\mu S/US} = (0.0026, 0.0009, F^+ = 0.7)]$  or  $[C_{\mu S/US} = (0.0026, 0.0005, F^+ = 1.3)]$  re-establishes the aerofoil performance to the equivalent status of control achieved when operating the AJVGs steadily at  $C_{\mu} = 0.004$  for  $\alpha > \alpha_{stall}$ .

### Performance characteristics of the NACA 23012C aerofoil section

Figures 7.16 to 7.18 show the effect of operating the spanwise array of AJVGs located at 12% chord either continuously or intermittently on the normal force, wake profile drag and quarter-chord pitching moment performance. Throughout the angle of attack range up to stall, the addition of momentum either steady or pulsed neither increases nor decreases the normal force, wake profile drag and quarter-chord pitching moment coefficients of the aerofoil. Only when the aerofoil passes the stall angle of attack does the effect of employing steady and unsteady AJVGs yield substantial improvements in the aerodynamic performance of the aerofoil. The steady or periodic addition of momentum by the spanwise array of AJVGs re-energises the boundary layer adjacent to the aerofoil surface. This results in the suppression of boundary-layer separation on the top surface of the aerofoil and, hence, an increase in suction pressure as well as a reduced momentum deficit across the wake.

Examination of the normal force-curve (see Figure 7.16) shows that with the AJVGs operating steadily at  $C_{\mu} = 0.0027$  the maximum normal force,  $C_{Nmax}$ , is increased by about 40% and stall angle of attack,  $\alpha_{stall}$ , delayed by about  $3^{\circ}$  to  $\alpha_{stall} = 18^{\circ}$ . Increasing steady blowing to  $C_{\mu} = 0.004$  further delays the stall angle of attack by another  $2^{\circ}$ , to  $\alpha_{stall} \approx 20^{\circ}$ , but without significant further improvement in  $C_{Nmax}$ . By comparison, pulsing the AJVGs at either  $F^+ = 0.7$  or  $F^+ = 1.3$  at the mean steady blowing rate of  $C_{\mu} = 0.0027$ , is sufficient to delay the stall angle of attack to  $\alpha_{stall} = 20^{\circ}$ .

The effects of employing steady and unsteady AJVGs on the wake profile drag coefficients, measured at one chord length downstream of the aerofoil are shown in Figure 7.17. The intersection of two gradients of the wake profile drag coefficient curve is known as *drag-rise* as shown in Figure 7.17. Operating the spanwise array of AJVGs

continuously at  $C_{\mu} = 0.0027$  delays the drag divergence of the unblown aerofoil by about  $4^{\circ}$  to  $\alpha \approx 18^{\circ}$ . Increasing the amount of steady blowing to  $C_{\mu} = 0.004$  further delays the drag divergence by another  $2^{\circ}$  to  $\alpha \approx 20^{\circ}$ . Similar efficiency in delaying drag divergence by steady AJVGs operating at  $C_{\mu} = 0.004$  was obtained when the spanwise array of AJVGs were operated intermittently. Figure 7.18 shows that oscillatory blowing at either  $[C_{\mu S/US} = (0.0026, 0.0009, F^{+} = 0.7)]$  or  $[C_{\mu S/US} = (0.0026, 0.0005, F^{+} = 1.3)]$  delays the drag divergence till  $\alpha \approx 20^{\circ}$ .

The stability of the aerofoil in terms of pitching moment at the quarter-chord is highlighted by the ability of the steady and unsteady AJVGs to delay pitching moment break (see Figure 7.18). For the unblown aerofoil, the pitching moment break occurs at  $\alpha \approx 15^{\circ}$  and it is delayed by about  $3^{\circ}$  to  $\alpha \approx 18^{\circ}$  with AJVGs operating at  $C_{\mu} = 0.0027$ . Increasing the amount of steady blowing to  $C_{\mu} = 0.004$  further delays the pitching moment break by another  $2^{\circ}$  to  $\alpha \approx 20^{\circ}$ . The effectiveness of unsteady AJVGs operating at either  $[C_{\mu S/US} = (0.0026, 0.0009, F^{+} = 0.7)]$  or  $[C_{\mu S/US} = (0.0026, 0.0005, F^{+} = 1.3)]$  compared to steady AJVGs operating at  $C_{\mu} = 0.0027$ , is once again observed with the delay of the pitching moment break by about  $5^{\circ}$  to  $\alpha \approx 20^{\circ}$ .

Figure 7.19 offers a comprehensive view of the effectiveness of the AJVG to enhance the NACA 23012C aerofoil performance relative to the momentum requirements of the flow control system, especially at angles of attack beyond stall. Accounting for the incremental normal force,  $DC_N$ , per unit  $C_{\mu}$  of the flow control devices, it is apparent that for angles of attack up to  $\alpha = 18^{\circ}$ , it is desirable to utilise AJVGs operating intermittently at  $[C_{\mu S/US} = (0.0026, 0.0001, F^{+} = 2.0)]$  after which the pulsing frequency should be reduced to  $[C_{\mu S/US} = (0.0026, 0.0005, F^{+} = 1.3)]$ .

Plotting the incremental normal force  $[DC_N = |C_{N(\text{blown})} - C_{N(\text{unblown})}|]$  variation with the total blowing momentum coefficient  $[C_{\mu \text{total}} = (C_{\mu} + \langle C_{\mu} \rangle)]$  demonstrates the saving of the mass flux (and ensuing momentum) requirements for a given normal force increment (see Figure 7.20). An increment of 0.5 in the normal force would require operating the AJVGs continuously at  $C_{\mu \text{total}} \approx 0.0041$  but when the AJVG were made unsteady at  $F^{+} = 1.3$  the total blowing momentum coefficient required is only about 0.0031, a saving of approximately 25%.

Of interest is the characterisation of the length,  $L$ , used to define the dimensionless pulsing frequency,  $F^+ \left( = \frac{fL}{U_\infty} \right)$ . Initially the definition of the dimensionless pulsing frequency, as suggested by Seifert et al (1996), contains a variable length scale corresponding to the length of the naturally separated flow region over the aerofoil. For a given dimensionless pulsing frequency say,  $F^+ = 1.0$ , the (dominant) pulsing frequency,  $f$ , has to be decreased as the length of the boundary-layer separation increases with increasing angle of attack (see Figure 7.21). This length scale was considered “tedious” because the pulsing frequency has to be varied continuously with the length of the separated flow region as the angle of attack is increased beyond  $\alpha \approx 12^\circ$  as illustrated in Figure 7.21. Defining the onset of trailing-edge separation as when the trailing-edge pressure coefficient,  $C_{pte}$ , goes from a positive value to zero, Figure 7.1 shows that for the unblown NACA 23012C aerofoil  $C_{pte} = 0$  at about  $\alpha = 12^\circ$ . Alternatively, the length scale could be based on the distance between the actuator and the aerofoil trailing edge that would fix  $F^+$  over the angle of attack range tested. For the unsteady AJVG tests, the dimensionless pulsing frequency is, therefore, based on the convenient distance between the AJVG exit and the aerofoil trailing edge.

### Surface and wake pressure fluctuations

The installation of the dynamic pressure transducers into the surface of the aerofoil section and into the wake rake array allows for the measurement of pressure fluctuations along the chord of the aerofoil surface and across the wake traverse. This is an important aspect of flow control because the change of pressure character, such as minimising the amplitude of pressure fluctuations by means of steady or unsteady blowing, may have a potential benefit for buffet control [see Mabey (1972)]. The variation of pressure fluctuations along the chord of the aerofoil surface and across the wake traverse with and without AJVGs operating (either continuously or intermittently) were studied for the angles of attack beyond stall,  $\alpha > 15^\circ$  (see Figures 7.22 to 7.25). One important observation is that the pressure fluctuations on the top surface of the aerofoil is almost parallel with no (significant) peak frequency and that the amplitude of

fluctuation,  $\langle C_p \rangle$ , increases or decreases with angle-of-attack and whether blowing (either steady or unsteady) is utilised.

Figure 7.4 shows that at  $\alpha = 18^\circ$ , the uncontrolled boundary layer separates from the aerofoil upper surface at  $x/c \approx 0.22$  because it is unable to withstand the especially severe adverse pressure gradient over the rear of the aerofoil section. This separated boundary layer or shear layer contains large-scale turbulent structures that contribute to the high-level pressure fluctuations observed along the chord of the aerofoil upper surface (see Figure 7.22). The shedding of these turbulent structures into the wake downstream of the aerofoil trailing edge results in the subsequent increase of pressure fluctuations across the wake traverse (see Figure 7.23). Employing either steady or unsteady AJVGs enables the transfer of high momentum fluid from the freestream flow to the lower momentum fluid adjacent to the aerofoil upper surface. The increased momentum transfer across the shear layer re-energises the retarded boundary layer on the top surface of the aerofoil enabling it to negotiate the especially severe adverse pressure gradient as the AJVGs penetrate downstream. As a result, boundary-layer separation on the aerofoil surface is delayed and the momentum defect across the wake traverse is reduced. The attached (and relatively thin) controlled boundary layer contains small-scale turbulent structures that contribute to the low-level pressure fluctuations observed along the chord on the aerofoil surface and across the wake traverse (see Figures 7.22 and 7.23).

Increasing the angle of attack to  $\alpha = 20^\circ$  results in a complete separation of the boundary layer on the aerofoil upper surface downstream of  $x/c \approx 0.15$ , as well as an increased momentum defect across the wake traverse. However, Figure 7.24 shows that the level of pressure fluctuations along the chord of the aerofoil surface at  $\alpha = 20^\circ$  is slightly lower than that at  $\alpha = 18^\circ$ . Some light may be shed on this phenomenon by the observations of Yon and Katz (1998), where they distinguished two regimes of stall, i.e. shallow stall and deep stall over a rectangular aerofoil. The shallow stall regime first appears  $2^\circ$  or  $3^\circ$  after the first indications of trailing-edge separation. In this regime “stall cells” is the predominant feature of the separated region on the aerofoil surface. The large amplitude (or high level) pressure fluctuations that occur on the aerofoil surface within the “stall cells” increase with angle of attack up stall. Increasing the angle of attack beyond stall takes the aerofoil into the deep stall regime resulting in the

loss of the “stall cells” and thus a reduction in the amplitude (or level) of surface pressure fluctuations. Figure 7.26 illustrates the variation of the surface pressure fluctuations at different chordwise positions downstream of the AJVG exit ( $0.2 < x/c \leq 1.0$ ) with increasing angle of attack. This figure shows the surface pressure fluctuations increases after the onset of trailing-edge separation, at  $\alpha \approx 12^\circ$ , and peaks at about  $\alpha = 18^\circ$ . Based on the observation of Yon and Katz (1998) it is hypothesised that the increase of the surface pressure fluctuations between  $12^\circ \leq \alpha \leq 18^\circ$  is due to the increasing amplitude of pressure fluctuations within the “stall cells”; and at  $\alpha > 18^\circ$ , the surface pressure fluctuations decrease due to the loss of the “stall cells”. Conversely, Figure 7.25 shows an increased level of pressure fluctuations across the wake traverse, especially at W3, compared with  $\alpha = 18^\circ$  indicating the continuing increase in the size of the wake (see also Figures 7.5 and 7.6).

Figures 7.24 and 7.25 show that installing a spanwise array of AJVGs at 12% chord and operating it continuously at  $C_\mu = 0.0027$  fails to exert any control over the stalled flow at  $\alpha = 20^\circ$ . This amount of steady blowing is seen to increase the pressure fluctuations along the chord on the aerofoil upper surface and across the wake traverse, especially at W2, when compared with the unblown aerofoil. Employing oscillatory blowing at either  $F^+ = 0.7$  or  $F^+ = 1.3$  at the mean steady blowing rate of  $C_\mu = 0.0027$  significantly reduce the level of pressure fluctuations on the aerofoil surface and across the wake traverse. Corresponding efficiency of steady blowing to reduce the level of pressures fluctuations on both the aerofoil surface and across the wake traverse is only achieved when the amount of blowing is increased from  $C_\mu = 0.0027$  to  $C_\mu = 0.004$ .

The analysis of the pressure fluctuations along the chord on the aerofoil surface and across the wake traverse, especially at  $\alpha = 20^\circ$ , further confirms the fact that operating the AJVGs intermittently at  $[C_{\mu S/US} = (0.0026, 0.0005, F^+ = 1.3)]$  re-establishes the aerofoil performance to the equivalent status of control achieved when blowing steadily at  $C_\mu = 0.004$  but with a saving in total blowing mass flow of about 25%.

## Summary of steady and unsteady AJVG tests on the NACA 23012C aerofoil under quasi-steady flow conditions

The above discussions detail the experimental results comparing the effect of operating an array of AJVGs located at 12% chord either continuously or intermittently on the aerodynamic performance of the NACA 23012C aerofoil. Experiments were conducted at City University's T2 low speed wind tunnel for the angle of attack range  $-6^{\circ} \leq \alpha < 22^{\circ}$  at a Reynolds number based on chord of  $Re_c = 1.1 \times 10^6$  and a freestream Mach number of  $M_{\infty} = 0.10$ . The blowing momentum coefficients and dimensionless pulsing frequencies employed was in the range of  $0.0 < C_{\mu} \leq 0.01$  and  $0.3 < F^+ \leq 2.0$  respectively.

The key findings from the investigation show that:

- i) Employing AJVGs either steady or unsteady resulted in significant aerodynamic performance enhancements for the NACA 23012C aerofoil at  $\alpha > 12^{\circ}$ .
- ii) The steady-state mass flow (and ensuing momentum) requirements can be reduced by up to 25% when operating the AJVGs periodically.
- iii) For a given mean steady blowing unsteady AJVGs is more effective in augmenting aerofoil aerodynamic performance for angles of attack beyond stall compared with steady AJVGs. Introducing steady blowing at  $C_{\mu} = 0.0027$  delays the stall angle of attack by about  $3^{\circ}$  to  $\alpha = 18^{\circ}$  and increases the pressure fluctuations along the chord of the aerofoil surface and across the wake traverse when compared with the unblown aerofoil. Whereas unsteady blowing at either  $[C_{\mu S/US} = (0.0026, 0.0009, F^+ = 0.7)]$  or  $[C_{\mu S/US} = (0.0026, 0.0005, F^+ = 1.3)]$  delays stall by about  $5^{\circ}$  to  $\alpha = 20^{\circ}$  and significantly reduces the pressure fluctuations on both the aerofoil surface and across the wake traverse.

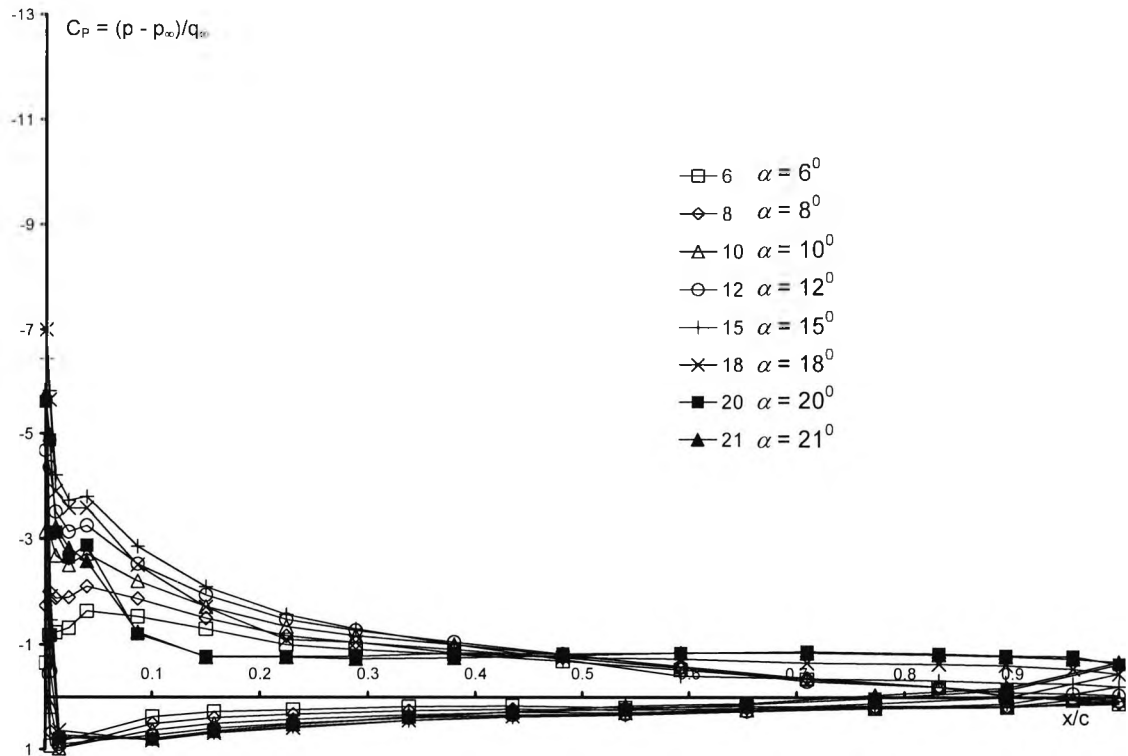


Figure 7.1: Sensitivity of chordwise surface pressure distributions to angle of attack for unblown NACA 23012C at  $Re_c = 1.1 \times 10^6$  and  $M_\infty = 0.10$

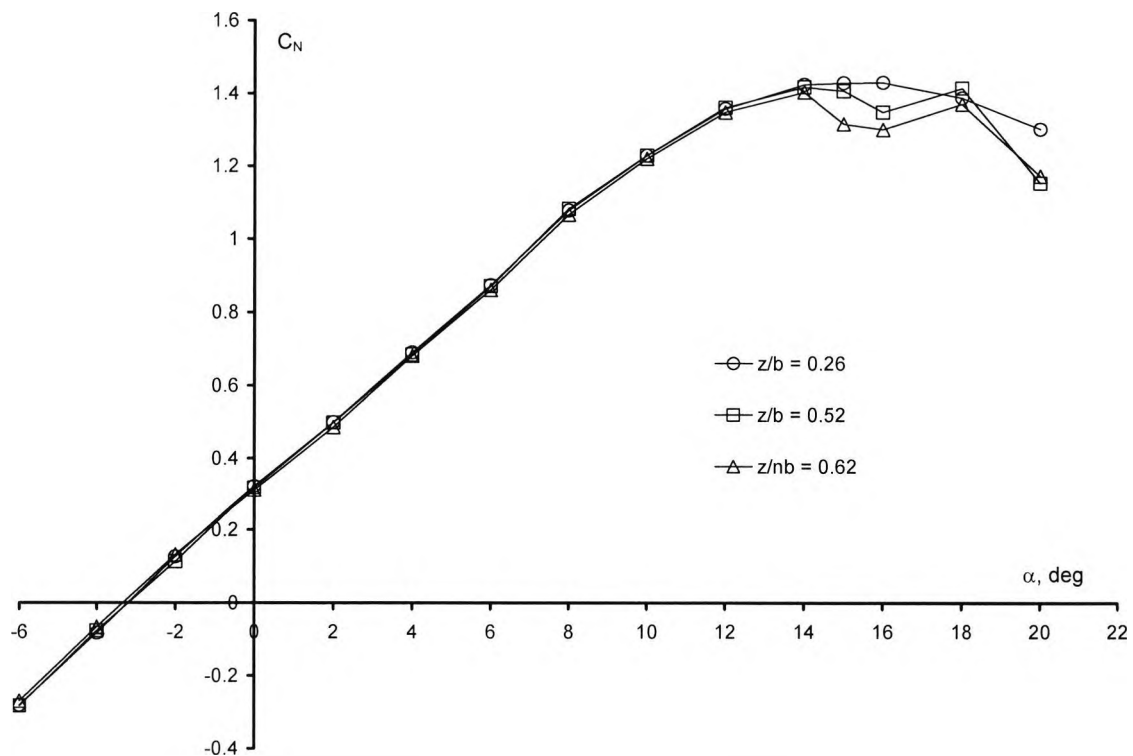


Figure 7.2: Spanwise variation of normal force coefficient with angle of attack for the unblown NACA 23012C at  $Re_c = 1.1 \times 10^6$  and  $M_\infty = 0.10$

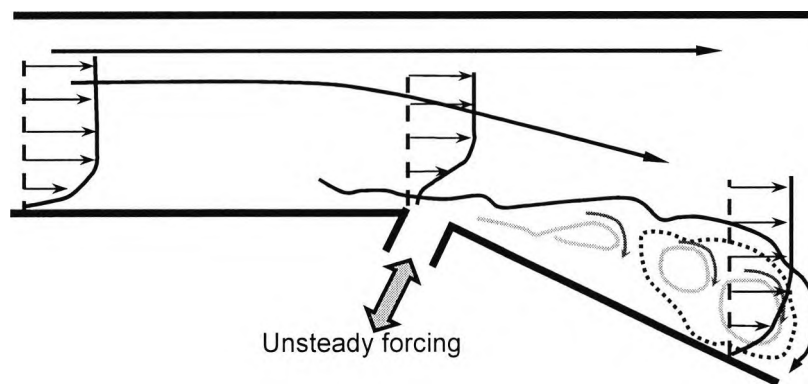


Figure 7.3: Schematic of the vortex dynamics in the diffuser subject to unsteady forcing [Narayanan and Banaszuk (2003)]

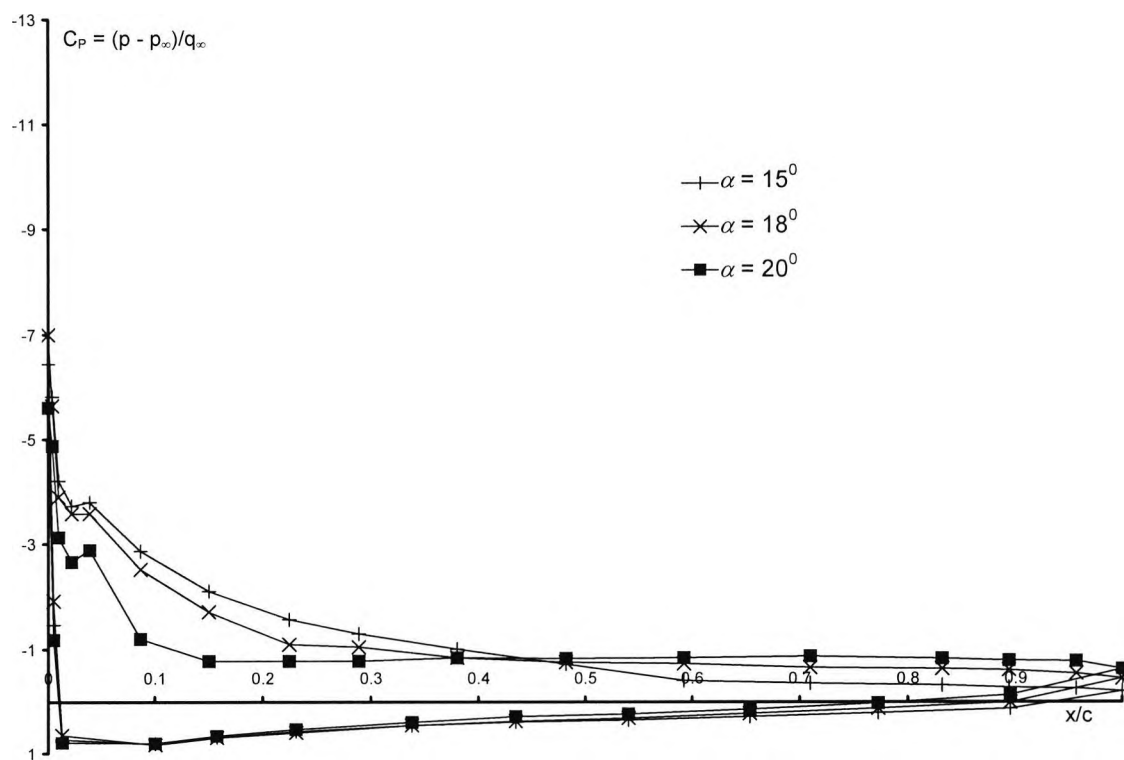


Figure 7.4: Sensitivity of chordwise surface pressure distributions to angle of attack for unblown NACA 23012C at  $Re_c = 1.1 \times 10^6$  and  $M_\infty = 0.10$

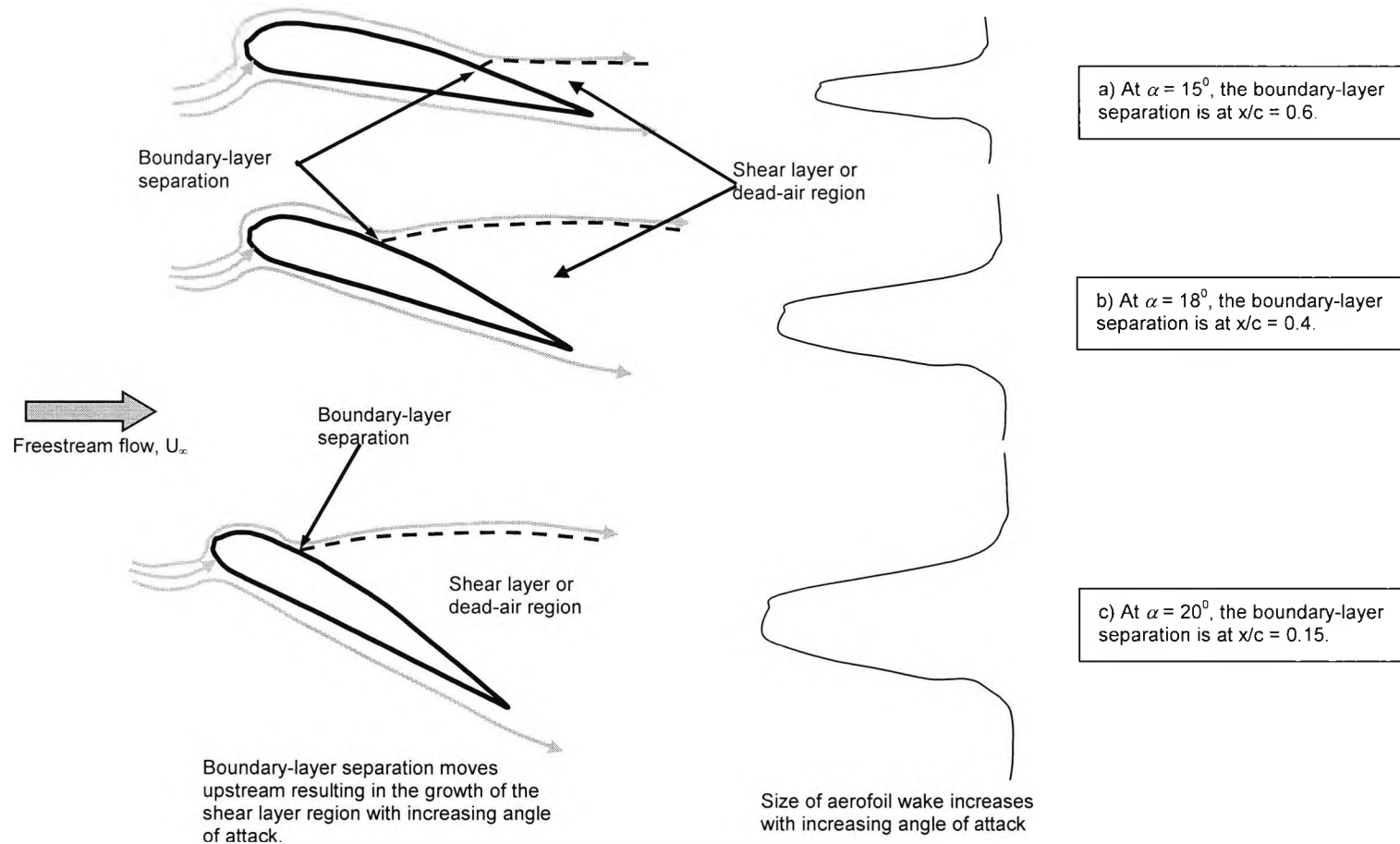


Figure 7.5: Illustration of rear boundary-layer separation, shear layer and wake profile growth with increasing angle of attack

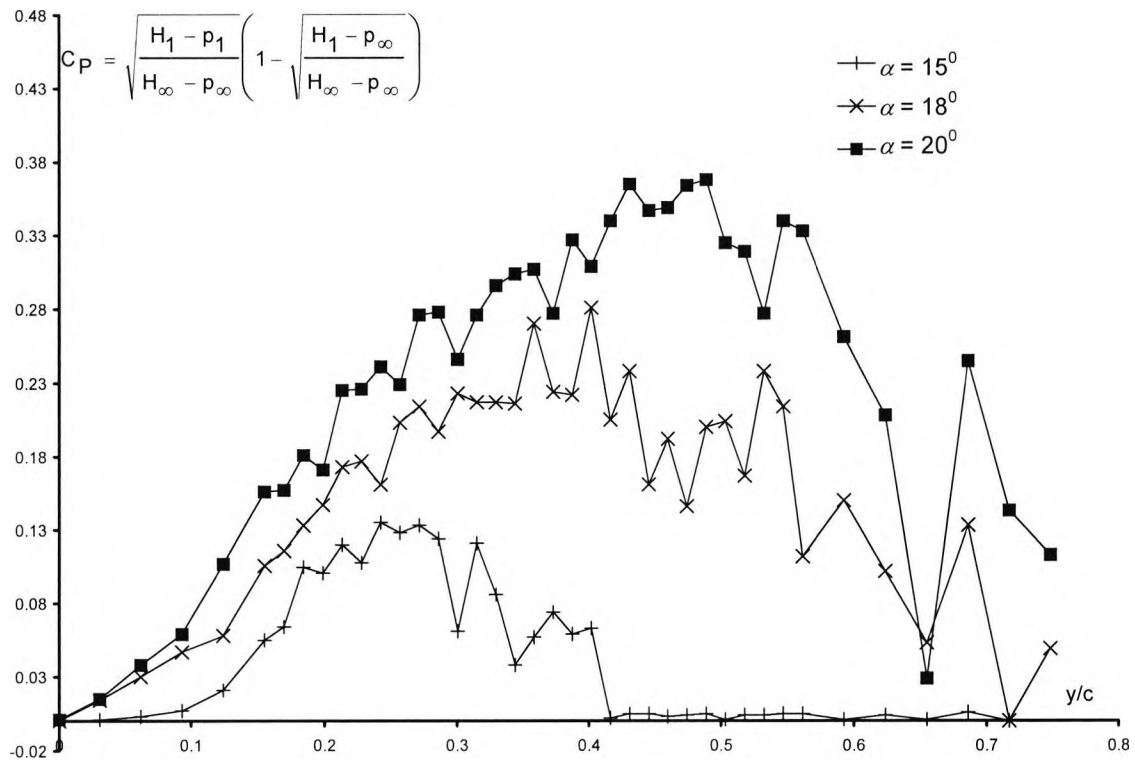


Figure 7.6: Wake profiles, measured one chord length downstream of the model trailing edge, for unblown NACA 23012C at  $Re_c = 1.1 \times 10^6$  and  $M_\infty = 0.10$

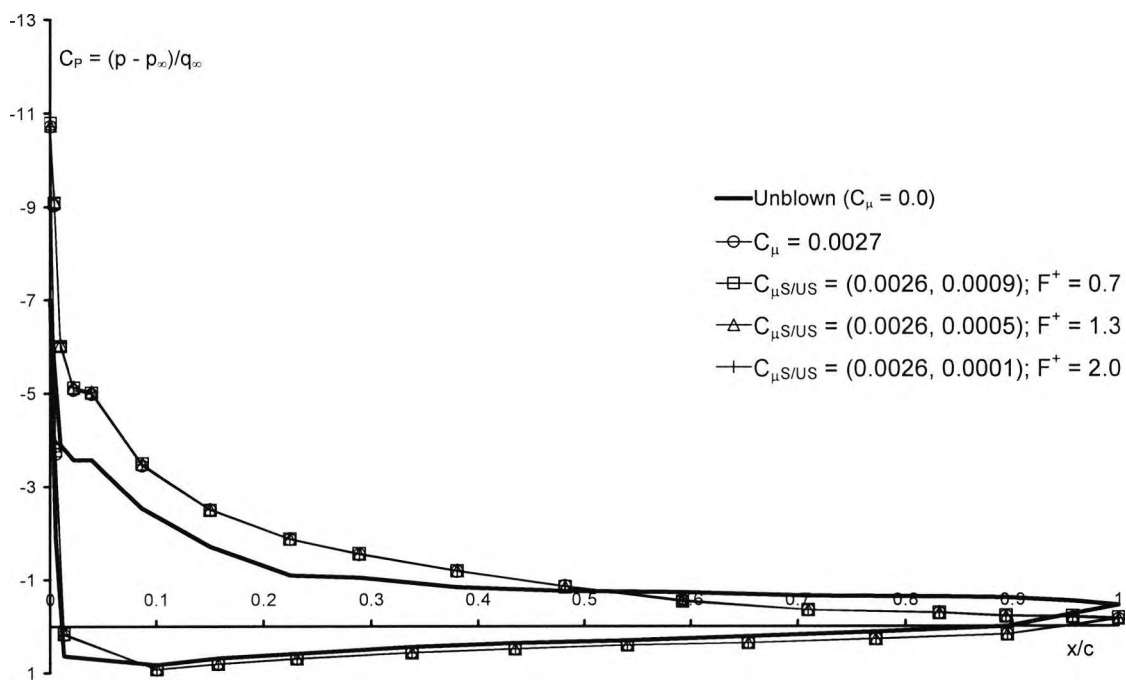


Figure 7.7: Sensitivity of chordwise surface pressure distributions to steady and pulsed AJVGs operating from  $x/c = 0.12$  for NACA 23012C at  $\alpha = 18^\circ$ ,  $Re_c = 1.1 \times 10^6$  and  $M_\infty = 0.10$

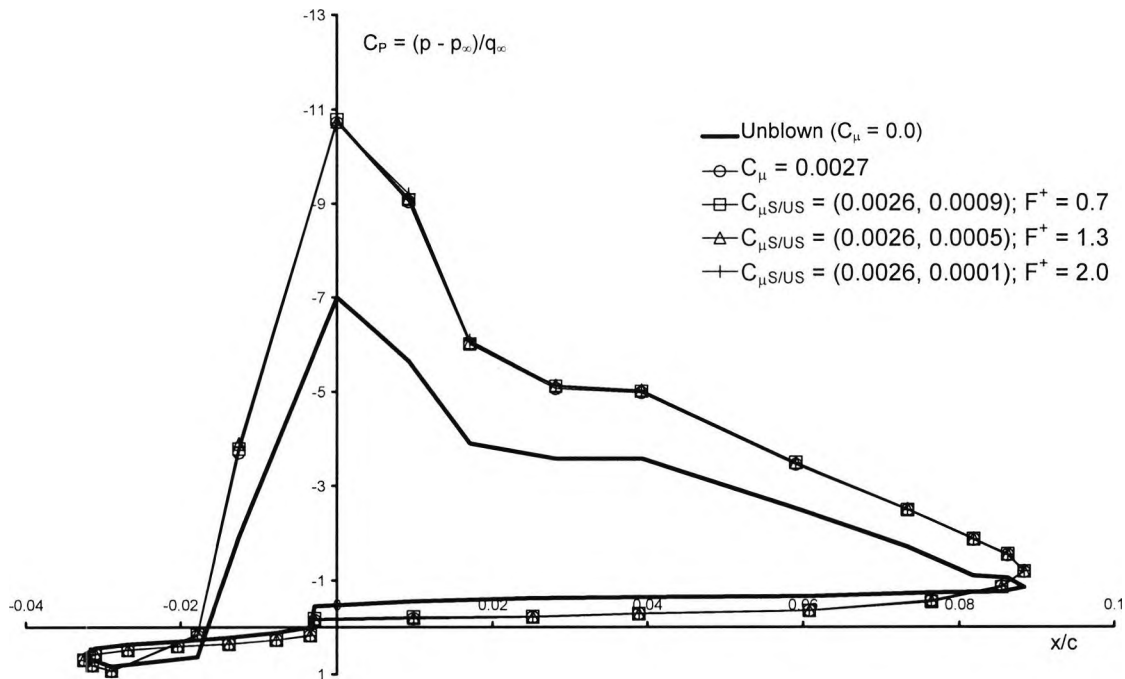


Figure 7.8: Sensitivity of leading edge suction to steady and pulsed AJVGs operating from  $x/c = 0.12$  for NACA 23012C at  $\alpha = 18^\circ$ ,  $Re_c = 1.1 \times 10^6$  and  $M_\infty = 0.10$

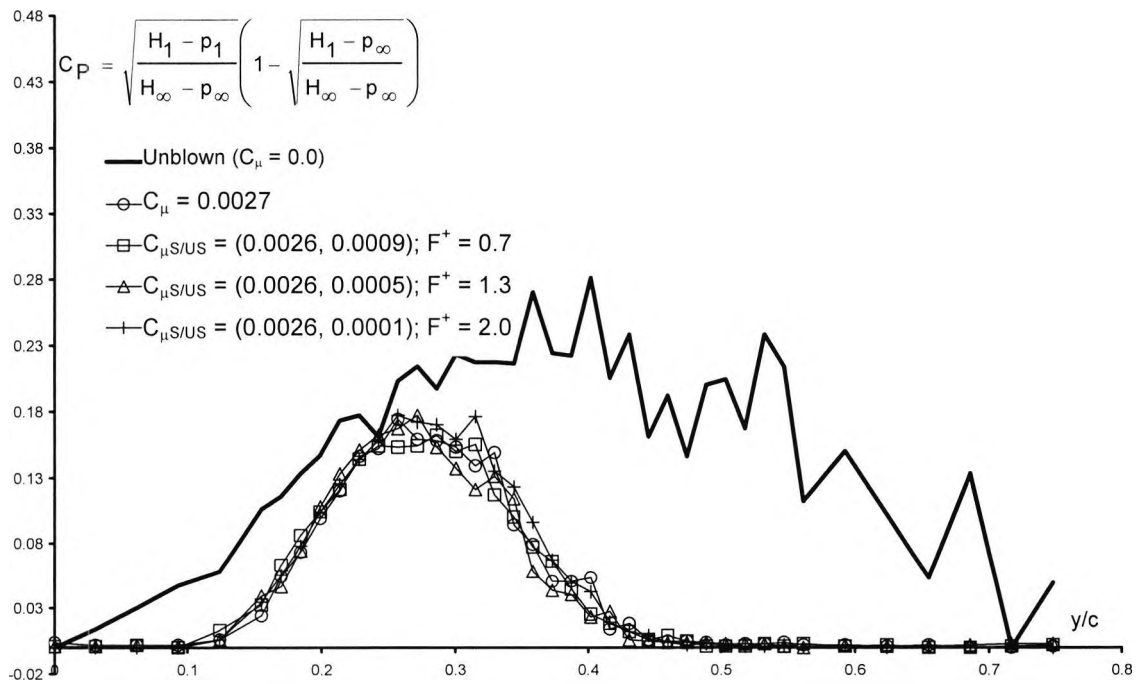


Figure 7.9: Wake profiles, measured one chord length downstream of the model trailing edge, with steady and pulsed AJVGs operating from  $x/c = 0.12$  for NACA 23012C at  $\alpha = 18^\circ$ ,  $Re_c = 1.1 \times 10^6$  and  $M_\infty = 0.10$

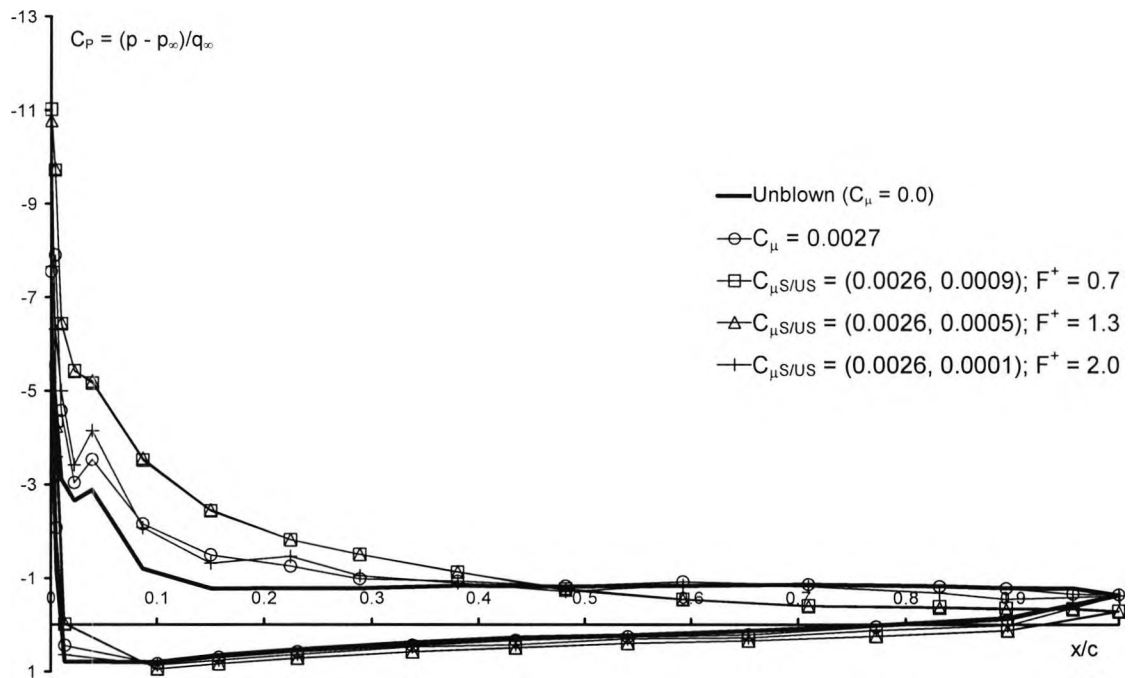


Figure 7.10: Sensitivity of chordwise surface pressure distributions to steady and pulsed AJVGs operating from  $x/c = 0.12$  for NACA 23012C at  $\alpha = 20^\circ$ ,  $Re_c = 1.1 \times 10^6$  and  $M_\infty = 0.10$

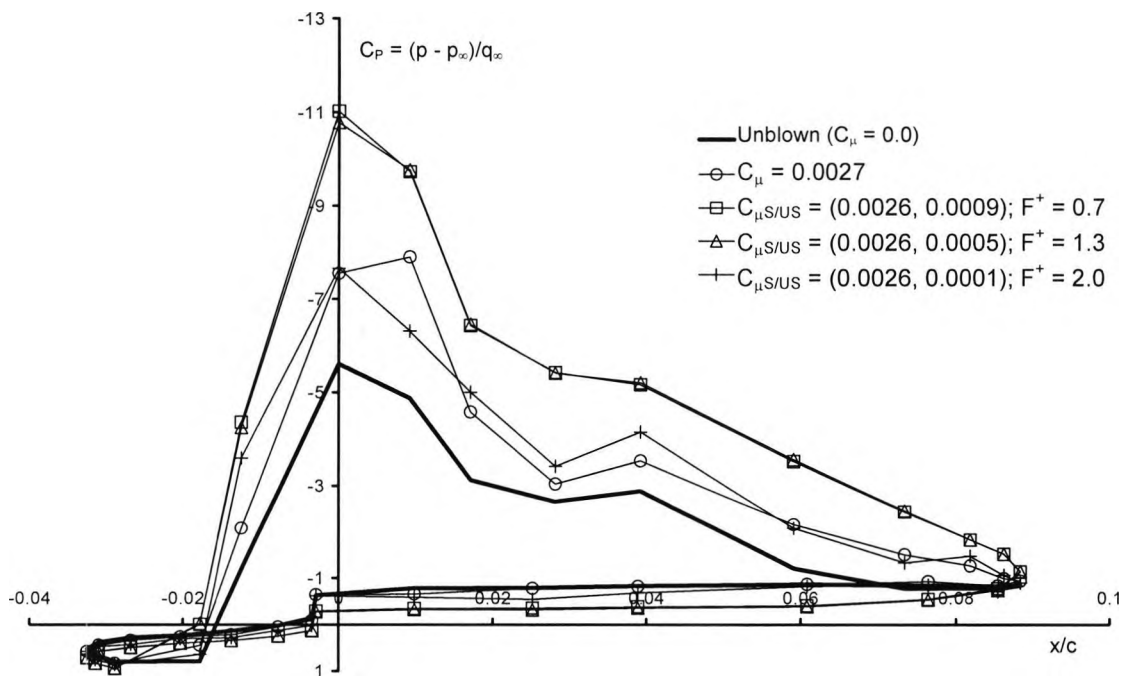


Figure 7.11: Sensitivity of leading edge suction to steady and pulsed AJVGs operating from  $x/c = 0.12$  for NACA 23012C at  $\alpha = 20^\circ$ ,  $Re_c = 1.1 \times 10^6$  and  $M_\infty = 0.10$

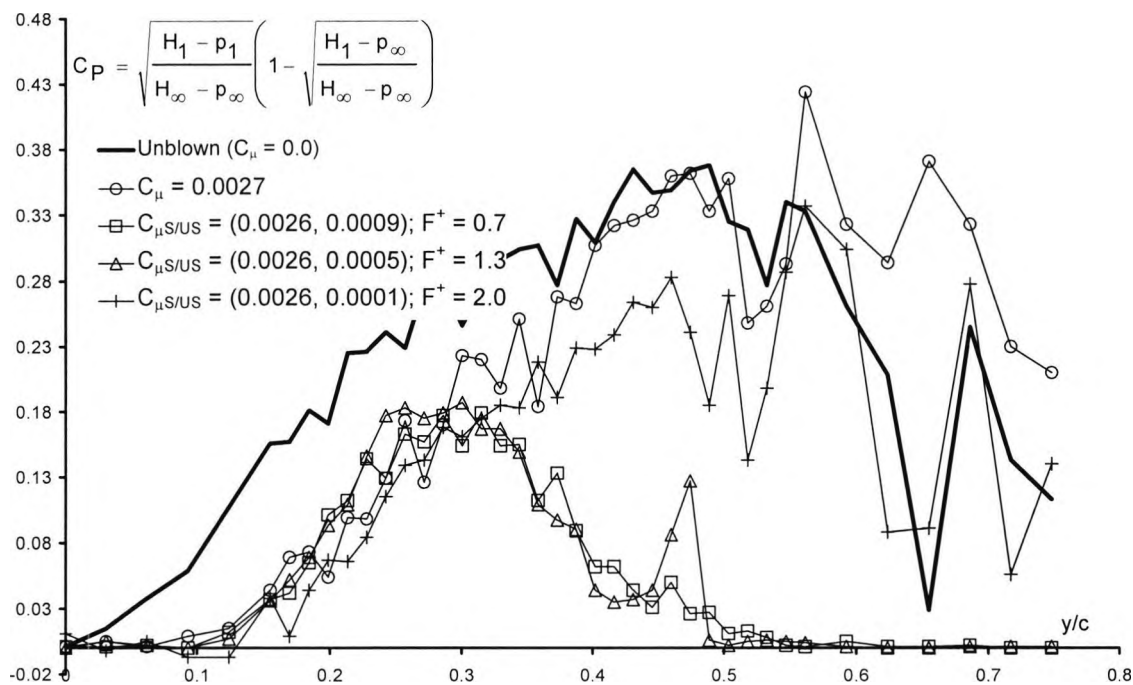


Figure 7.12: Wake profiles, measured one chord length downstream of the model trailing edge, with steady and pulsed AJVGs operating from  $x/c = 0.12$  for NACA 23012C at  $\alpha = 20^\circ$ ,  $Re_c = 1.1 \times 10^6$  and  $M_\infty = 0.10$

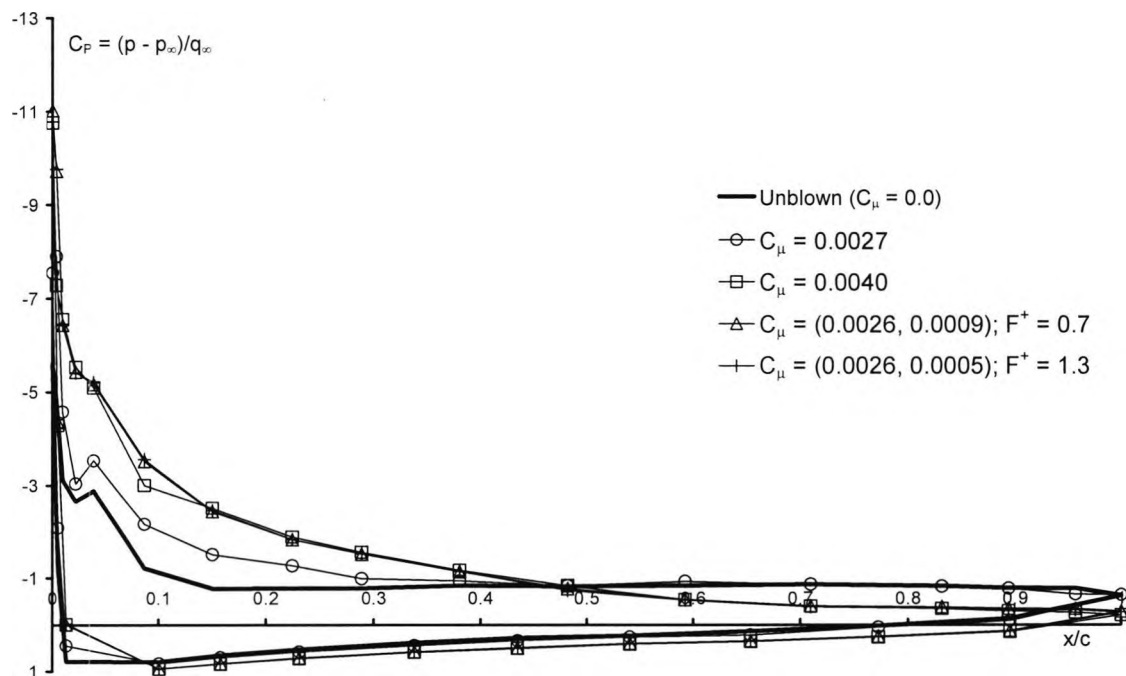


Figure 7.13: Sensitivity of chordwise surface pressure distributions to steady and pulsed AJVGs operating from  $x/c = 0.12$  for NACA 23012C at  $\alpha = 20^\circ$ ,  $Re_c = 1.1 \times 10^6$  and  $M_\infty = 0.10$

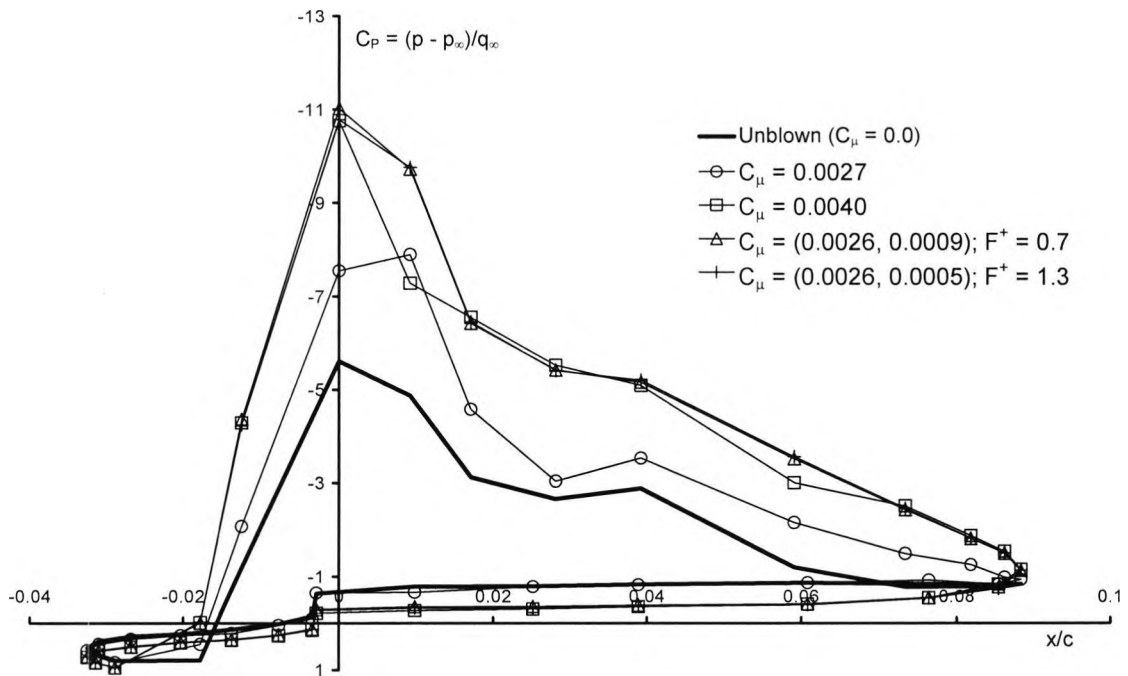


Figure 7.14: Sensitivity of leading edge suction to steady and pulsed AJVGs operating from  $x/c = 0.12$  for NACA 23012C at  $\alpha = 20^\circ$ ,  $Re_c = 1.1 \times 10^6$  and  $M_\infty = 0.10$

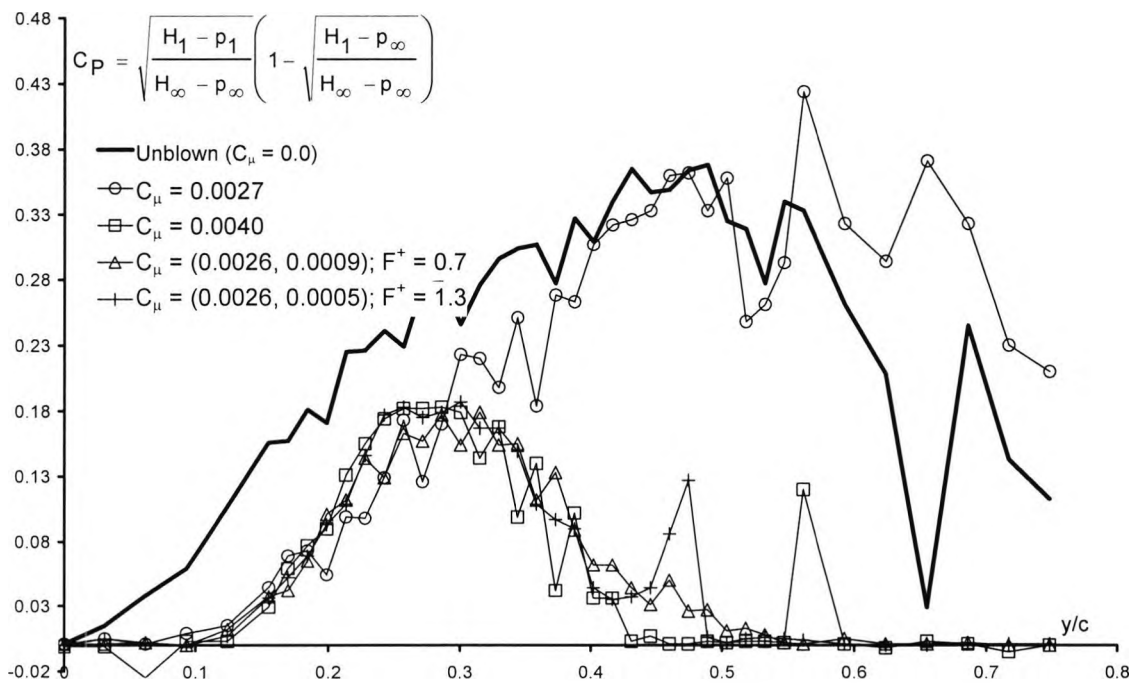


Figure 7.15: Wake profiles, measured one chord length downstream of the model trailing edge, with steady and pulsed AJVGs operating from  $x/c = 0.12$  for NACA 23012C at  $\alpha = 20^\circ$ ,  $Re_c = 1.1 \times 10^6$  and  $M_\infty = 0.10$

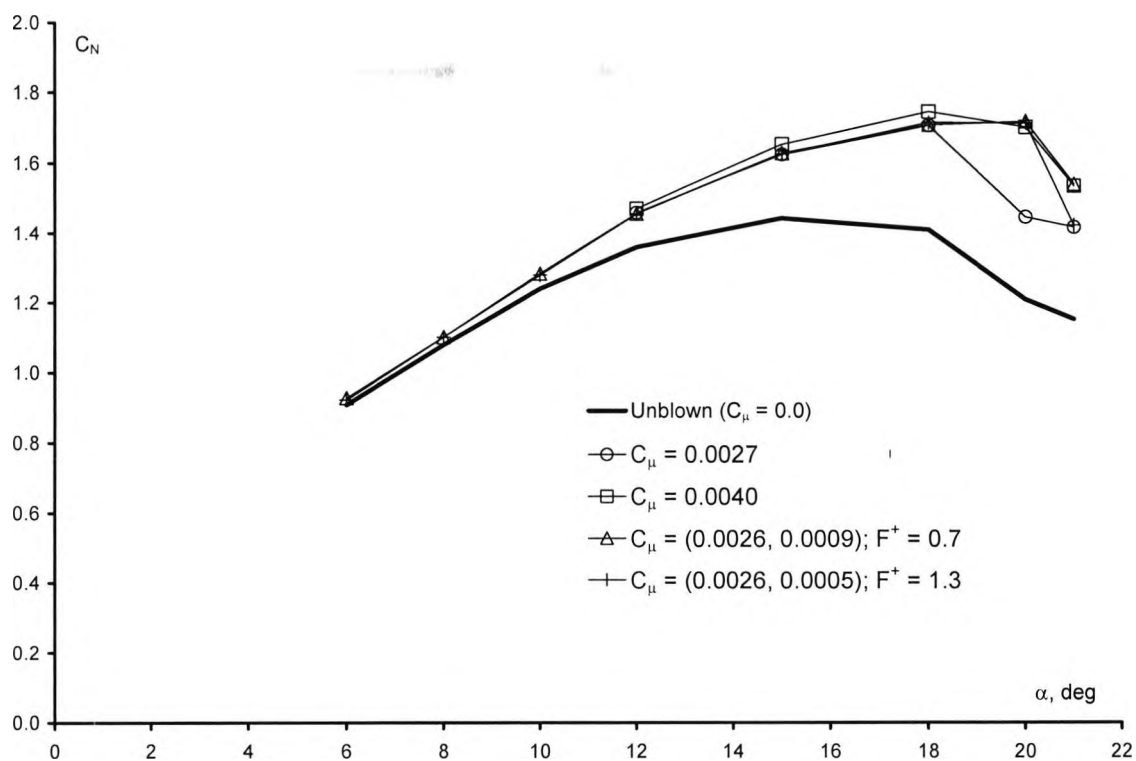


Figure 7.16: Variation of normal force coefficient with angle of attack to steady and pulsed AJVGs operating from  $x/c = 0.12$  for NACA 23012C,  $Re_c = 1.1 \times 10^6$  and  $M_{\infty} = 0.10$

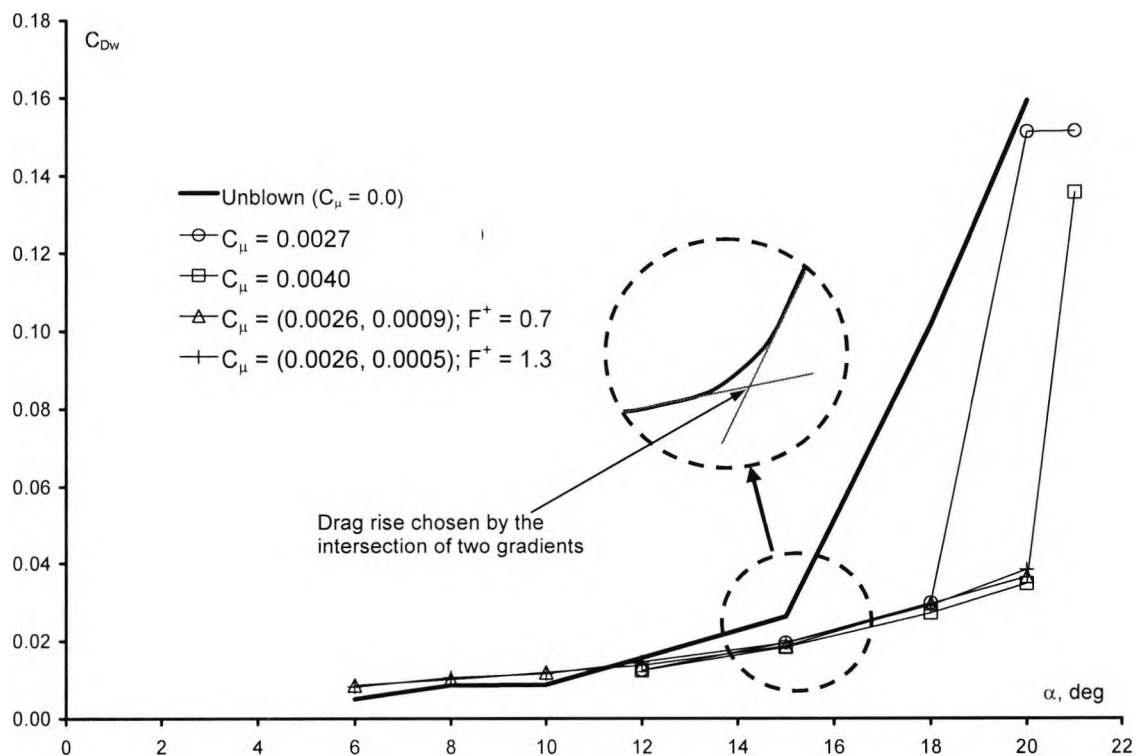


Figure 7.17: Variation of wake profile drag coefficient with angle of attack to steady and pulsed AJVGs operating from  $x/c = 0.12$  for NACA 23012C,  $Re_c = 1.1 \times 10^6$  and  $M_{\infty} = 0.10$

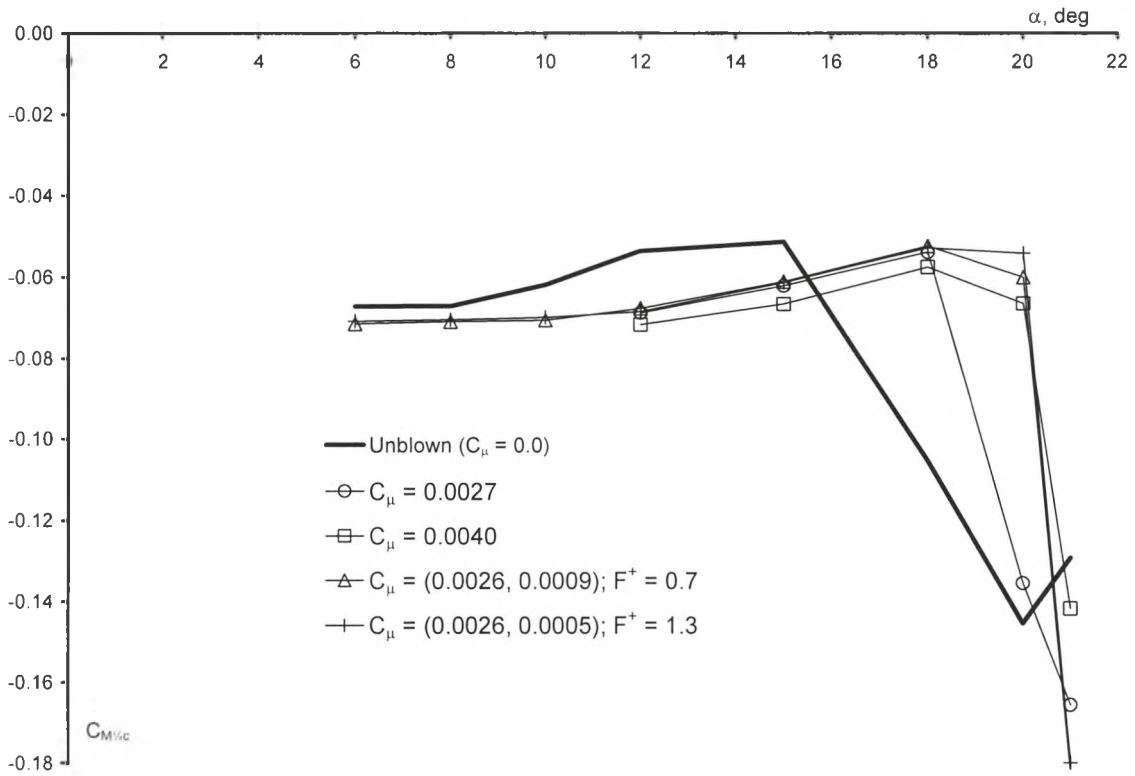


Figure 7.18: Variation of  $1/4$ -chord pitching moment coefficient with angle of attack to steady and pulsed AJVGs operating from  $x/c = 0.12$  for NACA 23012C,  $Re_c = 1.1 \times 10^6$  and  $M_\infty = 0.10$

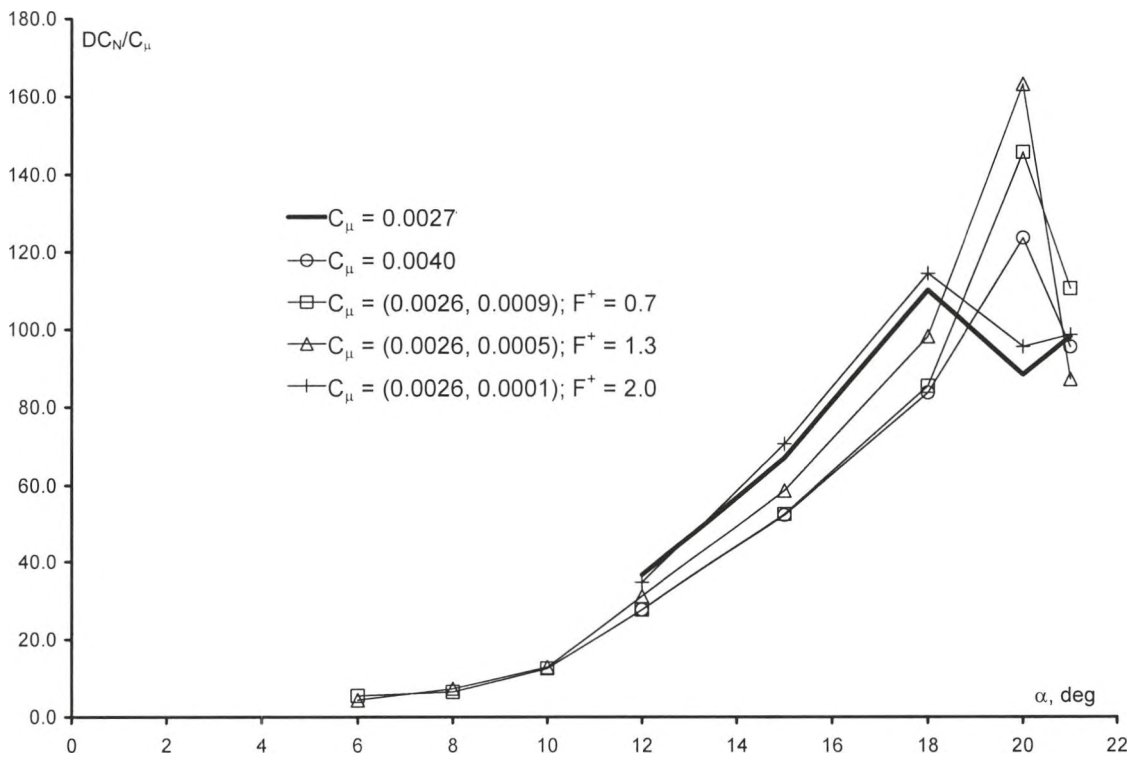


Figure 7.19: Variation of normal force coefficient increment with angle of attack to steady and pulsed AJVGs operating from  $x/c = 0.12$  for NACA 23012C,  $Re_c = 1.1 \times 10^6$  and  $M_\infty = 0.10$

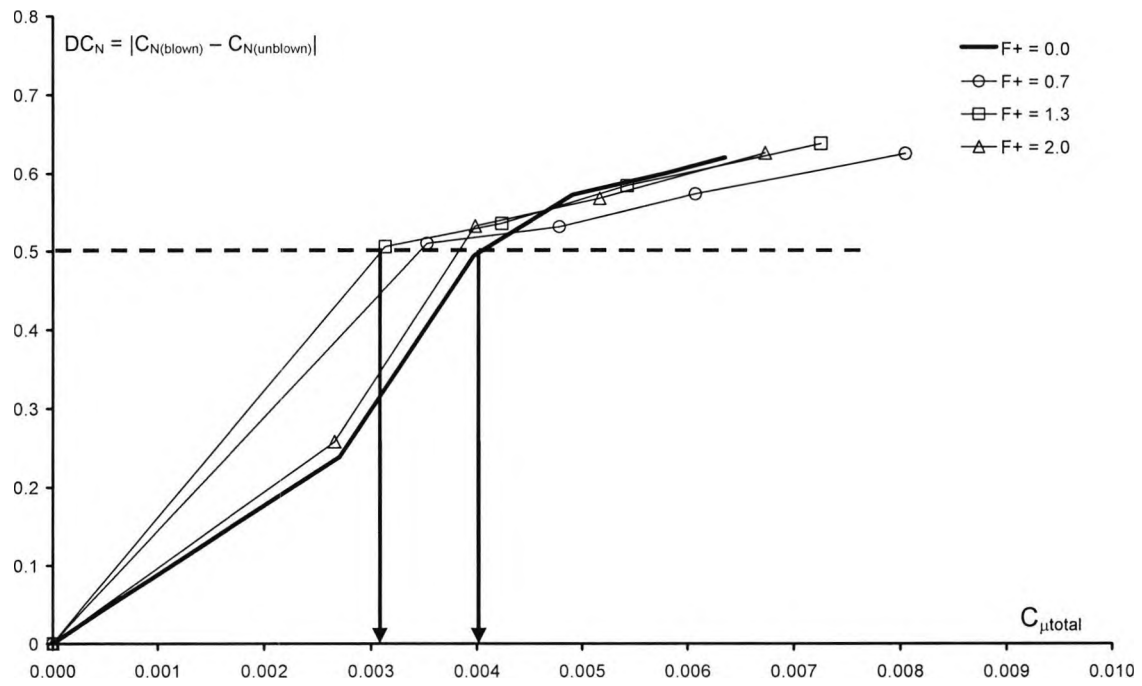


Figure 7.20: Centreline variation of normal force coefficient increments with  $C_{\mu, \text{total}}$  for NACA 23012C at  $\alpha = 20^\circ$ ,  $Re_c = 1.1 \times 10^6$  and  $M_\infty = 0.10$

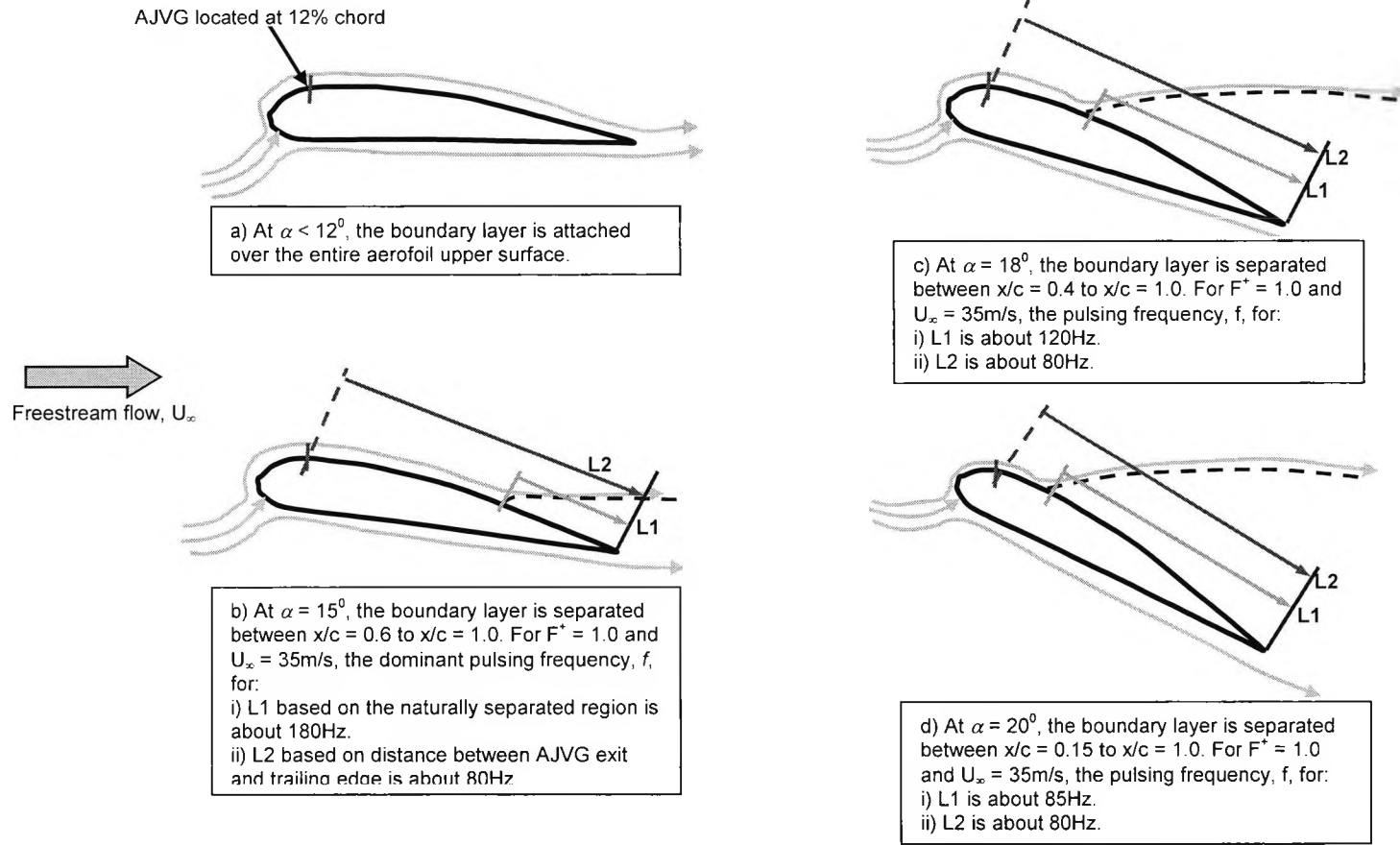


Figure 7.21: Illustration demonstrating the effect of varying the length scale  $L$  to define the dimensionless pulsing frequency  $F^+$

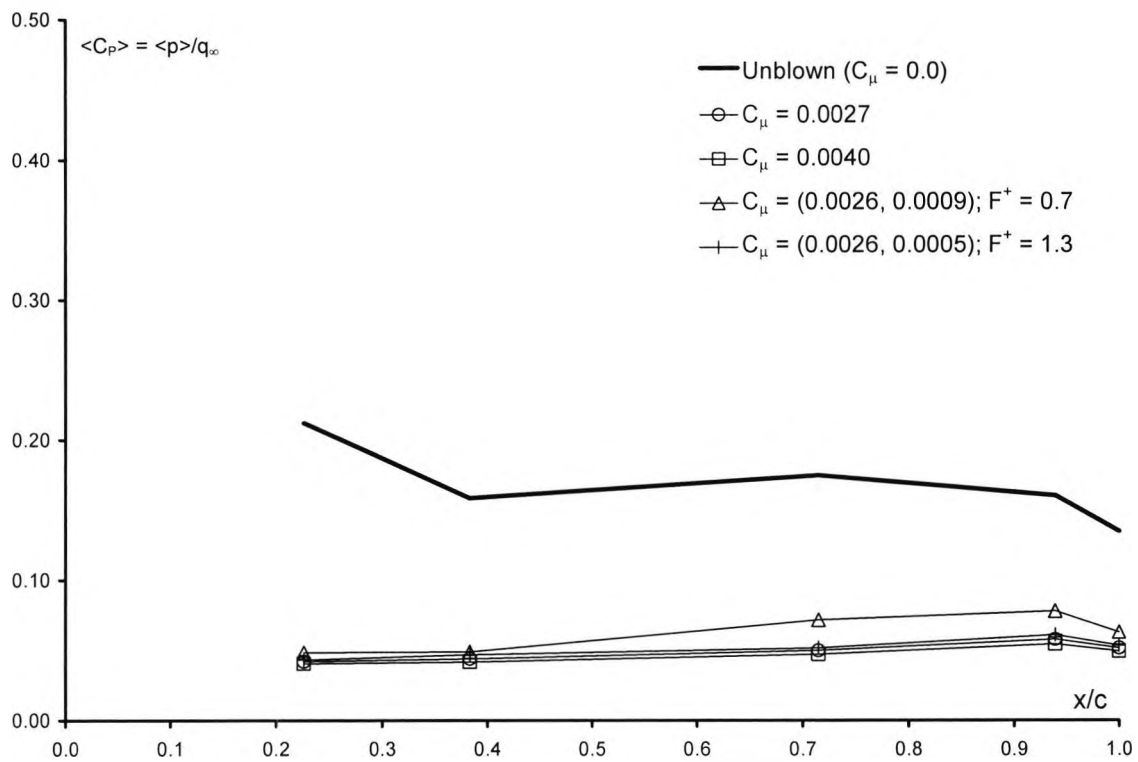


Figure 7.22: Variation of root-mean-square pressure fluctuations along the aerofoil top surface to steady and pulsed AJVGs operating from  $x/c = 0.12$  for NACA 23012C at  $\alpha = 18^\circ$ ,  $Re_c = 1.1 \times 10^6$  and  $M_\infty = 0.10$

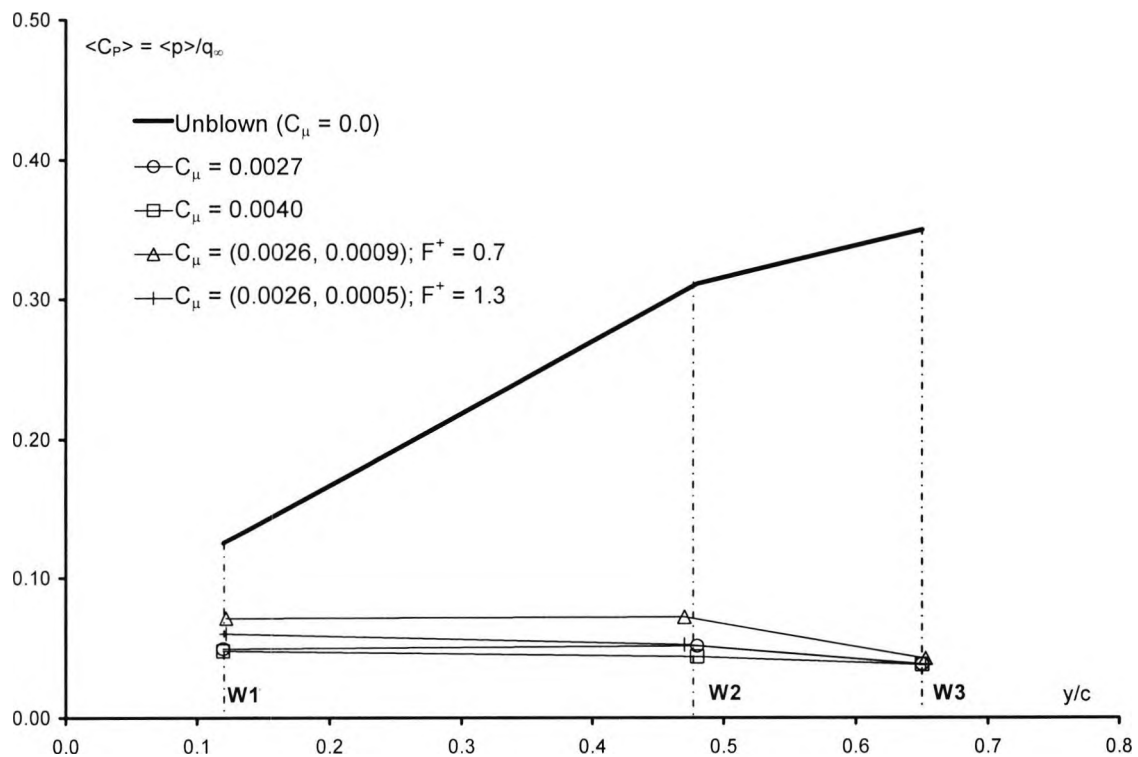


Figure 7.23: Variation of root-mean-square pressure fluctuations across the wake traverse to steady and pulsed AJVGs operating from  $x/c = 0.12$  for NACA 23012C at  $\alpha = 18^\circ$ ,  $Re_c = 1.1 \times 10^6$  and  $M_\infty = 0.10$

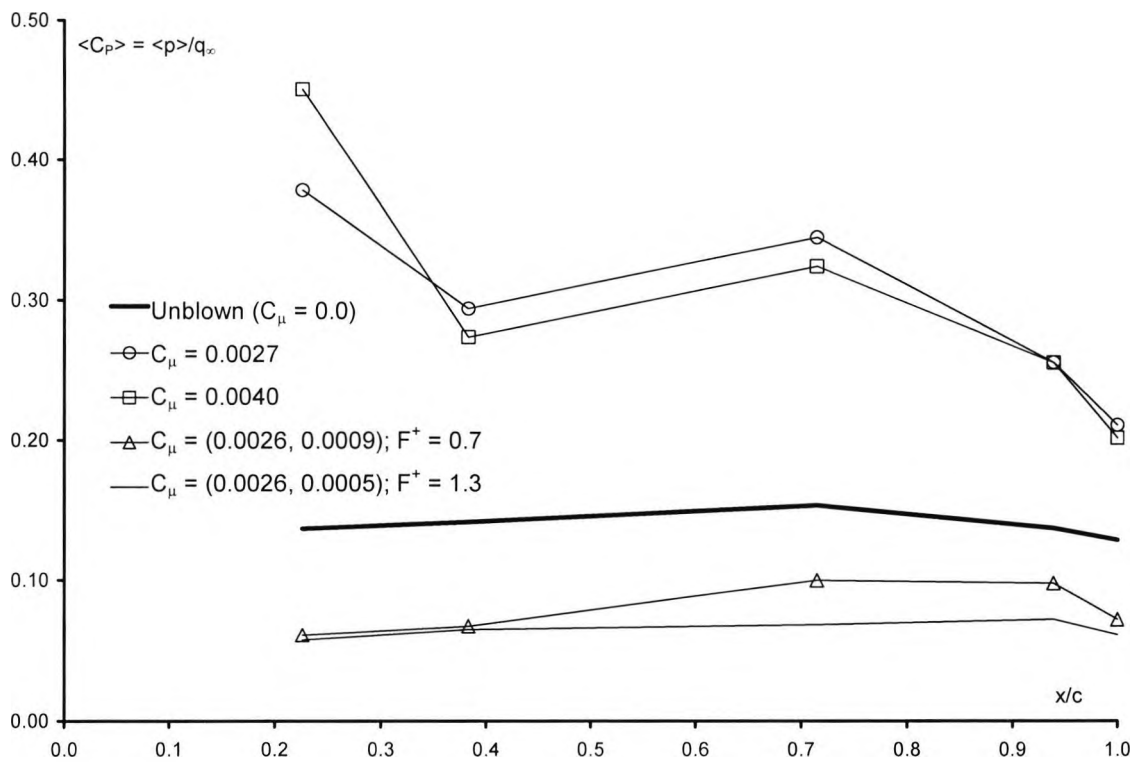


Figure 7.24: Variation of root-mean-square pressure fluctuations along the aerofoil top surface to steady and pulsed AJVGs operating from  $x/c = 0.12$  for NACA 23012C at  $\alpha = 20^\circ$ ,  $Re_c = 1.1 \times 10^6$  and  $M_\infty = 0.10$

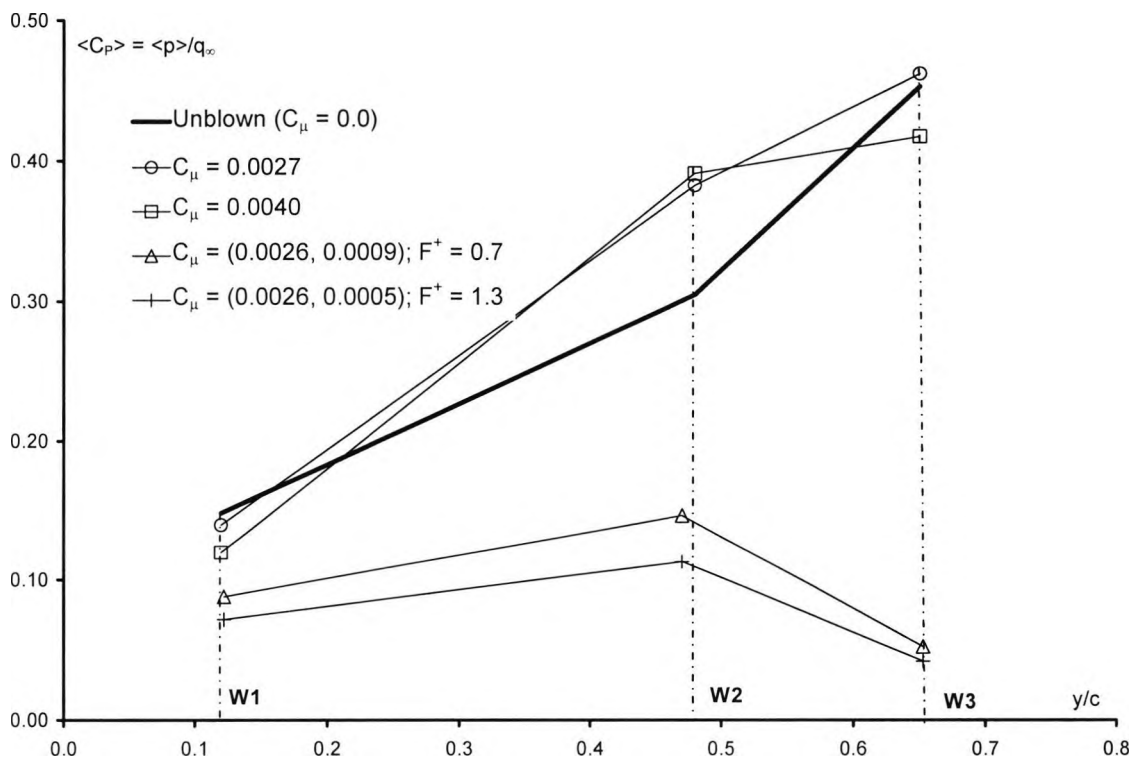


Figure 7.25: Variation of root-mean-square pressure fluctuations across the wake traverse to steady and pulsed AJVGs operating from  $x/c = 0.12$  for NACA 23012C at  $\alpha = 20^\circ$ ,  $Re_c = 1.1 \times 10^6$  and  $M_\infty = 0.10$

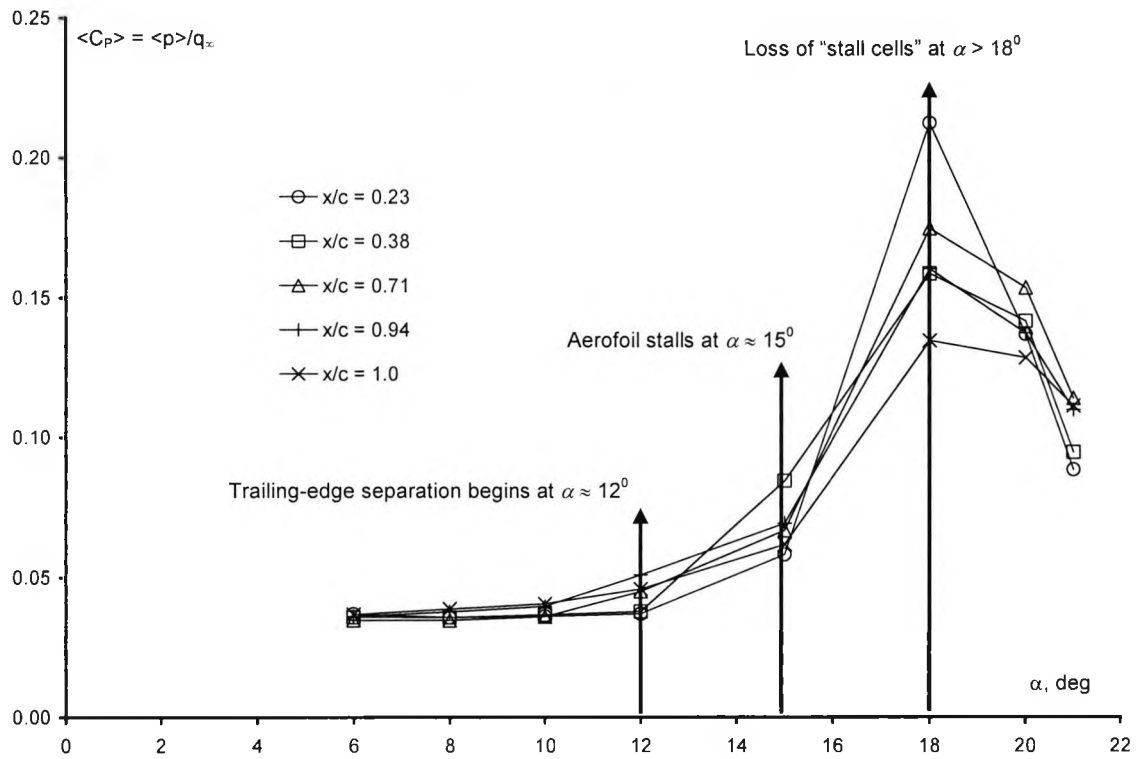


Figure 7.26: Variation of root-mean-square pressure fluctuations along the aerofoil top surface at different chordwise positions for the unblown NACA 23012C at  $Re_c = 1.1 \times 10^6$  and  $M_\infty = 0.10$

## 8. Concluding remarks

The first Defence Aerospace Research Partnership (DARP) experimental research programme is a collaborative effort between City University and University of Glasgow, and supported by the Engineering and Physical Science Research Council (EPSRC), Westland Helicopters Ltd. (WHL) and DSTL (formerly DERA). The aim of the research programme is to:

- i) Investigate the potential of employing steady AJVGs to control or eliminate the dynamic stall process on an oscillating aerofoil.
- ii) Deduce the optimum AJVG geometrical configuration to control three-dimensional quasi-steady separation on a swept leading-and trailing-edge wing, remembering that rotor blade dynamic stall of a helicopter in high-speed forward flight occurs primarily between the azimuth angles  $230^\circ < \Psi < 310^\circ$ .
- iii) Investigate the prospect of utilising unsteady AJVGs to reduce the steady-state blowing mass flow rate required to significantly improve the aerodynamic performance of an aerofoil.

The experimental research programme comprised three different wind tunnel testing regimes as outlined below:

### i) Dynamic Stall Control

Wind tunnel tests were conducted on an unswept oscillating RAE 9645 aerofoil section of chord length 500mm in the University of Glasgow Handley Page low-speed wind tunnel ( $Re_c = 1.5 \times 10^6$ ). The sinusoidal-pitching motion tests were conducted at  $\alpha = (15 + 10 \sin \omega t)$  deg, for the reduced oscillation frequency range of  $0.01 \leq k \leq 0.181$ . The aerofoil section was equipped with an array of 28 equi-spaced, co-rotating AJVGs across the span located at 12% and 62% chord with the AJVGs operating at jet momentum blowing coefficients between  $0.0 \leq C_\mu \leq 0.01$ .

### ii) Swept-Wing Experiment

Wind tunnel tests were conducted on a swept wing ( $\Lambda = 35^\circ$ ) half model section with parallel leading and trailing edges, constant chord ( $c = 232\text{mm}$ ), semi-span

( $s = 958\text{mm}$ ) and aspect ratio of 4.5, in an incidence range  $0^\circ < \alpha < 20^\circ$  in the City University T2 low speed wind tunnel ( $Re_c = 0.5 \times 10^6$ ). Installed in the top surface of the swept wing is a spanwise array of AJVGs located at 10% chord with jet momentum values in the range of  $0.0 \leq C_\mu < 0.01$ .

### iii) Pulsed Blowing Experiment

Wind tunnel tests were conducted on an unswept NACA 23012C aerofoil section of chord length 482.6mm at angles of attack  $6^\circ < \alpha < 21^\circ$  in the City University T2 low-speed wind tunnel ( $Re_c = 1.1 \times 10^6$ ). The blowing momentum coefficients and non-dimensional pulsing frequencies employed were in the range of  $0.0 \leq C_\mu < 0.01$  and  $0.3 \leq F^+ \leq 2.0$  respectively. The aerofoil section was equipped with an array of 15 equispaced, co-rotating AJVGs across the span located at 12% and 62% chord; but only the forward array of AJVGs was utilised in the experimental study.

The results of the tests above have demonstrated that installing AJVGs in both the RAE 9645 and NACA 23012C aerofoils, representing typical high-lift sections of modern helicopter blades, has permitted considerable enhancement of the aerofoil performance characteristics under steady and unsteady flow conditions. These include:

- i) The amelioration of dynamic stall on the RAE 9645 aerofoil oscillating with a sinusoidally pitching motion defined by  $\alpha = (15 + 10\sin\omega t)\text{deg}$ , and at the reduced oscillation frequency,  $k$ , of 0.05 and 0.1, with continuous blowing from the front AJVG array ( $x/c = 0.12$ ) at relatively low-blowing momentum coefficients  $C_\mu = 0.01$ .
- ii) Utilising unsteady AJVGs to maintain aerodynamic performance enhancements attributable to steady AJVGs whilst reducing the steady-state blowing mass flux (and ensuing momentum) requirements. At  $\alpha = 20^\circ$ , operating an array of AJVGs located at 12% chord continuously at  $C_\mu = 0.004$  completely repatriated the stalled flow and increased the aerofoil performance to  $DC_N/C_\mu \approx 120$ . When the steady state blowing is reduced, say, to,  $C_\mu = 0.0027$  the benefit diminishes with  $DC_N/C_\mu \approx 90$ . At this mean blowing setting, operating the AJVGs intermittently at  $[C_\mu = (0.0026, 0.0005); F^+ = 1.3]$  re-establishes and enhances the aerofoil performance to  $DC_N/C_\mu \approx 160$  with a saving of total blowing mass flux of about 25%.

Additionally, varying the geometric configuration of the AJVGs installed on the top surface of a swept wing demonstrated that the preferred AJVG installation is one with the jet efflux directed towards the wing root at  $\phi = 30^\circ$  and  $\psi = -90^\circ$ . The incorporation of either steady or pulsed AJVG as a means of viscous flow control into a full-scale helicopter rotor blade could be of particular interest to the rotorcraft industry. The potential to:

- enhance the aerodynamic performance characteristics of rotor blades at the azimuth locations where high-lift is required,
- reduce shock induced boundary layer separation [see Rao (1988)], and
- control or assuage dynamic stall

should permit a step function improvement in overall rotor blade performance.

## 9. Recommendations for future work

The success of the first DARP experimental research programme, as shown in Figure 9.1, has led to the initiation of the second DARP *interactive* experimental and computational research programme with the specific aim to undertake research that will enable a smart rotor to be flown on a demonstrator aircraft in 2007-2008. One of the themes in the second Rotorcraft Aeromechanics DARP programme is related to the development of a “*smart rotor*”.

The work on the “*smart rotor*” focuses on utilising smart flow control devices such as airjet vortex generators (steady and pulsed), synthetic jets and oscillating flaps to enhance the performance of a helicopter rotor blade. These flow control methods have been extensively studied both experimentally (AJVGs) and numerically (AJVGs, smart flap and synthetic jets) with each device offering a significant potential to control the flow field of the blade and enhance its post-stall performance. The proposed work under the smart rotor technology theme, a collaborative effort between City University, University of Glasgow and Southampton University, includes:

- Computational and experimental parametric studies assessing the effectiveness of pulsed and/or synthetic AJVGs to maintain the aerodynamic performance of the RAE 9645 aerofoil attributed to steady AJVGs whilst reducing the mass flux (and momentum). The interactive experimental and computational regime will concentrate on the aerofoil under quasi-steady flow condition as well as on an aerofoil undergoing oscillatory and constant pitch rate (ramp) motions [*City University and University of Glasgow*].
- Computational and experimental parametric studies assessing the effectiveness of an oscillating trailing-edge flap, and the ensuing combination in wind tunnel testing of steady, pulsing or synthetic AJVGs with the oscillating trailing-edge flap, to control or eliminate the dynamic stall process on an oscillating and constant pitch rate RAE 9645 aerofoil [*City University and University of Glasgow*].
- Analytical studies using Westland Helicopters (WHL) design codes to evaluate the integration of the chosen smart flow control devices into the full-scale rotor to establish blade performance, loads, vibration and aeroelastic stability [*Southampton University*].

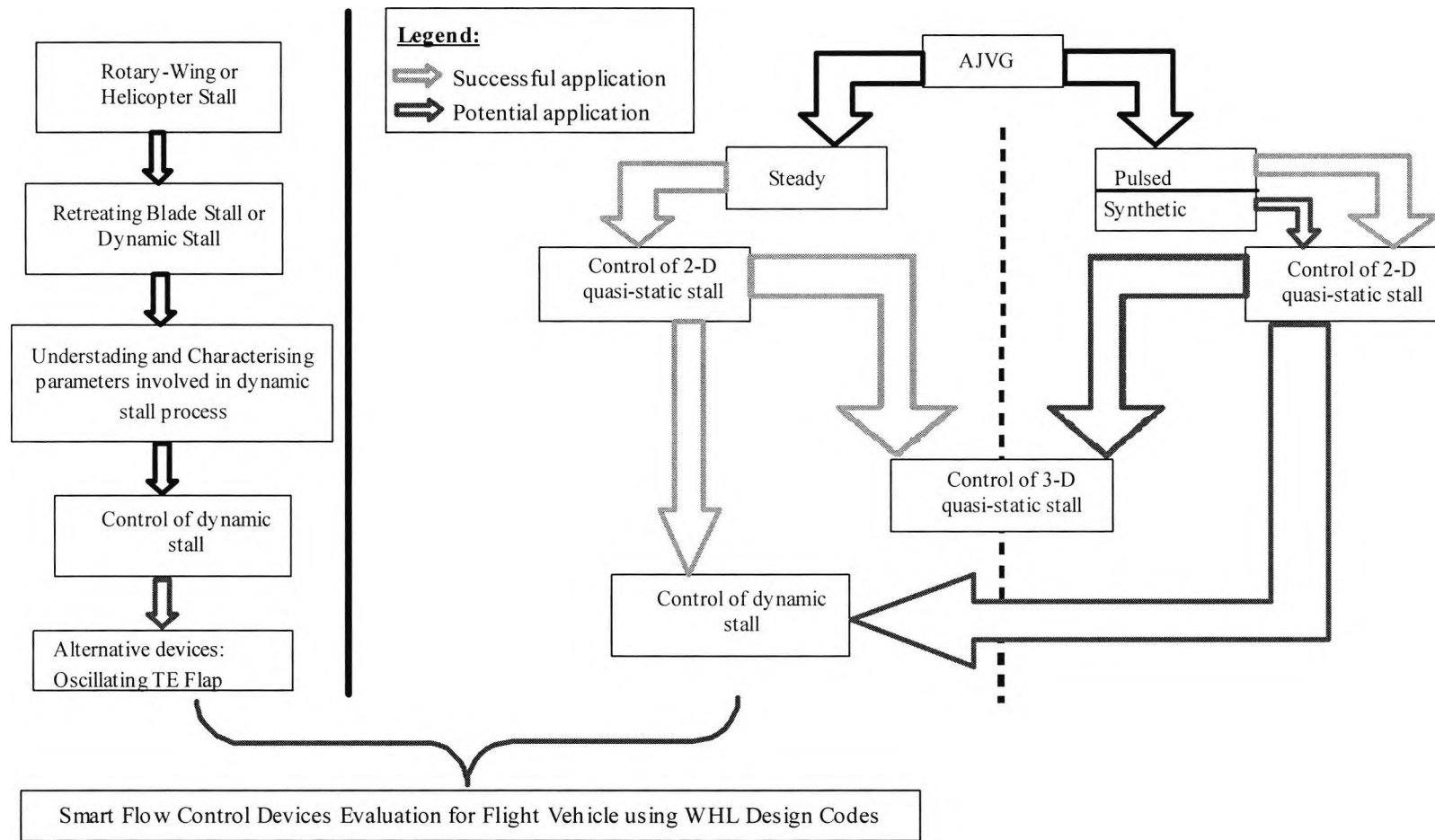


Figure 9.1: Schematic of the DARP smart flow control research programme

## References

1. Ahmed, S., and Chandrasekhara, M.S., "Reattachment Studies of an Oscillating Aerofoil Dynamic Stall Flowfield", AIAA Journal, Vol 32, No 5, 1994, pp 1006-1012
2. Akanni, S.D., and Henry, F.S., "Numerical calculations of air-jet vortex generators in turbulent boundary layers", CEAS European Forum on 'High Lift & Separation Control', Paper 16, 1995.
3. Alferai, M., and Acharya, M., "Controlled leading-edge suction for the management of unsteady separation over pitching aerofoils", AIAA paper 95-2188, 26<sup>th</sup> AIAA Fluid Dynamics Conference, 1995.
4. Amitay, M., and Glezer, A., "Role of Actuation Frequency in Controlled Flow Reattachment over a Stalled Aerofoil", AIAA Journal, Vol 40, No 2, 2002, pp 209-216.
5. Anders, J.B., and Watson, R.D., "Aerofoil Large-Eddy Breakup Devices for Turbulent Drag Reduction", AIAA Paper 85-0520, 1985.
6. Ashill, P.R., and Riddle, G.L., "Control of leading-edge separation on a cambered delta wing", AGARD-CP-548, Paper No 11, October 1993.
7. Ashill, P.R., Riddle, G.L., and Stanley, M.J., "Control of Three-Dimensional Separation on Highly-Swept Wings", ICAS-94-4.6.2, 1994, pp 2012-2026.
8. Ashill, P.R., Riddle, G.L., and Stanley, M.J., "Separation control on highly-swept wings with fixed or variable camber", The Aeronautical Journal, Vol 99, No 988, Oct 1995, pp 317-327.
9. Bar-Server, A., "Separation Control on an Airfoil by Periodic Forcing", AIAA Journal, Technical Notes, Vol 27, No 6, 1989, pp 820-821.

10. Beddoes, T.S., "Onset of leading-edge separation effects under dynamic conditions and low Mach numbers", 34<sup>th</sup> Annual Nation Forum of the AHS, 1978.
11. Bendat, J.S. and Piersol, A.G., "Random Data: Analysis and Measurement Procedures", Wiley-Interscience, 1971.
12. Berg, B. van den, and Elsenaar, A., "Measurements in a three-dimensional incompressible turbulent boundary layer in an adverse pressure gradient under infinite swept wing conditions", NLR TR 72092 U, 1972.
13. Bousman, W.G., "A Qualitative Examination of Dynamic Stall from Flight Test Data", AHS 53<sup>rd</sup> Annual Forum Proceedings, 1997, pp 368-387.
14. Bradley, R.G., and Wray, W.O., "A Conceptual Study of Leading-Edge-Vortex Enhancement by Blowing", Journal of Aircraft, Vol 11, No 1, 1974, pp 33-38.
15. Broadley, I., and Garry, K.P., "Effectiveness of vortex generator position and orientation on highly swept wings", AIAA paper 97-2319, 1997.
16. Bushnell, D.M., "Turbulent drag reduction for external flows", AIAA Paper 83-0227, 1983.
17. Campbell, J.F., "Augmentation of Vortex Lift by Spanwise Blowing", Journal of Aircraft, Vol 13, No 9, 1976, pp 727-732.
18. Carr, L.W., McAllister, K.W., and McCroskey, W.J., "Analysis of the development of dynamic stall based on oscillating airfoil experiments", NASA Technical Note D-8382, 1977.
19. Carr, L.W., and McAllister, K.W., "The effect of a leading-edge slat on the dynamic stall of an oscillating aerofoil", AIAA Paper 83-2533, AIAA Aircraft Design, Systems and Technology Meeting, 1983.

20. Carr, L.W., "Progress in Analysis and Prediction of Dynamic Stall", *Journal of Aircraft*, Vol 25, No 1, 1988, pp 6-17.
21. Carta, F.O., "Dynamic Stall of Swept and Unswept Oscillating Wings", AGARD CPP 386, Paper 2, 1985.
22. Cambridge Electronic Design Ltd, "Spike 2 for Windows – Version 4.00", 2001.
23. Chan, W., and Brocklehurst, A., "Performance enhancement evaluation of an actuated trailing edge flap", *The Aeronautical Journal*, Vol 105, no 1049, July 2001, pp 391-399.
24. Chandrasekhara, M.S., and Carr, L.W., "Flow Visualisation Studies of the Mach Number Effects on Dynamic Stall of an Oscillating Aerofoil", *Journal of Aircraft*, Vol 27, No 6, 1990, pp 516-522.
25. Chandrasekhara, M.S., and Carr, L.W., "Compressibility Effects on Dynamic Stall of Oscillating Aerofoils", AGARD CP-552, Paper 3, 1995.
26. Chandrasekhara, M.S., Wilder, W.S., and Carr, L.W., "Boundary-Layer-Tripping Studies of Compressible Dynamic Stall Flow", *AIAA Journal*, Vol 34, No 1, 1996, pp 96-103.
27. Chandrasekhara, M.S., Wilder, W.C., and Carr, L.W., "Competing Mechanisms of Compressible Dynamic Stall", *AIAA Journal*, Vol 36, No 3, 1998, pp 387-393.
28. Chandrasekhara, M.S., Wilder, M.C., and Carr, L.W., "Compressible Dynamic Stall Control Using a Shape Adaptive Aerofoils" AIAA Paper 99-0650, 1999.

29. Chandrasekhara, M.S., Martin, P.B., and Tung, C., "Compressible Dynamic Stall Control using a Variable Droop Leading Edge Aerofoil", AIAA Paper 2003-0048, 41<sup>st</sup> Aerospace Sciences Meeting and Exhibit, Jan 2003.
30. Chang, P.K., "Separation of Flow", International Series of Monographs in Interdisciplinary and Advanced Topics in Science and Engineering, Vol. 3, Pergamon Press, 1970.
31. Cheeseman, I.C., "The Application of Circulation Control by Blowing to Helicopter Rotors", Journal of The Royal Aeronautical Society, Vol 71, No 679, July 1967, pp 451-467.
32. Chopra, I., "Development of a Smart Rotor", 19<sup>th</sup> European Rotorcraft Forum, Paper N6, 1993.
33. Compton, D.A., and Johnston, J.P., "Streamwise Vortex Production by Pitched and Skewed Jets in a Turbulent Boundary Layer", AIAA Journal, Vol 30, No 3, 1992, pp 640-647.
34. Coton, F.N., and Galbraith, R.A.McD., "An experimental study of dynamic stall on a finite wing", The Aeronautical Journal, Vol 103, No 1015, May 1999, pp 229-236.
35. Coton, F.N., Galbraith, R.A.McD., and Green, R.B., "The effect of wing planform shape on dynamic stall", The Aeronautical Journal, Vol 105, No 1045, 2001, pp 151-159.
36. Crook, A., Sadri, A.M., and Wood, N.J., "The Development and Implementation of Synthetic Jets for the Control of Separated Flow", AIAA Paper 99-3176, 17<sup>th</sup> Applied Aerodynamics Conference, 1999.
37. Duraisamy, K., and Baeder, J.D., "Active Flow Control Concepts for Rotor Aerofoils Using Synthetic Jets", AIAA 2002-2835.

38. Ekaterinaris, J.A., "Numerical Investigations of Dynamic Stall Active Control for Incompressible and Compressible Flows", AIAA Paper 2000-4333.
39. Esmile, K., Hosking, L., and Marshall, W.S.D., "Some experiments on the flow in the boundary layer of a 450 sweptback wing of aspect ratio 4", Cranfield College of Aeronautics Report 69, February 1953.
40. Feszty, D., Gillies, E.A., and Vezza, M., "Alleviation of Rotor Blade Dynamic Stall via Trailing Edge Flap Flow Control", AIAA Paper 2003-0020, 41<sup>st</sup> Aerospace Sciences Meeting and Exhibit, Jan 2003.
41. Freestone, M.M., "Preliminary tests at low speed on vorticity produced by air-jet vortex generators", RM 85/1 City University, London, 1985.
42. Fricke, F.R., "Pressure fluctuations in separated flows", *Journal of Sound and Vibration*, Vol 17, No 1, 1971, pp 113-123.
43. Gad-el-Hak, M., and Blackwelder, R.F., "The discrete vortices from a delta wing", *AIAA Journal*, Vol 23, June 1985, pp 961-962.
44. Geissler, W., and Raffel, M., "Dynamic Stall Control by Aerofoil Deformation", 19<sup>th</sup> European Rotorcraft Forum, Paper C2, 1993.
45. Gracey, M.W., Niven, A.J., and Galbraith, R.A.McD, "A Consideration of Low-Speed Dynamic Stall Onset", 15<sup>th</sup> European Rotorcraft Forum, Paper 11, 1989.
46. Gracey, M.W., Niven, A.J., Coton, F.N., Galbraith, R.A.McD, and Jiang, D., "A correlation indicating incipient dynamic stall", *The Aeronautical Journal*, Vol 100, Vol 997, 1996, pp 305-311.
47. Green, R.B., Galbraith, R.A.McD., and Niven, A.J., "Measurements of the Dynamic Stall Vortex Convection Speed" *The Aeronautical Journal*, Vol 96, No 958, 1992, pp 319-325.

48. Green, R.B., and Galbraith, R.A.McD., "Dynamic recovery to fully attached aerofoil flow from deep stall", *AIAA Journal*, Vol 33, No 8, 1995, pp 1433-1440.
49. Greenblatt, D., and Wygnanski, I., "Effect of Leading-Edge Curvature and Slot Geometry on Dynamic Stall Control", *AIAA Paper 2002-3271*.
50. Hanagud, S., Roglin, R.L., and Nagesh Babu, G.L., " Smart Aerofoils for Helicopter Control", 18<sup>th</sup> European Rotorcraft Forum, Paper 119, 1992.
51. Ham, N.D., "Helicopter stall alleviation using individual-blade control", 10<sup>th</sup> European Rotorcraft Forum, Paper 50A, 1984.
52. Heller, H.H., Bliss, D.B., and Windall, S.E., "Incipient Stall Detection through Unsteady-Pressure Monitoring on Aircraft Wings", *Journal of Aircraft*, Vol 9, No 2, 1972, pp 186-188.
53. Henry, F.S., and Pearcey, H.H., "Numerical Model of Boundary-Layer Control Using Air-Jet Generated Vortices", *AIAA Journal*, Vol 32, No 12, 1994, pp 2415-2424.
54. Hinze, J.O., "Turbulence: An Introduction to its Mechanism and Theory", McGraw-Hill, 1959.
55. Horstmann, K.H., H.Köster, H., Polz, G., "Development of new aerofoil sections for helicopter rotor blades", 8<sup>th</sup> European Rotorcraft Forum, Paper 2.2, 1982.
56. Horstmann, K.H., H.Köster, H., Polz, G., "Improvement of two blade sections for helicopter rotors", 10<sup>th</sup> European Rotorcraft Forum, Paper 1, 1984.
57. Houghton, E.L., and Boswell, R.P., "Further aerodynamics for engineering students", Edward Arnolds (Publishers) Ltd, 1969.

58. Innes, F., "An experimental investigation into the use of vortex generators to improve the performance of a high lift system", PhD Thesis, City University, London, 1995.
59. Johnson, W., "Helicopter Theory", Dover Publications Inc., 1980.
60. Johnston, J.P., and Nishi, M., " Vortex Generator Jets – Means for Flow Separation Control", AIAA Journal, Vol 28, No 6, 1990, pp 989-994.
61. Jones, R.T., "Effects of sweep back on boundary layer and separation", NACA R 884, 1947.
62. Katz, Y., Nishri, B., Wygnanski., "The delay of turbulent boundary layer separation by oscillatory active control", Phys. Fluids A, Vol 1, No 2, 1989, pp 179-181.
63. Küchemann, D., "Types of Flow on Swept Wings", Journal of the Royal Aeronautical Society, Vol 57, 1953, pp 683-699.
64. Küpper, C., "A study of the application of air-jet vortex generators to intake ducts", PhD Thesis, City University, London, 1999.
65. Küpper, C., and Henry, F.S., "A numerical study of the application of vane and air-jet vortex generators", The Aeronautical Journal, Vol 105 , No 1047 , 2001, pp 255-265.
66. Kufeld, R.M., Balough, D.L., Cross, J.L., Stuebaker, K.F., Jennison, C.D., and Bousman, W.G., "Flight Testing the UH-60A Airloads Aircraft", American Helicopter Society 50<sup>th</sup> Annual Forum Proceedings, May 1994, pp 557-578.
67. Leishman, J.G., "Modelling Sweep Effects on Dynamic Stall", Journal of the American Helicopter Society, July 1989, pp 18-29.

68. Lewington, N.P., Peake, D.J., Henry, F.S., Kokkalis, A., and Perry, J., "The Application of Air-Jet Vortex Generators to Control the Flow on Helicopter Rotor Blades", Proc. of 26<sup>th</sup> European Rotorcraft Forum, Paper 52, 2000.
69. Lewington, N.P., Peake, D.J., Henry, F.S., and Singh, C., "Numerical modelling of air-jet vortex generators in streamwise pressure gradients" The Aeronautical Journal, Vol 105, No 1049, 2001, pp 401-407.
70. Lewington, N.P., "Enhancing Lift on a Three-Element High Lift Aerofoil System by Installing Air-Jet Vortex Generators", PhD Thesis, City University, London, 2001.
71. Mabey, D.G., "Analysis and Correlation of Data on Pressure Fluctuations in Separated Flow", Journal of Aircraft, Vol 9, No 9, 1972, pp 642-645.
72. Mabey, D.G., Welsh, B.L., and Pyne, C.R., "The development of leading-edge notches to improve the subsonic performance of wings of moderate sweep", European Forum on Aeroelasticity and Structural Dynamics, Paper 89-017, 1989.
73. Mabey, D.G., and Pyne, C.R., "Tangential leading-edge blowing on a combat aircraft configuration", ICAS-94-4.6.1, 1994, pp 2001-2011.
74. Magill, J.C., and McManus, K.R., "Exploring the Feasibility of Pulsed Jet Separation Control for Aircraft Configurations", Journal of Aircraft, Vol 38, No 1, 2001, pp 48-56.
75. Magill, J., Bachmann, M., Rixon, G., and McManus, K., "Dynamic Stall Control Using a Model-Based Observer", AIAA 2001-0251, 39<sup>th</sup> AIAA Aerospace Sciences Meeting and Exhibit, 2001.
76. Maskell, E.C., "Flow separation in three dimensions", RAE R Aero 2565, 1955.

77. McAllister, K.W., and Carr, L.W., "Water Tunnel Visualisations of Dynamic Stall", *Journal of Fluids Engineering*, Vol 101, September 1979, pp 376-380.
78. McCloud III, J.L., and McCullough, G.B., "Wind-Tunnel Tests of a Full-Scale Helicopter Rotor with Symmetrical and with Cambered Blade Sections at Advance Ratios from 0.3 to 0.4", *NACA Technical Note 4367*, 1958.
79. McCloud III, J.L., Hall, L.P., and Brady, J.A., "Full-Scale Wind-Tunnel Tests of Blowing Boundary-Layer Control Applied to a Helicopter Rotor", *NASA Technical Note D-335*, 1960.
80. McCroskey, W.J., "Recent developments in rotor blade stall", *AGARD-CP-111*, Paper 15, 1972.
81. McCroskey, W.J., Carr, L.W., and McAllister, K.W., "Dynamic stall experiments on oscillating aerofoils", *AIAA Paper 74-125*.
82. McCroskey, W.J., "The phenomenon of dynamic stall", *NASA Technical Memorandum 81264*, 1981.
83. McCroskey, W.J., McAllister, K.W., Carr, L.W., and Pucci, S.L., "An Experimental Study of Dynamic Stall on Advanced Airfoil Sections: Volume 1 – Summary of the Experiment", *NASA Technical Memorandum 84245*, 1982.
84. McCroskey, W.J., "Unsteady Aerofoils", *Annual Review of Fluid Mechanics*, Vol 14, 1982, pp 285-311.
85. McManus, K., Legner, H.H., and Davis, S.J., "Pulsed Vortex Generator Jets for Active Control of Flow Separation", *AIAA Paper 94-2218*, 25<sup>th</sup> Fluid Dynamics Conference, June 1994.
86. McManus, K.R., Joshi, P.B., Legner, H.H., and Davis, S.J., "Active Control of Aerodynamic Stall Using Pulsed Jet Actuators", *AIAA Paper 95-2187*, 26<sup>th</sup> AIAA Fluid Dynamics Conference, June 1995.

87. McManus, K., Ducharme, A., Goldey, C., and Magill, J., "Pulsed Jet Actuators for Suppressing Flow Separation", AIAA Paper 96-0442, 34<sup>th</sup> Aerospace Sciences Meeting & Exhibit, January 1996.
88. McManus, K., and Magill, J., "Separation Control in Incompressible and Compressible Flows Using Pulsed Jets", AIAA Paper 96-1948, June 1996.
89. Mikhail, M.N., "Optimum design of Internal Flow Passages with Specific Reference to Wind Tunnel Contractions", PhD Thesis, Carleton University, Ottawa, Canada, 1976.
90. Nagib, H., Kiedaisch, J., Greenblatt, D., Wagnanski, I., and Hassan, A., "Effective Flow Control for Rotorcraft Applications at Flight Mach Numbers", AIAA Paper 2001-2974, 31<sup>st</sup> AIAA Fluid Dynamics Conference and Exhibit, 2001.
91. Narayanan, S., and Banaszuk, A., "Experimental study of a novel active separation control approach", AIAA Paper 2003-60, January 2003.
92. Nguyen, K., and Chopra, I., "Effects of Higher Harmonic Control on Rotor Performance and Control Loads", Journal of Aircraft, Vol 29, No 3, 1992, pp 336-342.
93. Nguyen, K., "Active Control of Helicopter Blade Stall", Journal of Aircraft, Vol 35, No1, 1998, pp 91-98.
94. Nishri, B., and Wagnanski, I., "Effects of Periodic Excitation on Turbulent Flow Separation from a Flap", AIAA Journal, Vol 36, No 4, 1998, pp 547-556.
95. Oliver, A.G., "Air jet vortex generators for wind turbines", PhD Thesis, City University, London, 1997.

96. Pauley, W.R., and Eaton, J.K., "Experimental Study of the Development of Longitudinal Vortex Pairs Embedded in a Turbulent Boundary Layer", *AIAA Journal*, Vol 26, No 7, 1988, pp 816-823.
97. Pearcey, H.H., "Shock induced separation and its prevention", *Boundary Layer & Flow Control*. Vol. 2, Pergammon Press, New York, 1961, pp. 1170-1344.
98. Pearcey, H.H., Rao, K., and Sykes, D.M., "Inclined Air-jets as Vortex Generators to Suppress Shock Induced Separation", *AGARD Conference Proceedings* 534, 1993.
99. Rao, K., "Use of air-jet vortex generators to control shock induced boundary layer separation", PhD thesis, City University, London, 1988.
100. Reuster, J.G., and Baeder, J.D., "Effects of Plunging on Flow Control for Pitching Airfoils", *AIAA Paper* 2001-2976.
101. Robinson, M.C., Helin, H.E., and Luttges, M.W., "Control of Wake Structure Behind an Oscillating Aerofoil", *AIAA Paper* 86-2282
102. Sankar. Y.L., and Tassa, Y., "Compressibility Effects on Dynamic Stall of an NACA 0012 aerofoil", *AIAA Journal*, Vol 19, No 5, 1981, pp 557-558.
103. Schubauer, G.B., and Spangenberg, W.G., "Forced Mixing in Boundary Layers", *Journal of Fluid Mechanics*, Vol. 8, 1960, pp. 10-32.
104. Seifert, A., Bachar, T., Koss, D., Shepshelovich, M., and Wygnanski, I., "Oscillatory Blowing: A Tool to Delay Boundary-Layer Separation", *AIAA Journal*, Vol 31, No 11, 1993, pp 2052-2060.
105. Seifert, A., Daraby, A., Nishri, B., and Wygnanski, I., "The effects of forced oscillations on the performance of airfoils", *AIAA Paper* 93-3264.

106. Seifert, A., Darabi, A., and Wygnanski, I., "Delay of Airfoil Stall by Periodic Excitation", *Journal of Aircraft*, Vol 33, No 4, 1996, pp 691-698.
107. Selby, G.V., Lin, J.C., and Horward, F.G., "Control of low-speed turbulent separated flow using jet vortex generators", *Experiments in Fluids*, Vol 12, 1992, pp 394-400.
108. Shih, C., Lourenco, L., Van Dommelen, L., and Krothapalli, A., "Unsteady Flow Past an Aerofoil Pitching at a Constant Rate", *AIAA Journal*, Vol 30, No 5, 1992, pp 1153-1161
109. Shortal, J.A., and Maggin, B., "Effect of Sweepback and Aspect Ratio on Logitudinal Stability Characteristic of Wings at Low Speeds", *NACA Technical Note 1093*, 1946.
110. Singh, C., Peake, D.J., Coton, F., Galbraith, R.A.McD., and Kokkalis, A., "The application of air-jet vortex generators to control the flow on helicopter rotor blades under quasi-steady and unsteady conditions", *Proc. of 29<sup>th</sup> European Rotorcraft Forum*, Paper 52, 2003.
111. Singh, C., Peake, D.J., Coton, F., Kokkalis, A., and Galbraith, R.A.McD., "The application of air-jet vortex generators to suppress flow separation on helicopter rotor aerofoil sections under quasi-steady and unsteady conditions", *AIAA Paper 2004-0045*.
112. St. Hilaire, A.O., Carta, F.O., Fink, M.R., and Jepson, W.D., "The Influence of Sweep on the Aerodynamic Loading of an Oscillating NACA 0012 Aerofoil", Vol 1 – *Technical Report, NASA CR 3092*, 1979.
113. Taylor, H.D., "Summary Report on Vortex Generators", *United Aircraft Corporation Research Laboratories*, Report R-05280-9, 1950.
114. Teves, D., Nisel, G., Blaas, A., and Jacklin, S., "The Role of Active Control in Future Rotorcraft", *21<sup>st</sup> European Rotorcraft Forum*, Paper III-10, 1995.

115. Thibert, J.J., and Gallot, J., "Advanced research on helicopter blade aerofoils", 6<sup>th</sup> European Rotorcraft Forum, Paper No 49, 1980.
116. Van Den Berg, B., and Elsenaar, A., "Measurements in a three-dimensional incompressible turbulent boundary layer in an adverse pressure gradient under infinite swept wing conditions", NLR TR 72092 U, 1972.
117. Vronsky, T., "High Performance Cost-Effective Large Wind Turbine Blades Using Air-Jet Vortex Generators", ETSU W/41/00541/REP, 1999.
118. Wallis, R.A., "The use of airjets for boundary layer control", Aeronautical Research Laboratories, Australia, Aero note no 110, 1952.
119. Wallis, R.A., "A preliminary note on a modified type of air-jet for boundary layer control", Aeronautical Research Council, CP No 513, 1956.
120. Weaver, D., McAllister, K.W., and J. Tso, "Suppression of Dynamic Stall by Steady and Pulsed Upper-Surface Blowing", NASA Technical Paper 3600, 1996.
121. Wilby, P.G., "The aerodynamic characteristics of some new RAE blade sections, and their potential influence on rotor performance", Vertica, Vol 4, 1980, pp 121-133.
122. Wilby, P.G., "An experimental investigation of the influence of a range of aerofoil design features on dynamic stall onset", 10<sup>th</sup> European Rotorcraft Forum, Paper No 2, 1984.
123. Wu, J.M, Lu, X.Y, Denny, A.G., Fan, M., and Wu, J.Z., "Post-stall Flow Control on an Aerofoil by Local Unsteady Forcing", AIAA Paper 97-2063.
124. Wagnanski, I., "Method and apparatus for delaying the separation of flow from a solid surface", U.S.Patent 5 209 438, 1993.

125. Wynanski, I., "Boundary Layer and Flow Control by Periodic Addition of Momentum (Invited)", AIAA Paper 97-2117, 4<sup>th</sup> AIAA Shear Flow Control Conference, 1997.
126. Yon, S.A., and Katz, J., "Study of the Unsteady Flow Features on a Stalled Wing", AIAA Journal, Vol 36, No 3, 1998, pp 305-312.
127. Yu, Y.H., Lee, S., McAllister, K.W., Tung, C., and Wang, C.M., "Dynamic Stall Control for Advanced Rotorcraft Application", AIAA Journal, Vol 33, No 2, 1995, pp 289-295.

## Appendix A: Aerofoil/wing pressure orifice locations

<u>RAE 9645</u>			<u>NACA 23012C</u>			<u>Swept wing</u>		
Orifice	x	y	<i>Static</i>			<i>z/b = 0.50</i>	<i>z/b = 0.25 &amp; 0.75</i>	
	(mm)	(mm)	Orifice	x	y	Orifice	x	y
				(mm)	(mm)		(mm)	(mm)
1	485	2	1	0	0	1	0.2	-0.3
2	450	9	2	2	4	2	1	0.3
3	410	17	3	5	8	3	2	1.4
4	370	24	4	11	14	4	4	2.7
5	330	28	5	19	19	5	8	4.4
6	290	33	6	42	29	6	12	6.3
7	250	37	7	72	35	7	17	7.9
8	210	40	8	108	40	8	23	10.1
9	170	41	9	139	42	9	30	11.9
10	135	42	10	184	43	10	37	13.0
11	100	41	11	233	41	11	46	14.4
12	70	37	12	286	37	12	58	16.7
13	50	34	13	342	29	13	70	17.4
14	38	30	14	401	19	14	81	17.4
15	25	25	15	431	12	15	93	14.1
16	13	18	16	462	5	16	116	11.0
17	5	11	17	483	-1	17	128	7.4
18	2	6	18	432	-2	18	151	3.7
19	1	5	19	373	-4	19	168	0.1
20	0	0	20	316	-7	20	174	-7.4
21	1	-2	21	261	-10	21	186	7
22	4	-5	22	210	-13	22	197	6
23	10	-7	23	163	-15	23	203	5
24	25	-10	24	111	-16	24	215	3
25	50	-13	25	76	-15	25	220	2
26	100	-16	26	49	-14	26	232	0
27	200	-18	27	6	-9	27	186	-7
28	325	-14	28	2	-6	28	139	-14
29	400	-8	<i>Dynamic</i>			29	93	-17
30	475	-2	Orifice	x	y	30	46	-14
				(mm)	(mm)	31	23	-12
			1	6	-9	32	3	-7
			2	0	0	33	1	-6
			3	108	40	34	0.4	-5
			4	184	43	35	0.0	-1
			5	342	29			
			6	29	0			
			7	483	-1			